

Coulomb Interaction and Transport in Graphene Structures

Zur Erlangung des akademischen Grades eines

DOKTORS DER NATURWISSENSCHAFTEN

von der Fakultät für Physik des Karlsruher Instituts für Technologie (KIT)

genehmigte

DISSERTATION

von

Dipl. Phys. Michael Schütt
aus Offenburg

Tag der mündlichen Prüfung: 25.01.2013

Referent: Prof. Dr. A. D. Mirlin

Korreferent: Prof. Dr. J. Schmalian

To my wife

*For giving me a haven in troubling times,
for her endless support and for keeping my
feet on the ground when physics pulls to
hard.*

To my parents

*For the unconditioned trust I received, for
stimulating my curiosity and for everything
else.*

Contents

1	Introduction	1
2	Basics	5
2.1	Graphene	5
2.1.1	Definition	5
2.1.2	The Tight-Binding Approach	6
2.1.3	The Dirac Hamiltonian	8
2.1.4	Differences Between Graphene and Fermi-Liquid	9
2.2	Coulomb Interaction	10
2.2.1	Interaction Effects in a 2D Electron Gas in Contrast to Graphene	12
2.3	Field Theoretical Formulation and Notation	12
2.4	The Keldysh Formulation	14
2.4.1	Keldysh Objects	14
2.5	The Kinetic Equations	17
2.5.1	Derivation of the Kinetic Equation	18
2.5.2	The Hydrodynamic Equations	22
3	Coulomb Interaction in Graphene: Previous Analysis	27
3.1	Coulomb Interaction in Graphene at Zero Temperature	27
3.1.1	Renormalization Group Analysis	27
3.1.2	The Polarization-Operator	29
3.1.3	The Scattering Rate	32
3.1.4	Discussion	33
4	Coulomb Interaction in Graphene: Finite Temperature Analysis	35
4.1	The Polarization Operator at Finite Temperature	35
4.1.1	The RPA Screened Interaction	38
4.1.2	Plasmons	38
4.2	The Rates at Finite Temperature	41
4.2.1	Quantum Scattering Rate in Graphene	41
4.2.2	Dephasing Rate at High Temperatures	46
4.2.3	Energy Relaxation Rate	46
5	Transport	49
5.1	Basics	49
5.1.1	Drude Theory	49
5.1.2	Transport in Graphene	51
5.2	Previous Works	53
5.2.1	The Kinetic Equation for Graphene	53

5.2.2	The Functional Approach	54
5.2.3	The Conductivity in Graphene	58
5.2.4	Non Analytic Corrections	60
5.3	Hydrodynamics for Graphene	62
5.3.1	The local Hydrodynamic picture	62
5.3.2	Derivation of the non-local Hydrodynamics	64
5.4	Diagrammatic Analysis	65
5.4.1	Transport Scattering Rate due to Inelastic Collisions	66
5.4.2	Transport Scattering Rate: Results	68
5.4.3	Collision-Limited Conductivity	70
5.4.4	Qualitative Discussion of the Effect of Disorder and Comparison with Experiments	72
6	Coulomb Drag in Graphene: Basics and Previous Work	75
6.1	Definition of Coulomb Drag	75
6.1.1	Classical Description	76
6.2	Coulomb Drag in 2DEG	77
6.2.1	Coulomb Drag in Graphene in Contrast to Coulomb Drag in 2DEG	77
6.3	Coulomb Drag in Graphene: a Brief History	78
6.4	The Perturbative Approach	78
7	Coulomb Drag in Graphene: The Kinetic Equation Approach	81
7.1	The Two Layer Kinetic Equation	81
7.1.1	Formulation of the Two Layer Kinetic Equation	81
7.1.2	The Ansatz for the Two Layer System	83
7.1.3	The Effective Kinetic Equations and Thermalization	84
7.2	The Coulomb Drag Resistivity in Graphene	86
7.2.1	Asymptotics of the Resistivity and its Numerical Evaluation	88
7.2.2	Discussion of the Results and Their Validity	92
7.2.3	Comparison to Experiment	95
8	Coulomb Drag in Graphene: Generalizations and Further Developments	97
8.1	Multilayer Drag	97
8.2	The Hall Drag and Magnetodrag	99
8.2.1	Applicability of the Kinetic Equation	99
8.2.2	The Kinetic Equation in the Presence of a Magnetic Field	100
8.2.3	Asymptotics of the Hall Drag	103
8.2.4	Properties and Analysis of the Hall Drag	105
8.2.5	Magnetic Field Induced Drag at the Dirac Point	107
8.2.6	Comparison to Experiment	108
8.3	Higher-Order Drag	109
8.3.1	The Vanishing of the Leading Order	109
8.3.2	The Changes Due to Higher Order-Drag	111
8.4	Drude-Like Picture for Drag	115
9	Conclusion	119

A	Keldysh Objects and the Kinetic Equation	123
A.1	Keldysh Self-energy and Keldysh Polarization Operator	123
A.1.1	The Keldysh Self-energy in Lowest Order	123
A.1.2	The Keldysh Polarization Operator	124
A.2	The Collision Integral	124
A.2.1	Coulomb interaction: Lowest Order	125
A.2.2	Coulomb Interaction: Sub-leading Contributions	127
A.3	The Linearized Collision Kernel	131
B	Polarization and Rates	133
B.1	Polarization Operator	133
B.2	Calculating the Rates	135
B.2.1	Definitions of the Rates	135
B.2.2	Simplifying the Integrand	136
B.2.3	Results for the Rates	138
B.3	Scattering Rates from the Generalized Golden Rule	142
C	Effective Kinetic Equations and Collision Integrals	145
C.1	Solution of the Effective Kinetic Equation	145
C.1.1	The Functional Approach	145
C.1.2	Derivation of the Effective Kinetic Equation for Coulomb Drag of Two Layers	146
C.1.3	The Effective Kinetic Equation for Three Layers	148
C.1.4	The Effective Kinetic Equation in Presence of a Magnetic Field	149
C.2	The Integrals Appearing within the Effective Kinetic Equation	150
C.2.1	Simplification of the Generalized Vertex Functions (GVF)	151
C.2.2	Insights to the Collision Kernel	152
C.2.3	The Collision Kernels Involving the Imbalance Mode	153
C.3	The Asymptotics	154
C.3.1	The Limit of Small Chemical Potential	155
C.3.2	The Limit of Large Chemical Potential	157
D	Correlated Disorder and Diffusive Corrections to the Higher-Order Drag	163
D.1	Estimation of Diffusive Higher Order-drag	163
D.2	Estimation of Correlated Disorder Contributions	165
D.2.1	A. Short-Range Correlations: Correlated Impurity Scattering	165
D.2.2	B. Long-Range Correlations: Correlated Macroscopic Inhomogeneities	167
	Bibliography	183

1

Chapter 1

Introduction

It was less than a decade ago that in Manchester a material was synthesized for the first time in a controlled way [1] whose properties at first sight seem implausible. What Andre Geim and Konstantin Novoselov managed to fabricate is graphene [2], a mono-layer of carbon atoms forming a planar (2D) honeycomb structure. Since it is only one atom thick, graphene is a truly two-dimensional crystal, something that for thermodynamic reasons was thought not to exist [3, 4]. The way they managed to isolate graphene is legendary; which amongst several other steps, scotch tape to peel the layers off prepared graphite samples is involved. The material they managed to identify afterwards on their substrate has since then written superlatives with its unique properties. From the mechanical point of view, experiments showed that graphene is the strongest material ever measured [5]. It appears to be essentially impermeable to any gases [6], and graphene based membranes turn out to be Helium-Leak-Tight but allow water to permeate [7]. Graphene has a remarkably high thermal mobility [8] and even its optical properties are fascinating, since this one atom thick layer of carbon atoms absorbs almost exactly $\pi\alpha \approx 2.3\%$ (α being the fine structure constant) of white light [9], quite an amount for a one atom thick material. On the other hand 97.7% is transmitted making it essentially transparent. Nonetheless graphene layers exhibit very good electronic properties with mobilities that exceed $100,000\text{cm}^2\text{V}^{-1}\text{s}^{-1}$ [10]. Due to this high mobility graphene exhibits the quantum Hall effect already at room temperature [11]. It is in this context not at all surprising that Andre Geim and Konstantin Novoselov got the Nobel Prize of Physics in 2010, only a few years after their discovery of graphene.

Since 2004 the number of graphene related works has grown tremendously (from 155 in 2004 to 9,878 in 2012 for graphene related topics in the web of science). The discovery of graphene essentially created a complete field within physics dealing with the properties of graphene and possible applications. But on top of all this, the most astonishing fact is that graphene has developed within a few years from a subject of basic research towards a material that is heading towards its first commercial applications. Current road-maps suggest the development of graphene based touch screens and rollable E-paper within a few years from now [12]. In slightly longer terms there are many other applications suggested. As examples we may name terahertz detectors or high frequency transistors, which rely on the unique electronic properties of graphene.

In view of the seemingly well planned and focused road-map of applications one might get the impression that graphene is a material that is already fully understood and the only task left is to harvest possible applications. The surprising and wonderful fact, instead, is that graphene has still many mysteries and there seems so far no end in the unveiling of astonishing properties.

Looking at the electronic structure, there are several approaches to graphene: coming from semi-

conductor physics graphene may be viewed as a semiconductor with zero bandgap whereas scientists working with metallic systems may refer to graphene as a semimetal. From the pure fact that both terms are used, one can already conclude that graphene somehow “sits between the chairs”. It is indeed possible to tune, by gating, the charge carrier concentration from hole like carriers through a charge neutral point, the so-called Dirac point, towards electron like carriers and reach there, if sufficiently many carriers are present, metallic behavior. At the Dirac point, however, graphene is not insulating, as one may expect due to the absence of charge carriers. There is a minimal conductivity left of the order of e^2/h [13]. Whichever classification is favored, the key point of graphene’s electronic structure is the peculiar behavior of its charge carriers. The compelling fact¹ about the quasi-particles in graphene is that they obey the equations of motion of massless relativistic particles [14], i.e., the Dirac equation. The resulting consequences are observable in experiments and even allow for verification of some phenomena, like the “zitterbewegung” [13, 15] responsible for the minimal conductivity, which instead of a large particle collider usually required for ultra-relativistic phenomena, is seen within a table top experiment. The need to deal with relativistic particles is a rather uncommon feature in condensed matter systems since the focus in these systems is on low energies. Particles with low energies usually do not reach relativistic velocities which forces us to look for a different reason to explain the relativistic behavior. It is known that symmetry can provide us with such a mechanism [14]. In graphene the lattice itself provides us with the symmetry needed to gain massless quasi-particles. It is very important to stress that the particles velocity is way smaller than the speed of light; the crucial point is, that due to the lattice symmetry this smaller velocity appears to them as if they move with the speed of light. We may avoid confusion by calling the true speed of light c and the fake speed of light the particles in graphene exhibit v_F . Whereas free particles obey the Lorentz symmetry with respect to c , the quasi-particles in graphene do so with v_F . The ultra-relativistic physics that is gained by this symmetry unveils itself in phenomena usually only discussed in high energy physics. These phenomena are now experimentally verified in condensed matter systems like the Klein tunneling [16] through potential barriers.

The question that we dedicate our attention to in this thesis is: *what is the influence of Coulomb interaction on the electronic properties of graphene?*

The motivation to study interaction effects is the observation, that due to the higher and higher quality of the samples available these days [10], interaction effects should become more and more relevant and more easily measurable. A classical experimental setting in this regard is the Coulomb drag [17, 18] that relies on the interaction between two electronically separated layers. But manifestations of the Coulomb interaction appear already in much simpler setups. The electrical current in graphene for example, is affected by Coulomb interaction. If one ignores the lattice, this sounds unlikely since current is protected by momentum conservation due to Galilean invariance. In real systems, a lattice affects this naive picture allowing for umklapp scattering, which is responsible for the T^2 -dependence of conductivity in Fermi-liquids. In graphene the electronic properties are governed by the boundary of the Brillouin zone, which via umklapp scattering processes forms effectively graphene’s Lorentz symmetry and thus leads to relaxation of the current due to the Coulomb interaction.

We will in this work consider both conductivity of clean graphene and Coulomb drag in double layer graphene. But first, we must determine the effective strength of the Coulomb interaction.

The effective coupling strength α_g in free graphene (a counterpart of the fine structure constant of

¹From the Big Bang Theory: “The Einstein Approximation”, (Season 3, Episode 14), (2009-2010 Premiered on CBS)
Howard: Sheldon, what the hell are you doing?

Sheldon: Same thing I’ve been doing for three days. Trying to figure out why electrons behave as if they have no mass when traveling through a graphene sheet.

quantum electrodynamics) is of order unity. This might raise the question whether interaction can induce gaps in the system. However, experiments on free-standing graphene show no indication of a gap down to very low temperatures [19]. To be able to proceed analytically, we will assume that α_g is small. This is the case for the majority of experiments where graphene on insulating dielectric substrates is studied.

However, when interaction is perturbative one might wonder what discriminates the setup from the well-known high energy picture of quantum electrodynamics (QED). In QED, ultra-relativistic particles move nearly as fast as the interaction between them, making them essentially non-interacting. In graphene it is the fact that, although its quasi-particles behave ultra-relativistically, they appear, in contrast to the electrodynamics obeying the Lorentz symmetry with respect to c , as completely non-relativistic. From the point of view of the quasi-particles in graphene we are in an ultra-relativistic (with respect to v_F) setup that interacts faster than “light” (the maximal speed of graphene quasi-particles v_F). It is this delicate but crucial point of explicit and strong Lorentz symmetry breaking that forms the heart of the phenomenon we will refer to as forward scattering resonance — a resonance that creates interesting changes in the electronic behavior of the system. Within this work we will consider scattering rates that possess non-trivial structure due to this phenomenon. Furthermore, we will see how this forward scattering resonance condenses into a direction dependent equilibrium ansatz, that allows us to solve analytically the kinetic equation. In this regard, this resonance guides us throughout this work and will provide us with rich physics and interesting effects to deal with.

This thesis is organized as follows:

In **Chapter 2**, we establish the basic language and provide the elementary concepts, like the forward scattering resonance, needed to understand the peculiarity of graphene.

With **Chapter 3** an overview is given on the phenomena related to the interplay of the Coulomb interaction and graphene. We will show that in some respect, the problem is ill-defined at the Dirac point.

The resolution to this obstacle is given in **Chapter 4**, where we focus on the electronic structure at the Dirac point. In this chapter we will determine the quasi-particle lifetime, dephasing rate and energy relaxation rate within the random phase approximation, which turns out to be a suitable way at finite temperature.

Starting with **Chapter 5**, we will consider transport phenomena in graphene. We will present the method of previous works and explain the underlying connection to the foregone chapter. For clarity, we will cover two different approaches to transport, the kinetic equation used by previous works and a diagrammatic calculation of the conductivity within the random phase approximation. We will see that both methods complement each other. Further we will present the hydrodynamic formulation of the transport in graphene.

Subsequently we, will introduce the effect of Coulomb drag in **Chapter 6** and briefly describe the activities that have been performed in the field.

Chapter 7 is dedicated to the studies of the physics governing the Coulomb drag in graphene. In this chapter we will employ the kinetic equation approach to the Coulomb drag and will introduce the phenomenon of thermalization that appears between the layers.

In the following **Chapter 8**, we extend the formulation of the Coulomb drag towards multi-layer drag and Hall drag. We will present a possible extension towards higher order drag and we will present a Drude-like formulation, which allows for a more intuitive approach to the problem.

Finally, we finish in **Chapter 9** with a conclusion and a summary of the obtained results.

2 Chapter 2

Basics

To those who do not know mathematics it is difficult to get across a real feeling as to the beauty, the deepest beauty, of nature ...

R. Feynman, The Character of Physical Law (1965) Ch. 2

For any serious discussion of a problem one needs to fix some basic language. This chapter is dedicated to provide briefly the basics of graphene, the Coulomb interaction and the formalism we are going to use throughout this work. Each of the topics deserves a far more complete discussion, which we cannot provide within this work but for which we will refer to literature within the corresponding sections.

2.1 Graphene

2.1.1 Definition

What is graphene [2, 20]?

Graphene is a flat monolayer of carbon atoms tightly packed into a two-dimensional (2D) honeycomb lattice, and is a basic building block for graphitic materials of all other dimensionalities. It can be wrapped up into 0D fullerenes, rolled into 1D nanotubes or stacked into 3D graphite.

A.K. Geim and K.S. Novoselov The rise of graphene [2]

Its diversity has made graphene a promising material with a plethora of ideas for possible applications. Since graphene is a fairly good conductor [13, 21], considering its one atom thickness, a valid question is why it conducts, or — to rephrase that — how the process of transport works in graphene. Of course, there are several known phenomena that affect transport, such as disorder or phonons, but, as will be shown, even the Coulomb interaction will affect transport in graphene. At this point we wish to remind the reader that the Coulomb interaction conserves the total momentum of the system. Thus, in systems where transport is affected by the Coulomb interaction it is clear that additional ingredients have to be taken into account. In condensed matter systems this is the lattice, which breaks the translation symmetry and turns momentum into quasi-momentum. When including the lattice, the Coulomb interaction can relax the current, since the quasi-momentum is still conserved but not the original kinetic momentum. The process allowing for relaxation is the umklapp scattering [22].

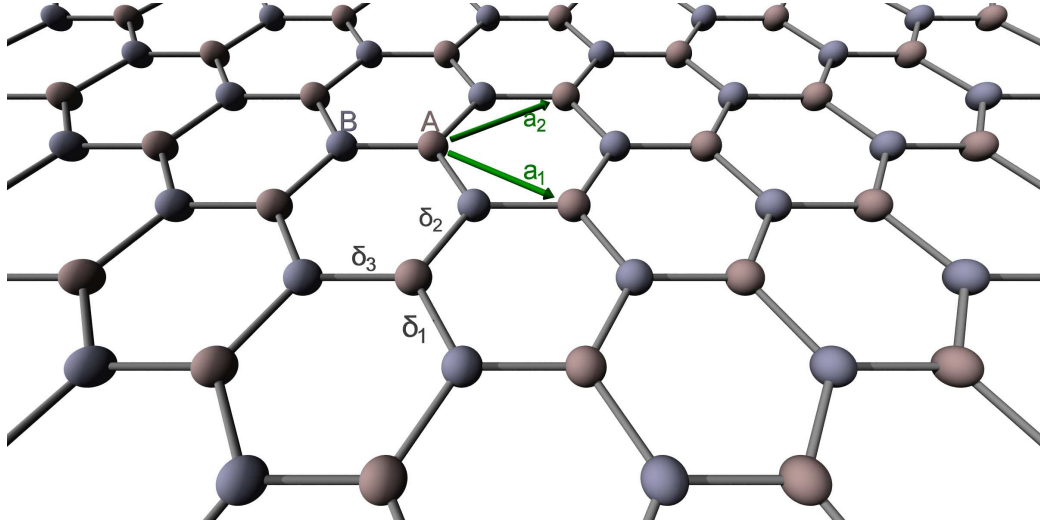


Figure 2.1: *The lattice of graphene with a colored emphasis on the sublattice separation.*

However, if one considers an effective field theory the lattice disappears, hence the Coulomb interaction seemingly can not relax the current due to Galilean invariance. In this work we will argue in terms of symmetries, rather than lattice properties, although these symmetries arise from the lattice. We will see that in graphene a Lorentz symmetry emerges allowing for relaxation of the current by the Coulomb interaction. Thus, the focus of our attention in this work is on the phenomena related to the electronic structure and the transport properties of graphene in presence of the Coulomb interaction.

2.1.2 The Tight-Binding Approach

Graphene owes his lattice structure to the sp^2 -bonding of the carbon atoms. Without going into the details of the chemistry of the bonds the crucial input we need to describe its electronic structure is the fact that it forms a honeycomb lattice. This is not part of the regular two dimensional Bravais lattices, since translation of single atom positions will not form periodically the hexagonal structure. To overcome this problem one chooses a basis containing two neighboring carbon atoms gaining a Bravais lattice that has triangular structure. One should note that since we need to have two identical atoms within the basis, we have explicitly created a symmetry that will manifest itself in a touching of the bands as shown in Fig. 2.2. But let us proceed step by step and define now a proper structure to describe graphene.

Let us designate the two different atoms of the basis A and B and the two vectors spanning the lattice

$$\vec{a}_1 = \frac{a}{2}(3, \sqrt{3})^T \quad \text{and} \quad \vec{a}_2 = \frac{a}{2}(3, -\sqrt{3})^T. \quad (2.1)$$

This is the nomenclature that is illustrated in Fig. 2.1.

Within the tight-binding approach we now assume that due to the overlap of atomic orbitals there is a finite probability for an electron to hop to one of its nearest neighboring atoms. Within this simplified model we can therefore think about hopping of electrons from one atom to its neighboring

ones with an amplitude of t :

$$H = -t \sum_{\langle i,j \rangle, \sigma} \left(a_{\sigma,i}^\dagger b_{\sigma,j} + h.c. \right) = \sum_{\langle i,j \rangle, \sigma} \begin{pmatrix} a_{\sigma,i}^\dagger & b_{\sigma,i}^\dagger \end{pmatrix} \cdot \begin{pmatrix} 0 & -t \\ -t & 0 \end{pmatrix} \cdot \begin{pmatrix} a_{\sigma,j} \\ b_{\sigma,j} \end{pmatrix}.$$

The notation $\langle i, j \rangle$ indicates the nearest neighbors of the Bravais lattice, where a and b distinguish the sublattices (atoms A and B) on the operator level. Further we take into account electrons with different spins σ . If we proceed by transforming into momentum space we obtain

$$H = \sum_{k, \sigma} \begin{pmatrix} a_{\sigma,k}^\dagger & b_{\sigma,k}^\dagger \end{pmatrix} \cdot \begin{pmatrix} 0 & -t \sum_j e^{ik\delta_j} \\ -t \sum_j e^{-ik\delta_j} & 0 \end{pmatrix} \cdot \begin{pmatrix} a_{\sigma,k} \\ b_{\sigma,k} \end{pmatrix}.$$

The dispersion of the electronic system is now given by the eigenvalues of this Hamiltonian. The δ_s that appear here are the vectors connecting the nearest neighbors as shown in Fig. 2.1 and read:

$$\delta_1 = \frac{a}{2}(1, -\sqrt{3})^T \quad \delta_2 = \frac{a}{2}(1, \sqrt{3})^T \quad \delta_3 = a \quad (2.2)$$

The Dispersion of Graphene

The dispersion of graphene was calculated more than half a century before its discovery [23]. Within the above nearest-neighbor calculation the dispersion is given by

$$\epsilon(k) = \pm t \left| \sum_j e^{ik\delta_j} \right| = \pm t \sqrt{3 + 2 \cos(\sqrt{3}k_y a) + 4 \cos\left(\frac{\sqrt{3}}{2}k_y a\right) \cos\left(\frac{3}{2}k_x a\right)}. \quad (2.3)$$

A graphical illustration of this dispersion can be seen by Fig. 2.2. The bandwidth is of the order of eV , which is determined by the scale of the parameter t (a microscopic property). Since we are interested in macroscopic properties we need to know the low energy behavior of electronic excitations in graphene, which means that the physics we are mainly interested in will be around the K -points¹, where the energy is zero,

$$K = \left(\frac{2\pi}{3a}, \frac{2\pi}{3\sqrt{3}a} \right) \quad \text{and} \quad K' = \left(\frac{2\pi}{3a}, -\frac{2\pi}{3\sqrt{3}a} \right).$$

These are the points where the dispersion is exactly zero. One should note that these points are not an artefact of the nearest-neighbor calculation. The existence of the K -points and the dispersion close to it follows from symmetry considerations [14, 24, 25]. If we expand the surrounding dispersion we arrive at a dispersion of the form

$$\epsilon(p) \approx \pm \underbrace{\frac{3}{2}ta}_{v_F} |p| + O\left(\frac{p}{K}\right)^2. \quad (2.4)$$

Subsequently, we will derive an effective Hamiltonian that will describe the physics around those K -points.

¹It is worth to note that the K -point is at the boundary of the Brillouin zone. This means that a symmetry that arises from the K -point can have non-Galilean contributions, which correspond to umklapp scattering processes.

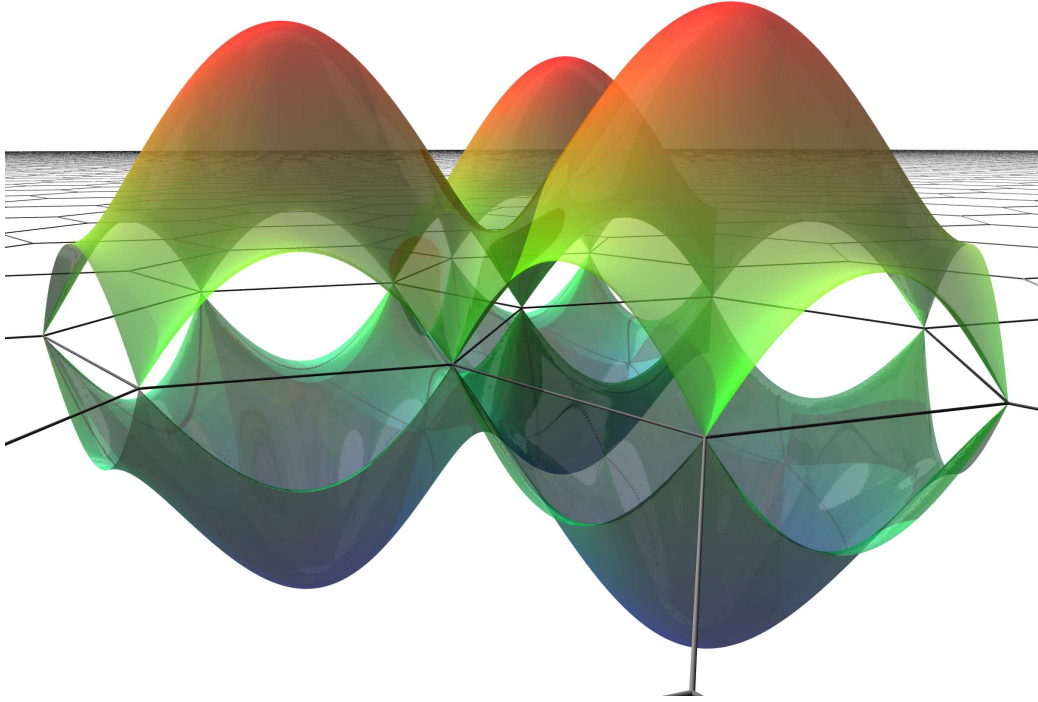


Figure 2.2: *The dispersion of graphene in the reciprocal lattice. The figure shows three Brillouin zones to demonstrate the formation of the two inequivalent K points in graphene.*

2.1.3 The Dirac Hamiltonian

The Hamiltonian around the K -points can be derived if one expands the previous form of the Hamiltonian in small momenta around the momentum K or similarly K' :

$$\begin{aligned}
 -t \sum_j e^{\pm i(K+p)\delta_j} &= -t i (e^{\pm iK\delta_1} p\delta_1 + e^{\pm iK\delta_2} p\delta_2 + e^{\pm iK\delta_3} p\delta_3) = \\
 &= -t a \frac{3i + \sqrt{3}}{2} (ip_x \pm p_y) = v_F (p_x \mp ip_y) e^{i\varphi} \stackrel{\text{up to a phase}}{=} v_F \boldsymbol{\sigma} \cdot \vec{p}. \quad (2.5)
 \end{aligned}$$

Thus the low energy physics of the electronic system in graphene appears to follow the Dirac-Hamiltonian. By simple replacement of v_F with c one obtains the ultra-relativistic Hamiltonian describing for example massless neutrinos in particle physics. Although this means that the behavior of our excitations is ultra relativistic one should note that there is no true speed of light involved. In graphene the Fermi velocity is $v_F \approx \frac{c_0}{300}$, which definitely allows for a non-relativistic treatment. It is a property of the lattice that creates, due to interference, electronic excitations that behave in an ultra-relativistic manner without actually reaching the true speed of light. This is what we refer to when speaking about ultra-relativistic physics in graphene.

We see in the Hamiltonian above Eq. (2.5) that, since we neglect spin orbit-coupling, there is no signature of spin left, which means we can treat spin as a mere degeneracy. Furthermore we have the

freedom to choose the point to expand around for the low energy model, namely K or K' . In both cases, we arrive at the same Hamiltonian (up to a phase), which means that we have an additional degeneracy due to the valley we expand around, the so-called valley degree of freedom. In total we therefore have a degeneracy $N = 4$ in graphene.

2.1.4 Differences Between Graphene and Fermi-Liquid

Having derived the basics of graphene it is worth looking back and recapitulating what distinguishes it from the usual Fermi liquid (FL) systems. We will concentrate on properties that will be important for our purpose. From the perspective of electronic properties one of the most crucial differences is the group velocity. For this reason we compare (for simplicity) a Fermi liquid, in systems with a parabolic dispersion², with graphene:

$$\text{Graphene } \epsilon = v_F |\vec{p}|$$

$$\text{Parabolic FL } \epsilon = \vec{p}^2 / (2m)$$

$$\vec{v} = \frac{\partial \epsilon(\vec{p})}{\partial \vec{p}} = v_F \frac{\vec{p}}{\epsilon}, \quad (2.6)$$

$$\vec{v} = \frac{\partial \epsilon(\vec{p})}{\partial \vec{p}} = \frac{\vec{p}}{m}. \quad (2.7)$$

It is essential to notice, that the absolute value of the velocity in graphene is constant. With higher momentum a parabolic spectrum has a higher velocity but in graphene that is not the case. The reason is the ultra-relativistic physics we are dealing with. In this sense, the velocity and the momentum in graphene are two essentially different quantities. This distinguishes graphene from a parabolic Fermi-liquid where momentum and velocity differ only by a constant. As we will see below, the impact of this difference becomes particularly dramatic in the vicinity of the Dirac point.

When treating FL systems one linearizes around the Fermi energy and argues that within this approximation the electronic excitations have constant velocity. To compare the two systems within the linearized FL approximation we will look at the energy conservation represented in terms of delta-distribution constraints for the situation of a small transferred momentum $\vec{q} = \vec{p}_2 - \vec{p}_1 = \vec{p}_{1'} - \vec{p}_{2'}$. The general form of the constraint is given by

$$\delta \left[\vec{q} \left(\frac{\partial \epsilon(\vec{p}_1)}{\partial \vec{p}_1} - \frac{\partial \epsilon(\vec{p}_{1'})}{\partial \vec{p}_{1'}} \right) + \frac{1}{2} \vec{q} \left(\frac{\partial^2 \epsilon(\vec{p}_1)}{\partial \vec{p}_1 \partial \vec{p}_1} + \frac{\partial^2 \epsilon(\vec{p}_{1'})}{\partial \vec{p}_{1'} \partial \vec{p}_{1'}} \right) \vec{q} \right]. \quad (2.8)$$

Further we assume that we are in a close vicinity of the Fermi-surface ($|\vec{p}_1| \approx p \approx |\vec{p}_{1'}|$). In the next step we will focus on the angular dependency between the momenta and consider therefore the difference up to π ($\gamma_{q1'} - \gamma_{q1} = \delta\gamma \bmod \pi$).

The expansion around small $\delta\gamma$ ($\delta\gamma \ll 1$) helps to gain insight into the difference between the parabolic Fermi liquid and graphene:

Graphene

Parabolic FL

$$\delta \left[v_F q \left(\sin(\gamma_{q1}) \delta\gamma \right) + \frac{v_F q^2}{p_F} \sin^2(\gamma_{q1}) + O(\delta\gamma^2) \right], \quad (2.9) \quad \delta \left[v_F q \left(\sin(\gamma_{q1}) \delta\gamma \right) + \frac{v_F q^2}{p_F} + O(\delta\gamma^2) \right]. \quad (2.10)$$

²Parabolic Fermi liquid in this context requires on top of the Fermi liquid configuration that the dispersion is close to free particles. Since Fermi liquid usually implies a linearization of the dispersion, parabolic Fermi liquid may sound strange. The crucial point to make is that already the quantity of the total number of particles needs to specify the dispersion beyond the linearized dispersion. Instead of having some mixed picture of Fermi liquid and semi-classical model we will consider a parabolic dispersion for the situations the non-linearized dispersion affects the system.

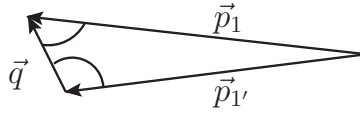


Figure 2.3: Illustration of the position of momenta \vec{p}_1 and $\vec{p}_{1'}$ to each other as well of the angles $\vec{q}\vec{p}_1 = qp_1 \cos(\gamma_{q1})$ and $\vec{q}\vec{p}_{1'} = qp_{1'} \cos(\gamma_{q1'})$.

A consequence of this analysis is that in graphene it is more likely that forward scattering occurs, as compared to a parabolic FL, this is known as the (FSR). This is seen by the appearance of $\sin \gamma_{q1}$ in the second order contribution in Eq. (2.9) as compared to Eq. (2.10). In Fig. 2.3 the correspondence of angles of with $\gamma_{q1} \approx 0$ or $\gamma_{q1} \approx \pi$ to forward scattering is shown. This statement is not restricted to small momenta only, the curvature argument is only particularly transparent. The possibility of forward scattering is already obvious when writing down the energy and the momentum conservation with the constraint of collinear momenta. In such a situation the two conservation laws are simultaneously fulfilled. The above estimation gives us some insight as to how the singularity in this case looks like and how it is may be cut off by curvature. On those general terms it becomes clear that only few dispersions, namely the truly linear ones, will exhibit the sensitivity to forward scattering processes.

One should mention that within the control parameter $v_F q^2 / p_F$ the regime where this difference appears can be formally reduced until it vanishes when the Fermi momentum reaches infinity. This means that graphene will indeed show behavior of a Fermi liquid if the chemical potential is high enough ($v_F q^2 / (p_F) \lll 1$). Still, the forward scattering resonance will be a feature present in graphene and dominating its physics.

Another quite relevant point distinguishing graphene from a parabolic FL is the density of states (DOS). This quantity reflects the properties of the spectra in a peculiar way such that the constant DOS of a two dimensional parabolic FL has to be contrasted with

$$\nu(\epsilon) = \int \frac{d^2 p}{(2\pi)^2} \delta(\epsilon - v_F |\vec{p}|) = \frac{|\epsilon|}{2\pi v_F^2}. \quad (2.11)$$

So in graphene the DOS per spin and valley is vanishing at the Dirac point.

The three effects we have discussed here (forward scattering resonance, vanishing DOS and difference of velocity and momentum) are the ones to which we will trace back almost all the peculiarities of graphene discussed in this work.

2.2 Coulomb Interaction

We may find illustrations of the highest doctrines of science in games and gymnastics, in traveling by land and by water, in storms of the air and of the sea, and wherever there is matter in motion.

J. Maxwell, Introductory Lecture on Experimental Physics held at Cambridge

One of the most basic forces relevant to our everyday life is the force that comes with electromagnetic charges. It appears in astonishing many ways in our daily routine and belongs to the basic things even pupils learn at school. The electrostatic interaction between charges, the Coulomb interaction, is

not only a well-studied force, it is also always present in a system with charged particles. The non-interacting description of graphene already shows physical properties unusual enough in condensed matter physics to warrant looking more closely at the effects the Coulomb interaction can induce.

Nevertheless, the emphasis we put on Coulomb interaction in graphene might confuse the reader, since it is clear that by its nature the Coulomb interaction is always present and involved in the dynamics of charged particles. So one should make it clear as to why in the field of condensed matter one often discards the Coulomb interaction entirely or treats it like a short-range interaction instead, which the bare Coulomb interaction is clearly not. The main reason for this is screening.

The electrostatic interaction between particles can be strongly reduced by inducing charge separation between different charge carriers. For example, if one puts a charged particle into a fluid of charge carriers it will repel equally charged particles in its surrounding, creating a region that appears to be slightly charged with opposite charge when compared to the mean charge density of the fluid. This process, called Thomas–Fermi screening, can reduce the relevance of interaction enormously. This does not necessarily mean that particles stop interacting at all but that the nature of interaction between two particles becomes more local, maybe even short-range due to screening³.

At the same time one knows that, for example in Luttinger liquids [27–33], reduced dimensionality can enhance the effects of interaction strongly, which may even change the nature of the quasi-particles in the system.

Due to its two-dimensional structure and, even more, due to its vanishing density of states (DOS) at the Dirac (K or K') point, screening is very weak or even absent in graphene, demanding that we really need to consider the proper long-range Coulomb interaction. So the question is: How important is the Coulomb interaction for the electronic properties of graphene?

If one looks up the basic properties of matter-light interaction one comes across the coupling strength of the electromagnetic interaction, the fine structure constant

$$\alpha = \frac{e^2}{4\pi\epsilon_0\hbar c_0} \stackrel{\hbar=1}{=} \frac{e^2}{4\pi\epsilon_0 c_0} \approx \frac{1}{137}. \quad (2.12)$$

Its low value implies that the interaction of light and matter is rather weak in vacuum. But in graphene it turns out that c_0 is replaced by v_F , enhancing the coupling strength by a factor 300,

$$\alpha_g = \frac{e^2}{4\pi\epsilon_0\epsilon_r v_F} \approx \frac{2.2}{\epsilon_r}, \quad (2.13)$$

where ϵ_r is the dielectric constant⁴. One can interpret this as a consequence of the slower velocity v_F for the Dirac fermions which causes an enhanced interaction since the effective time particles interact is increased.

Due to the possibility of strong coupling in the system there have been several attempts to find signatures like exciton condensation or a Stoner instability [36–38], which would create a gap in the

³There is an important difference between screening in 3D and 2D. Whereas screening in 3D yields exponential suppression of the interaction for distances larger than the screening length, forming effectively point like interaction if screening length is comparable with Fermi-length. The 2D case is different. There screening appears to form a power law dependence similar to a quadrupole for large distances [26]. The Coulomb interaction is thus screened algebraically.

⁴In three dimensions the coupling constant of the coulomb interaction, that enters an effective model, is itself effective since high energy processes allow modifications of the coupling constant [34]. Nevertheless is the coupling constant for graphene the bare coulomb interaction (up to screening by the substrate). This is due to the inability of high energy excitations to screen the coulomb interaction in two dimensions [35].

spectrum. Since this has not yet been observed and since graphene on substrates gains an additional reduction of the Coulomb interaction strength by screening (ϵ_r) our approach to the problem will be perturbative in α_g while keeping the Coulomb interaction as a long-range interaction.

Treating the long-range Coulomb interaction perturbatively and considering the fact that we have ultra-relativistic particles, one could think that we are dealing with QED, the theory of interactions between light and matter. Obviously, nearly every condensed matter system may ultimately be reduced to the non-relativistic limit of the “real” QED. This way, we end up with effective theories describing the low energy behavior of our system. In graphene the low energy model is described by Eq. (2.5), which corresponds to an ultra-relativistic theory. This means that although the particles behave like massless Dirac fermions moving at the Fermi velocity v_F , their “speed of light” is not the speed the Coulomb interaction propagates with, which is c . From the viewpoint of the Coulomb interaction we are still in a non-relativistic theory. Thus the quasi particles in graphene interact instantaneously, although the theory that describes them without interactions is Lorentz-invariant. From the point of view of a Dirac fermion (v_F) we have a “faster than light” interaction (c) in graphene. This makes the treatment of the Coulomb interaction in graphene quite different from the treatment within QED.

2.2.1 Interaction Effects in a 2D Electron Gas in Contrast to Graphene

The Fermi liquid theory is based upon Landau’s quasi-particle picture, which requires that small excitations with an energy close to the Fermi energy ($\epsilon/\epsilon_F \ll 1$) need to have a much smaller energy broadening (decay rate Γ) to be well-defined quasi-particles [39, 40]. This statement appears to hold as long as there is no symmetry breaking induced by the interaction. In 2d electron gases (2DEG) it can happen that even with screening the character of the interaction may remain long-range, which may lead to singularities that change the thermodynamic quantities of the system. Still those systems appear to be Fermi liquids in the sense that the quasi-particle picture stays largely intact [41].

Graphene at the Dirac point behaves differently since screening is less effective. This leads to consequences in the quasi-particle picture, causing it to show marginal Fermi-liquid behavior [42]. In this sense graphene is more sensitive to Coulomb interaction than usual 2DEGs.

In disordered 2DEGs the situation becomes more complicated since one needs to consider the interplay of Coulomb interaction and disorder effects [43, 44]. Since our particular interest is in the effects induced by Coulomb interaction we will not consider the interplay of interactions and disorder that appears in the diffusive limit, like the Altshuler-Aronov type contributions.

2.3 Field Theoretical Formulation and Notation

It seems that if one is working from the point of view of getting beauty in one’s equations, and if one has really a sound insight, one is on a sure line of progress

P. Dirac, The Evolution of the Physicist’s Picture of Nature

The field theoretical formulation, especially in quantum mechanics, is a very elegant, intuitive description, since the complexity that appears in the presence of many particles is completely absorbed into the usage of fields. The basic idea of this is of course very old, since hydrodynamics basically already builds upon such an interpretation. The usage of this formulation will allow us to define a proper language to express the physics we will discuss within this work. For details we refer to the literature [39, 40, 45–47] on this subject for details. In this section we will only briefly sketch the formalism prerequisite for our further discussion. It will not be the only method to describe our system but it

is a particularly beautiful one, bringing to the surface a lot of fundamental and interesting insights of the physics governing the phenomena we are looking for.

The Hamiltonian describing the physics of our model at energies that are small enough to keep the approximation of a conic spectrum ($\epsilon \lesssim 1eV$) is given by

$$\begin{aligned} \hat{H} &= \hat{H}_0 + \hat{V} \\ &= \sum_{\nu} \int d^2r \hat{\Psi}_{\nu}^{\dagger}(\vec{r}) \left(-iv_F \boldsymbol{\sigma} \cdot \vec{\nabla} \right) \hat{\Psi}_{\nu}(\vec{r}) + \frac{1}{2} \sum_{\nu, \nu'} \int d^2r_1 d^2r_2 \hat{\Psi}_{\nu}^{\dagger}(\vec{r}_1) \hat{\Psi}_{\nu'}^{\dagger}(\vec{r}_2) \frac{e^2}{\epsilon |\vec{r}_1 - \vec{r}_2|} \hat{\Psi}_{\nu'}(\vec{r}_2) \hat{\Psi}_{\nu}(\vec{r}_1). \end{aligned} \quad (2.14)$$

The spinors $\hat{\Psi}$ have two components in the sublattice space, σ_i are Pauli matrices operating in this space. The index ν labels N independent degrees of freedom (in graphene $N = 4$ accounts for the spin and valleys degeneracies). We set $\hbar = 1$. First we will focus on the case of undoped graphene and set the chemical potential (relative to the Dirac point) to zero, $\mu = 0$. It will be no problem to restore the chemical potential later, but the way to do so will be explained when needed.

The retarded (advanced) Green's function of the noninteracting Hamiltonian \hat{H}_0 (the bare Green's function) in the energy-momentum space has the form

$$G_0^{R,A}(\epsilon, \vec{p}) = \frac{\epsilon \mathbb{1} + v_F \boldsymbol{\sigma} \cdot \vec{p}}{(\epsilon \pm i0)^2 - v_F^2 p^2}. \quad (2.15)$$

The Green's functions have a matrix structure inherited from the Hamilton operator. An appropriate way to deal with the system is to rotate it into its eigenbasis. The two eigenstates one obtains this way correspond to the two chiral states of the system. If the direction of the momentum is fixed the two chiralities correspond to the lower or upper branch of the conic spectrum (particle and hole). Alternatively one can introduce the projection operators that distinguish between the two chiral states:

$$\mathcal{P}_{\pm}(\vec{p}) = \frac{\mathbb{1} \pm \boldsymbol{\sigma} \cdot \vec{n}}{2}, \quad (2.16)$$

where $\vec{n}_p = \vec{p}/p$ is the unit vector in the direction of momentum. With the help of Eq. (2.16) the matrix Green's function, Eq. (2.15), can be decomposed into the superposition of the two Green's functions corresponding to the states with + and - chiralities

$$G_0^{R,A}(\epsilon, \vec{p}) = \mathcal{P}_+(\vec{p}) G_{0+}^{R,A}(\epsilon, \vec{p}) + \mathcal{P}_-(\vec{p}) G_{0-}^{R,A}(\epsilon, \vec{p}), \quad (2.17)$$

where

$$G_{0\pm}^R(\epsilon, \vec{p}) = \frac{1}{\epsilon + i0 \mp v_F p} \quad (2.18)$$

and $G_{0\pm}^A(\epsilon, \vec{p}) = \left[G_{0\pm}^R(\epsilon, \vec{p}) \right]^*$. For later purposes we will need the quasi-particle spectral weight

$$\mathcal{A}_0(\epsilon, \vec{p}) = \frac{1}{2i} \left[G_0^R(\epsilon, \vec{p}) - G_0^A(\epsilon, \vec{p}) \right] = -\frac{\pi}{2\epsilon} \left(\epsilon \mathbb{1} + v_F \boldsymbol{\sigma} \cdot \vec{p} \right) \left[\delta(\epsilon - v_F p) + \delta(\epsilon + v_F p) \right]. \quad (2.19)$$

Using the projection operators, we decompose the spectral weight as follows:

$$\mathcal{A}_0(\epsilon, \vec{p}) = \mathcal{P}_+(\vec{p}) \mathcal{A}_{0+}(\epsilon, \vec{p}) + \mathcal{P}_-(\vec{p}) \mathcal{A}_{0-}(\epsilon, \vec{p}), \quad (2.20)$$

$$\mathcal{A}_{0\pm}(\epsilon, \vec{p}) = -\pi \delta(\epsilon \mp v_F p). \quad (2.21)$$

It is worth noting that for Dirac particles, the spectral weight $\mathcal{A}_0(\epsilon, \vec{p})$ is not given by the imaginary part of the Green's function $G_0^R(\epsilon, \vec{p})$, because the latter contains the Pauli matrix σ_y . However, within each chirality the conventional relation holds: $\mathcal{A}_{0\pm}(\epsilon, \vec{p}) = \text{Im } G_{0\pm}^R(\epsilon, \vec{p})$.

The interaction is treated by performing a Hubbard-Stratonovich transformation. After this the Hamiltonian reads:

$$\hat{H} = \sum_{\nu} \int d^2r \hat{\Psi}_{\nu}^{\dagger}(\vec{r}) \left(-iv_F \boldsymbol{\sigma} \cdot \vec{\nabla} + \phi(\vec{r}) \right) \hat{\Psi}_{\nu}(\vec{r}) + \int d^2r \phi(\vec{r}) D_0^{-1}(\vec{r}) \phi(\vec{r}) \quad (2.22)$$

The momentum space representation of the propagator of the Hubbard-Stratonovich field is given by:

$$D_0(\vec{q}) = \frac{2\pi\alpha_g v_F}{|\vec{q}|}, \quad (2.23)$$

which is of course just the Fourier-transformed Coulomb interaction (the 2d Fourier transformation of the 3d interaction $\alpha_g v_F / r$).

2.4 The Keldysh Formulation

... non-equilibrium may be a source of order. Irreversible processes may lead to a new type of dynamic states of matter which I have called "dissipative structures"

Prigogine, Nobel Lecture

Non-equilibrium setups turn out to extend the richness of physical systems enormously, which itself makes it worth being able to describe them. At first glance it may seem unnecessary for our purpose to make the effort of dealing with a more complicated formalism since for Chap. 3 and 4 we deal only with equilibrium setups. But as we will see later in this work, when we start investigating transport phenomena in graphene, having a theory capable of dealing with non-equilibrium setups is quite useful.

The QFT we have introduced so far is a zero temperature QFT since we were operating on pure ground states without taking any thermodynamics into account. The way we will incorporate thermodynamics is general enough to account for non-equilibrium situations as well as equilibrium and is usually referred to as Keldysh formalism [48]. While there are easier ways to take thermodynamics into account as long as one limits oneself to equilibrium physics, and while that is what we will mainly consider, there is a big advantage in choosing the more powerful but slightly complicated Keldysh formalism, namely the natural extension of the latter towards quantum kinetic equations. Even within the diagrammatic equilibrium calculations we will hence use the Keldysh formalism. This will allow us to compare the diagrammatic and the quantum kinetic equation points of view in a particularly transparent way.

The complexity that appears when dealing with the more general non-equilibrium case is well covered in the corresponding literature [49, 50] and will not be explained within this work. We will only briefly sketch some of the details, mainly to provide the notation, since a more profound explanation is beyond the scope of this work. Still we will try to briefly motivate the appearance of the additional complexity when possible.

2.4.1 Keldysh Objects

A very intuitive way to gain some insights into the Keldysh formalism is to use the field integral representation of the QFT. Within this representation we consider the following:

The action involves an integration over time. So one considers the time evolution of the model from a thermodynamic state at $t_{-\infty} = -\infty$ up to the state at $t_{\infty} = \infty$ in the distant future. Since we do not know about the state in the distant future, unless we have a constraint like the system being in equilibrium or the adiabatic limit, we will subsequently evolve the system back to $t_{-\infty}$. Thus, the total time evolution operator from $t_{-\infty}$ to $t_{-\infty}$ via t_{∞} is the unity operator. Nevertheless by causing artificial changes in this time evolution (source fields) one captures the physics that governs even non-equilibrium setups. By referring to the field evolving from $t_{-\infty}$ to t_{∞} as ψ_1 -field and respectively ψ_2 -field for the opposite case, we explicitly see the connection to the previously introduced field theory and gaining the perception that the price of dealing with non-equilibrium setups is paid by an additional structure in the fields. The dynamics will involve both of the fields, which is a consequence of not specifying the state we are evolving to.

Using the idea of two fields living on different time branches we can write the partition sum as

$$Z = \int \mathcal{D}[\bar{\psi}, \psi] e^{iS(\bar{\psi}, \psi)}, \quad (2.24)$$

where the action is given by

$$S(\bar{\psi}, \psi) = \int dx dx' \sum_{\substack{i \in \{1,2\} \\ j \in \{1,2\}}} \bar{\psi}_i(x) \check{G}_{ij}^{-1}(x, x') \psi_j(x') + \int dx \left(V_1 \bar{\psi}_1(x) \psi_1(x) - V_2 \bar{\psi}_2(x) \psi_2(x) \right) \quad (2.25)$$

In comparison to the previously introduced field theory the fields now have an additional Keldysh structure, since we have to differentiate between the forward and backward time evolution. Therefore the Green's functions now gain an additional matrix structure due to the Keldysh formalism. That said, the separation in ψ_1 and ψ_2 according to the parts of the time contour turns out not to be the most convenient form.

The Keldysh Rotation

A proper analysis of the causal structure of the formalism unveils[49, 50] that the condition $\check{G}_{++} + \check{G}_{--} - \check{G}_{+-} - \check{G}_{-+} = 0$ is fulfilled as long as we are not dealing with an acausal operator like in full counting statistics. Since for Fermions the field operators $\bar{\psi}$ and ψ are two independent fields we can transform them individually following the transformation rules of Larkin and Ovchinnikov [51]. Within this transformation the correlators read

$$-i \langle \psi_i(t) \bar{\psi}_j(t') \rangle = \check{G}_{ij}(t, t') = \begin{pmatrix} G^R(t, t') & G^K(t, t') \\ 0 & G^A(t, t') \end{pmatrix}_{ab}. \quad (2.26)$$

This rotation induces a rotation for the source field as well. It transforms such that $V_{\text{cl}(q)} = \frac{1}{2} (V_1 \pm V_2)$ and as a consequence $\check{V} = \mathbb{1} V_{\text{cl}} + \sigma_1^K V_q$ holds. The Coulomb interaction that is decoupled into Hubbard-Stratonovich fields acquires in the very same way its Keldysh structure one obtains,

$$\check{\phi} = \begin{pmatrix} \varphi_c & \varphi_q \\ \varphi_q & \varphi_c \end{pmatrix} = \frac{1}{2} \begin{pmatrix} \varphi_1 + \varphi_2 & \varphi_1 - \varphi_2 \\ \varphi_1 - \varphi_2 & \varphi_1 + \varphi_2 \end{pmatrix}. \quad (2.27)$$

Within these rotated forms we gain the propagators by

$$\langle \varphi_c \varphi_q \rangle = \frac{i}{2} D^R, \quad \langle \varphi_q \varphi_c \rangle = \frac{i}{2} D^A, \quad (2.28)$$

$$\langle \varphi_c \varphi_c \rangle = \frac{i}{2} D^K, \quad \langle \varphi_q \varphi_q \rangle = 0. \quad (2.29)$$

With these objects we are now well equipped to perform diagrammatics.

The Keldysh Formalism in Equilibrium

If one approaches the equilibrium state there is a crucial simplification of the formalism since the Keldysh Green's function is known due to the fluctuation dissipation theorem and given by

$$G_0^K(\epsilon, \vec{p}) = f(\epsilon) \left[G_0^R(\epsilon, \vec{p}) - G_0^A(\epsilon, \vec{p}) \right] = 2if(\epsilon) \mathcal{A}_0(\epsilon, \vec{p}), \quad (2.30)$$

where the fermionic thermal factor is given by $f(\epsilon) = \tanh(\epsilon/2T)$. In the equilibrium situation the Keldysh component D^K of the interaction propagator satisfies

$$D^K(\omega, \vec{q}) = 2ig(\omega) \mathcal{A}_D(\omega, \vec{q}), \quad (2.31)$$

with $g(\omega) = \coth(\omega/2T)$.

The Self-energy and Polarization in Keldysh Formalism

Within the first part of this work we will mainly use the quantum field theoretical description. Two objects will be dominating the discussions. The first of these objects is the self-energy, which is physically related to the interaction induced reaction of the particles' propagation properties. Self-energy can renormalize the velocity and can create a finite lifetime in the sense that interaction induced scattering processes are likely enough to allow the particle to escape its (almost eigen-) state. To investigate the influence of Coulomb interaction on electronic transport in graphene it is crucial to calculate the self-energy. Again we will keep the discussion brief since the self-energy is a common object in QFT and its general properties and definitions are well explained in literature [39, 45–47, 50].

The full Keldysh Green's function for Eq. (2.14) is, due to the Dyson series, expressed through \check{G}_0

$$\check{G} = \left(\check{G}_0 - \check{\Sigma} \right)^{-1} \quad (2.32)$$

where Σ is the full self-energy. In the lowest order in the fully dressed propagator of Coulomb interaction \check{D} the retarded self-energy is given by

$$\Sigma_0^R = \frac{i}{2} \left(D^K \circ G_0^R + D^R \circ G_0^K \right), \quad (2.33)$$

where the symbol \circ denotes the operator product which within the integral representation translates into integration over all internal energies and momenta (see Eq. (A.2) for details of its derivation). In equilibrium this equation will be simplified due to equations (2.30) and (2.31) such that the spectral weight of the self-energy is given by

$$\Sigma_0^R - \Sigma_0^A = - \left[(f + g) \text{Im} D^R \right] \circ (G^R - G^A). \quad (2.34)$$

Splitting the self-energy into the chiral basis we obtain,

$$\text{Im} \Sigma_{\pm}^R = \text{Im} \Sigma_c^R \pm \text{Im} \Sigma_v^R = - \text{Im} D^R (f + g) \circ \text{Tr} \left[\mathcal{A} \mathcal{P}_{\pm} \right], \quad (2.35)$$

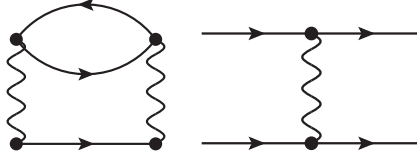


Figure 2.4: *Left:* is the diagram we refer to as the Golden Rule level diagram. In App. A.2.1 it is explicitly shown how this diagram relates to the Golden Rule process illustrated on the right side of this figure. Alternatively one can consider the imaginary part of this diagram, which via the optical theorem relates the right panel. **Right:** The illustration of the Golden Rule process. This corresponds to the matrix element $|\mathcal{M}_0|^2$ of collisions.

with

$$\text{Im } \Sigma_\epsilon^R = -\frac{1}{2} \text{Im } D^R(f+g) \circ \text{Tr } \mathcal{A}, \quad (2.36)$$

$$\text{Im } \Sigma_v^R = -\frac{1}{2} \text{Im } D^R(f+g) \circ \text{Tr } \mathcal{A} \boldsymbol{\sigma} \cdot \vec{n}_p. \quad (2.37)$$

Clearly, the bare Coulomb interaction (whose propagator is purely real) does not yield an imaginary part of the self-energy, so that one has to take into account retardation effects. Hence the analogous procedure of defining the self-energy should be applied to take into account the response of the electronic system onto the interaction. The lowest order response is the polarization operator. If one continues to resum the interaction contributions using only the polarization operator contributions one obtains the random phase approximation (RPA). The screened Coulomb interaction in RPA takes the form

$$D_{\text{RPA}}^R(\omega, \vec{q}) = \frac{D_0(q)}{1 + D_0(q) N \Pi^R(\omega, \vec{q})} \quad (2.38)$$

where N is the number of flavors. Below we will also consider the interaction propagator at the Golden Rule (GR) level (see Fig. 2.4) which corresponds to expanding Eq. (2.38) to the second order in D_0 (including only a single polarization operator),

$$D_{\text{GR}}^R(\omega, \vec{q}) = -D_0^2(q) N \Pi^R(\omega, \vec{q}). \quad (2.39)$$

The lowest order of interaction (D_0 purely) does not affect the system except due to a RG contribution (see Sec. 3.1.1). The dynamical screening in Eq. (2.38) is expressed through the bare polarization operator (see Eq. (A.4))

$$\Pi^R = \frac{i}{2} \text{Tr} \left(G_0^R \circ G_0^K + G_0^K \circ G_0^A \right). \quad (2.40)$$

2.5 The Kinetic Equations

Until now we have used the very elegant formulation in terms of a quantum field theory, where we have quoted Dirac as one of the founders. The technique we will focus on in the following section seems to be as different as the views of its founders seem to be:

Elegance should be left to shoemakers and tailors

L. Boltzmann, reported by Arnold Berliner. Die Naturwissenschaften

The Boltzmann equation is a quite pragmatic way to deal with a many-particle system, since its properties are basically completely absorbed into a probability distribution in an effectively single-particle phase space. The system's dynamics are completely governed by operators acting on the Boltzmann distribution.

The Keldysh formalism from the previous Sec. 2.4 enables us to connect the field theoretical description with the rather old technique of the Boltzmann equation. Since the Boltzmann equation is a purely classical theory without the knowledge of quantum uncertainty there must be a deep separation we have to overcome. The Keldysh objects like the electronic propagators follow the rule of quantum mechanics to have a real space representation and a momentum space representation. They cannot have both (as long as coordinate and momenta are conjugated variables). A way to achieve a compromise is the Wigner transformation.

The prerequisite is to introduce relative and center of mass coordinates:

$$\vec{R} = \frac{1}{2}(\vec{x}_1 + \vec{x}_2) \quad \vec{r} = \vec{x}_1 - \vec{x}_2 \quad (2.41)$$

$$T = \frac{1}{2}(t_1 + t_2) \quad t = t_1 - t_2 \quad (2.42)$$

$$X = (\vec{R}, T) \quad x = (\vec{r}, t). \quad (2.43)$$

Now the idea is that, since the relevant scale for quantum mechanics is usually the small scale on which the quantum fluctuations live on, we will use the relative coordinates as “quantum coordinates” whereas the center of mass coordinates take on the role of classical coordinates. If so, momentum and energy $p = (E, \vec{p})$ are well defined even in the presence of the real space coordinates X . So in principle one can handle functions $h(X, p)$ but it is quite important to remember that (X, p) is not an element of the classical phase-space! We proceed by defining the Wigner transformed Greens function:

$$G(X, p) = \int dx e^{-ixp} G(X + x/2, X - x/2). \quad (2.44)$$

With the help of this representation we manage now to have a language to draw the connection between the Keldysh formalism and the Boltzmann equation.

2.5.1 Derivation of the Kinetic Equation

The derivation of the kinetic equation can be found in the literature [49, 50, 52]. Since it is an involved derivation with critical assumptions made and since we are using both techniques to gain insights into the model, we will briefly sketch the derivation following the notation of Rammer and Smith [49].

The starting point to do so is the Dyson series, which, within a general operator formulation, can be expressed as

$$\check{G} = \check{G}_0 + \check{G}_0 \circ \check{\Sigma} \circ \check{G} \quad \Rightarrow (\check{G}_0^{-1} - \check{\Sigma}) \circ \check{G} = \mathbf{1} \quad \Rightarrow [\check{G}_0^{-1} - \check{\Sigma} \circ \check{G}] = 0 \quad (2.45)$$

The kinetic equation we are going to formulate is one for fermions, which means we will use the fermionic Keldysh structure. Then the Keldysh component of the Dyson series forms:

$$\underbrace{(G_0^{-1} - \Sigma^R) \circ G^K - G^K \circ (G_0^{-1} - \Sigma^A)}_{[(G_0^{-1} - R_\Sigma) \circ G^K] - i\{\mathcal{A}_\Sigma \circ G^K\}} + \underbrace{G^R \circ \Sigma^K - \Sigma^K \circ G^A}_{i\{\Sigma^K \circ \mathcal{A}_G\} - [\Sigma^K \circ R_G]} = 0 \quad (2.46)$$

Using the short notation of Rammer and Smith [49], namely $2R_O = O^R + O^A$ and $2i\mathcal{A}_O = O^R - O^A$ (O is any operator). We further use the convention $[,]$ for the commutator and $\{ , \}$ for the anti-commutator. In these terms the last equation reads:

$$\underbrace{[(G_0^{-1} - R_\Sigma) \circ G^K]}_{\tilde{G}_0^{-1}} - i\{\mathcal{A}_\Sigma \circ G^K\} + i\{\Sigma^K \circ \mathcal{A}_G\} - [\Sigma^K \circ R_G] = 0. \quad (2.47)$$

The operator \tilde{G}_0^{-1} here is the renormalized operator we will use for brevity from now on.

We consider all appearing Greens functions to be Wigner transformed, which is why the convolution of operators is more complicated than it looks at first glance. For any operators A, B the convolution can be rewritten as:

$$(A \circ B)(X, p) = e^{\frac{i}{2}(\partial_X^A \partial_p^B - \partial_p^A \partial_X^B)} A(X, p) B(X, p) \quad (2.48)$$

the notation for derivatives acting on A is given by $\partial_X^A = (-\partial_T, \nabla_{\vec{R}})$ for real space and analog $\partial_p^A = (-\partial_E, \nabla_{\vec{p}})$ for the momentum space, whereas the product is given with an additional sign $\partial_X^A \partial_p^A = -\partial_T \partial_E + \nabla_{\vec{R}} \nabla_{\vec{p}}$. The complexity of Eq. (2.48) is due to the strong non-locality generally generated by integrating over internal variables. If the spacial and temporal length scales ($\partial_X O$) the operators come with are much larger than the scale of the quantum effects ($\partial_p O$), one can do a ‘‘local approximation’’ (i.e. $\partial_X O \partial_p O \ll 1$) which reduces Eq. (2.48) to

$$\{A \circ B\} \approx AB + BA + \frac{i}{2} \left([\partial_X^A A, \partial_p^B B] - [\partial_p^A A, \partial_X^B B] \right), \quad (2.49)$$

$$[A \circ B] \approx AB - BA + \frac{i}{2} \left(\{ \partial_X^A A, \partial_p^B B \} - \{ \partial_p^A A, \partial_X^B B \} \right). \quad (2.50)$$

Considering the first commutator in Eq. (2.47) and doing the local approximation we obtain:

$$[\tilde{G}_0^{-1} \circ G^K] \approx \tilde{G}_0^{-1} G^K - G^K \tilde{G}_0^{-1} + \frac{i}{2} \left(\{ \partial_X \tilde{G}_0^{-1}, \partial_p G^K \} - \{ \partial_p \tilde{G}_0^{-1}, \partial_X G^K \} \right). \quad (2.51)$$

The last equation unveils a problem that can appear when the Green’s functions have additional matrix structure, namely that the leading contribution in the expansion of Eq. (2.51) does not vanish. At this point we have to put some details about graphene into the derivation since otherwise we would need to deal with Wigner lines, some more complicated objects that appear in the presence of non-Abelian gauge fields [53], for example. It is the fact that within the chiral basis the Hamiltonian becomes diagonal that will help us to treat this problem.

The Chiral Basis

In Sec. 2.3 we showed the simplification of the formalism by using a chiral basis. This means that since we can write our objects as:

$$G = \mathbb{P}_+ G_+ + \mathbb{P}_- G_- \quad \text{and} \quad \Sigma = \mathbb{P}_+ \Sigma_+ + \mathbb{P}_- \Sigma_-, \quad (2.52)$$

we have already a clear splitting into the chiral objects. To establish a complete chiral structure we explicitly rotate into the chiral basis by usage of: ($\vec{n}_p = \vec{p}/p$):

$$U_p = \frac{1}{\sqrt{2}} \begin{pmatrix} e^{i\theta/2+i\pi/4} & e^{-i\theta/2+i\pi/4} \\ e^{i\theta/2-i\pi/4} & -e^{-i\theta/2-i\pi/4} \end{pmatrix} \quad \text{with} \quad e^{i\theta} = (\vec{n}_p)_x + i(\vec{n}_p)_y. \quad (2.53)$$

The rotation U can be understood more easily by looking at the way they act on the Pauli matrices

$$U\sigma\vec{a}U^\dagger = \sigma_z\vec{n}_p\vec{a} - \sigma_x(\vec{n}_p \times \vec{a}) \quad U\sigma_zU^\dagger = -\sigma_y. \quad (2.54)$$

Applying the rotation now yields:

$$UGU^\dagger = \begin{pmatrix} G_+ & 0 \\ 0 & G_- \end{pmatrix} \quad \text{and} \quad U\Sigma U^\dagger = \begin{pmatrix} \Sigma_+ & 0 \\ 0 & \Sigma_- \end{pmatrix}. \quad (2.55)$$

The Kinetic Equation in the Chiral Basis

Eq. (2.51) considerably simplifies after the rotation with U given in Eq. (2.53), indicating that the chiral basis is the natural basis to treat this problem.

$$\begin{aligned} U[\tilde{G}_0^{-1}; G^K]U^\dagger &\approx \underbrace{U\tilde{G}_0^{-1}U^\dagger UG^KU^\dagger - UG^KU^\dagger U\tilde{G}_0^{-1}U^\dagger}_{=0\cdot 1} + \frac{i}{2}U\left(\underbrace{\{\partial_X\tilde{G}_0^{-1}, \partial_p G^K\}}_{\approx 0} - \{\partial_p\tilde{G}_0^{-1}, \partial_X G^K\}\right)U^\dagger \\ &= -\frac{i}{2}\{U\partial_p\tilde{G}_0^{-1}, \partial_X U^\dagger UG^KU^\dagger\} = \frac{i}{2}\{U(\partial_T + \tilde{v}_F\sigma\nabla_R), U^\dagger UG^KU^\dagger\} \\ &= i\left[\partial_T + \tilde{v}_F\sigma_z\vec{n}_p\nabla_R + \tilde{v}_F\sigma_x(\vec{n}_p \times \nabla_R)\right]UG^KU^\dagger \end{aligned} \quad (2.56)$$

Here \tilde{v}_F is the renormalized velocity that originates from \tilde{G}_0^{-1} . The most significant changes are due to the cancellation that becomes transparent within the diagonal basis, another simplification is that we assume that the inverse bare Green's function does not depend on the spatial coordinates X and hence its derivative disappears. The full kinetic equation now appears as a matrix equation of the following form:

$$\begin{pmatrix} \partial_T + \tilde{v}_F\vec{n}_p\nabla_R & -\tilde{v}_F\vec{n}_p \times \nabla_R \\ -\tilde{v}_F\vec{n}_p \times \nabla_R & \partial_T - \tilde{v}_F\vec{n}_p\nabla_R \end{pmatrix} \begin{pmatrix} G_+^K & 0 \\ 0 & G_-^K \end{pmatrix} = 2 \begin{pmatrix} \mathcal{A}_{\Sigma_+} G_+^K & 0 \\ 0 & \mathcal{A}_{\Sigma_-} G_-^K \end{pmatrix} - 2 \begin{pmatrix} \Sigma_+^K \mathcal{A}_{G_+} & 0 \\ 0 & \Sigma_-^K \mathcal{A}_{G_-} \end{pmatrix}. \quad (2.57)$$

Focusing on the diagonal parts only and using the notation $\gamma \in \{+1, -1\}$ for the chirality, one obtains:

$$\left(\partial_T + \gamma\tilde{v}_F\vec{n}_p\nabla_R\right)G_\gamma^K = 2\left(\mathcal{A}_{\Sigma_\gamma}G_\gamma^K - \Sigma_\gamma^K\mathcal{A}_{G_\gamma}\right). \quad (2.58)$$

A form more closely resembling the Boltzmann equation can be obtained by assuming \mathcal{A}_γ to be a peaked function, which close to equilibrium gives rise to $G_\gamma^K = 2if_\gamma\mathcal{A}_\gamma$. From a conceptual level this is a crucial step since with this assumption one deals with well defined quasi-particles. These quasi-particles are fully described by a distribution function that solves an equation like the Boltzmann equation. By integration over ϵ Eq. (2.58) reduces to

$$Lf_\gamma^{\text{OS}} \equiv \left(\partial_T + \gamma\tilde{v}_F\vec{n}_p\nabla_R\right)f_\gamma^{\text{OS}} = i\left(\Sigma_\gamma^K - 2if_\gamma^{\text{OS}}\mathcal{A}_{\Sigma_\gamma}\right) \equiv -\text{St}[f], \quad (2.59)$$

where f_γ^{OS} is the distribution function taken on the mass shell (On Shell). In this fashion the equation is very close to the Boltzmann equation [54] $Lf = -\text{St}[f]$ but one should note that although f is a function of \vec{r} and \vec{p} simultaneously it is not quite a Boltzmann function since f is not a probability measure of the phase space. The distribution function f is called a Wigner quasi-probability distribution. We therefore use the term kinetic equation instead of Boltzmann equation.

Since in equilibrium the distribution function used within the Keldysh formalism is the symmetrised Fermi distribution we may as well write the equation in the unsymmetrised form. This is not only for transparency reasons but also serves to make the connection to the Boltzmann equation more explicit. Hence we use $f(\epsilon) = 1 - 2n(\epsilon)$ where in equilibrium we recover the Fermi distribution n_F . The kinetic equation reads in the abstract manner introduced above:

$$\mathcal{L}n = -I_{\text{Coll}}[n]. \quad (2.60)$$

We use for brevity $\mathcal{L}n = Lf_\gamma^{\text{OS}}$ and $I_{\text{Coll}}[n] = \text{St}[f]$. In Appendix A it is explicitly shown how to obtain the collision kernel Eq. (A.17) from the formulation in terms of Green's functions Eq.(A.7). Thus, this appendix provides valuable insights into the connection of quantum field theory and kinetic equation.

The Berry Phase and Coupling to External Fields

We assumed in the previous section that the bare Green's function does not contain external fields, which involve center of mass coordinates. Hence we used $\partial_X G_0^{-1} = 0$ for a good reason. But let us now assume to have an external electric field in a gauge invariant form $\vec{E} = -\nabla\phi - \partial_t\vec{A}$. So using Eq. (2.56) we can follow each step as before except for the one previously mentioned, where we used $\partial_X G_0^{-1} = 0$. For this part we need to be more careful, so that when using the Green's function $G_0^{-1} = (\epsilon - \phi) \mathbb{1} - \vec{\sigma}(\vec{p} - \vec{A})$ one reads

$$U\partial_X G_0^{-1}\partial_p G^K U^\dagger = U\left(-\nabla_R\phi\nabla_p G^K - \vec{\sigma}\partial_T\vec{A}\partial_\epsilon G^K\right)U^\dagger. \quad (2.61)$$

Now we need to remind ourselves that the rotation U is momentum dependent. The contribution coming with the vector potential does not involve derivatives with respect to \vec{p} and is therefore relatively straightforward. The contribution involving the scalar potential is more complicated since it leads to additional terms that involve the rotation U (since $UG^K U^\dagger = G_{\text{diag}}^K$, see Eq. (2.55)):

$$U\left(\nabla_p G^K\right)U^\dagger = U\left(\nabla_p U^\dagger G_{\text{diag}}^K U\right)U^\dagger = \nabla_p G_{\text{diag}}^K + \underbrace{U\left(\nabla_p U^\dagger\right)G_{\text{diag}}^K + G_{\text{diag}}^K\left(\nabla_p U\right)U^\dagger}_{\text{Berry phase contribution}}. \quad (2.62)$$

With the help of Eq. (2.53) we see that $\nabla_p U_p = i/2U_p\sigma_z\nabla_p\theta$, which simplifies the above expression to:

$$U\left(\nabla_p G^K\right)U^\dagger = \nabla_p G_{\text{diag}}^K + \frac{1}{2}\nabla_p\theta\left[i\sigma_y, G_{\text{diag}}^K\right] = \nabla_p G_{\text{diag}}^K - \frac{1}{2}\nabla_p\theta\sigma_x\left(G_+^K - G_-^K\right), \quad (2.63)$$

where $\nabla_p\theta = (n_z \times n_p) 1/p$ comes with the part we refer to as the Berry phase contribution (adiabatic change of the rotation U).

We see that as in the previous case we get contributions to the Liouvillian that are off-diagonal. But since the collision kernel is purely diagonal there will be no relaxation of those processes meaning that they correspond to constraints the system obeys.

Another interesting point one should mention follows from Eq. (2.59), which is the observation that $\gamma \vec{v}_F \vec{n}_p = \vec{v}$, which suggests one, to consider n as a function of ϵ and \vec{v} obtaining:

$$\mathcal{L}n = \left(\partial_T + \vec{v} \nabla_R + e \vec{E} \vec{v} \partial_\epsilon \right) n = -I_{\text{Coll}}[n]. \quad (2.64)$$

It is worth noting that in the case of allowing a local equilibrium $\mu(\vec{r}) = \mu + \vec{r} \nabla \mu$ and $T(\vec{r}) = T + \vec{r} \nabla T$, whereupon the corresponding gradients have to be smooth on the scale of the collision integrals, one can deal with temperature gradients as well. In cases where this holds not true one has to be more careful taking the temperature gradients into account. A Possible way of doing so is with the help of an artificial local gravitational field as initially introduced by Luttinger in Ref. [55]. Further details on the effects on the kinetic equation can be found in Ref. [56].

2.5.2 The Hydrodynamic Equations

Starting from the kinetic equation which resides in the quasi-classical world we might consider going one step further towards a purely classical description of the system. Such a description is given by the hydrodynamic equations which will serve us by expressing the phenomena of transport in simple physical terms. Within this section we will consider the example of the parabolic Fermi liquid case to express the basic ideas and to get familiar with the concept. A more detailed discussion on the subject can be found in Ref. [57, 58].

The Conserved Fields

Using the kinetic equation of a system we can, given that the scattering length of the collision integral is short enough, derive the hydrodynamic equation. This means that we started with a non-equilibrium field theory to derive the distribution function of quasi-classical quasi-particles to regain a classical field theory describing a liquid of those quasi-particles. There is one crucial precondition that has to be fulfilled, namely that the system of quasi-particles has to be dominated by interactions between the quasi-particles in order to resemble the characteristics of a liquid and not of a gas. This is exactly translated into the condition that the scattering length of the collision integral is short enough, since it provides the ultraviolet cutoff of a corresponding classical field theory.

The way to proceed towards the hydrodynamic equation is by defining the hydrodynamic objects which in general read:

$$\Psi(\vec{R}, T) = \langle \psi(\vec{R}, T) \rangle = \frac{1}{\rho} \int \frac{d^n p}{(2\pi)^n} \psi(\vec{R}, T, \vec{p}) n(\vec{R}, T, \vec{p}). \quad (2.65)$$

In such an abstract formulation, the density ρ , for example, is given by:

$$\rho(\vec{R}, T) = \int \frac{d^n p}{(2\pi)^n} n(\vec{R}, T, \vec{p}). \quad (2.66)$$

Surely this seems to be very general but one easily recognizes that the velocity field \vec{u} for a parabolic Fermi liquid is for example given by the replacement $\psi(\vec{R}, T, \vec{p}) \rightarrow \vec{p}/m$. By this construction the current is given by $\vec{j}(\vec{R}, T) = e \rho(\vec{R}, T) \vec{u}(\vec{R}, T)$.

To gain the hydrodynamic equations we have to integrate out the quantum variables we constructed originally as relative coordinates for the Wigner transformation.

For example:

$$\int \frac{d^n p}{(2\pi)^n} \left(\partial_T + \vec{v}(\vec{p}) \nabla_R + e \vec{E} \nabla_p \right) n(\vec{R}, T, \vec{p}) = \partial_T \rho(\vec{R}, T) + \nabla_R \left(\rho(\vec{R}, T) \vec{v}(\vec{R}, T) \right) = 0$$

$$= \int \frac{d^n p}{(2\pi)^n} \text{St}[n], \quad (2.67)$$

where we have used that the boundary term coming from $\nabla_p n(\vec{R}, T, \vec{p})$ disappears at infinity as well as the fact that the integration over the collision integral vanishes, due to a symmetry all collision kernels have provided they conserve the particle number.

This way we managed to obtain the continuity equation, one of the fundamental equations of hydrodynamics. To derive the equation of motion we need to introduce the pressure tensor measuring the velocity variation locally.

$$P_{\alpha\beta} = \int \frac{d^n p}{(2\pi)^n} \left(\vec{v}(\vec{p}) - \vec{u}(\vec{R}, T) \right)_\alpha \left(\vec{v}(\vec{p}) - \vec{u}(\vec{R}, T) \right)_\beta n(\vec{R}, T, \vec{p})$$

$$= -\rho \vec{u}_\alpha \vec{u}_\beta + \int \frac{d^n p}{(2\pi)^n} \vec{v}(\vec{p})_\alpha \vec{v}(\vec{p})_\beta n(\vec{R}, T, \vec{p}) \quad (2.68)$$

The next step is to multiply the kinetic equation by \vec{p} , leading to:

$$\int \frac{d^n p}{(2\pi)^n} \vec{p} \left(\partial_T + \vec{v}(\vec{p}) \nabla_R + e \vec{E} \nabla_p \right) n(\vec{R}, T, \vec{p})$$

$$= m \partial_T \left(\rho(\vec{R}, T) \vec{u}(\vec{R}, T) \right) + e \vec{E} \rho(\vec{R}, T) + m \frac{\partial}{\partial \vec{R}_\alpha} \int \frac{d^n p}{(2\pi)^n} \vec{v}(\vec{p})_\alpha \vec{v}(\vec{p})_\beta n(\vec{R}, T, \vec{p})$$

$$= m \partial_T \left(\rho(\vec{R}, T) \vec{u}(\vec{R}, T) \right) + e \vec{E} \rho(\vec{R}, T) + m \frac{\partial}{\partial \vec{R}_\alpha} \left(\rho \vec{u}_\alpha \vec{u}_\beta \right) + m \frac{\partial}{\partial \vec{R}_\alpha} P_{\alpha\beta} = 0. \quad (2.69)$$

The integral over the collision kernel gives zero again, since the total conservation of momentum requires it. The above equation can be simplified by usage of the continuity equation to obtain:

$$\rho \left(\partial_T \vec{u} + \frac{e}{m} \vec{E} + (\vec{u} \nabla_R) \vec{u} \right) + \nabla_R P = 0. \quad (2.70)$$

We have used particle and momentum conservation to gain hydrodynamic equations that avoid involving the collision integral. In fact there is one more fundamental conservation law calling for yet another hydrodynamic equation. Multiplying the equation with $p^2/(2m)$ one easily recognizes that the collision kernel disappears due to energy conservation. Including the liquid's temperature as

$$m/2 \langle [\vec{v}(\vec{p}) - \vec{u}(\vec{R}, T)]^2 \rangle = m/2 \text{Tr}(P) = n/2 \rho(\vec{R}, T) \mathcal{T}(\vec{R}, T) \quad (2.71)$$

(to reduce confusion we distinguish the center of mass time T and the temperature \mathcal{T} in this chapter) and introducing the heat current given by

$$\vec{q}(\vec{R}, T) = m/2 \langle [\vec{v}(\vec{p}) - \vec{u}(\vec{R}, T)]^2 [\vec{v}(\vec{p}) - \vec{u}(\vec{R}, T)] \rangle, \quad (2.72)$$

one reads:

$$\begin{aligned} \int \frac{d^n p}{(2\pi)^n} \frac{\vec{p}^2}{2m} \left(\partial_T + \vec{v}(\vec{p}) \nabla_R + e \vec{E} \nabla_p \right) n(\vec{R}, T, \vec{p}) \\ = \partial_T \left[\frac{n}{2} \rho \mathcal{T} + \frac{1}{2} m \rho \vec{u}^2 \right] + \nabla_R \left[\vec{q} + m P \vec{u} + \frac{n}{2} \rho \mathcal{T} \vec{u} - \frac{m}{2} \rho \vec{u}^2 \vec{u} \right] - \vec{j} \vec{E} = 0 \end{aligned} \quad (2.73)$$

with the current as defined in the beginning of this section.

The hydrodynamic equations we derived here are those related to conservation laws. In fact, it is also possible to define hydrodynamic equations for non-conserved quantities at the cost that the collision integral does not vanish, making the situation more complicated. In principle the collision kernel could create interactions with other hydrodynamic fields and, in the worst case that the quantity cannot be described by hydrodynamic equations, it would call for an infinite hierarchy of equations. This point is relevant as momentum conservation does not lead to current conservation in graphene, putting us in the position where we must necessarily deal with the collision kernel.

The Navier Stokes Equation

Having derived the hydrodynamic equations for the conserved quantities like density, momentum (velocity) and energy it appears that the objects we have needed to do so have not yet yielded a defining hydrodynamic equation. Hence we need to gain equations for the stress tensor (2.68) and the heat current (2.72). If one uses the Fermi liquid distribution in local equilibrium it turns out that Eq. (2.68) becomes $P_{\alpha\beta} = \delta_{\alpha\beta} \rho \mathcal{T} / m$ in the same way Eq. (2.72) becomes $\vec{q} = 0$. Additionally, the temperature field $\mathcal{T}(\vec{R}, T)$ is constant since we are in equilibrium. The equations we arrive at using these constraints on the hydrodynamic equations ((2.67), (2.70) and (2.73)) are the Euler equations,

$$\partial_T \rho + \nabla_R (\rho \vec{v}) = 0, \quad \rho \left(\partial_T \vec{u} + \frac{e}{m} \vec{E} + (\vec{u} \nabla_R) \vec{u} \right) + \frac{1}{m} \nabla_R (\rho \mathcal{T}) = 0, \quad (2.74)$$

$$\partial_T \left[\frac{n}{2} \rho \mathcal{T} + \frac{1}{2} m \rho \vec{u}^2 \right] + \nabla_R \left[\frac{n+2}{2} \rho \mathcal{T} \vec{u} - \frac{m}{2} \rho \vec{u}^2 \vec{u} \right] - \vec{j} \vec{E} = 0. \quad (2.75)$$

Still we want to do better and allow for non-equilibrium contributions within the stress tensor and the heat current. We therefore expand the distribution function in small variations around the local equilibrium ($n = n_F - \frac{\partial n}{\partial \epsilon} h$) obtaining a linearized kinetic equation. We will assume to have solved the linearized kinetic equation. This means that we have a set of functions h corresponding to different modes solving the kinetic equation. The pressure tensor and heat current then gain corrections ($P_{\alpha\beta} = P_{\alpha\beta}^0 + \delta P_{\alpha\beta}$ and $\vec{q} = \vec{q}^0 + \delta \vec{q}$) due to:

$$\delta P_{\alpha\beta} = \int \frac{d^n p}{(2\pi)^n} (\vec{v} - \vec{u})_\alpha (\vec{v} - \vec{u})_\beta \frac{\partial n_F}{\partial \epsilon} h \quad \delta \vec{q} = \int \frac{d^n p}{(2\pi)^n} (\vec{v} - \vec{u})^3 \frac{\partial n_F}{\partial \epsilon} h \quad (2.76)$$

In Fermi liquid systems it turns out that the pressure tensor and the heat current can be, up to some constants, mapped back to the hydrodynamic fields determined by the Euler equations. One then gets (see Ref. [57, 58] for further details):

$$P_{\alpha\beta} = \delta_{\alpha\beta} \rho \mathcal{T} / m - \eta \left[\frac{1}{2} \left(\nabla_R^\alpha \vec{u}^\beta + \nabla_R^\beta \vec{u}^\alpha \right) - \nabla_R \vec{u} \delta_{\alpha\beta} \right] \quad \vec{q} = \kappa \nabla \mathcal{T}, \quad (2.77)$$

where η is the viscosity of the system. With these additional equations one obtains the Navier-Stokes equation (see [57, 58]). Calling $p = \rho\mathcal{T}/m$ the local pressure we can rewrite the equation of motion, arriving at:

$$\rho \left(\partial_T \vec{u} + \frac{e}{m} \vec{E} + (\vec{u} \nabla_R) \vec{u} \right) + \nabla_R p = \frac{\eta}{2} \left[\Delta_R \vec{u} - \nabla_R (\nabla_R \vec{u}) \right], \quad (2.78)$$

with the viscosity η appearing as the part responsible for the non-local contributions (higher order derivatives). Since solving the kinetic equation is usually a rather difficult task, there are several ways to perform a controlled expansion such as the Chapman-Enskog expansion (development) that corresponds to a systematic expansion in the distribution function in such a way that the number of modes one needs to solve the linearized kinetic equation for is reduced. This way one can also go beyond the Navier-Stokes-equation towards Burnett equations and further. Since we will solve the kinetic equation for graphene anyway, a detailed discussion of the Chapman-Enskog expansion is not necessary. We refer to the literature [52, 57] for further details.

One might get an impression that in the equations above we have never used the constraint that the length scale the hydrodynamic fields live on need to be much larger than the scattering length defined by the collision kernel. Of course this impression would be wrong, since the constraint has been used. The pressure tensor and the heat current will call for an infinite hierarchy of hydrodynamic equations if one tries to approach the ultra violet cut-off. This is because the distribution function depends on momentum in contrast to the hydrodynamic fields, to overcome the problem of fewer degrees of freedom the hydrodynamic formulation needs more (infinity many) fields. The scattering length comes into play since pressure tensor and the heat current know about this length scale. The exact details may differ strongly with the system one considers, which is why we refer again to Ref. [57].

Having introduced all the necessary methods and having introduced the system we are going to look at, we will now proceed with the discussion of the previous work on Coulomb interaction in graphene.

3

Chapter 3

Coulomb Interaction in Graphene: Previous Analysis

How quick are we to learn, that is, to imitate what others have done or thought before. And how slow to understand, that is, to see the deeper connections. Slowest of all, however, are we in inventing new connections or even applying old ideas in a new field.

Frits Zernike, Nobel lecture

Now that the basics of the system we are dealing with and our formulation of it have been introduced we will try to gain some basic insights into the problem itself. To do so we will follow some of the calculations that have been done previously and will try to conclude on how to best deal with the problem.

3.1 Coulomb Interaction in Graphene at Zero Temperature

Most previous studies of the Coulomb interaction have, for simplicity, been done at zero temperature. Following their line of arguments, within the established formulation for this work, we will investigate the system and discuss the problems that have arisen in previous considerations, and towards the end of this chapter we will argue why the problem in general is so tough.

3.1.1 Renormalization Group Analysis

The first insights into the system will be gained by a renormalization group analysis. The main purpose here is to understand how the system behaves on different scales. There have been more involved studies [42, 59] about the RG flow behaves in graphene but for the physics we want to discuss it is enough to look only at the leading order. In previous studies [60] it has been shown that in the leading order the theory is renormalizable and that the electrical charge is not at all renormalized for which reason we will look at the velocity renormalization only.

The Objects to Renormalize

We start by defining the objects we will renormalize by decomposing the retarded self-energy into two terms:

$$\Sigma^R = \Sigma_c^R \mathbb{1} + \Sigma_v^R \boldsymbol{\sigma} \cdot \vec{n}_p. \quad (3.1)$$

The real parts of Σ_ϵ^R and Σ_v^R give rise to the corrections to the energy and Fermi velocity, respectively:

$$\delta\epsilon = -\text{Re}\Sigma_\epsilon^R(\epsilon, \vec{p}), \quad (3.2)$$

$$\delta v_F = \text{Re}\Sigma_v^R(\epsilon, \vec{p})/p. \quad (3.3)$$

In order to fix the unrenormalized energy, we introduced the Z factor

$$Z(\epsilon, \vec{p}) = 1 - \frac{\text{Re}\Sigma_\epsilon^R(\epsilon, \vec{p})}{\epsilon}, \quad (3.4)$$

so that $\epsilon - \text{Re}\Sigma_\epsilon^R(\epsilon, \vec{p}) = Z(\epsilon, \vec{p})\epsilon$. The renormalized Fermi velocity then takes the form

$$v_F^* = v_F Z(\epsilon, \vec{p}) \left[1 + \frac{\text{Re}\Sigma_v^R(\epsilon, \vec{p})}{v_F p} \right]. \quad (3.5)$$

Using Eqs. (3.4) and (3.5), we write the retarded Green's function as

$$G^R(\epsilon, \vec{p}) = Z \left[(\epsilon - iZ \text{Im}\Sigma_\epsilon^R) \mathbb{1} - \left(v_F^* + \frac{iZ \text{Im}\Sigma_v^R}{p} \right) \boldsymbol{\sigma} \cdot \vec{p} \right]^{-1}, \quad (3.6)$$

where the imaginary parts are given by Eq. (2.37).

Note that in this representation the velocity acquires a non-zero imaginary part. This is a manifestation of the fact that within the chiral basis the self-energy is diagonal, as the Green's function, which therefore induces the usual imaginary part that can be interpreted as the lifetime of the chiral states.

The most singular terms in the renormalized velocity v_F^* , coupling constant $\alpha_g^* = e^2/\epsilon v_F^*$, and the Z -factor can be summed up by means of the renormalization group approach [60].

The Renormalization Group Approach

The lowest order of relevant contributions to the self-energy is the Fock diagram or exchange term. The self-energy, as given by Eq. (2.33), can be simplified for the case of a bare interaction ($D^R = D_0 = D^A$ hence $D^K = 0$), zero temperature and considering energies close to the Dirac point ($f \xrightarrow{T \rightarrow 0} \text{sign}(\epsilon)$) such that we obtain:

$$\Sigma_0(\epsilon_1, \vec{p}_1) = -i \int \frac{d^2\vec{p}_1}{(2\pi)^2} \int \frac{d\epsilon_2}{2\pi} D_0(\vec{p}_1 - \vec{p}_2) G_0(\epsilon_2, \vec{p}_2). \quad (3.7)$$

In RG terms we are now in the situation that \vec{p}_2 and ϵ_2 are the corresponding "fast" fields whereas \vec{p}_1 and ϵ_1 are the "slow" ones. The object we are particularly interested in is δv_F given in Eq. (3.3). Hence we project onto the part that is proportional to $\boldsymbol{\sigma}\vec{p}$, which yields:

$$\begin{aligned} \delta v_F(\epsilon_1, \vec{p}_1) &= \frac{1}{2p_1^2} \text{Tr} \left[\boldsymbol{\sigma}\vec{p}\Sigma_0 \right] \\ &= -\frac{\alpha_g v_F \pi}{p_1} \int_{\Lambda_1 < v_F p_2 < \Lambda_2} \frac{d^2\vec{p}_2}{(2\pi)^2} \int \frac{d\epsilon_2}{2\pi} \frac{\vec{p}_1 \vec{p}_2}{p_1 p_2 |\vec{p}_1 - \vec{p}_2|} (-\pi) \left(\delta(\epsilon_2 - v_F p_2) + \delta(\epsilon_2 + v_F p_2) \right) \\ &\quad \stackrel{p_1 \ll p_2}{\approx} \frac{\alpha_g v_F}{4} \int_{\Lambda_1 < v_F p_2 < \Lambda_2} \frac{dp_2}{p_2} = \frac{\alpha_g v_F}{4} \ln \left(\frac{\Lambda_2}{\Lambda_1} \right) \end{aligned} \quad (3.8)$$

Since this was a perturbative calculation it is of course only valid as long as the coupling strength is small enough, $\alpha_g \ll 1$. For the renormalized quantities at the energy scale $\Lambda_1 = \epsilon$ we get ($\Lambda_2 = \Lambda$):

$$v_F^*(\epsilon) = v_F \left(1 + \frac{\alpha_g}{4} \ln \frac{\Lambda}{\epsilon} \right), \quad (3.9)$$

$$\alpha_g^*(\epsilon) = \frac{\alpha_g}{1 + \frac{\alpha_g}{4} \ln \frac{\Lambda}{\epsilon}}, \quad (3.10)$$

Here Λ is the ultraviolet energy cutoff (bandwidth) and the on-shell relation between ϵ and p is assumed. At finite temperature T the renormalization stops at $\max[\epsilon, T]$. In lowest order the RG flow equation from Ref. [42] appears to read:

$$\frac{d \ln(Z)}{d \ln(E_c)} = \frac{\alpha_g^2}{6}, \quad \frac{d\alpha_g}{d \ln(E_c)} = \frac{\alpha_g^2}{2}. \quad (3.11)$$

Hence we can determine the flow of the quasi-particle weight as a function of the coupling strength, which yields:

$$Z(\epsilon) = \exp \left\{ -\frac{1}{3} [\alpha_g - \alpha_g^*(\epsilon)] \right\} = \exp \left[-\frac{1}{12} \frac{\alpha_g^2 \ln \frac{\Lambda}{\epsilon}}{1 + \frac{\alpha_g}{4} \ln \frac{\Lambda}{\epsilon}} \right] \geq 1 - \frac{\alpha_g}{12} + O(\alpha_g^2) \simeq 1.$$

For energies below T (which we will focus on below) the renormalized velocity and the Z -factor are independent of energy. Since for $\alpha_g \ll 1$ the corrections to unity in the renormalized Z -factor are parametrically small, in what follows we set $Z = 1$.

As an important consequence we see from Eq. (3.9) that for small energies close to the Dirac point the correction to the velocity is such that it increases. Of course it cannot increase arbitrarily since at some point our approximation that the Coulomb interaction is much faster than the Fermi velocity breaks down. At that point we would need to consider a proper QED treatment, where we can already a priori say that the particle velocity is not renormalized towards faster velocities forever. This consideration is of course purely academic, but emphasizes that the theory itself is not contradictory. The most important point in this observation is that for low enough energies the coupling strength α_g decreases. So if a perturbative treatment is possible in the very beginning its applicability can only become better when approaching lower energies.

Further detail about where the model can flow towards and what the relevant scales would be can be found within the Ref. [59].

Knowing the rough behavior of the model under the changing of scales we will now try to gain insights into the processes that happens in graphene in the presence of Coulomb interaction. To do so we will analyze graphene's ability to polarize.

3.1.2 The Polarization-Operator

The polarization operator contains the information of the system's response to interaction. We defined the polarization operator in Eq. (2.40). Transforming it into the energy and momentum basis one finds:

$$\Pi^R(\omega, \vec{q}) = - \int \frac{d^2p}{(2\pi)^2} \int \frac{d\epsilon}{2\pi} f(\epsilon) \text{Tr} \left\{ \mathcal{A}_0(\epsilon, \vec{p}) \times \left[G_0^R(\epsilon + \omega, \vec{p} + \vec{q}) + G_0^A(\epsilon - \omega, \vec{p} - \vec{q}) \right] \right\}, \quad (3.12)$$

where $G_0^{R,A}$ are bare Green's functions, Eq. (2.15). The momentum integrals that appear in this expression can be conveniently evaluated using elliptic coordinates as described in Appendix B.1.

In the zero temperature limit, Eq. (B.1) simplifies and leads to

$$\Pi^R(\omega, q) = \frac{1}{16} \frac{q^2}{\sqrt{v_F^2 q^2 - (\omega + i0)^2}}. \quad (3.13)$$

Taking the imaginary part of the polarization operator, Eq. (3.13), yields the well-known expression:[60]

$$\text{Im } \Pi^R(\omega, \vec{q}) = \frac{1}{16} \text{Re} \frac{q^2 \text{sign} \omega}{\sqrt{\omega^2 - v_F^2 q^2}}. \quad (3.14)$$

One can see that the imaginary part of the polarization operator is non-vanishing only if $\omega > v_F q$ and shows a divergence at the ‘‘light cone’’ $\omega = v_F q$.

To understand the vanishing of the imaginary part of the polarization operator at $\omega < v_F q$, it is instructive to analyze [61, 62] the kinematic restrictions for elementary processes. It is easy to see that an on-shell electron-hole pair can be created if (left panel of Fig. 3.1)

$$\omega \geq v_F q. \quad (3.15)$$

To see this more properly one should look at the kinematics, meaning that we consider a real process (on the mass-shell) with a transferred energy ω such that $\epsilon_1 - \epsilon_2 = \omega$ and momentum transfer \vec{q} such that $\vec{p}_1 - \vec{p}_2 = \vec{q}$. When using these constrains one needs to remember, that for electron-hole creation the signs of the energies need to be different ($\text{sign}(\epsilon_1) + \text{sign}(\epsilon_2) = 0$), one obtains:

$$2v_F^2 p_1 p_2 \left(1 + \cos \left(\angle [\vec{p}_1, \vec{p}_2] \right) \right) = \omega^2 - v_F^2 q^2, \quad (3.16)$$

which clearly shows the condition from Eq. (3.15).

This should be contrasted to the energy and momentum conservation of on-shell electron-electron scattering processes, whose kinematics unveil (right panel of Fig. 3.1)

$$2v_F^2 p_1 p_2 \left(1 - \cos \left(\angle [\vec{p}_1, \vec{p}_2] \right) \right) = v_F^2 q^2 - \omega^2, \quad (3.17)$$

which implies the condition

$$\omega \leq v_F q. \quad (3.18)$$

Thus, if we restrict our consideration to on-shell particles, electron-electron scattering processes only create electron-hole pairs under the condition $\omega = v_F q$, when $\text{Im } \Pi$ diverges. As follows from Eq. (3.17), scattering processes that satisfy $\omega = v_F q$ correspond to forward scattering with $\angle [p_1, p_2] = 0$.

From Eqs. (2.39) and (3.13) we obtain the golden rule (GR) (see Fig. 2.4) interaction propagator at zero T :

$$\begin{aligned} D_{\text{GR}}^R(\omega, q) &= -\frac{N}{16} \frac{(2\pi\alpha_g v_F)^2}{\sqrt{v_F^2 q^2 - (\omega + i0)^2}}, \\ \text{Im } D_{\text{GR}}^R(\omega, q) &= -\frac{\alpha_g^2 N v_F^2 \pi^2}{4} \text{Re} \frac{\text{sign} \omega}{\sqrt{\omega^2 - v_F^2 q^2}}. \end{aligned} \quad (3.19)$$

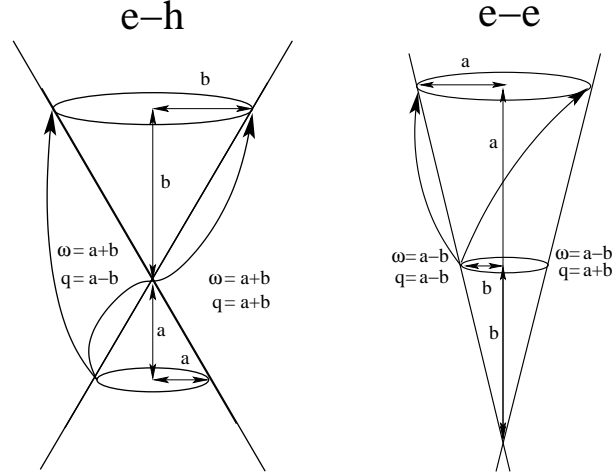


Figure 3.1: Schematics of electron-hole (e-h) creation (left panel) vs electron-electron (e-e) scattering (right panel) near the Dirac point for $\mu = 0$. The hole-hole scattering processes are analogous to those shown in the right panel. We set $v_F = 1$ for brevity. In both panels the possible transferred momenta satisfy $|a - b| \leq |\vec{q}| \leq a + b$ (only the extreme cases of minimal and maximal q are shown). For e-h creation $\omega = a + b$, so that $\omega \geq qv_F$, whereas for e-e scattering the kinematic restrictions yield $\omega = a - b \leq qv_F$.

After the RPA resummation [plugging in Eq. (3.13) into Eq. (2.38)], the imaginary part of the zero- T interaction propagator takes the form

$$\text{Im } D_{\text{RPA}}^R(\omega, q) = -\frac{\alpha_g^2 N v_F^2 \pi^2}{4} \frac{\text{sign } \omega \text{ Re } \sqrt{\omega^2 - v_F^2 q^2}}{\omega^2 - v_F^2 q^2 \left(1 - \frac{\pi^2}{32} \alpha_g^2 N^2\right)}. \quad (3.20)$$

It is seen that the divergence at $\omega = v_F q$ that occurred in the golden rule interaction propagator, Eq. (3.19), is now eliminated. Moreover, the imaginary part of the propagator is zero at the light cone $\omega = v_F q$. Therefore, the forward scattering divergence that arises on the golden rule level disappears within RPA, yielding a zero scattering rate on the RPA level. This is a manifestation of a highly singular character of the zero-temperature problem. We will show that the singular behavior can be controlled by considering a finite temperature allowing for an unambiguous treatment of the system even at zero temperature by considering the limit $T \rightarrow 0$. Otherwise RPA is only justified within a large N treatment.

General Kinematic Details

One might think that if one considers the relaxation of particles by excitation of more particles the constraints given by Eq. (3.15) and (3.18) may wash out. This is not the case. To understand this more properly we consider an arbitrary transferred momentum that similarly to Eq. (3.16) and (3.17) fulfills:

$$\vec{q}^2 = (\vec{p}_i - \vec{p}_f)^2 = v_F^2 (\epsilon_i^2 + \epsilon_f^2 - 2\text{sign}(\epsilon_i \epsilon_f) \epsilon_i \epsilon_f \cos(\phi_{if})) = v_F^2 \omega^2 + 2v_F^2 \epsilon_i \epsilon_f (1 - \text{sign}(\epsilon_i \epsilon_f) \cos(\phi_{if})) \quad (3.21)$$

The relation between ω and \vec{q} in general reads:

$$\frac{q^2 - \omega^2}{2\epsilon_i \epsilon_f} \leq 0, \quad (3.22)$$

incorporating both of above discussed limits into one equation.

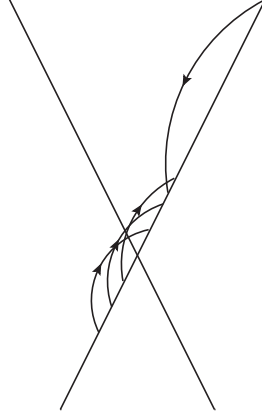


Figure 3.2: *Illustration of relaxation of a hot electron via excitation of many electron hole pairs.*

Now if we consider a particle with $\epsilon > 0$ and want it to relax into several electron-hole pairs we can define several transferred momenta $\vec{q}_1, \vec{q}_2, \vec{q}_3, \dots$ and energies $\omega_1, \omega_2, \dots$. Due to energy and momentum conservation we have:

$$\sum_n \vec{q}_n = 0, \quad \sum_n \omega_n = 0. \quad (3.23)$$

Since we are interested in a particle relaxing by creation of electron-hole pairs we consider \vec{q}_1 and ω_1 to be the energy and momentum the initial particle lost. Further we want the state the particle relax to, to be on the same side of the Dirac cone (see Fig. 3.2) which implies $q_1^2 \geq \omega_1^2$. Since at the Dirac point we assume to be able to relax only via creation of electron-hole pairs, all other momenta satisfy $q_{n>1}^2 \leq \omega_{n>1}^2$. With help of the conservation laws we obtain:

$$|\vec{q}_1| = \left| - \sum_{n>1} \vec{q}_n \right| \leq \sum_{n>1} |\vec{q}_n| \leq \sum_{n>1} |\omega_n|. \quad (3.24)$$

If we consider relaxation we want to deposit energy in the creation of the electrons and holes implying that all $\omega_{n>1}$ have the same sign and the right hand side of Eq. (3.24) equals $|\omega_1|$. This means again that the only processes possible in such a situation, are exactly collinear and thus having only a zero measure. The RPA kills contributions that exist only and singular the single line $\omega = |\vec{q}|$ as in the previous case explicitly shown in Eq. (3.20).

3.1.3 The Scattering Rate

Taking into account RPA makes the interaction disappear at the single line $\omega = |\vec{q}|$, where kinematically interaction could affect the particles. Nonetheless have previous works [61, 63] approached this problem

and obtained a quasi-particle lifetime. Within the introduced formulation we will sketch a way to obtain a similar result. It is important to note though, that the calculation one needs to perform to obtain the previous lifetime is ill defined.

To do so we will use the GR interaction defined in Eq. (3.19), instead of the RPA screened interaction. We will use the imaginary part of the self-energy (Eq. (2.35)) and its zero temperature limit (see RG 3.1.1). But the focus this time is on including the effects that come from the polarizability of graphene by using the GR interaction (see Eq. (3.19)). So we are dealing with (on shell):

$$\text{Im } \Sigma_\lambda(\epsilon = v_F \vec{p}, \vec{p}) \stackrel{v_F=1}{=} -2 \sum_{\lambda'} \int \frac{d^2 \vec{q}}{(2\pi)^2} \int_{-\epsilon}^{\epsilon} \frac{d\omega}{2\pi} \text{Im } D_{\text{GR}}^R(\omega, q) \mathcal{A}_{0\lambda'} \text{Tr} [\mathcal{P}_\lambda \mathcal{P}_{\lambda'}] \quad (?). \quad (3.25)$$

Doing the ω integration with the constraint $|\omega| < |\epsilon|$ one recognizes that this constraint transforms into $|p - \lambda\lambda'|\vec{p} - \vec{q}| < p$ which is only fulfilled for $\lambda\lambda' = 1$. This states that at zero temperature and the corresponding lowest order in polarization corrections a particle will never turn into a hole due to electron-electron interaction. Using again the elliptical coordinates (see App. B.1) we manage to obtain:

$$\text{Im } \Sigma_\lambda(\epsilon = v_F \vec{p}, \vec{p}) = -\frac{\alpha_g^2 N}{128} \int_p^\infty d\xi \int_{-p}^p d\eta \frac{(\xi + \eta) \sqrt{\xi + p}}{p\sqrt{p + \eta}} \text{Re} \frac{1}{\sqrt{(\xi - p)(p - \xi)}} \quad (?). \quad (3.26)$$

At this step one pretty well recognizes the trouble one has at the single line $\omega = q$ which in above formula translates into $\xi = p$. The expression as it is given above is strictly speaking zero since the electrons can not create electron-hole pairs (see the previous section) except for the one singular line where the integrand appears to be divergent. One can assume the following relation to be true:

$$\text{Re} \frac{1}{\sqrt{(\xi - p)(p - \xi)}} \sim \delta(\xi - p) \quad (?). \quad (3.27)$$

If so, we gain for the quasi-particle lifetime, as was previously seen in the literature [61]:

$$\text{Im } \Sigma_\lambda(\epsilon = v_F \vec{p}, \vec{p}) \sim -\frac{\alpha_g^2 N}{48} p \quad (?). \quad (3.28)$$

This calculation shows how the above (see Sec. 3.1.2) discussion manifests itself in quantities like the quasi-particle lifetime, making the calculation rather difficult. Furthermore, the lifetime obtained in Eq. (3.28) does not appreciate the complexity of the problem. We will present in Sec. 4.2.1 a way to unambiguously define a proper quasi-particle lifetime at the Dirac point which significantly differs from Eq. (3.28).

3.1.4 Discussion

In view of the singular character of the problem, at zero temperature the imaginary part of the self-energy is highly sensitive to changes of the electron dispersion [62]. The Fermi velocity depends logarithmically on the momentum or energy [60], Eq. (3.9), due to the renormalization by the Coulomb interaction.

In Eq. (3.14) we have neglected the momentum dependence of v_F which leads to a separation of the two regions defined by Eqs. (3.15) and (3.18), see the left-hand side of Fig. 3.3. The electron-hole

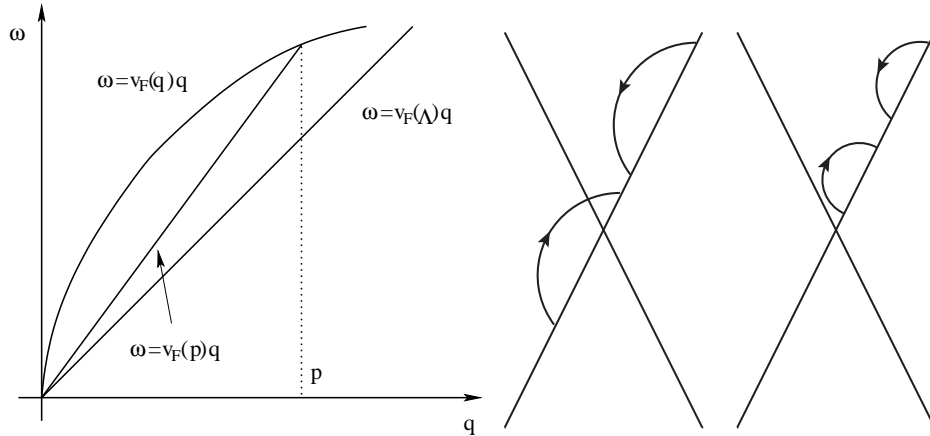


Figure 3.3: *Left:* Interaction-induced dispersion correction near the Dirac cone. The electron-hole creation ($\omega \geq v_F(q) q$) and electron-electron scattering ($\omega \leq v_F(p) q$) regions do not overlap, so that the zero-temperature inelastic scattering rate is zero. *Middle:* Illustration of the only relaxation process at zero temperature. *Right:* Illustration of the relaxation process possible at finite temperature.

creation [$\omega \geq v_F(q) q$] and electron-electron scattering [$\omega \leq v_F(p) q$] regions are then separated due to the renormalization-induced nonlinearity of the electron dispersion, which leads to the vanishing of the zero- T scattering rate already at the golden rule level. This supports our statement that in the strict zero-temperature case the question of the influence of Coulomb interaction on graphene is an ill defined problem.

Nevertheless, at finite temperature the situation is essentially different. First, the conditions (3.15) and (3.18) will be smeared by temperature, since not only relaxation processes of the type shown in the middle part of Fig. 3.3 take place but as well processes of the type shown in the right-hand side of Fig. 3.3. Second, for energy scales smaller than T the renormalization of the Fermi velocity is cut off by temperature and hence, the linearity of the dispersion relations is restored: renormalization reduces merely to a T -dependence of the Fermi velocity. Therefore, when discussing the finite- T physics of inelastic scattering on scales $\lesssim T$ we will disregard the renormalization-induced nonlinearity of the dispersion. Furthermore whenever we will use the notation v_F for $\epsilon \lesssim T$ we will mean the renormalized value of the velocity $v_F^*(T)$ and omit the asterisk for brevity.

4

Chapter 4

Coulomb Interaction in Graphene: Finite Temperature Analysis

Heat, like gravity, penetrates every substance of the universe, its rays occupy all parts of space.

J. Fourier, The Analytical Theory of Heat

One of the main purposes of this work is to get insights into the electronic processes that take place in graphene in the presence of Coulomb interaction. We discussed the problems that arise in case of zero temperature in the previous chapter. Our attempt to resolve these problems is to introduce finite temperature to the system. The reason to do so is rather simple. It is not only experimental fact to have finite temperature it creates as well a broadening in the distribution function reflecting the overall presence of electron-hole pairs at the Dirac point. The point of those pairs is that they might screen Coulomb interaction and help to resolve the forward scattering resonance. Hence we look first at the polarizability of graphene at finite temperature and afterwards investigate its consequences for the scattering processes.

4.1 The Polarization Operator at Finite Temperature

The natural starting point is again Eq. (3.12) which contains at finite temperature a broadened distribution function allowing now not only for electron-hole creation but as well electron-electron scattering with thermally activated electrons. So one of the problems discussed in the previous Chap. 3, namely the fact that electron-electron scattering and electron-hole creation have only a subspace of measure zero in common is overcome by the presence of thermally activated electrons. Gaining the polarization operator for the finite temperature case will hence allow us to do a well defined RPA approximation of the interaction. The actual calculation of the polarization operator is rather long which is the reason why the details can be found in the appendix B.1.

It turns out that the effect of finite temperature on the screening in graphene is much more pronounced than in conventional metals with finite Fermi-surface and quadratic electronic dispersion. Indeed, the linearity of the spectrum of Dirac fermions gives rise to a strong (linear) energy dependence of the density of states in two dimensions, whereas for the parabolic spectrum the density of states is constant. In the latter case, the polarization operator is essentially independent of temperature. This is not the case for Dirac particles.

Let us consider the undoped graphene first, i.e. the chemical potential lies at the Dirac point ($\mu = 0$). The typical electron-hole pairs that participate in the screening of Coulomb interaction at finite temperature live within the energy window of order T . This strongly changes the polarization operator at $qv_F, \omega \lesssim T$. To simplify the notations at non-zero temperature, we introduce the dimensionless variables according to

$$Q = \frac{v_F q}{2T}, \quad \Omega = \frac{\omega}{2T}. \quad (4.1)$$

We use the general expression for the polarization operator, Eqs. (B.1) and (B.2) from Appendix B.1. Considering four different regions shown in Fig. 4.1, we simplify these equations in each of the cases, which allows us to treat the problem analytically.

The four regions are defined by the conditions:

- Region 1: $Q \ll 1$ and $Q < |\Omega|$
- Region 2: $1 \ll Q$ and $Q < |\Omega|$
- Region 3: $Q \ll 1$ and $|\Omega| < Q$
- Region 4: $1 \ll Q$ and $|\Omega| < Q$

The need to deal with those four regions is due to the non-analyticity of the polarization operator for forward scattering $Q = \Omega$ and due to the additional length scale we got from temperature. The forward scattering creates naturally a division of the Ω - Q -plane, whereas the comparison with the temperature is ad-hoc introduced to explore the different regimes we cannot properly explore for momenta of order temperature ($Q \sim 1$).

The regimes 2 and 4 correspond to situations where the presence of the thermal broadening becomes less effective, hence the leading terms should correspond to the zero temperature result. The regions 1 and 3 are the ones dominated by thermal broadening and are therefore most relevant to understand the way the formally ill-defined problem can be resolved. In region 3 we deal with the polarization effects caused by thermally activated electrons whereas region 1 corresponds to electron-hole processes within the thermally broadened window around the Dirac point.

As shown in Appendix B.1, the leading-order terms with non-vanishing imaginary part form the following simplified polarization operator:

$$\Pi^R(\Omega, Q) = \frac{T}{v_F^2} \begin{cases} \frac{\ln 2}{\pi} \left[1 - \frac{|\Omega|}{\sqrt{\Omega^2 - Q^2}} \right] + \frac{i}{8} \frac{Q^2 \tanh(\Omega/2)}{\sqrt{\Omega^2 - Q^2}}, & \text{(region 1)} \quad |\Omega| > Q \\ \frac{\ln 2}{\pi} + \frac{Q^2 \Omega \arcsin\left(\frac{\Omega}{Q}\right)}{8\pi \sqrt{\Omega^2 - Q^2}} + \frac{i \ln 2}{\pi} \frac{\Omega}{\sqrt{Q^2 - \Omega^2}}, & \text{(region 3)} \quad |\Omega| < Q \\ -\frac{\zeta\left(\frac{3}{2}\right)(2 - \sqrt{2})}{8\sqrt{\pi} \sqrt{\Omega^2 - Q^2}} \sqrt{Q} + \frac{i \operatorname{sign} \Omega}{8} \frac{Q^2}{\sqrt{\Omega^2 - Q^2}}, & \text{(region 2)} \quad |\Omega| > Q \\ \frac{1}{8} \frac{Q^2}{\sqrt{Q^2 - \Omega^2}} + \frac{i}{\sqrt{2\pi}} \frac{\sqrt{Q} e^{-Q} \sinh \Omega}{\sqrt{Q^2 - \Omega^2}}, & \text{(region 4)} \quad |\Omega| < Q \end{cases} \quad \begin{matrix} Q \ll 1 \\ \\ \\ Q \gg 1 \end{matrix} \quad (4.2)$$

In the case of large momenta, $Q \gg 1$, we recover the zero-temperature result as we should. For $Q \ll 1$, the polarization operator substantially differs from the zero-temperature expression. We will

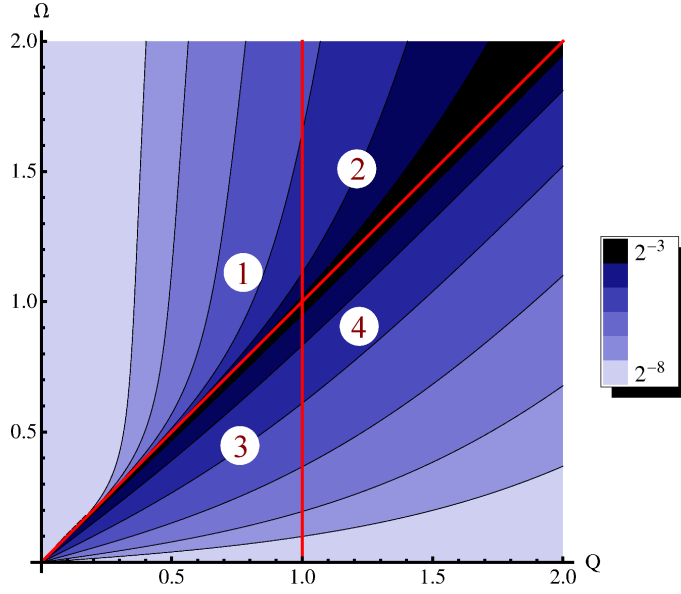


Figure 4.1: *Imaginary part of the polarization operator in the frequency-momentum plane. Four regions of dimensionless variables Ω and Q (see text) are indicated. The magnitude of $\text{Im}\Pi^R(\Omega, Q)$ is encoded by the logarithmic color-scale.*

discuss this case in more detail in Sec. 4.1.1. The separation between $\Omega < Q$ and $\Omega > Q$ is dictated by the non-analytical structure of the polarization operator, see Eq. (4.2), which originates from the forward scattering resonance discussed in Sec. 2.1.4.

In the regimes 1 and 3 in which the thermal screening is important it is possible to extend the above discussion towards finite chemical potential by including a chemical potential within the thermal factors. This way Eq. (3.12) stays unchanged except of the distribution function that changes according to $f(\epsilon) \rightarrow f(\epsilon - \mu)$. Adapting the calculations one finds (for $\hat{\mu} = \mu/2T$)

$$\Pi^R(\Omega, Q) = \frac{T}{v_F^2} \begin{cases} \frac{\ln(2 \cosh(\hat{\mu}))}{\pi} \left[1 - \frac{|\Omega|}{\sqrt{\Omega^2 - Q^2}} \right] + \frac{i}{8} \frac{Q^2}{\sqrt{\Omega^2 - Q^2}} \frac{\sinh(\Omega)}{\cosh(2\hat{\mu}) + \cosh(\Omega)}, & \text{(region 1)} \\ \frac{\ln(2 \cosh(\hat{\mu}))}{\pi} + \frac{Q^2}{8\pi} \frac{\Omega \arcsin\left(\frac{\Omega}{Q}\right)}{\sqrt{\Omega^2 - Q^2} \cosh^2(\hat{\mu})} + \frac{i \ln(2 \cosh(\hat{\mu}))}{\pi} \frac{\Omega}{\sqrt{Q^2 - \Omega^2}}, & \text{(region 3)} \end{cases} \quad (4.3)$$

The contributions we have considered here describe the interplay of temperature induced screening and chemical potential screening. As clearly visible when comparing Eq. (4.3) with Eq. (4.2) is the ability of dynamical screening unchanged.

The original question we have focused on is the system's behavior due to Coulomb interaction which is shown in Ch. 3 to be most severe at the Dirac-point for which reason we keep within this chapter the finite chemical potential most of the time out of business.

4.1.1 The RPA Screened Interaction

The real part of the polarization operator, Eq. (4.2), for $Q \ll 1$ is determined by temperature and leads therefore to the screening of Coulomb interaction according to

$$\lim_{\Omega \rightarrow 0} D_{\text{RPA}}^R(\Omega, Q) = \frac{D_0(Q)}{1 + D_0(Q) N \Pi^R(0, Q)} = \frac{v_F^2 \pi}{NT \ln 2} \left(\frac{\alpha_g N \ln 2}{Q + \alpha_g N \ln 2} \right), \quad (4.4)$$

which yields the screening length

$$l_{\text{scr}} = \frac{v_F}{2\alpha_g N T \ln 2}. \quad (4.5)$$

Thus at finite temperature the system does screen the long range Coulomb interaction. Note that for $Q \ll \alpha_g N$, the RPA propagator becomes independent of the interaction constant α_g ,

$$D_{\text{RPA}}^R(\Omega, Q) \Big|_{Q \ll \alpha_g N} \simeq \frac{1}{\Pi^R(\Omega, Q)}, \quad (4.6)$$

as in conventional systems with Coulomb interaction. We will see, however, that the dominant contributions to relaxation rates are determined by higher transferred momenta $Q \gtrsim \alpha_g N$, where the peculiarities of the finite- T screening in graphene are crucially important.

4.1.2 Plasmons

In Region 1, the real part of the polarization operator in Eq. (4.2) may become negative, leading to emergence of plasmon excitations. The plasmon dispersion $\Omega_p(Q)$ is determined by the zero of

$$1 + D_0 N \text{Re} \Pi^R = \frac{\alpha_g N Q \ln 2}{(\Omega^2 - Q^2)^{3/2}} \left[\Omega - \frac{(\alpha_g N \ln 2 + Q) \sqrt{Q}}{\sqrt{Q + \alpha_g N \ln 2}} \right], \quad (4.7)$$

yielding

$$\Omega_p(Q) = \frac{(\alpha_g N \ln 2 + Q) \sqrt{Q}}{\sqrt{Q + 2\alpha_g N \ln 2}}. \quad (4.8)$$

For $Q \rightarrow 0$, this simplifies to $\Omega_p(Q) \propto \sqrt{\alpha_g N Q}$. A non-zero imaginary part of the polarization operator Eq. (4.2) in the corresponding region implies that these plasmons have a finite lifetime. The decay rate of plasmon excitations is given by

$$\Gamma_p(\Omega, Q) = \frac{(\Omega^2 - Q^2)^{3/2}}{\alpha_g N Q \ln 2} D_0(Q) \text{Im} \Pi^R(\Omega, Q), \quad (4.9)$$

which yields

$$\Gamma_p(\Omega, Q) \Big|_{\Omega = \Omega_p(Q)} = \frac{\pi \Omega}{16 \ln 2} (\Omega^2 - Q^2) \Big|_{\Omega = \Omega_p(Q)} \leq \frac{\pi \Omega^3}{16 \ln 2} \Big|_{\Omega = \Omega_p(Q)}. \quad (4.10)$$

Remarkably, Eq. (4.10) indicates a good quasi-particle behavior for plasmons which is, as we will see in Sec. 4.2.1, not true for electronic excitations. The situation is somewhat similar to Luttinger liquid where plasmons are almost perfect quasi-particles, whereas, from the point of view of fermionic excitations, the Luttinger liquid represents a paradigmatic example of a non-Fermi-liquid.

The discussion of the plasmons is one of the few situations where we should really consider to check their appearance in the presence of finite chemical potential. Taking a look at Eq. (4.3) and reminding the definition of the plasmon resonance (4.7) it becomes clear that by simply replacing $\ln 2 \rightarrow \ln(2 \cosh \hat{\mu})$ we got the dispersion of the plasmons for arbitrary chemical potential as long as the momentum stays small $Q \ll 1$. We identify two different asymptotics of the dispersion and the plasmon broadening (in dimension full units $q^*(\mu) = \alpha_g N T \ln[2 \cosh(\mu/(2T))]$):

$$\omega_p = \begin{cases} \sqrt{q^*(\mu)v_F q} & v_F q \ll 2q^*(\mu) \\ v_F q + \frac{(q^*)^2}{2v_F q} & 2q^*(\mu) \ll v_F q \end{cases}, \quad \Gamma_p = \begin{cases} \frac{\pi}{16} \frac{\alpha_g N v_F q}{2T \cosh^2\left(\frac{\mu}{2T}\right)} \sqrt{q^* v_F q} & v_F q \ll 2q^*(\mu) \\ \frac{\pi}{32} \frac{\alpha_g N q^* v_F q}{2T \cosh^2\left(\frac{\mu}{2T}\right)} & 2q^*(\mu) \ll v_F q \end{cases}, \quad (4.11)$$

which support earlier statements of the good quasi-particle picture for plasmons in the case of larger chemical potential (note that $v_F q \ll T$ is always assumed).

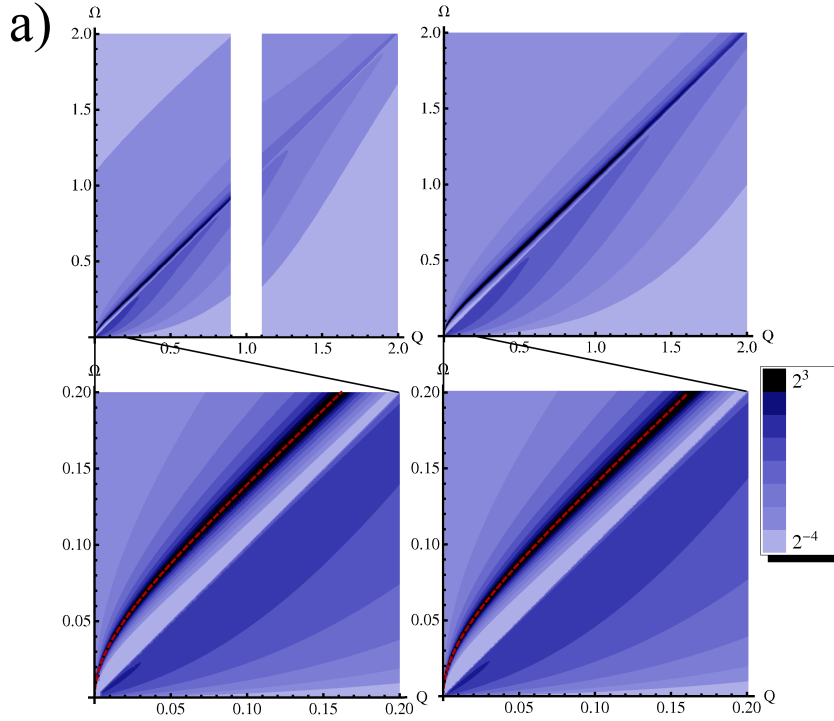


Figure 4.2: *Imaginary part of RPA interaction. Left: using an analytic approximation, right: by numerical evaluation of Eqs. (B.1) and (B.2). Dashed lines indicate the plasmon dispersion (see Eq. (4.7)).*

Fig. 4.2 and Fig. 4.3 demonstrates that Eq. (4.2) for the polarization operator yields a remarkably good approximation for evaluation of the imaginary part of the RPA-interaction,

$$\text{Im } D_{\text{RPA}} = - \frac{ND_0^2 \text{Im } \Pi^R}{\left(1 + ND_0 \text{Re } \Pi^R\right)^2 + \left(ND_0 \text{Im } \Pi^R\right)^2}. \quad (4.12)$$

[see also Eq. (B.12) in Appendix B.2]. In Fig. 4.2b we see the plasmon peak in the RPA interaction propagator, which is strongly asymmetric and is suppressed around the light cone, so that $\text{Im } D_{\text{RPA}} = 0$ exactly at $\Omega = Q$.

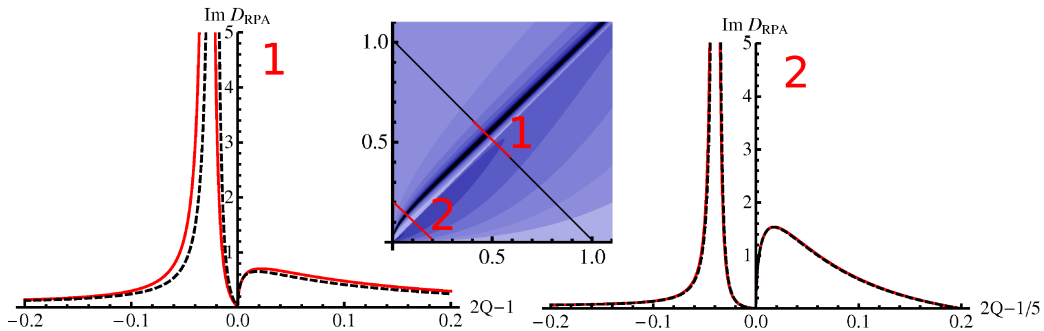


Figure 4.3: Cross-sections through the plots of Fig. 4.2 from $(\Omega, Q) = (1, 0)$ to $(\Omega, Q) = (0, 1)$ (1) from $(\Omega, Q) = (0.2, 0)$ to $(\Omega, Q) = (0, 0.2)$ (2). Solid curves: analytic approximation; dashed curves: numerical integration. For all plots the interaction strength is $\alpha_g N = 1/3$.

Further one recognizes in Fig. 4.2 that on the right hand side of the plasmon peak where interactions with the electronic continuum are possible a feature is present that can be interpreted as strongly broadened plasmon peak as it is known from plasmons entering the electronic continuum in conventional 3 dimensional metals. The notion plasmon is of course misleading for this object since due to interactions it is not a well defined excitation. When talking about plasmons we will therefore always refer to the well defined peaked structure whose dispersion is given by Eq. (4.7).

Validity of RPA

Let us now discuss the status of the RPA in graphene. In the previous Chap. 3 we have argued that at zero temperature the only way of controlling RPA is via the large N treatment. Meaning that we assume to have numerous independent flavors in the system making the leading density response the dominant contribution. If N is not assumed to be large and in view of the absence of the screening, the non-RPA diagrams are parametrically the same as those included in the RPA. Furthermore, as discussed in the end of Sec. 3.1.2, the renormalization-induced curvature of the spectrum (which is also beyond the RPA) may dramatically affect the results obtained within the RPA.

Nevertheless at finite T , the T -induced screening of the interaction, Eq. (4.4), restores the validity of the RPA for $q \ll T/v_F$ ($Q \ll 1$) even for $N \sim 1$. Indeed, the $1/q$ -singularity of the long-range Coulomb interaction is not compensated in the denominator of Eq. (4.12) because the polarization operator at finite T is no longer linear-in- q . The situation becomes similar to that in conventional metals with a finite Fermi-surface, where the RPA is justified for $q \ll k_F$ (and $\alpha_g \ll 1$). In undoped graphene the role of k_F is played by T/v_F , which in effect establishes an analog of a finite Fermi-surface. Therefore, for $q \ll T/v_F$ the RPA does sum up the most singular interaction-induced terms. All other terms are non-singular because of the screening. This means that all the observables that are dominated by the collisions with the momentum transfer smaller than T/v_F can be calculated (even with the correct numerical prefactors) within the RPA. The RPA result for those observables that are dominated by $qv_F \sim T$ is parametrically correct, but the value of the prefactor cannot be found using the RPA.

Below we employ the finite- T RPA for calculation of various scattering rates in graphene. For the sake of generality, we keep N as a large parameter. In what follows we focus on the case $\alpha_g N \ll 1$, but whenever the rate under consideration is dominated by $qv_F \lesssim T$, the condition $N \gg 1$ can be removed so that we are allowed to use the RPA for $N \sim 1$.

4.2 The Rates at Finite Temperature

We figured out that RPA is controllable within the finite temperature calculation. Further we briefly discussed the screening properties and plasmonic properties of graphene. With this knowledge at hand we will try now to understand the consequences for the electronic system. For this reason we calculate various inelastic scattering rates in clean graphene at finite temperature. More specifically, we focus on the quantum scattering rate (and dephasing) and the energy relaxation rate induced by the RPA-screened Coulomb interaction. The quantum scattering rate determines the lifetime of quantum states (plane waves) and is related to the dephasing rate. The energy relaxation rate governs the relaxation of the quasi-particle distribution function.

Although the origin of all these rates is the same, the inelastic electron-electron collisions, these rates may strongly differ from each other. For instance, this is exactly what happens in diffusive metals [43, 64] because of the infrared-singular collision kernel. Another prominent example of a non-trivial behavior of relaxation rates related to the infrared singularities is a Luttinger liquid (disordered or clean) [27–33]. On the other hand, within the Fermi-liquid theory of clean metals all the inelastic scattering rates behave in the same way, since the characteristic frequency and momentum transfer in the course of electron-electron collisions is determined by temperature. The goal of this section is to understand whether the situation in clean graphene is similar to the Fermi-liquid or not.

As we have already seen in Sec. 4.1, the behavior of the polarization operator at finite temperature is highly non-trivial. This leads to a rather rich behavior of the scattering rates.

It turns out that, in addition to the temperature scale, two more characteristic scales appear which are relevant for relaxation rates: $\alpha_g^2 N^2 T$ and $\alpha_g N T$. In this section we will distinguish between the four regimes (I-IV) as shown in Fig. 4.4. The contributions to each of the scattering rates from different

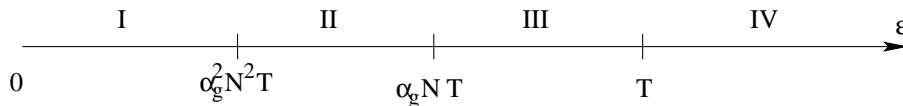


Figure 4.4: Characteristic energy scales separating domains of distinct behavior of the rates.

regions (1-4, see Fig. 4.1) of the momentum-frequency plane are calculated separately.

4.2.1 Quantum Scattering Rate in Graphene

One of the main manifestations of the inelastic scattering in electronic systems is the interaction-induced dephasing. In order to analyze the effects of dephasing in graphene, we will follow the route suggested by earlier works on 2D (in particular, diffusive) systems [43]. A natural first step is to calculate the quantum scattering rate τ_q^{-1} which is given by the imaginary part of the quasi-particle self-energy taken on the mass-shell. Indeed, for conventional metals with parabolic dispersion, in the high-temperature (ballistic since not diffusive: $T\tau \gg 1$) regime, the dephasing rate τ_ϕ^{-1} to leading

order is given by τ_q^{-1} (see Ref. [65]). In the diffusive regime, the scattering kernel acquires an infrared singularity leading to a divergent τ_q^{-1} at finite T . This is a manifestation of the fact that the single-particle self-energy is not a gauge-invariant object; no divergencies occur in observable (gauge-invariant) quantities, such as, e.g., dephasing rate. However, even when the quantum scattering rate diverges, the calculation of it turns out to be instructive: a parametrically correct result for the dephasing rate can be obtained from the expression for τ_q^{-1} supplemented with an appropriate infrared cutoff. It is thus useful to begin with analyzing τ_q^{-1} .

Quantum Scattering Rate: Definitions

The peculiarity of graphene is that the self-energy is a matrix in the sublattice space, which has a non-zero imaginary part, $\text{Im } \Sigma_v$ [Eq. (2.37)], in the off-diagonal components. Therefore, the definition of the quantum scattering time in graphene is actually not unique. Indeed, one can associate with the quantum scattering rate the on-shell value of the imaginary correction to the energy in the full Green's function, $\text{Im } \Sigma_\epsilon$ [Eq. (2.36)], similarly to the conventional Fermi-liquid theory:

$$\frac{1}{2\tau_q(\epsilon)} = -\theta(\epsilon) \text{Im } \Sigma_\epsilon(v_F p, \vec{p}) \Big|_{p=\epsilon/v_F} - \theta(-\epsilon) \text{Im } \Sigma_\epsilon(-v_F p, \vec{p}) \Big|_{p=-\epsilon/v_F}. \quad (4.13)$$

Here we have taken the self-energy at the “+” mass-shell for $\epsilon > 0$ corresponding to the positive energies, $\epsilon = v_F p$, and at $\epsilon < 0$ on the “-” mass-shell. For undoped graphene we clearly have

$$\frac{1}{\tau_q(\epsilon)} = \frac{1}{\tau_q(-\epsilon)}, \quad (4.14)$$

due to particle hole symmetry ($\mu = 0$). Within the RPA the explicit expression for the imaginary part of the total self-energy Σ_ϵ taken at $\epsilon = v_F p$ reads:

$$\begin{aligned} \text{Im } \Sigma_\epsilon(v_F p, \vec{p}) = & -\frac{\pi}{2} \int \frac{d\omega}{2\pi} \left[g(\omega) + f(v_F p - \omega) \right] \int \frac{d^2 q}{(2\pi)^2} \text{Im } D^R(\omega, \vec{q}) \\ & \times \left[\delta(v_F p - \omega - v_F |\vec{p} - \vec{q}|) + \delta(v_F p - \omega + v_F |\vec{p} - \vec{q}|) \right]. \end{aligned} \quad (4.15)$$

Alternatively, one can introduce the lifetime of the “+” and “-” chiral states through the corresponding self-energies, from Eq. (2.35)

$$\frac{1}{2\tau_\pm(\epsilon)} = -\text{Im } \Sigma_\pm(\epsilon, \vec{p}) \Big|_{p=|\epsilon|/v_F}, \quad (4.16)$$

which yields

$$\frac{1}{\tau_+(\epsilon)} = \frac{1}{\tau_-(-\epsilon)}. \quad (4.17)$$

Using Eqs. (2.35) and (2.19), we get for the self-energy of electrons (+ chirality)

$$\begin{aligned} \text{Im } \Sigma_+(v_F p, \vec{p}) = & -\frac{\pi}{2} \int \frac{d\omega}{2\pi} \left[g(\omega) + f(v_F p - \omega) \right] \int \frac{d^2 q}{(2\pi)^2} \text{Im } D^R(\omega, \vec{q}) \\ & \times \left[\left(1 + \frac{\vec{p}(\vec{p} - \vec{q})}{p|\vec{p} - \vec{q}|} \right) \delta(v_F p - \omega - v_F |\vec{p} - \vec{q}|) + \left(1 - \frac{\vec{p}(\vec{p} - \vec{q})}{p|\vec{p} - \vec{q}|} \right) \delta(v_F p - \omega + v_F |\vec{p} - \vec{q}|) \right]. \end{aligned} \quad (4.18)$$

for the “own” mass-shell ($\epsilon = +v_F p$), and

$$\begin{aligned} \text{Im } \Sigma_+(-v_F p, \vec{p}) &= -\frac{\pi}{2} \int \frac{d\omega}{2\pi} [g(\omega) + f(-v_F p - \omega)] \int \frac{d^2 q}{(2\pi)^2} \text{Im } D^R(\omega, \vec{q}) \\ &\times \left[\left(1 - \frac{\vec{p}(\vec{p} - \vec{q})}{p|\vec{p} - \vec{q}|} \right) \delta(-v_F p - \omega - v_F |\vec{p} - \vec{q}|) + \left(1 + \frac{\vec{p}(\vec{p} - \vec{q})}{p|\vec{p} - \vec{q}|} \right) \delta(-v_F p - \omega + v_F |\vec{p} - \vec{q}|) \right]. \end{aligned} \quad (4.19)$$

for the “wrong” (hole) mass-shell ($\epsilon = -v_F p$).

The main formal difference between the two relaxation rates, Eqs. (4.13) and (4.16), which are related by

$$\frac{1}{\tau_q(\epsilon)} = \frac{1}{2\tau_+(\epsilon)} + \frac{1}{2\tau_-(\epsilon)}, \quad (4.20)$$

is in the appearance of Dirac factors $1 \pm \cos \theta$ in Eqs. (4.18) and (4.19) where $\theta = \arccos(\vec{p}\vec{p}'/pp')$ is the scattering angle between the incoming momentum \vec{p} and the momentum $\vec{p}' = \vec{p} - \vec{q}$ after scattering. This factor is related to the additional Berry phase in the problem of Dirac particles, which arises due to the overlap of Bloch functions and, in particular, forbids the backscattering within the same chirality and valley (see Eq. (A.20)). Note that for well-defined quasi-particles (i.e., in a Fermi-liquid situation) the self-energy at a “wrong” mass-shell would never be relevant. However, if the quasi-particle broadening is larger than the characteristic energy, this is no longer the case, so that Eq. (4.19) may then contribute to the observables.

In Eq. (4.18), the term with $1 + \cos \theta$ corresponds to the electron-electron scattering (right panel of Fig. 3.1) which is determined by the contribution of region 3 in Fig. 4.1. The term with $1 - \cos \theta$ is due to electron-hole scattering (electron-hole pairs, left panel of Fig. 3.1) accompanied by the excitation of plasmons and is determined by the contribution of region 1 in Fig. 4.1. The latter contribution is suppressed for the forward scattering $\theta = 0$ because of the Dirac factor. Furthermore, at zero temperature only the electron-electron processes are allowed by the kinematic restrictions.

At finite T , however, the situation is different for the low-energy domains I and II ($\epsilon < \alpha_g NT$), where the contributions of the electron-electron and electron-hole scattering to the inelastic quantum scattering rates are of the same order. This means that the low-energy electron-type and hole-type quasi-particles are strongly correlated by the mutual inelastic scattering, whereas at higher energies ($\epsilon > \alpha_g NT$, corresponding to domains III and IV) the electronic and hole subsystems are only weakly coupled with each other, in agreement with Ref. [62].

As we will see below, depending on the energy range, Fig. 4.4, both τ_q^{-1} and τ_{\pm}^{-1} may be larger or smaller than the quasi-particle’s energy. When the quasi-particle’s broadening is small, the two rates coincide since the inelastic scattering is dominated by small scattering angles θ and the Dirac factors reduce to 0 and 1. At the lowest energies (domains I and II), both τ_q^{-1} and τ_{\pm}^{-1} exceed the energy which makes the notion of mass-shell not well-defined. In particular, due to the inelastic broadening, the electronic excitation (+ chirality) has tails at negative energies which overlap with the hole mass-shell.

Furthermore, as shown in Sec. 4.2.3, the characteristic rate of the energy relaxation (energy mixing due to the diffusion over energy) at low energies is of the same order as the quantum scattering rate, so that the electronic excitations constantly explore the hole mass-shell and vice versa. In this situation, the broadening of quasi-particles of a given chirality is an effect described by the total scattering rate τ_q^{-1} , according to Eq. (4.20), rather than Eq. (4.16). Therefore, in what follows, we will mostly focus on the Fermi-liquid-type total rate τ_q^{-1} , formally defined in Eq. (4.13).

τ_q	I	II	III	IV
$qv_F \sim \omega$	T	$(\alpha_g NT)^2/\epsilon$	$\alpha_g NT$	$\alpha_g NT$
Regions	1,2,3,4	1,3	3	3

Table 4.1: Momentum/frequency scales and regions of the Q - Ω plane that dominate the quantum scattering rate τ_q^{-1} in different domains (I,II,III, and IV) of energy ϵ .

Quantum Scattering Rates: Results and Discussion

The evaluation of integrals involved in the calculation of the total quantum scattering rate τ_q^{-1} is outlined in Appendix B.2. The result depends on the energy range (see Fig. 4.4)

$$\frac{1}{2\tau_q(\epsilon)} \approx \begin{cases} c_1 \frac{T}{N} \sqrt{\frac{\epsilon}{T}}, & \epsilon \ll \alpha_g^2 N^2 T, \quad \text{I} \\ c_2 \alpha_g T, & \alpha_g^2 N^2 T \ll \epsilon \ll \alpha_g NT, \quad \text{II} \\ c_3 \alpha_g T, & \alpha_g NT \ll \epsilon. \quad \text{III, IV} \end{cases} \quad (4.21)$$

Here $c_1 \sim 1$, $c_2 = 3\pi/2$, and $c_3 = 2\beta(2)/\pi$ are numerical coefficients of order unity, $\beta(x)$ is the Dirichlet beta function and $\beta(2)$ is the Catalan constant. Note that for energies in regimes II, III, and IV, the number of independent flavors N drops out from the expression for τ_q . The comparison of the asymptotic expressions (4.21) with the exact numerical evaluations is shown in Fig. 4.5).

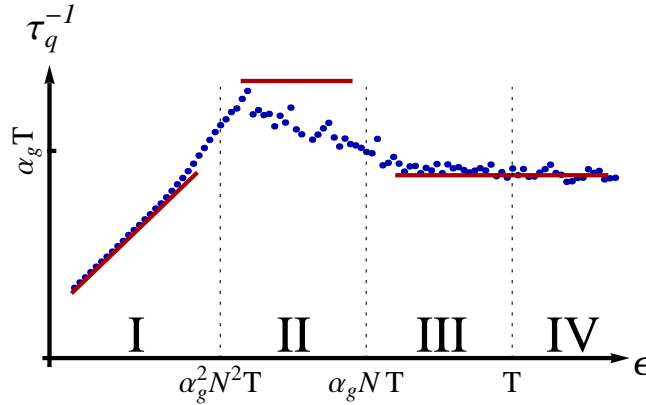


Figure 4.5: Quantum scattering rate for $\alpha_g N = 4 \times 10^{-3}$ (double logarithmic scale). Dots: exact values obtained by numerical evaluation; solid lines: analytical asymptotics, Eq. (4.21).

As we will explain within the next few lines the obtained rates are dominated by different values of momenta transferred during the collision. Furthermore, depending on the energy range the main contribution may come from different regions of the Q vs. Ω plane (Fig. 4.1) as shown in Table 4.1.

In regime I the result is determined by momenta of order temperature and therefore all four regions contribute in the same way: $\tau_q^{-1} \sim (\epsilon T)^{1/2}/N$. All scattering angles θ contribute to the result in regime I. In order to evaluate the numerical prefactor c_1 one needs the knowledge of the screened

interaction in the crossover around $qv_F \sim T$, which is beyond the analytic approximations for the polarization operator used above. For energies in regime II the dominant contributions come from regions 3 (electron-electron scattering) and 1 (electron-hole scattering); in both of them all scattering angles θ contribute. In regimes III and IV the main contribution to the quantum scattering rate stems from the region 3 (electron-electron scattering) and is dominated by the forward scattering ($\theta \lesssim \alpha_g NT/\epsilon \ll 1$).

An important feature of the quantum scattering rate is its non-monotonic energy dependence, see Eq. (4.21) and Fig. 4.5: with increasing energy the quasi-particle broadening first grows in regime I, has a maximum at $\epsilon \sim \alpha_g^2 N^2 T$, then decreases in regime II, and finally becomes energy-independent. The maximum of τ_q^{-1} occurs due to the resonant emission/absorption of plasmonic excitations. We will see below that the non-monotonicity of the energy dependence is related to the peculiar properties of the dynamical screening in graphene and is a characteristic feature of all inelastic scattering rates in graphene.

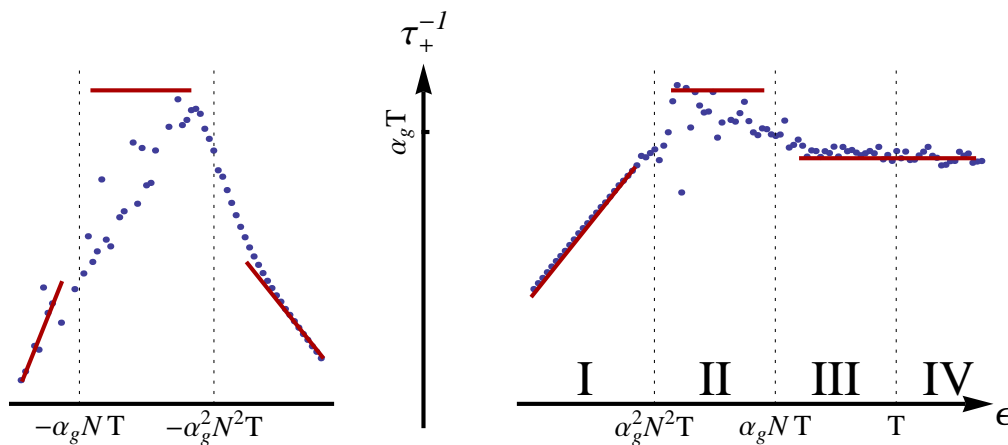


Figure 4.6: Quantum scattering rate τ_+^{-1} for the + chirality (electrons) for $\alpha_g N = 4 \times 10^{-3}$ (double logarithmic scale). Dots: exact values obtained by numerical evaluation; solid lines: analytical asymptotics (see Appendix B.2).

In Fig. 4.6 we show the results for the quantum scattering rate of electrons, τ_+^{-1} , defined in Eq. (4.16). One sees that Fig. 4.6 represents an “unfolding” of Fig. 4.5 into the contributions of “own” ($\epsilon > 0$) and “wrong” ($\epsilon < 0$) mass-shells, according to Eq. (4.20). The hole mass-shell with $\epsilon < 0$ is probed by electrons due to the strong quasi-particle broadening. At positive energies in the regimes III and IV ($\epsilon > \alpha_g NT$), the total scattering rate τ_q^{-1} is dominated by the electronic scattering rate τ_+^{-1} .

In contrast to the naive expectation ($\tau_q^{-1} \sim \alpha_g^2 NT$) based on the Fermi golden rule result, the quantum scattering rate calculated within the RPA is proportional to α_g (and does not depend on N) for $\epsilon \gg \alpha_g^2 N^2 T$ and is independent of α_g at the lowest energies. This enhancement of the inelastic scattering for $\alpha_g N \ll 1$ is a result of peculiar screening properties of graphene at finite T which leads to a non-analytic behavior of the rate as a function of the natural four-fermion coupling constant α_g^2 . This behavior bears a certain similarity to the behavior of the quantum scattering rate in a spinful Luttinger liquid [27, 28].

Since the RPA quasi-particle broadening in domain I may overlap with the higher-energy domains, where the quantum scattering rate is of the order of $\alpha_g T$, one can speculate that the characteristic

strength of inelastic scattering is given by $\tau_q^{-1}(\epsilon) \sim \alpha_g T$ also at low energies. Of course, the calculation based on the lowest-order RPA diagrams for the self-energy is then insufficient. Moreover, the typical observables at finite temperatures are dominated by $\epsilon \sim T$ (the border between domains III and IV), where the quasi classical broadening is smaller than energy and the above calculation is justified. The low-energy inelastic relaxation may become relevant in the context of spectroscopy under strongly non-equilibrium conditions, for example, in problems related to tunneling into a non-equilibrium state (cf. Ref. [32, 33]). In this situation the inelastic effects can be treated within the quantum-kinetic approach including non-RPA contributions, similarly to one-dimensional problems [32, 33].

It is crucial to notice, that the quasi-particle lifetime we obtain in this section differs strongly from the naive calculation performed in Sec. 3.1.3. The lifetime we obtained becomes infinite if we approach the zero temperature case $\tau_q \propto (\alpha_g T)^{-1} \xrightarrow{T \rightarrow 0} \infty$ and is not determined by the quasi-particle energy as Eq. (3.28) suggests.

4.2.2 Dephasing Rate at High Temperatures

Let us now discuss the dephasing rate. The result for the quantum scattering rate obtained for the clean graphene allows us to evaluate the dephasing rate relevant to weak (anti)localization in the ballistic regime [66] of high temperatures $T\tau_{\text{dis}} \gg 1$, where τ_{dis} is the elastic mean free time due to scattering off impurities. It is worth noting that this condition may coexist with the condition $\tau_\phi \gg \tau_{\text{dis}}$ which allows long interfering paths in the weak-localization experiment. Indeed, the inelastic scattering is suppressed with decreasing α_g (even though in a non-trivial way) so that one expects that τ_ϕ can be made arbitrary long.

The result for the quantum scattering rate, Eq. (4.21), remains intact (up to the change of the prefactor) when we calculate it in a self consistent way an appropriate estimation for the dephasing rate is:

$$\tau_\phi^{-1} \propto \int_{(T\tau_\phi)^{-1}}^{\infty} dQ \dots \quad (4.22)$$

This happens due to the fact that the characteristic momenta dominating the integrals for the quantum scattering rate in regimes II, III, and IV is of the same order as the resulting rate [see Table 4.1 and Eq. (4.21)], both are $\sim \alpha_g T$ for $N \sim 1$ (for $N \gg 1$, the characteristic momenta are much higher than $1/\tau_q$). In regime I of lowest energies, the characteristic momentum transfer is much higher than the rate. Therefore, in all these regimes the infrared cutoff is redundant and the dephasing rate is given by the quantum scattering rate, Eq. (4.21), similarly to the case of conventional metals in the ballistic regime [65]. Although, in contrast to the conventional case, the characteristic transferred frequencies are much smaller than temperature. Since the characteristic energies involved in the transport coefficients are of order of T , we conclude that in the ballistic regime the interference effects are governed by

$$\frac{1}{\tau_\phi} \sim \alpha_g T. \quad (4.23)$$

4.2.3 Energy Relaxation Rate

Let us now discuss the energy relaxation time in clean graphene. In Sec. 4.2.1 we have seen that the typical momentum or energy transfer during the electron-electron collision is much smaller than temperature. In this situation, the energy relaxation occurs through multiple scattering processes

which can be viewed as diffusion in energy space (see, e.g., Ref. [67]). The characteristic energy relaxation rate is given by the diffusion coefficient of this problem, which amounts to introducing the factor $\mathcal{K}_E = \omega^2/T^2$, see Appendix B.2.1, into the collision kernel. More rigorous calculation of the energy relaxation or equilibration rates can be done using the language of kinetic equation; here we only estimate the typical rate τ_E^{-1} within the energy diffusion picture.

Once the quantum scattering rate is obtained, the calculation of the energy relaxation rate can be done using the same steps as described in the previous section. Technically, the integrals in Eq. (4.15) are only slightly changed, which leads, however, to a substantial difference between the two rates. The detailed calculation can be found in appendix B.2. The result is:

$$\frac{1}{\tau_E(\epsilon)} \sim \begin{cases} \frac{T}{N} \sqrt{\frac{\epsilon}{T}}, & \text{I} \\ \frac{\alpha_g^2 NT}{\sqrt{\epsilon/T}} \ln\left(\frac{\epsilon/T}{\alpha_g^2 N^2}\right), & \text{II, III} \\ \alpha_g^2 NT \left(\frac{\epsilon}{T}\right)^{3/2} \ln\left(\frac{1}{\alpha_g N}\right), & \text{IV} \end{cases} . \quad (4.24)$$

In particular, we have the following estimates for the energy relaxation rate at characteristic energies separating the regimes:

$$\frac{1}{\tau_E(\epsilon)} \sim \begin{cases} \alpha_g T, & \epsilon \sim \alpha_g^2 N^2 T, \\ \alpha_g^{3/2} N^{1/2} T \ln\left(\frac{1}{\alpha_g N}\right), & \epsilon \sim \alpha_g N T, \\ \alpha_g^2 N T \ln\left(\frac{1}{\alpha_g N}\right), & \epsilon \sim T. \end{cases} . \quad (4.25)$$

Again the obtained rates are dominated by different momentum scales and by contributions of different regions as shown in Tab. 4.2. Due to the factor \mathcal{K}_E all contributions except in regime IV are now determined by momenta of order temperature, which does not allow us to find the numerical value of the prefactors analytically.

Furthermore, in fact, the above calculation based on the energy diffusion is not justified for “hot electrons” with high energies, $\epsilon > T$. Indeed, within our consideration, the characteristic energy transfer dominating the energy relaxation in regime IV turns out to be much higher than T , in contrast to the original assumption. Therefore, the estimate, Eq. (4.24) for regime IV cannot be trusted and another approach is needed for this regime.

τ_E	I	II	III	IV
$qv_F \sim \omega$	T	T	T	ϵ
Regions	1,2,3,4	1,2,3,4	1,2,3,4	4

Table 4.2: Momentum/frequency scales and regions of the Q - Ω plane that dominate the energy relaxation rate τ_E^{-1} in different domains (I,II,III, and IV) of energy ϵ .

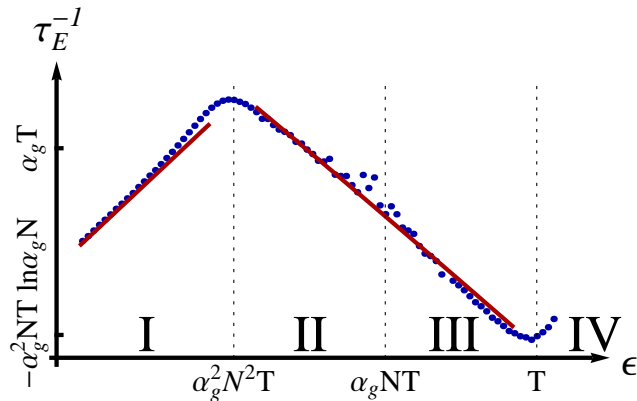


Figure 4.7: Energy relaxation rate for $\alpha_g N = 4 \times 10^{-3}$ (double logarithmic scale), obtained from the energy-diffusion consideration. Dots: exact values obtained by numerical evaluation; solid lines: analytical asymptotics, Eq. (4.24). Since the energy-diffusion approximation employed in the calculation is not justified in regime IV, we do not present the results in this regime for $\epsilon \gg T$.

The numerical results for the energy relaxation rate are shown in Fig. 4.7 together with the analytical asymptotics, Eq. (4.24). One sees that the energy relaxation has a minimum at $\epsilon \sim T$, where we recover, up to the logarithmic factor $|\ln \alpha_g|$, the golden rule result $\tau_E^{-1} \sim \alpha_g^2 N T$. At lower energies the inelastic scattering is enhanced due to the resonance in the RPA interaction propagator (the resonant condition correspond to $\epsilon \sim \alpha_g^2 N^2 T$), whereas at high energies the energy relaxation is stronger because of the large phase space available for inelastic processes. We remind the reader, however, that at $\epsilon > T$ the above calculation based on the energy-diffusion approximation is not justified. In order to find the correct relaxation of the distribution functions in this regime of hot electrons, one should solve the corresponding kinetic equation (see Sec. 5.2.1).

Experiments, able to observe the consequences we discussed in this Chapter are very non-trivial. This is because the graphene samples need to be clean enough, that Coulomb interaction induced scattering can overcome the disorder induced scattering. Further the temperature has to stay below the threshold, where phonons become important and several other constraints, e.g. large enough samples to observe electron-electron interaction, have to be fulfilled as well. Nonetheless in the recent years experiments made huge progress in getting closer to the regime described here.

Although the experimental status of the quasi-particle lifetime in graphene is not yet clarified, there are experimental attempts to measure the quasi-particle lifetime in graphene [68, 69] evidently demonstrating the relevance of this work.

A recent experiment [70] measured the relaxation process of hot electrons at finite chemical potential, which is not yet what we described in this Chapter but clearly shows that the experiments are on their way towards the relaxation processes we discussed here.

5 Chapter 5

Transport

.... Und andererseits zeigen die glänzenden Erfolge der drahtlosen Telegraphie so deutlich, wie wohl fast nie zuvor in der Physik, dass auch die subtilste, aus rein wissenschaftlichen Zwecken und nur mit den feinsten Hilfsmitteln unternommene Untersuchung sich in unserem Zeitalter der Technik und Naturwissenschaft zu einer außerordentlich wichtigen und praktischen Bedeutung entwickeln kann.

P. Drude, Antrittsrede 1906

Transport is one of the most fascinating parts in condensed matter physics. It not only involves the knowledge of the electronic structure of the system but as well how this structure changes, how external forces change the occupation of the states. Transport measurements have a long history in physics, they have been studied for quite some time and have become one of the standard techniques for experimentalists. Thus the phenomenon of transport has become a cornerstone of today's scientific community. The purpose of this chapter is to present some introductory views on transport before considering the special situation of graphene. The transport phenomena in graphene are described in a twofold way since it allows deeper insights to have more than one perspective. There is no way the introductory part about transport could be complete since the topic is far too rich. We will instead provide an intuitive picture which will serve us as comparison throughout this work.

5.1 Basics

We will start the introductory part, considering the parabolic spectra of non-relativistic particles which we will compare the relativistic transport in graphene.

5.1.1 Drude Theory

The very basic idea leading to the Drude theory is to think about the material, the transport is observed in, as consisting of ions at rest and electrons scattering between them. In this situation a force like the electric field will accelerate the electrons in the direction of the external field. Essential for the Drude theory is the idea that with increasing velocity of the electrons their scattering probability increases as well. This is in e.g. if the distribution of ions define a mean scattering length. Formally we may write:

$$\frac{d}{dt}\vec{v}(t) = \frac{q}{m}\vec{E} - \frac{1}{\tau}\vec{v}(t), \quad (5.1)$$

as a differential equation for a single particle's averaged velocity. The driving force is given by the electric field \vec{E} acting on the electric charge q and τ is the average time between two scattering processes. The stationary solution of the Drude equation is $\vec{v}_0 = \tau q/m\vec{E}$ which implies within the Drude picture the current:

$$\vec{J} = nq\vec{v}_0 = \frac{\tau q^2 n}{m} \vec{E} = \sigma \vec{E}. \quad (5.2)$$

Where n is the density of electrons participating in this picture.

Surely the Drude picture is simplistic but still it describes pretty well a lot of phenomena, e.g. the conductivity of electrons, which is a Quantity that will be essential within this work. Still, the picture of transport introduced so far is very phenomenological and to gain additional understanding on how the friction in the Drude picture appears we will try to derive a very similar formula from the Boltzmann equation.

Drude Theory within kinetic equation approach

We will reformulate the above simple picture into the language we have derived in Sec. 2.5. The benefit of this reformulation is not only to have proper many-body language. It will also allow us to gain some more insights into the origin of the scattering rate. The central equation we deal with is

$$e\vec{E}\nabla_p n(\vec{p}) = -I_{\text{Coll}}[n] = - \int \frac{d^2 p'}{(2\pi)^2} W_{pp'} [n(\vec{p}) - n(\vec{p}')], \quad (5.3)$$

where the collision integral measures the probability of scattering into and out of the state with momentum \vec{p} . To proceed, we look for the linear response of the system. We perform an expansion around the equilibrium distribution function n_F . To do so we will first try to understand the deviations of an equilibrium system as a response to a small electric field.

A fermionic system in equilibrium is described by the Fermi distribution function $n_F(\epsilon)$. If we switch on the electric field there will appear a growing shift in the momentum distribution of the system. If we take into account relaxation processes the complete Fermi-ball will change its location in momentum space. Thus we read in terms of the dispersion $\epsilon(\vec{p} + \tau_p e\vec{E})$ where τ_p^{-1} is the momentum relaxation rate. If the electric field is weak enough we can expand the equilibrium distribution function around this perturbation having $n(\epsilon(\vec{p} + \tau_p e\vec{E})) \approx n_F(\epsilon(\vec{p})) - \partial_\epsilon n_F(\epsilon(\vec{p}))\tau_p e\vec{E}\vec{v}$ with $\vec{v} = \nabla_p \epsilon(\vec{p})$. A consequence of this parametrization is that the current reads

$$\vec{j} = e \int \frac{d^2 p}{(2\pi)^2} \vec{v} n(\vec{p}) = -e^2 \int \frac{d^2 p}{(2\pi)^2} \vec{v} \partial_\epsilon n_F(\epsilon(\vec{p})) \tau_p \vec{E} \vec{v} \approx \frac{1}{2} e^2 v_F^2 \tau_{pF} \nu_F \vec{E}. \quad (5.4)$$

In the last step of this equation we used the approximation that the Fermi energy is much larger than the considered temperature. This approximation that is fairly good for most metals. The latter approximation allowed us to evaluate everything at the Fermi energy including the density of states ν_F .

Going back to the Boltzmann equation, Eq. (5.3), we will use the fact that the equilibrium distribution function, per definition, annihilates the collision kernel $I_{\text{Coll}}[n_F] = 0$. Thus we end up with an equation specifying the transport scattering rate, which for simplicity is projected on the direction of

\vec{E} :

$$v_F^2 \partial_\epsilon n_F(\vec{p}) = \int \frac{d^2 p'}{(2\pi)^2} W_{pp'} \left[\partial_\epsilon n_F(\epsilon(\vec{p})) \tau_p v_F^2 - \partial_\epsilon n_F(\epsilon(\vec{p}')) \tau_{p'} \vec{v}_p \vec{v}_{p'} \right] \\ \stackrel{|\vec{p}| \approx p_F \approx |\vec{p}'|}{\approx} \int \frac{d^2 p'}{(2\pi)^2} W_{pp'} \partial_\epsilon n_F(\epsilon(\vec{p})) \tau_{pF} \left[v_F^2 - \vec{v}_p \vec{v}_{p'} \right]. \quad (5.5)$$

So in the very end we will have the scattering rate

$$\tau_{pF}^{-1} = \int \frac{d\varphi}{2\pi} \mathcal{W}_\varphi (1 - \cos \varphi), \quad (5.6)$$

traced back to some effective scattering kernel \mathcal{W}_φ with the transport factor $(1 - \cos \varphi)$ involving the angle φ between \vec{p} and \vec{p}' . Due to this appearance the scattering rate that comes with transport related quantities like current is usually referred to as transport rate since it has an intrinsic suppression of scattering processes that do not change the direction ($\varphi = 0$). The Boltzmann equation then reads:

$$e \vec{E} \cdot \nabla_{\vec{p}} n_F(\vec{p}) = - \frac{n(\vec{p}) - \langle n(\vec{p}) \rangle_\varphi}{\tau_{pF}}, \quad (5.7)$$

where $\langle n(\vec{p}) \rangle_\varphi$ is the direction average that reflects the isotropy of the impurity scattering. The deeper reason for the direction average is hidden in between Eqs. (5.5) and (5.6) and comes from the fact that isotropic variations of the distribution function like density variation or energy density variation are not affected by impurity scattering.

5.1.2 Transport in Graphene

When it comes to transport the first thing to mention is that graphene is a fairly good conductor [13, 21]. It is of prime importance to understand which scattering mechanism finally determine the conductivity of graphene. The usual suspects responsible for current limiting scattering processes are disorder scattering or, if temperature is high enough, phonon scattering. In this work we focus on the Coulomb interaction which apparently is not a member of the usual suspects. In Galilean invariant systems the Coulomb interaction with exception of the umklapp scattering does not affect current. We thus take a closer look at the current operator of both systems.

The Dirac Current

With the ultra-relativistic Dirac Hamilton operator the system inherited the Dirac current operator as well. The definition of the Dirac current operator apparently differs from the conventional current used in standard condensed matter systems. Let us take a closer look at those differences. If one starts with the Dirac-Equation: $-i v_F \vec{\sigma} \cdot \vec{\nabla} \psi = i \frac{\partial}{\partial t} \psi$, one obtains the continuity equation

$$\frac{\partial}{\partial t} |\psi|^2 = - \vec{\nabla} \cdot (v_F \psi^\dagger \vec{\sigma} \psi), \quad (5.8)$$

which implies the Dirac-current

$$\vec{j} = e v_F \psi^\dagger(\vec{r}, t) \vec{\sigma} \psi(\vec{r}, t) = e v_F \text{Tr} \left(\underbrace{\vec{\sigma} \psi(\vec{r}, t) \psi^\dagger(\vec{r}, t)}_{iG_{2,1}(0,0)} \right). \quad (5.9)$$

The Green's function G_{-+} is a Keldysh Green's function as defined in Sec. 2.4. This structure of the current is significantly different from

$$\vec{j} = \frac{1}{2m} \left(\psi^\dagger \hat{p} \psi - (\hat{p} \psi^\dagger) \psi \right), \quad (5.10)$$

obtained from the non-relativistic Schrödinger equation. Still both currents unveil that current is proportional to velocity ($\vec{j} \propto \vec{v}$). However, in graphene $|\vec{v}| = v_F$ which is completely constant for arbitrary energies (within the Dirac cone).

Comparison

The main difference between the two systems is the form of the velocity, Eqs. (2.6) and (2.7)) as explained in Sec. 2.1.4. When it comes to transport the main point in graphene is that the current can be relaxed by processes that do conserve momentum. Such a scattering process is illustrated in Fig. 5.1. One recognizes that the presence of both bands simultaneously is needed since otherwise momentum conservation protects the current. Therefore, it is expected that for large chemical potential graphene exhibits the usual Fermi liquid behavior.

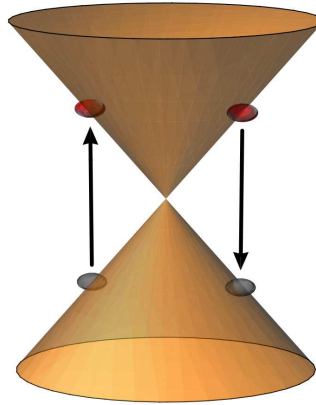


Figure 5.1: A sketch of graphene's dispersion with a process that annihilates the current. Electron (red) hole (gray) pair annihilates by creating another electron hole pair. The process chosen is suppressed by Dirac factors but sketches more intuitively the kind of processes that lead to current relaxation.

Scattering processes involving phonons or impurities allow momentum transfer out of the electronic system. Therefore both mechanisms do not conserve momentum from the point of view of the electronic system. Hence, those processes relax current in both systems in graphene and in usual Fermi liquids. The Coulomb interaction is always fulfilling the momentum conservation. In a Galilean invariant system, current is always proportional to momentum and therefore conserved. This is not true in an ultra relativistic system where conservation of momentum does not imply the conservation of current. In graphene the Coulomb interaction, although conserving momentum, will relax the current leading to a scattering process that should be taken into account when describing transport.

5.2 Previous Works

In previous works by Fritz et al. [71] and Kashuba [72], it has been shown that within the formalism of the Boltzmann equation one can access the problem of Coulomb interaction dominated transport in graphene. The path they suggest will be sketched and explained in the following sections. However, we will use one simplification, namely the large N approximation. The large N approximation basically discards the right diagram in Fig. 5.2. This choice is in so far controllable that in the limit many flavors it becomes exact. We know by comparison with the previous works [71, 72] that for the case $N = 4$, corresponding to real graphene, the difference in the numerical prefactor for the conductivity as compared to the $N = \infty$ approximation is $\approx 8\%$. As will be discussed in Chaps. 6 and 7, the diagram on the left-hand side of Fig. 5.2 is the only one in this order allowing for Coulomb drag between two layers.

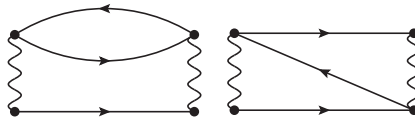


Figure 5.2: *The two possible second order self-energy diagrams leading to a two particle scattering process on collision kernel level.*

We will see that by choosing only the diagram involving a polarization operator (left-hand side of Fig. 5.2) we will catch all the relevant physics in the system as we will discuss later in Sec. 5.4.

5.2.1 The Kinetic Equation for Graphene

We have derived the kinetic equation for graphene in Sec. 2.5. What is left to show is the form of the collision kernel for the Coulomb interaction in graphene and on which scale the kinetic equation is valid. In Chap. 4 we discussed the energy relaxation rate in graphene determining the relevant scale for the rate to be temperature (see appendix B.2.3). Deriving the kinetic equation we need to keep in mind that due to the gradient expansion (see Sec. 2.5) the temporal and spatial variations of the distribution function need to be small on the scale of temperature. With this in mind we continue with the collision kernel. But first we will introduce a more transparent basis we will perform our calculation in.

The velocity in graphene is fixed via $\vec{v}(\epsilon, \vec{p}) = v_F^2 \vec{p} / \epsilon$ and the kinetic equation is taken on the mass shell. We change the usual notation in terms of momentum and chirality according to

$$\sum_{\lambda} \int \frac{d^2 p}{(2\pi)^2} g(v_F \lambda |\vec{p}|, \vec{p}) = \int d\epsilon \int d\hat{v} \nu(\epsilon) g(\epsilon, \epsilon \vec{v}). \quad (5.11)$$

The system is now described by the particle's energy and its direction encoded in \vec{v} . The measure of the angular integral (direction weight) is given by $2\pi d\hat{v} = d\phi$ (from $d^2 p = p dp d\phi$) and we used $2\pi v_F^2 \nu(\epsilon) = |\epsilon|$ for further simplification. The advantage of this formulation is that for a given velocity the chiral symmetry has been absorbed into the particle's energy making it an explicit symmetry of the corresponding integrals. Collecting the degrees of freedom $dx_i = d\epsilon_i d\hat{v}$ and subsequently using the notation $\{x_i\} = \{x_1, x_2, x_1', x_2'\}$ and $d\{x_i\} = dx_1 dx_2 dx_1' dx_2'$ we found a very short and elegant formulation for the problems allowing to keep the focus on the physics.

The way we discussed the Drude theory via Boltzmann equation it is natural to build up the collision integral:

$$I_{\text{Coll}}[n] = -\frac{1}{\nu(\epsilon_1)} \int d\{x_i\}_{i \in \{2,1',2'\}} K(\{x_i\}) \left\{ n(t, x_1)[1 - n(t, x_2)]n(t, x_{1'})[1 - n(t, x_{2'})] - [1 - n(t, x_1)]n(t, x_2)[1 - n(t, x_{1'})]n(t, x_{2'}) \right\}, \quad (5.12)$$

where the collision integral kernel is

$$K(\{x_i\}) = (2\pi)^3 \delta(\epsilon_1 - \epsilon_2 + \epsilon_{1'} - \epsilon_{2'}) \delta(\epsilon_1 \vec{v}_1 - \epsilon_2 \vec{v}_2 + \epsilon_{1'} \vec{v}_{1'} - \epsilon_{2'} \vec{v}_{2'}) |\langle x_1, x_2 | U | x_{1'}, x_{2'} \rangle|^2 \nu(\epsilon_1) \nu(\epsilon_2) \nu(\epsilon_{1'}) \nu(\epsilon_{2'}). \quad (5.13)$$

The matrix element of the Coulomb interaction reads:

$$|\langle x_1, x_2 | U | x_{1'}, x_{2'} \rangle|^2 = N |D(q)|^2 \theta_{1,2} \theta_{1',2'}. \quad (5.14)$$

Here $D(q)$ is the interaction propagator usually chosen to be the bare Coulomb propagator Eq. (2.23) but here it can as well be replaced by the RPA screened interaction propagator Eq. (2.38). The chiral overlap of an incoming particle with the outgoing one is defined by

$$\theta_{\gamma_1, \gamma_2} = \text{Tr} \left[\mathcal{P}_{\gamma_1}(\vec{p}_1) \mathcal{P}_{\gamma_2}(\vec{p}_2) \right] = \frac{1}{2} [1 + \gamma_1 \gamma_2 \hat{p}_1 \hat{p}_2] = \frac{1}{2} [1 + \vec{v}_1 \vec{v}_2]. \quad (5.15)$$

It is the same object that determined the difference between the quantum scattering rate and the chiral scattering rate in Sec. 4.2.1. Its appearance is special for Dirac fermions, which is why we will term them Dirac factors.

The derivation of the general form of the kinetic equation for graphene has been presented in Sec. 2.5. A detailed calculation on determining the collision integral from the field theoretical formulation is given in appendix A.2.1.

The next step in gaining transport properties is to linearize the collision kernel (see App. A.3). Therefore we expand the distribution function around equilibrium,

$$n(t, x) = n_F(\epsilon) - T \frac{\partial n_F(\epsilon)}{\partial \epsilon} h(t, x), \quad (5.16)$$

gaining the linearized collision integral,

$$\delta I_{\text{coll}} = \frac{1}{\nu(\epsilon_1)} \int d\{x_i\}_{i \in \{2,1',1'\}} W(\{x_i\}) \left\{ h(t, x_1) - h(t, x_2) + h(t, x_{1'}) - h(t, x_{2'}) \right\}, \quad \text{with the kernel} \quad (5.17)$$

$$W(\{x_i\}) = \frac{(2\pi)^3 \delta(\epsilon_1 - \epsilon_2 + \epsilon_{1'} - \epsilon_{2'}) \delta(\epsilon_1 \vec{v}_1 - \epsilon_2 \vec{v}_2 + \epsilon_{1'} \vec{v}_{1'} - \epsilon_{2'} \vec{v}_{2'}) |\langle x_1, x_2 | U | x_{1'}, x_{2'} \rangle|^2 \nu(\epsilon_1) \nu(\epsilon_2) \nu(\epsilon_{1'}) \nu(\epsilon_{2'})}{16 \cosh\left(\frac{\epsilon_1 - \mu}{2T}\right) \cosh\left(\frac{\epsilon_2 - \mu}{2T}\right) \cosh\left(\frac{\epsilon_{1'} - \mu}{2T}\right) \cosh\left(\frac{\epsilon_{2'} - \mu}{2T}\right)}. \quad (5.18)$$

Still, even for the linearized collision integral it is far from trivial to solve the kinetic equation at this stage. Following the previous literature we will find a powerful method to do so.

5.2.2 The Functional Approach

We will now introduce the method that has been used by Fritz et al. [71] and Kashuba [72] to solve the Boltzmann equation. The method we are going to introduce is the reformulation of the kinetic equation into a functional. This is very similar to the formulation of the equations of motion in terms of the Langrange function which by functional variation allows to reobtain the equations of motion.

Reformulation of the kinetic equation

If we use the linearized collision kernel Eq. (5.17) and applying it to Eq. (5.12) we gain

$$\left(i\Omega h(x) + e \frac{\vec{E}\vec{v}}{T} \right) T \frac{\partial n_F(\epsilon)}{\partial \epsilon} = -\delta I_{\text{coll}}[h]. \quad (5.19)$$

Where we assumed a homogeneous sample but a very slowly oscillating external field $E = E(t)$ causing the additional $i\Omega$ term. Our aim is to reformulate this equation in a language that allows an easy treatment of approximate solutions of the Eq. (5.19). Suppose we have a solution h_s that solves the kinetic equation. Then a reformulation of the problem to a nonlinear functional $F(h)$ is done by the demand that $F(h)$ is minimized for the solution h_s only. This is exactly what is done within the Lagrange formalism, where the solution of the equations of motions minimizes the Lagrangian. Thus via functional variation we should regain the kinetic equation. The constraint

$$\frac{\delta F(h)}{\delta h} = 0 \quad (5.20)$$

needs to be equivalent to Eq. (5.19). One can verify that

$$F(h) = \int dx_1 \nu(\epsilon_1) \frac{\partial n_F}{\partial \epsilon_1} \left[e \vec{E} \vec{v}_1 h_1 + i \frac{T\Omega}{2} h_1^2 \right] + \frac{1}{8} \int d\{x_i\} W(\{x_i\}) [h_1 - h_2 + h_{1'} - h_{2'}]^2 \quad (5.21)$$

indeed yields Eq. (5.19) by functional variation of Eq. (5.21) (for brevity $h_i = h(x_i)$). The only additional input needed is about the symmetry properties of the integral kernel. The symmetries of Eq. (5.18) are due to the invariance under simultaneous exchange of 1 and 1' as well as 2 and 2' and additionally the invariance by simultaneously exchanging 1 and 2 as well as 1' and 2'. Note that the second symmetry is essential, it corresponds to the hermiticity of $\delta I[h] - i\Omega h$ which will become clear later.

One should note that these symmetries are also responsible when one is trying to derive the hydrodynamic equations from the kinetic equation (see Sec. 2.5.2). This is because the equations that correspond to conserved quantities, like particle number (density) or energy (energy density) do not involve the collision integral, since they are conserved. Thus there needs to be a symmetry within the collision kernel responsible for this conservation.

We have now reformulated the problem of solving the kinetic equation into the problem of minimizing the functional F . Assuming h to be an analytic function linear in \vec{E} allows one to write its series expansion in terms of (see Sec. 5.2.4 for non-analytic contributions)

$$h(x) = \sum_{i=0}^{\infty} \kappa_i \epsilon^i + \sum_{i=0}^{\infty} \chi_i \epsilon^i \vec{E} \vec{v}. \quad (5.22)$$

This reformulation corresponds then to the task of solving a linear equation by inverting an infinite dimensional matrix.

Still one can ask why to bother inventing a functional $F(h)$ instead of putting the series expansion (5.22) into the linearized kinetic Eq. (5.19). The answer is quite simple, the reason to proceed this way is that we would like to have an algebraic equation where the κ_i and χ_i are constants, which does not follow straightforwardly by plugging in the series expansion (5.22) into the linearized kinetic Eq. (5.19). To transform the integro-differential equation properly into an algebraic one we need to have a well defined integral measure that tells us how to deal with the free parameters within the linear kinetic Eq. (5.19). This is the reason to choose the apparent detour of defining the functional (5.21).

General considerations about the approximation scheme

We will now provide a general discussion of the method we are going to use as it has been done in the previous articles [71, 72]. Instead of thinking about the reformulation in terms of a functional, we will for pedagogical reasons think about the reformulation in terms of a linear equation in the spirit of the linear algebra $A|h\rangle = |b\rangle$ with A being a linear operator acting on $|h\rangle$. In this language one recognizes that the hermiticity of A provides us with the possibility to solve formally the linear equation by rotating into the basis A is diagonal in. In this rotated basis A , which is now diagonal can be represented as $\sum_n |h'_n\rangle a_n \langle h'_n|$ with the eigenvector $|h'\rangle$ and the corresponding eigenvalue a_n . The equation then reads $\sum a_n |h'_n\rangle - |b'_n\rangle = 0$ and is uniquely solvable if none of the eigenvalues a_n vanishes. It can happen that some a_n are zero but the corresponding b_n are zero as well, the system remains solvable but is no longer uniquely solvable. In such a situation we can still restrict our space of solutions to the eigenmodes that are not zero modes (modes that have a vanishing eigenvalue). We then, can formally write the solution as $|h'\rangle = \sum a_m^{-1} |b'_m\rangle$ (with m counting only non-zero eigenvalues). This way one might recognize that the best approximations are done by keeping those eigenstates that have a “small” eigenvalue a_m (if non-vanishing states $|b'_m\rangle$ do not vary too much). This is the basic idea we want to follow in our attempt to find an approximation. A slightly different view on this can be gained by thinking about the introduced procedure in terms of the image \mathcal{B} and the kernel of the operator A . Then, restricting our space to deal only with the image we can formally define the inverse of A . A further restriction onto a small subspace $\mathcal{X} \subset \mathcal{B}$ of the image \mathcal{B} can be sufficient for the solution of the linear equation if this subspace \mathcal{X} is chosen such that it covers the most important parts of A . A clever way to do so is to choose the subspace in such a way that the target space $A^{-1}\mathcal{X}$ contains the essential properties of the operator A^{-1} . Therefore small eigenvalues of A are the selection criteria. It will turn out later that for our purpose the eigenvalues are parametrically controllable making the approximation scheme exact in certain limits.

The functional comes into play when we have identified the modes we have chosen to use as the approximated subspace. Then those modes provide use with an ansatz $|h_{\text{Ansatz}}\rangle = \sum \chi_n |h_n\rangle$ that plugged into the functional $f(h) = \langle h|A|h\rangle - 2\langle h|b\rangle$ and performing a differentiation with respect to the χ_n gives us an algebraic linear equation for the χ_n namely $\sum_m \chi_m \langle h_n|A|h_m\rangle - \langle h_n|b\rangle = 0$ due to the hermiticity of A . To provide a simple picture of the abstract discussion we dealt with, we have chosen

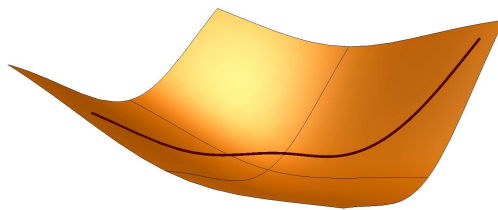


Figure 5.3: *Illustration of a function sub-manifold (black line) passing by the minima of a functional (orange plane) in function space.*

to use Fig. 5.3 as a sketch on how the choice of the sub-manifold due to selection of the eigenvalues

substantially influences the quality of the solution. In this sketch the purpose of the functional is to provide us with an easy way of gaining a new minimum inside the sub-manifold whose distance (hence quality) is minimized but restricted to the choice of the manifold.

The plan is, now to find a proper ansatz by studying the integral kernel of $\delta I[h]$ given by Eq. (5.17) and using this ansatz together with the functional $F(h)$ Eq. (5.21) to gain an algebraic equation for the coefficients that parametrize our solution.

Discussion of the ansatz

The general considerations from above have unveiled that for our case of a fixed driving term $e\vec{E}\vec{v}$ that plays the role of $|b\rangle$ we have to look for modes minimizing the collision kernel Eq. (5.18). Note that we skip the part of the kernel that is related to $i\Omega$ which in this discussion will be only used as regularization for cases the kinetic equation is not solvable otherwise. This limit corresponds to Coulomb interaction dominating other scattering mechanism like $i\Omega$ and τ_{dis}^{-1} . One recognizes at first that there are two zero modes due to the delta functions in $W(\{x_i\})$ namely $h_{ec} \propto \epsilon$ and $h_{mc} \propto \epsilon\vec{E}\vec{v}$. These zero modes are due to particle, energy and momentum conservation (see 2.5.2). The fact that the zero mode corresponding to particle and energy conservation does not couple to the driving term is, in above terms, reflected by the statement that $\langle h_{ec}|b\rangle = 0$, hence we can further on ignore those two zero modes (as long as dealing with pure transport). This is not true for the momentum conserving mode h_{mc} . Without regularization $i\Omega$ this one can make the problem unsolvable, since without any scattering the momentum mode will accelerate uncontrollably not allowing us to consider a stationary case.

Finding more relevant modes requires the knowledge of different energy scales in the integral kernel Eq. (5.18). Detailed calculations supplement this discussion and can be found App. C.2.2. As explained in Secs. 3.1.2 and 4.1 and Refs. [71, 72], on a golden rule level of interaction the collision kernel $W(\{x_i\})$ has a singularity that is due to forward scattering. In Eq. (5.17) one can identify some traces of this forward scattering resonance by setting all velocities in the collision kernel the same. This way one obtains a kind of three dimensional energy conservation constraint, indicating a divergent structure and leaves only the question of the relevant phase space for that to happen. Again, an investigation of this divergence can be found in more general terms in the App. C.2.2. With this forward scattering divergence all modes that do not efficiently suppress forward scattering relax quickly meaning that the collision kernel provides zero weight to the solution of the kinetic equation (if $T \neq 0$ [61]). There is exactly one mode that is not affected by this fast relaxation namely the velocity mode $h_v \propto \vec{E}\vec{v}$. This mode annihilates efficiently the collision kernel for the processes that are resonant in forward scattering. From these considerations it seems that taking only the momentum conserving and the velocity mode will provide us with the exact solution to the problem. Surely this is not correct since the divergence in the kernel is regularized, at finite T , by taking into account the RPA screening. Again, more details are provided in App. C.2.2. In total it turns out that the collision kernel itself for $\mu \ll T$ provides us with the scale $\alpha_g T$ as it is shown in Sec. 4.2.1. This is by a factor α_g^{-1} larger than the averaged transport related quantities given in Sec. 5.4.2. Hence the quality of the aforementioned approximation with only two modes is well-founded as long as Coulomb interaction dominates the structure of the kinetic equation $\Omega \ll \alpha_g^2 T$. One should mention that the ansatz discussed so far corresponds to direction dependent equilibration, which we will discuss in more detail in Sec. 7.1.2.

Assuming Coulomb interaction being the most relevant interaction we formulate the ansatz¹:

$$h_{\text{Ansatz}}(x) = \chi_0 \frac{e\vec{E}\vec{v}}{T^2} + \chi_1 \frac{\epsilon e\vec{E}\vec{v}}{T^2}, \quad (5.23)$$

for the distribution function. An extensive analysis on the precision of the ansatz Eq. (5.23) compared to contributions that relax parametrically fast is performed in Ref. [73]. With the ansatz at hand we will now proceed solving the kinetic equation.

5.2.3 The Conductivity in Graphene

Following the ideas sketched in the previous sections we are left with the functional Eq. (5.21) altered by the ansatz Eq. (5.23):

$$F(\chi_0, \chi_1) = \int dx_1 \nu(\epsilon_1) \frac{\partial n_F}{\partial \epsilon_1} \left[\left(\chi_0 + \frac{\epsilon_1}{T} \chi_1 \right) + i \frac{\Omega}{2T} \left(\chi_0 + \frac{\epsilon_1}{T} \chi_1 \right)^2 \right] + \frac{\chi_0^2}{8T^2} \int d\{x_i\} W(\{x_i\}) [\vec{v}_1 - \vec{v}_2 + \vec{v}_3 - \vec{v}_4]^2. \quad (5.24)$$

As we discussed above within the lines of Eq. (5.22) the χ_1 -mode, the zero mode, disappeared within the integral kernel due to momentum conservation. The only thing that is left to do now is the actual calculation which is done by minimizing $F(h_{\text{Ansatz}})$ with respect to χ_0 and χ_1 . While doing so it turns out that the following useful short forms will help compactifying the result:

$$I_{\text{Tr}} = \frac{1}{4T^3} \int d\{x_i\} W(\{x_i\}) (\vec{v}_1 - \vec{v}_2 + \vec{v}_3 - \vec{v}_4)^2, \quad (5.25)$$

$$A_n(\mu) = -\frac{1}{T} \int dx \nu(\epsilon) \frac{\partial n_F^\alpha(\epsilon)}{\partial \epsilon} \left(\frac{\epsilon}{T} \right)^n. \quad (5.26)$$

We finally end up with a set of algebraic linear equations

$$\begin{aligned} \frac{\partial F(h_{\text{Ansatz}})}{\partial \chi_0} &= A_0 + i \frac{\Omega}{T} (A_0 \chi_0 + A_1 \chi_1) - \chi_0 N I_{\text{Tr}} = 0, \\ \frac{\partial F(h_{\text{Ansatz}})}{\partial \chi_1} &= A_1 + i \frac{\Omega}{T} (A_1 \chi_0 + A_2 \chi_1) = 0. \end{aligned} \quad (5.27)$$

where we are using the short-hand notation introduced in App. C.1 in Eq. (7.13). The solution to the kinetic equation in the above approximation is

$$\begin{aligned} \chi_0 &= \frac{A_0 A_2 - A_1^2}{A_2 (N I_{\text{Tr}} - A_0 x) + A_1^2 i \frac{\Omega}{T}}, \\ \chi_1 &= \frac{A_1 N I_{\text{Tr}}}{i \frac{\Omega}{T} \left[(A_0 A_2 - A_1^2) i \frac{\Omega}{T} - A_2 N I_{\text{Tr}} \right]}. \end{aligned} \quad (5.28)$$

¹For quantities, governed by energies of order temperature (like the conductivity), this ansatz is controllable in powers of $\ln(1/\alpha_g)$. If, e.g., observables are governed by energies of order $\alpha_g T$ the situation changes. In Chap. 4, we found, that plasmons lead to a quantum scattering rate and energy relaxation rate of the same order (analogous behaves the transport scattering rate 5.4), which provides no selection of modes.

From Eq. (5.4) and the ansatz Eq. (5.23) follows the current

$$\vec{j} = eN \int \frac{d^2p}{(2\pi)^2} \vec{v}n(x) = \frac{e^2}{2} N (A_0\chi_0 + A_1\chi_1) \vec{E}. \quad (5.29)$$

Hence the conductivity reads:

$$\sigma = \frac{e^2 N}{2} (A_0\chi_0 + A_1\chi_1). \quad (5.30)$$

We see that for finite chemical potential ($A_1 \neq 0$) the DC conductivity ($\Omega \rightarrow 0$) diverges since χ_1 diverges. This limit reflects the case that the kinetic equation has no solution since there is no steady state to relax to.

At the Dirac point ($\mu = 0 \rightarrow A_1 = 0$) the conductivity is

$$\sigma = \frac{e^2 N}{2} A_0\chi_0 = \frac{e^2}{2} \frac{A_0^2}{NI_{\text{Tr}} - i\frac{\Omega}{T}A_0} \stackrel{\Omega=0}{=} \frac{e^2}{2} \frac{A_0^2}{I_{\text{Tr}}} \stackrel{\mu=0}{=} \frac{e^2}{h} \frac{0.7}{\alpha_g^2}. \quad (5.31)$$

This result has been obtained in previous Refs. [71, 72] and the DC limit will be determined in Sec. 5.4 within a diagrammatic analysis. It is worth noting that the I_{Tr} appears as scattering rate of the system ($I_{\text{Tr}} = (T\tau_{\text{tr}})^{-1}$), a fact which motivates some of the later notations (e.g. Eq. (7.13)).

If we consider the resistivity the full result reads ($Tz = -i\Omega$ or $T\tau z = 1$)

$$\rho = \frac{e^2}{2} \left[\frac{I_{\text{tr}}}{B_0^2} + \frac{z}{B_0} - \frac{B_1^2 I_{\text{tr}}^2}{B_0 (B_1^2 I_{\text{tr}} + B_2 z)} \right], \quad (5.32)$$

where we introduced an additional short-hand notation, which is particular useful for resistivities, namely

$$A_0 = B_0, \quad B_1 = N \frac{A_1}{A_0}, \quad B_2 = NA_2 - A_1 B_1. \quad (5.33)$$

There is a deeper reason in the fact that at the Dirac point conductivity is definable even in the clean case. The reason for this becomes more clear when we take a look at Fig. 5.3. The reason for creating the functional was to provide a systematic way to find the best approximation for the solution of Eq. (5.19). The functional defines a measure within this abstract language. It hence, tells us how to weight the modes, which finally leads to the measure $\nu(\epsilon) \frac{\partial n_F(\epsilon)}{\partial \epsilon}$. This way the functional approach defines a scalar product

$$\left\langle \left(\frac{\epsilon}{T} \right)^n \middle| \left(\frac{\epsilon}{T} \right)^m \right\rangle = -\frac{1}{T} \int dx \nu(\epsilon) \frac{\partial n_F(\epsilon)}{\partial \epsilon} \left(\frac{\epsilon}{T} \right)^{n+m} = A_{n+m}. \quad (5.34)$$

on the space of all possible modes (see Eq. (5.22)). If we use χ_n and κ_n as a short form for the corresponding mode we have $\langle \chi_n | \chi_m \rangle = A_{n+m} e^2 \vec{E}^2 / 2$, $\langle \chi_n | \kappa_m \rangle = 0$ and $\langle \kappa_n | \kappa_m \rangle = A_{n+m}$. For the description of graphene only χ_0 and χ_1 have been needed. The scalar product of their modes is A_1 which is an odd function of the chemical potential (see Eq. (C.18)) and disappears at the Dirac point. Hence, at the charge neutral point, where $\mu = 0$, the zero mode due to momentum conservation does not couple to an external electric field. As discussed in Sec. 5.2.2 this implies that at the Dirac point only the velocity mode is needed to take into account (see references [71, 72]). The limit of large chemical potential is not less interesting. Within the scalar product of the modes we can as well talk

about angles in the sense of $|\chi_n||\chi_m| \cos \theta_{n,m} = \langle \chi_n | \chi_m \rangle$ (we use as a norm $|\chi_n|^2 = \langle \chi_n | \chi_n \rangle$). This way, in the limit of large chemical potential, one gains $\cos \theta_{0,1} \approx 1 - \pi^2/(24\tilde{\mu}^2)$ (see Eq. (C.37)) indicating that the modes χ_0 and χ_1 become the same up to algebraically small contributions. The fact that the two modes become the same is somewhat natural since within the usual Fermi-liquid picture there is no deeper separation between velocity and momentum.

5.2.4 Non Analytic Corrections

The analysis performed previously so far is in fact not fully complete as long as we stay to the two mode description only. The basis we founded our expansion of possible modes on is given in Eq. (5.22). We could show (see App. C.2.2) that within this basis only two modes are relevant. In the notation of ϵ and \vec{v} we used explicitly the symmetry between particles and holes making the treatment significantly more easy. Unfortunately this basis masks a peculiarity we first observed in Sec. 3.1.2. In this specific section we explained that relaxation of particles by creation of holes is an inefficient process since it takes place only within a measure of zero in the phase space (due to kinematic reasons). This implies that the total number of excitations is a conserved quantity separately for particles and holes. A perturbation of the system could therefore create an asymmetry between particles and holes we have not included so far within our two mode ansatz. The authors of Ref. [74] noticed this curious fact and found a related slow mode similar to χ_0 we have not yet included.

Within our language, incorporating this particular mode alters the two mode ansatz towards a three mode ansatz:

$$h = \left(\kappa_0 + \kappa_1 \frac{\epsilon}{T} + \kappa_s \text{sign}(\epsilon) \right) + \frac{e\vec{E}\vec{v}}{T^2} \left(\chi_0 + \chi_1 \frac{\epsilon}{T} + \chi_s \text{sign}(\epsilon) \right). \quad (5.35)$$

A natural question that appears now is: do we really have all needed modes now?

The only problem with the previous discussion of the two mode ansatz is that we limited ourselves to analytic forms only. This means that the χ_s -mode has to be taken into account since χ_s is essentially constant and therefore similar to χ_0 . There is no counterpart to χ_1 , since the zero mode is actually not stable against the forward scattering resonance but is “accidentally” annihilated by the momentum conservation (see thermalization in the later Sec. 7.1.3). Thus changing signs will no longer allow this mode to be annihilated by momentum conservation. Hence, the only additional mode able to annihilate the forward scattering resonance is χ_s .

The purpose of this section is now to analyze the influence of this particular mode in contrast to the two mode case introduced previously.

The effective three mode kinetic equation

We discussed in Sec. 5.2.2 the method using a functional to determine the effective kinetic equation and in this context learned that only the choice of the ansatz matters for the quality of the approximated effective kinetic equation. By using the three mode ansatz Eq. (5.35) together with the functional given in Eq. (5.21) we gain an algebraic equation that reads ($z = -i\Omega/T$ or $z = 1/(T\tau_{\text{dis}})$):

$$\begin{pmatrix} A_0 \\ A_1 \\ A_{s0} \end{pmatrix} = \begin{pmatrix} I_{\text{tr}} + A_0 z & A_1 z & I_{\text{str}} + A_{s0} z \\ A_1 z & A_2 z & A_{s1} z \\ I_{\text{str}} + A_{s0} z & A_{s1} z & I_s + A_0 z \end{pmatrix} \begin{pmatrix} \chi_0 \\ \chi_1 \\ \chi_s \end{pmatrix} \quad (5.36)$$

where the new appearing objects have been straightforwardly adapted to the previous notation using:

$$I_s = \frac{1}{4T^3} \int d\{x_i\} W(\{x_i\}) \left(\text{sign}(\epsilon_1)\vec{v}_1 - \text{sign}(\epsilon_2)\vec{v}_2 + \text{sign}(\epsilon_3)\vec{v}_3 - \text{sign}(\epsilon_4)\vec{v}_4 \right)^2 \quad (5.37)$$

$$I_{\text{str}} = \frac{1}{4T^3} \int d\{x_i\} W(\{x_i\}) \left(\vec{v}_1 - \vec{v}_2 + \vec{v}_3 - \vec{v}_4 \right) \left(\text{sign}(\epsilon_1)\vec{v}_1 - \text{sign}(\epsilon_2)\vec{v}_2 + \text{sign}(\epsilon_3)\vec{v}_3 - \text{sign}(\epsilon_4)\vec{v}_4 \right) \quad (5.38)$$

and

$$A_{sn}(\mu) = -\frac{1}{T} \int dx \nu(\epsilon) \frac{\partial n_F^\alpha(\epsilon)}{\partial \epsilon} \text{sign}(\epsilon) \left(\frac{\epsilon}{T} \right)^n. \quad (5.39)$$

Before continuing to solve the effective kinetic equation we need to understand how it differs from Eq. (5.27). It is therefore convenient to analyze the kind of additional contributions we gained. The A_{sn} although appearing similar to the A_n have a shifted symmetry caused by the χ_s mode to appear with a term odd in energy. In this view χ_s behaves like χ_1 . A prior classification of χ_s is done by thinking about it as a velocity (χ_0) like mode with the symmetry of the zero mode (χ_1).

Let us now discuss the rate I_s by confirming first that indeed it is not divergent which would cause a fast relaxation of the mode. As already mentioned both layers have a conserved number of excitations which means that inter band collisions and intra band collisions happen separately forcing $\text{sign}(\epsilon_1\epsilon_2\epsilon_3\epsilon_4) = 1$. This means that the integral kernel of I_s can look like the one of I_{tr} , like $(\vec{v}_1 - \vec{v}_2 - \vec{v}_3 + \vec{v}_4)$ or like $(\vec{v}_1 + \vec{v}_2 - \vec{v}_3 - \vec{v}_4)$. These possibilities are all annihilated by the forward scattering constraint $\vec{v}_1 = \vec{v}_2 = \vec{v}_3 = \vec{v}_4$. An explicit calculation of this cancellation can be found in App. C.2.3.

Discussion of the significance of the third mode

We are now interested in the relevance of this third mode. The first observation we did is that the symmetry of the χ_s mode is odd which immediately implies that close to the Dirac point the interplay of χ_0 and χ_s disappears. Further we notice, that having two odd modes their interplay should be governed by the vicinity to the clean limit, in which the third mode, again is irrelevant. Thus a possible expansion may look:

$$\rho \frac{e^2}{2} \approx \frac{I_{\text{tr}}}{B_0^2} + \frac{z}{B_0} - \frac{B_1^2 I_{\text{tr}}^2}{B_0 (B_1^2 I_{\text{tr}} + B_2 z)} - \frac{\left[B_0 B_2 I_{\text{str}} + (B_0 B_1 A_{s1} - B_0 B_1^2 A_{s0} - A_{s0} B_2) I_{\text{tr}} \right]^2 z}{B_0^4 B_2 I_s (2B_1^2 I_{\text{tr}} + B_2 z)} \quad (5.40)$$

Here we kept in the denominator only the leading contributions of z and B_1 , which is proportional to μ . Hence we assume $z \ll 1$ and $\mu \ll 1$. For this discussion we need to know some of the asymptotics of the short-hand notations introduced. The calculation of those can be found in App. C.2.3 and states, that except of $B_1 \propto A_{s0} \propto I_{\text{str}} \propto \mu$, everything is constant up to quadratic contributions, close to the Dirac point. Then we have two distinct limits to deal with. If we assume $z \ll \mu^2$ we recognize that the additional contribution coming from the third mode disappears completely compared to the first three terms, which correspond to the two mode calculation Eq. (5.32). Thus the corrections appear as $O(z)$. In the regime of $z \gg \mu^2$ the last two contributions are proportional to μ^2 . But one of the terms coming from the two mode calculation has an additional z^{-1} enhancement which again allows us to skip the three mode contribution since it appears as $O(\mu^2)$ (instead of $O(\mu^2 z^{-1})$). In the vicinity of the Dirac point and of the clean case we re-obtain the two mode calculation.

Let us focus now on the situation of large chemical potential. In this situation I_{str} , I_s and I_{tr} are up to exponential small corrections the same. The same is true for the A_{sn} s, that are now up to exponentially small corrections appear to be the same as the A_n s (see App. C.2.3). Thus, we define $I_s - I_{\text{tr}} = \delta_s \ll 1$, $I_{\text{str}} - I_{\text{tr}} = \delta_{\text{str}} \ll 1$, $A_0 - A_{s0} = -\delta_{As0} \ll 1$ and $A_{s1} - A_1 = \delta_{As1} \ll 1$ to obtain the leading order in for large chemical potential. Again we only keep the leading orders of nominator and denominator and obtain

$$\rho \frac{e^2}{2} \approx \frac{I_{\text{tr}}}{B_0^2} + \frac{z}{B_0} - \frac{B_1^2 I_{\text{tr}}^2}{B_0 (B_1^2 I_{\text{tr}} + B_2 z)} - 2I_{\text{tr}} z^2 B_1 \frac{B_1^2 I_{\text{tr}} \delta_{As1} \delta_{As0} + B_2 B_1 \delta_{As0} \delta_{\text{str}} + B_2 \delta_{\text{str}} \delta_{As1}}{B_0^2 (B_1^2 I_{\text{tr}} + B_2 z)^2 (2z \delta_{As0} - 2\delta_{\text{str}})} \quad (5.41)$$

The deviations δ_{As0} and δ_{As1} are just exponentially small in μ/T with some prefactor of order 1. However the deviations δ_{str} and δ_s have additionally to the same exponential suppression a prefactor of order α_g^2 . Therefore as long as we are close to the clean limit where the Coulomb interaction determines the modes the denominator of the last term in Eq. (5.41) can not become zero. The corrections we gain then by the three mode calculation are exponentially small.

Concluding we can say that for large chemical potential and close to the Dirac point the two mode calculation is sufficient. Already within the choice of the collision kernel we considered large N contributions only which means that we will not gain more precision by including the third mode. On the other hand the concepts and ideas we managed to learn from the two mode calculation seem to allow us a conceptual and qualitative understanding of the physics governing the transport in graphene. Therefore although the two mode calculation gains additional corrections at $\mu \sim T$ we will continue performing only the two mode calculation to keep the discussion more clear allowing us to stay focused on the phenomena of transport in graphene.

5.3 Hydrodynamics for Graphene

In our pursuit of understanding the transport in graphene, there is one more step left to go. We have seen how the kinetic equation approach becomes very powerful using the ansatz based on the graphene intrinsic forward scattering resonance. The next setup to go is to extend the formulation towards a true hydrodynamic picture. We have seen in Sec. 5.2.2 that already the ansatz (5.23) is based on the assumptions that interactions dominate the system. Thus, a hydrodynamic formulation (see Sec. 2.5.2) is the next logical step [62, 73–76].

A hydrodynamic formulation implies to have local fields determining the macroscopic state of our system on top of the microscopic details. In Sec. 2.5.2 we sketched how the hydrodynamic equations appear from the kinetic equation almost without involving any microscopic details. This section is dedicated to the derivation and analysis of the hydrodynamic equations in graphene.

5.3.1 The local Hydrodynamic picture

The purpose of writing down the hydrodynamic equations is to add another perspective on the transport properties in graphene. Writing down the hydrodynamic equation as we did in Sec. 2.5.2, it turns out that we gain three equations but none for the current. The reason for this is of course that current itself is not conserved by the Coulomb collision term. We spend quite some effort on solving the kinetic equation. This allows us to write down the local hydrodynamic equations easily. In contrast to the discussion we had so far, the hydrodynamic equations involve the densities implying that the ansatz needs to have a non-directional component.

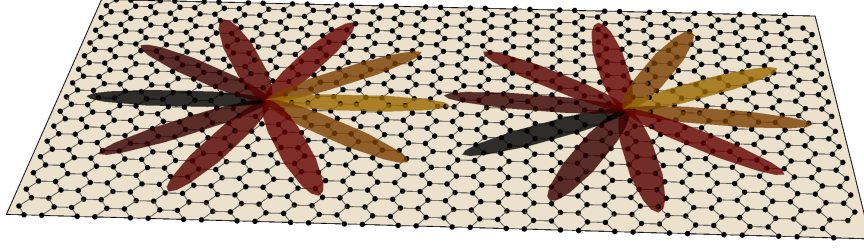


Figure 5.4: *Illustration of the concept of local direction dependent equilibrium (see Sec. 7.1.2). The distance between the spatial separated direction dependent equilibria needs to be at least the thermal length.*

In the spirit of Eq. (5.22) we will consider the two modes for transport. Which modes we discussed within this chapter, and add to this the two zero modes κ_0 and κ_1 (see Sec.5.22) responsible for the densities. The hydrodynamic fields we want to use to describe the system should be local quantities on the scale of temperature. The origin of this limitation is the kinetic equation itself which originated from the local approximation performed in Sec. 2.5. The conclusion there was that all real-space gradients and time derivatives need to be smaller than the relevant quantum scale. In Sec. 4.2 and Sec. 5.4.2 we showed that at the Dirac point, where the chemical potential will not serve us as a large energy scale, temperature comes into play and will be the most relevant scale for transport and energy relaxation rates. Thus, the real-space ultraviolet cut-off for the kinetic equation is given by the thermal length $l_T \propto T^{-1}$. On length scales larger than the thermal length we may as well allow local variation of the external fields. Further, since the collision kernel is a purely local object (see App. A) we might allow all the coefficient's that parametrize the modes κ and χ to vary in real-space coordinates. This yields the desired local ansatz. This implies a local direction dependent equilibrium sketched in Fig. 5.4. The hydrodynamic fields obtained within the approximation of the ansatz (5.23) read:

$$\rho = eN \int dx \nu(\epsilon) n = eNT^2 (A_0 \kappa_0 + A_1 \kappa_1), \quad (5.42)$$

$$\rho_E = N \int dx \nu(\epsilon) \epsilon n = NT^3 (A_1 \kappa_0 + A_2 \kappa_1), \quad (5.43)$$

$$\vec{j} = eN \int dx \nu(\epsilon) \vec{v} n = \frac{1}{2} e^2 N \vec{E} (A_0 \chi_0 + A_1 \chi_1), \quad (5.44)$$

$$\vec{j}_E = N \int dx \nu(\epsilon) \epsilon \vec{v} n = \frac{1}{2} eTN \vec{E} (A_1 \chi_0 + A_2 \chi_1), \quad (5.45)$$

where we are using the abbreviation A introduced in Eq. (5.25) for brevity. With these fields the local hydrodynamic equations can be expressed as:

$$\partial_t \rho + \nabla_r \vec{j} = 0, \quad \partial_t \rho_E + \nabla_r \vec{j}_E = 0, \quad (5.46)$$

$$\partial_t \vec{j} + \nabla_r \rho - e^2 N \vec{E} A_0 = -\frac{\vec{j}}{T \tau_{\text{dis}}} - I_{\text{tr}} \frac{A_2 \vec{j} - A_1 \vec{j}_E T / e}{A_2 A_0 - A_1^2}, \quad \partial_t \vec{j}_E + \nabla_r \rho_E - eN \vec{E} T A_1 = -\frac{\vec{j}_E}{T \tau_{\text{dis}}}. \quad (5.47)$$

Remarkably these equations generalize in a very intuitive way the results obtained for conductivity (5.31) previously. Further these equations highlight the interplay of electric current and energy

current with an easiness and intuition we have not seen in the matrix formulation. Assuming the fields to be static and homogeneous Eq. (5.46) appears to correspond to the some graphene-based Drude-like equations (see for comparison Eq.(5.1)).

5.3.2 Derivation of the non-local Hydrodynamics

The kinetic equation (5.12), we used so far lack one crucial ingredient that is needed to describe the non-local hydrodynamics, namely the viscosity. In Sec. 2.5 we derived the kinetic equation using the local approximation which essentially made the collision kernel a local object. To go beyond this approximation we need to understand the effects of the higher order terms in the gradient expansion as well as their origin. Tracing back the derivation of the kinetic equation (see App. A) we will end up with the self-energy as given in Eq. (A.2).

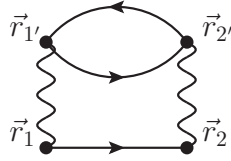


Figure 5.5: *The self-energy diagram involving the spatial coordinates*

If we just disregard any Keldysh structure, for now, we obtain from the diagram in Fig. 5.5:

$$\Sigma(\vec{r}_1, \vec{r}_2) = \int d\vec{r}_{1'} \int d\vec{r}_{2'} D_0(\vec{r}_1 - \vec{r}_{1'}) D_0(\vec{r}_{2'} - \vec{r}_2) G(\vec{r}_1, \vec{r}_2) \text{Tr} \left[G(\vec{r}_{1'}, \vec{r}_{2'}) G(\vec{r}_{2'}, \vec{r}_{1'}) \right]. \quad (5.48)$$

Performing the Wigner-transformation for each propagator and making use of the delta constraints that appear we can rewrite the equation, using $2\vec{q} = \vec{q}_1 + \vec{q}_2$ and $\delta\vec{q} = \vec{q}_1 - \vec{q}_2$ as total and relative transferred momentum, and obtain

$$\begin{aligned} \Sigma(\vec{R}_{12}, \vec{p}) = & \int d\vec{R}_{1'2'} \frac{d\delta q}{(2\pi)^2} e^{-i(\vec{R}_{12} - \vec{R}_{1'2'})\delta\vec{q}} \int \frac{dq}{(2\pi)^2} \frac{dp'}{(2\pi)^2} D_0(\vec{q} + \frac{\delta\vec{q}}{2}) D_0(\vec{q} - \frac{\delta\vec{q}}{2}) \\ & \times G(\vec{R}_{12}, \vec{p} - \vec{q}) \text{Tr} \left[G(\vec{R}_{1'2'}, \vec{p}') G(\vec{R}_{1'2'}, \vec{p}' + \vec{q}) \right]. \quad (5.49) \end{aligned}$$

This self-energy appears finally in the kinetic equation (see Eq. A.7) together with an additional convolution between different center of mass coordinates of the electronic propagator and the self-energy. Since Coulomb interaction is a long-range interaction we assume the non local structure of the self-energy to be more relevant than non-local contributions between electronic propagators. Assuming further that the center of mass dependence of $G(\vec{R}, \vec{p})$ is not only very weak but exclusively present in the distribution function f we observe that the complete calculation that has been performed in App. A.2.1 can be done without any further restrictions. Even more we can as well linearize the collision kernel arriving at:

$$\begin{aligned} \delta I_{\text{coll}} = & \frac{1}{\nu(\epsilon_1)} \int d\{x_i\}_{i \in \{2, 1', 2'\}} \tilde{W}(\{x_i\}) \int d\vec{R}_{1'2'} \frac{d\delta q}{(2\pi)^2} e^{-i(\vec{R}_{12} - \vec{R}_{1'2'})\delta\vec{q}} D_0(\vec{q} + \frac{\delta\vec{q}}{2}) D_0(\vec{q} - \frac{\delta\vec{q}}{2}) \\ & \times \left\{ h(\vec{R}_{12}, x_1) - h(\vec{R}_{12}, x_2) + h(\vec{R}_{1'2'}, x_{1'}) - h(\vec{R}_{1'2'}, x_{2'}) \right\}, \quad (5.50) \end{aligned}$$

$$\begin{aligned} \tilde{W}(\{x_i\}) &= 2\pi\delta(\epsilon_1 - \epsilon_2 + \epsilon_{1'} - \epsilon_{2'}) (2\pi)^2 \delta(\epsilon_1 \vec{v}_1 - \epsilon_2 \vec{v}_2 + \epsilon_{1'} \vec{v}_{1'} - \epsilon_{2'} \vec{v}_{2'}) \times \\ &\quad \times \frac{\theta_{1,2} \theta_{1',2'} \nu(\epsilon_1) \nu(\epsilon_2) \nu(\epsilon_{1'}) \nu(\epsilon_{2'})}{16 \cosh(\frac{\epsilon_1 - \mu_\alpha}{2T}) \cosh(\frac{\epsilon_2 - \mu_\alpha}{2T}) \cosh(\frac{\epsilon_{1'} - \mu_\beta}{2T}) \cosh(\frac{\epsilon_{2'} - \mu_\beta}{2T})}. \end{aligned} \quad (5.51)$$

This equation is particular useful. Assuming the distribution functions to be independent on the center of mass coordinates we recover the collision kernel (5.18) from the previous sections. Expanding the interaction propagator in $\delta\vec{q}$ we will be able to go beyond the local approximation. Since an expansion of the interaction propagator reads:

$$D_0(\vec{q} + \frac{\delta\vec{q}}{2}) \approx D_0(\vec{q}) - \frac{\delta\vec{q}}{2} \frac{\vec{q}}{q^2} D_0^2(q) + \frac{\delta\vec{q}}{2} \left(\frac{\vec{q} \otimes \vec{q} - q^2 \mathbf{1}}{2q^4} \right) \frac{\delta\vec{q}}{2} D_0^2(q), \quad (5.52)$$

it follows that the combinations of the propagators inside the non local collision integral read:

$$D_0(\vec{q} + \frac{\delta\vec{q}}{2}) D_0(\vec{q} - \frac{\delta\vec{q}}{2}) \approx D_0^2(\vec{q}) - \frac{D_0^2(q)}{q^2} \left(\frac{\delta\vec{q}}{2} \right)^2. \quad (5.53)$$

It is clear that the first term in this expansion creates naturally the local collision integral we took into account so far. Within the integration over $\vec{R}_{1'2'}$ the parameter $\delta\vec{q}$ can be understood as an operator acting on $\vec{R}_{1'2'}$. Thus we may write the symmetrised transformation explicit as:

$$\left(\frac{\delta\vec{q}}{2} \right)^2 \rightarrow \frac{1}{4} \left(\Delta_{R_{12}} + \Delta_{R_{1'2'}} - 2\nabla_{R_{12}} \nabla_{R_{1'2'}} \right), \quad (5.54)$$

where Δ_R is the Laplace operator with respect to \vec{R} . The leading non-local correction to the collision integral reads:

$$\begin{aligned} \delta I_{\text{coll}} &= -\frac{1}{8\nu(\epsilon_1)} \int d\{x_i\}_{i \in \{2,1',2'\}} \tilde{W}(\{x_i\}) \left(\frac{D_0(\vec{q})}{q} \right)^2 \\ &\quad \times \left\{ \Delta_{R_{12}} \left[h(\vec{R}_{12}, x_1) - h(\vec{R}_{12}, x_2) \right] + \Delta_{R_{1'2'}} \left[h(\vec{R}_{1'2'}, x_{1'}) - h(\vec{R}_{1'2'}, x_{2'}) \right] \right\}_{\vec{R}_{1'2'} \rightarrow \vec{R}_{12}}. \end{aligned} \quad (5.55)$$

We need to remember, that after applying the operator, the different coordinates \vec{R}_{12} and $\vec{R}_{1'2'}$ have to be evaluated at the same point. This way we defined how to extend the here presented theory towards viscosity contributions as shown in Eq. (2.78). With help of the viscosity we can understand the equilibration of non-local setups that e.g. appear when considering clean finite systems with different chemical potentials applied to. Thus, the here performed analysis provides an excellent starting point for the analysis of finite setups (see Sec. 9).

5.4 Diagrammatic Analysis

We have seen the description of transport in terms of the kinetic equation. Within the next section we will look at the transport properties at the Dirac point of clean graphene but using the diagrammatic approach known from chapters 3 and 4. We therefore continue the calculation of Chap. 4 but with an emphasis on transport.

5.4.1 Transport Scattering Rate due to Inelastic Collisions

In this section we calculate the transport relaxation rate due to inelastic collisions. The expression for the corresponding kernel Eq. (B.11) of the self-energy can be deduced from the interaction-induced correction to the conductivity, as described below. We are interested in the linear-response dc conductivity. The leading order perturbative correction to the conductivity due to Coulomb interaction is given by the two diagrams shown in Fig. 5.6.

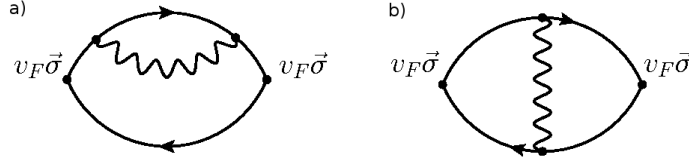


Figure 5.6: Diagrams describing the first-order interaction correction to the conductivity

In the absence of interaction, the conductivity of a clean graphene diverges at finite temperature. Therefore, we have regularized the diagrams by introducing a small broadening (δ) which mimics the finite lifetime due to weak disorder. The general analytic expression of the lowest-order interaction correction to the conductivity within the Keldysh formalism can be found in Ref. [44]. This correction can be split into two parts (Figs. 5.6a and 5.6b): $\delta\sigma = \delta\sigma^s + \delta\sigma^v$, where

$$\begin{aligned} \delta\sigma_{\beta\beta}^s = & -\frac{1}{4i} \int \frac{d^2p_1}{(2\pi)^2} \int \frac{d\epsilon_1}{2\pi} \int \frac{d^2p_2}{(2\pi)^2} \int \frac{d\epsilon_2}{2\pi} \frac{\partial f_1}{\partial \epsilon} \text{Tr} \left\{ j_\beta \left[G^R(1) - G^A(1) \right] j_\beta \right. \\ & \times \left[(f_2 + g) \left[D^R - D^A \right] \left[G^R(1) G^R(2) G^R(1) - G^A(1) G^A(2) G^A(1) \right] \right. \\ & \left. \left. + f_2 \left[G^R(1) \left[G^R(2) D^R - G^A(2) D^A \right] G^R(1) - G^A(1) \left[G^R(2) D^R - G^A(2) D^A \right] G^A(1) \right] \right] \right\} \quad (5.56) \end{aligned}$$

is the self-energy contribution and

$$\begin{aligned} \delta\sigma_{\beta\beta}^v = & -\frac{1}{4i} \int \frac{d^2p_1}{(2\pi)^2} \int \frac{d\epsilon_1}{2\pi} \int \frac{d^2p_2}{(2\pi)^2} \int \frac{d\epsilon_2}{2\pi} \frac{\partial f_1}{\partial \epsilon} \text{Tr} \left\{ j_\beta (f_2 + g) \left[D^R - D^A \right] \right. \\ & \times \left[G^R(1) G^R(2) - G^A(1) G^A(2) \right] j_\beta \left[G^R(2) G^R(1) - G^A(2) G^A(1) \right] \\ & \left. + 2j_\beta f_2 \left[G^R(1) - G^A(1) \right] \left[D^A G^R(2) j_\beta G^R(2) - D^R G^A(2) j_\beta G^A(2) \right] j_\beta \left[G^R(1) - G^A(1) \right] \right\} \quad (5.57) \end{aligned}$$

is due to the vertex correction. Here $j_\beta = ev_F\sigma_\beta$ is the current operator in graphene and we used the short-hand notations for the arguments of Green's functions: $1 = \vec{p}_1, \epsilon_1$ and $2 = \vec{p}_2, \epsilon_2$. We first trace out the sublattice structure and then regularize the divergent integrals by δ using essentially

$G_\lambda^R G_\lambda^A = \frac{1}{2i\delta} (G_\lambda^R - G_\lambda^A)$. The most divergent interaction-induced correction to the dc conductivity

$$\delta\sigma = -\frac{e^2 v_F^2}{4\delta^2} \int \frac{d\epsilon_1}{2\pi} \frac{\partial f}{\partial \epsilon_1} \int \frac{d\epsilon_2}{2\pi} \int \frac{d^2 p_1}{(2\pi)^2} \int \frac{d^2 p_2}{(2\pi)^2} \pi \left[\delta(\epsilon_1 - v_F p_1) + \delta(\epsilon_1 + v_F p_1) \right] \text{sign} \epsilon_1$$

$$\times \underbrace{\left[1 - \frac{(\vec{p}_1 \cdot \vec{p}_2)}{p_1 p_2} \right]}_{\text{Transport factor}} \underbrace{\left[1 + \frac{(\vec{p}_1 \cdot \vec{p}_2)}{p_1 p_2} \right]}_{\text{Dirac factor}} K_\Sigma(\epsilon_1, \epsilon_1 - \epsilon_2, \vec{p}_1, \vec{p}_1 - \vec{p}_2). \quad (5.58)$$

is then proportional to δ^{-2} . Here K_Σ is the integral kernel of the self-energy:

$$\text{Im} \Sigma_0^R(\epsilon, \vec{p}) = \int \frac{d^2 q}{(2\pi)^2} \int \frac{d\omega}{2\pi} K_\Sigma(\epsilon, \omega, \vec{p}, \vec{q}) \quad (5.59)$$

The correction, Eq. (5.58), is determined by the inelastic electron-electron scattering. In the diagrams of the leading order in bare interaction shown in Fig. 5.6, we have $K_\Sigma \propto \text{Im} D_0 = 0$, so that the inelastic corrections are zero. What remains in the first-order conductivity correction, Fig. 5.6, are the contributions responsible for the renormalization of the Fermi velocity in graphene coming from the real part of the self-energy; note that these contributions are less singular in δ^{-1} .

Thus, we have to consider higher order corrections. In Fig. 5.7 one can see all classes of second order skeleton diagrams. There are also the second-order diagrams of the ladder type, see Fig. 5.8. Such diagrams contribute only to the renormalization of v_F , similarly to the diagrams in Fig. 5.6, and their contribution has been already included into the calculation simply by the replacement $v_F \rightarrow v_F(T)$.

In the large N approximation, diagrams in Figs. 5.7d, 5.7e, and 5.7f dominate. Diagram 5.7f is the Coulomb drag diagram and yields a zero contribution at the Dirac point due to electron-hole symmetry (in later chapter we will investigate the drag contribution more carefully see chapters 6 and 7 and references [77, 78]). We are left with the diagrams 5.7d and 5.7e which correspond to the two diagrams shown in Fig. 5.6 with the second-order correction to the interaction instead of the bare one. For these two diagrams, Eq. (5.58) still holds with $K_\Sigma \propto \text{Im} D_1$. This suggests to replace the bare interaction lines shown in Fig. 5.6 by the RPA interaction lines, which would correspond to Eq. (5.58) with $K_\Sigma \propto \text{Im} D_{\text{RPA}}$. Note that even with the RPA-dressed interaction, Eq. (5.58) still yields a divergent contribution which we have regularized with δ .

Considering the two independent scattering processes with the transport scattering rates δ and τ_{tr}^{-1} such that we find the Drude conductivity in the form

$$\sigma = e^2 \int d\epsilon \rho(\epsilon) \left(-\frac{\partial n_F}{\partial \epsilon} \right) \frac{v_F^2 \tau_{\text{tr}}(\epsilon)}{2[1 + \tau_{\text{tr}}(\epsilon)\delta]}, \quad (5.60)$$

where $n_F(\epsilon) = [1 - f(\epsilon)]/2$ is the thermal Fermi distribution function and $\rho(\epsilon)$ is the thermodynamic density of states. Expanding this formula in $(\delta\tau_{\text{tr}})^{-1}$, we get the ‘‘interaction-induced’’ correction:

$$\delta\sigma = \frac{e^2 v_F^2}{4\delta^2} \int d\epsilon \frac{\partial f}{\partial \epsilon} \frac{\rho(\epsilon)}{\tau_{\text{tr}}(\epsilon)}. \quad (5.61)$$

Comparing Eq. (5.61) with Eq. (5.58) we can identify the interaction-induced transport scattering rate in graphene. The transport scattering rate obtained from the conductivity correction corresponds to the kernel \mathcal{K}_{tr} defined in Appendix B.2.1.

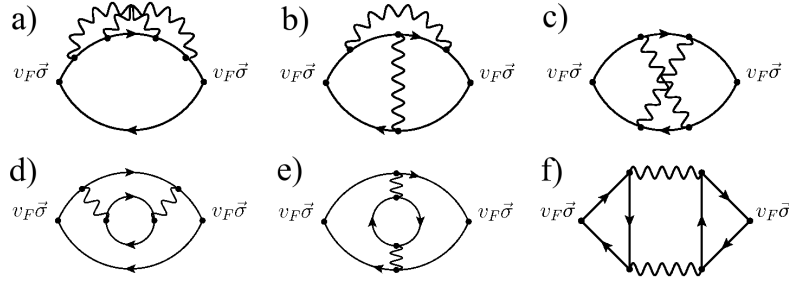


Figure 5.7: Second-order skeleton diagrams for the conductivity

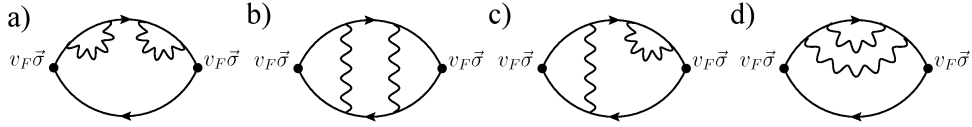


Figure 5.8: Examples of second-order diagrams for the conductivity that contribute to the renormalization of velocity.

Furthermore, the connection between the kernels in the transport scattering rate and the quantum scattering rate also follows from Eqs. (5.58), (5.59), and (5.61). One can see from Eq. (5.58) that in the transport scattering rate not only the contribution of forward scattering processes is suppressed as in conventional systems but also the contribution of the backward scattering. The latter suppression is due to the Berry phase of π in graphene.

In the above derivation we have assumed $\delta \gg \tau_{\text{tr}}^{-1}$ which allowed us to extract τ_{tr}^{-1} from the expansion of the conductivity in τ_{tr}^{-1} . Using the generalized GR approach, we show in Appendix B.3 that the expression for the transport scattering rate obtained in this way remains valid also for $\delta \rightarrow 0$.

5.4.2 Transport Scattering Rate: Results

Similarly to the quantum scattering rate, the transport rate is dominated by region 3 (see Fig. 4.1) in the regimes II, III, and IV. Again, this is not so for energies that are in the regime II. In this case, we have an additional contribution from region 1 (see Fig. 4.1), like in Sec. 4.2.1. The calculation outlined in App. B.2 yields

$$\frac{1}{\tau_{\text{tr}}(\epsilon)} \sim \begin{cases} \frac{T}{N} \sqrt{\frac{\epsilon}{T}}, & \text{I} \\ \alpha_g T, & \text{II} \\ \alpha_g^2 N T \left(\frac{T}{\epsilon} \right), & \text{III} \\ \alpha_g^2 N T \left(\frac{T}{\epsilon} \right)^2, & \text{IV} \end{cases} \quad (5.62)$$

The characteristic momenta dominating the transport scattering rate as well as the relevant regions in Q - Ω plane are shown in Table 5.1. The transport scattering rate in Regimes II and III are dominated by momenta much smaller than temperature, which allows us to find the numerical prefactors (given in Appendix B). Regimes I and IV is determined by momenta of order temperature, which does not allow us to find the numerical coefficient in these regimes. The analytical asymptotics are plotted alongside with the exact numerical result in Fig. 5.9.

τ_{tr}	I	II	III	IV
$qv_F \sim \omega$	T	$\alpha_g^2 N^2 T / \epsilon$	ϵ	T
Regions	1,2,3,4	1,3	3	3

Table 5.1: Momentum/frequency scales and regions of the Q - Ω plane that dominate the transport scattering rate τ_{tr}^{-1} in different domains (I,II,III, and IV) of energy ϵ .

Similarly to Sec. 4.2.3, we see a strong enhancement of the transport scattering rate in region II. When the energy approaches the temperature, the GR result

$$\tau_{\text{tr}}^{-1}(\epsilon \sim T) \sim \alpha_g^2 N T \quad (5.63)$$

is reproduced.

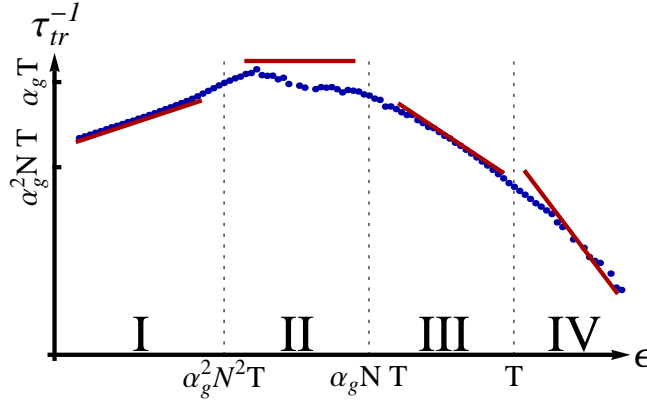


Figure 5.9: Transport scattering rate for $\alpha_g N = 4 \times 10^{-3}$ (double logarithmic scale). Dots: exact values obtained by numerical evaluation; solid lines: analytical asymptotics, Eq. (5.62).

Comparing the transport scattering rate with the energy relaxation rate,

$$\frac{\tau_{\text{tr}}}{\tau_{\text{E}}} \propto \ln \frac{1}{\alpha_g N}, \quad (5.64)$$

we observe that in the limit of small α_g the relaxation of energy due to the inelastic collisions occurs much faster than the velocity relaxation, $\tau_{\text{tr}} \gg \tau_{\text{E}}$. The difference between the two rates comes from the fact that the forward scattering in graphene is strongly enhanced. The RPA screening suppresses the contribution of scattering angles smaller than α_g thus regularizing the logarithmically divergent

contribution to the energy relaxation rate. On the other hand, the transport factor in \mathcal{K}_{tr} , see Eq. (5.58), kills the contribution of the forward scattering to the transport scattering rate much more efficiently than the RPA screening (this is the reason why the GR result for τ_{tr} is parametrically correct), so that no logarithmic factor arises in τ_{tr} .

The relation Eq. (5.64) justifies the hydrodynamic approach [62, 73, 74, 76]: the distribution functions of electrons and holes equilibrate within each type of carriers much faster than the direction of the velocity is changed. As a result, the distribution functions effectively depend only on the velocity direction. This means that the interaction-induced transport scattering rate entering the observables should be averaged over the temperature window:

$$\langle \tau_{\text{tr}}^{-1} \rangle = \frac{\int_0^{\infty} d\epsilon \rho(\epsilon) \frac{\partial f}{\partial \epsilon} \frac{1}{\tau_{\text{tr}}(\epsilon)}}{\int_0^{\infty} d\epsilon \rho(\epsilon) \frac{\partial f}{\partial \epsilon}}. \quad (5.65)$$

This energy-averaging procedure exactly corresponds to the solution of kinetic equation as we explained it in the previous Sec. 5.2 following the line of arguments given by Refs. [72] and [71].

Evaluating the integral in Eq. (5.65) numerically with the exact expression for the RPA propagators, we find

$$\langle \tau_{\text{tr}}^{-1} \rangle \simeq 0.989 \alpha_g^2 NT. \quad (5.66)$$

The numerical prefactor in this result is the same one obtains by dividing $I_{\text{Gtr}}(\mu = 0)$ (see Eq. (C.3.1)) by $A_0(\mu = 0)$ (see Eq. (C.37)) and thus agrees with that found in Ref. [72] for the direct interaction term. As we will see below, this averaged value of the transport scattering rate can be substituted into the Drude expression for the conductivity, which yields the parametrically correct result for the collision-dominated conductivity of clean graphene.

5.4.3 Collision-Limited Conductivity

Above, when calculating the conductivity, we have assumed that the finite lifetime of quasi-particles is provided by some artificially introduced broadening δ which mimics disorder. The introduction of the artificial lifetime allowed us to identify the contribution of the inelastic collisions to the transport scattering rate by considering the perturbative-in-interaction contributions to the conductivity. Let us now discuss the conductivity of clean graphene, or, more precisely, the conductivity of graphene in the regime when the inelastic collisions dominate over disorder scattering.

The conductivity of graphene at the Dirac point is a rather intricate quantity. In the absence of interaction, transport in the ballistic limit shows remarkable peculiarities in graphene.[20] The interplay between vanishing density of states and vanishing scattering rate leads to the non-universal conductivity that depends on the measurement details. In particular, finite size clean graphene sample of the “short-and-wide” geometry shows a behavior analogous to that of a normal diffusive metal. The zero- T conductivity of such a setup is $\sigma = 4 \times e^2/\pi h$. The same value of conductivity was predicted for an infinite sample with a large but finite electron lifetime. A different result, $\sigma = e^2/2h$, was found in the undoped graphene at a large frequency. At any non-zero value of the chemical potential, the conductivity of clean graphene is infinite. At finite temperature, energies within the temperature window contribute to the conductivity. This implies that the Dirac-point conductivity becomes infinite in the noninteracting case at any non-zero T .

As has been shown the previous Sec. 5.2 and in Refs. [62, 71, 72], the conductivity of clean undoped graphene becomes finite due to the inelastic electron-electron collisions. The estimate for the collision-limited conductivity can be obtained by substituting the typical value of interaction-induced transport scattering time, Eq. (5.63), and the typical density of thermally populated states, $\rho(T) \sim NT/v_F^2$, into the Drude formula, which yields

$$\sigma = \frac{e^2}{h} \rho(T) v_F^2 \tau_{tr}(T) \sim \frac{e^2}{h} \frac{NT}{v_F^2} v_F^2 \frac{1}{\alpha_g^2 NT} \sim \frac{e^2}{h} \frac{1}{\alpha_g^2}. \quad (5.67)$$

Note that the explicit dependence on T , N , and v_F drops out from this formula; however, the temperature dependence appears in Eq. (5.67) implicitly through the renormalization of α_g . A more rigorous calculation of the collision-limited conductivity requires the analysis of the kinetic equation (see Sec. 5.2 and Refs. [71, 72]). The fast energy relaxation discussed above not only simplifies such an analysis, but also reduces the kinetic equation to the hydrodynamic model [62, 73–76].

The consideration of Sec. 5.4.1, which allowed us to find the transport scattering rate from the expression for the conductivity, relied on the perturbative treatment of the interaction. This assumes the following hierarchy of the energy scales:

$$\tau_{tr}^{-1} \ll \delta \ll T. \quad (5.68)$$

The first inequality implies that the broadening of the Green's functions is due to the artificial “disorder” rate δ , whereas the second inequality establishes the ballistic regime which allows us to neglect the dressing of interaction by disorder. Since the characteristic frequency transfer in the transport scattering rate is of the order of the temperature, the resulting τ_{tr}^{-1} does not depend on δ as long as $\delta \ll T$. Furthermore, in App. B.3 we have calculated τ_{tr}^{-1} from the generalized GR approach for $\delta = 0$ and reproduced the transport kernel \mathcal{K}_{tr} from Appendix B.2. Therefore, we expect that the Drude formula, yielding Eq. (5.67), is applicable also for $\tau_{tr}^{-1} \gg \delta$, i.e. in the collision-dominated transport regime. This expectation is supported by the kinetic equation approach shown in Sec. 5.2 and the results of Refs. [62, 71, 72].

Assuming the validity of the Drude formula for $\delta \ll \tau_{tr}^{-1}$, we evaluate the conductivity using the energy-averaged transport scattering rate given by Eq. (5.66):

$$\sigma = \frac{e^2}{h} \frac{N\pi}{\langle \tau_{tr}^{-1} \rangle} \int_0^\infty d\epsilon \rho(\epsilon) \frac{\partial f}{\partial \epsilon} \approx \frac{e^2}{h} \frac{0.7}{\alpha_g^2} \quad (5.69)$$

This result is exactly the same obtained previously in Eq. 5.31 within the kinetic equation approach.

It is worth noting here that the kinetic equation approach (see Sec. 5.2.1) performed in analogy to Refs. [71, 72] was based on the GR calculation of the self-energies. As we have seen in Sec. 5.4.1, the RPA result for the transport scattering rate at relevant energies $\epsilon \sim T$ [as well as the energy-averaged characteristic rate, Eq. (5.65)] has the same form as given by the GR. Moreover, the averaging of the energy-dependent transport scattering rate using Eq. (5.65) yield the same numerical prefactor as follows from the kinetic equation with the GR collision integral [71, 72], see Eq. (5.66). Therefore, we conclude that the RPA resummation does not change the numerical prefactor of conductivity in the leading order in α_g^2 . In other words, unlike the quantum scattering (or dephasing) rate considered in Secs. 4.2.1 and 4.2.2, the calculation of the conductivity can be done within the Golden-Rule approach. The RPA resummation yields only sub-leading-in- α_g corrections to the conductivity. A treatment of

the Coulomb interaction like in the beginning of Sec. 5.2 is therefore accurate if the quantities one is looking for are transport related.

We want to emphasize that in case $\alpha_g N \gg 1$ and $N \gg 1$ the calculation can become controllable again since the biggest contributions to the interaction are due to the polarization operator, however the resummation (RPA) yields effective small interaction (small mean-field). Thus the above consideration remain, except that the regime $0 \leq \epsilon \leq \alpha^2 NT$ crosses the temperature. Therefore in Eq. (5.62) only regime I is relevant. Averaged over temperature one yields for the conductivity:

$$\sigma \propto \frac{e^2}{h} N^2, \quad (5.70)$$

which together with the conductivity from Eq.(5.69) matches perfectly with the large N analysis performed in Ref. [59]

5.4.4 Qualitative Discussion of the Effect of Disorder and Comparison with Experiments

In this Drude like picture we can discuss on the qualitative level the effect of disorder on the Dirac-point conductivity in graphene. For simplicity we set $N = 1$ below. In the absence of interaction, effect of disorder on transport in the ballistic regime is highly unconventional and strongly depends on the type of randomness [79–82]. On the other hand, as we have seen above, the interaction effects are crucially important for the transport already in a clean system. It is thus important to explore transport in realistic graphene structures, with both the electron-electron interaction and disorder taken into account.

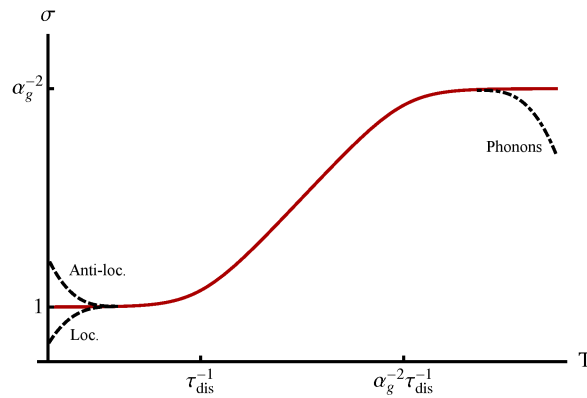


Figure 5.10: Schematic plot (only parametrical scales are given) of the temperature dependence of the Drude conductivity (in units of e^2/h ; solid line) $\alpha_g \ll 1/\ln(\Lambda\tau_{\text{dis}})$, where Λ is the bandwidth. For simplicity, the logarithmic temperature corrections to α_g which comes from the renormalization is not shown. Dashed lines: low- T behavior of the conductivity governed by quantum interference effects; depending on the character of disorder, the localization, antilocalization, or criticality (coincides with the solid line) may occur. Dash-dotted line: expected high- T behavior governed by electron-phonon scattering.

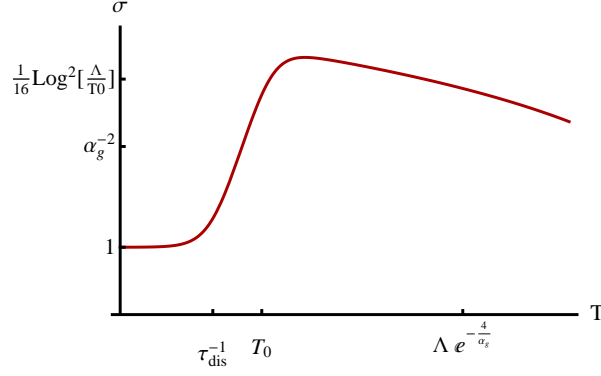


Figure 5.11: Schematic plot of the temperature dependence of the Drude conductivity (in units of e^2/h) for strong interaction, $\alpha_g \gg 1/\ln(\Lambda\tau_{\text{dis}})$. The characteristic scale T_0 is given by $T_0 \sim \tau_{\text{dis}}^{-1} \ln^2(\Lambda/T_0) \sim \tau_{\text{dis}}^{-1} \ln^2(\Lambda\tau_{\text{dis}})$. For possible deviations at low and high T (interference and phonon contributions, respectively), see Fig. 5.10

The role of disorder here is twofold: (i) potential disorder introduces velocity relaxation, thus contributing to the transport scattering rate:

$$\frac{1}{\tau_{\text{tr}}} \sim \alpha_g^2 T + \frac{1}{\tau_{\text{dis}}}, \quad (5.71)$$

and (ii) establishes a finite density of states already in the Dirac point:

$$\rho \propto T + \frac{1}{\tau_{\text{dis}}}. \quad (5.72)$$

Substituting these formulas into the Drude conductivity, we obtain the following result describing the crossover between the collision-dominated and disorder-dominated regimes:

$$\sigma \sim \frac{e^2}{h} \frac{T + \frac{1}{\tau_{\text{dis}}}}{\alpha_g^2 T + \frac{1}{\tau_{\text{dis}}}}. \quad (5.73)$$

This expected temperature dependence of the Drude conductivity is shown in Fig. 5.10 for the case weak interaction (or strong disorder), $\alpha_g \ll 1/\ln(\Lambda\tau_{\text{dis}})$ when the renormalization of α_g gives only small logarithmic corrections. For stronger interaction (or weaker disorder), $\alpha_g \gg 1/\ln(\Lambda\tau_{\text{dis}})$, the renormalization of

$$\alpha_g(T) = \frac{\alpha_g}{1 + \frac{\alpha_g}{4} \ln \frac{\Lambda}{T}},$$

becomes strong [so that the renormalized coupling “forgets” about its bare value, $\alpha_g(T) \rightarrow 4/\ln(\Lambda/T)$] already in the collision-dominated regime, see Fig. 5.11. One sees that, since the interaction-induced transport rate contains α_g^2 whereas the density of states of thermally excited quasi-particles does not, the two crossover T -scales appear, which establishes an intermediate regime of the ballistic transport,

$$\frac{1}{\tau_{\text{dis}}} \ll T \ll \frac{1}{\alpha_g^2 \tau_{\text{dis}}}.$$

Note that we neglected the phonon contribution to the relaxation rates (for estimate of their contribution, see, e.g. Ref. [66]) which becomes relevant at sufficiently high temperatures.

At $T \sim 1/\tau_{\text{dis}}$ the Drude conductivity becomes of the order of conductance quantum and the dephasing rate becomes of the order of T . At lower temperatures, the T dependence of the conductivity is governed by interference effects: localization, antilocalization, or critical behavior may occur, depending on the symmetry of disorder.[83–85] The crossover scale $1/\tau_{\text{dis}}$ in typical experiments on high-quality graphene is in the range $T \sim 1 - 100\text{K}$.

Transport measurements performed on suspended graphene [86] show significant changes in the conductivity as a function of temperature, as depicted in Fig. 5.12. The case of suspended graphene is more complicated since the appearance of flexural phonons dramatically influences the transport properties of graphene [87]. Nonetheless, depending on the specific details of the setup the system shows at low temperatures $T \propto \tau_{\text{dis}}^{-1}$ a disorder dominated conductivity and at very high temperatures T_{ph} a conductivity governed by flexural phonons. However, in between the conductivity is determined by Coulomb interaction if the temperature the phonons become relevant obeys $T_{\text{ph}} \gg (\alpha_g^2 \tau_{\text{dis}})^{-1}$ (see Fig. 5.10).

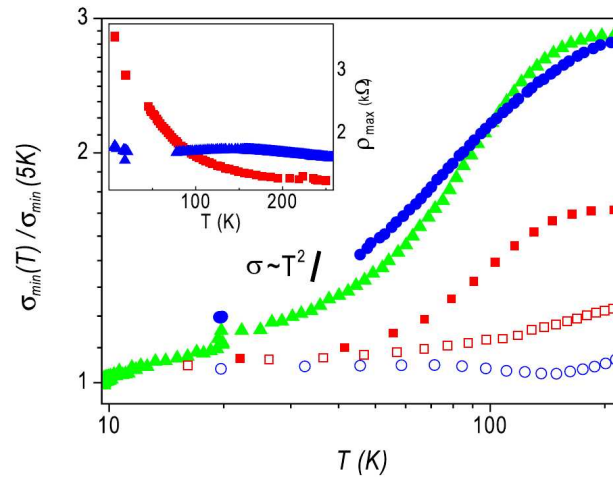


Figure 5.12: Conductivity measurement performed on suspended graphene from Ref. [86].

In the experimental data shown in Fig. 5.12 the rise of the conductivity is maybe due to the initiation of the Coulomb interaction dominated regime as indicated by Fig. 5.10.

Although experiments can not yet measure the regime described above they seem to have reached the threshold, which so far agrees very well with our theory. Thus we are quite optimistic to see experimental data measuring Coulomb dominated conductivity in the next few years.

6

Chapter 6

Coulomb Drag in Graphene: Basics and Previous Work

An alleged scientific discovery has no merit unless it can be explained to a barmaid.

Ernest Rutherford, As quoted in Einstein: The Man and His Achievement

This chapter is dedicated to a phenomenon that may look very simple at first sight but despite its apparent simplicity allows deep insights into the interplay of transport phenomena and Coulomb interaction. We will first define Coulomb drag, then continue with a simple Drude picture for the description of the effect and finally recapitulate previous work on this subject in 2DEG and in graphene.

6.1 Definition of Coulomb Drag

The concept of Coulomb drag is rather old [17, 18] but still attracts attention. One of the reasons is that experimental settings have become more controllable and more complex in the phenomena they manage to combine. Another facet of this attention is that Coulomb drag is, because its nature relies on the long-range character of the interaction and because of its delicate effects on the system, not as well studied as other effects of this age may be [88–91].

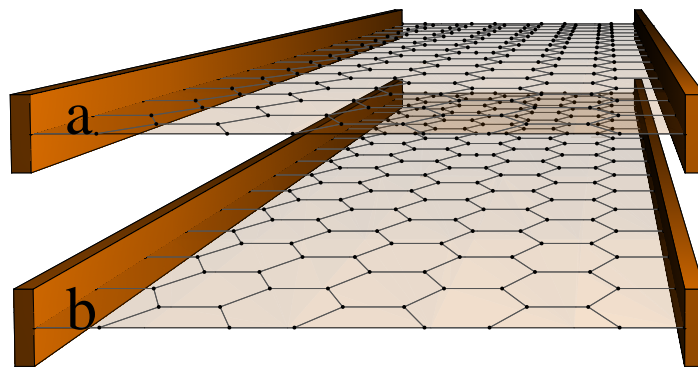


Figure 6.1: A sketch of the setting the Coulomb drag will be described in.

Still, the very basic idea of Coulomb drag is rather simple. Let us imagine we have two-layers of a two-dimensional conducting material, say a 2DEG or graphene, like it is shown in Fig. 6.1, but electronically decoupled. We refer to the two-layers as layer a and layer b . We need conducting materials since we will now consider two pass a current through one of them, for example layer a . A current in layer a means that we have an imbalance in the velocity (in a 2DEG also momentum) distribution of the system. The key to understand the phenomenon is that the Coulomb interaction in such a setup couples the layers and therefore transmits traces of the non-equilibrium configuration of layer a to layer b . If layer b is not attached to any conducting contact the transmitting traces will build up a charge imbalance that can be measured as a voltage. Altogether this means that Coulomb drag refers to the ability of such a system to show a transresistivity also referred to as drag resistivity,

$$\vec{j}_a \rho_D \propto \vec{E}_b. \quad (6.1)$$

If one compares it with the full resistivity tensor one can define in the situation of two interacting layers,

$$\begin{pmatrix} \vec{j}_a \\ \vec{j}_b \end{pmatrix} = \begin{pmatrix} \rho_{aa} & -\rho_D \\ -\rho_D & \rho_{bb} \end{pmatrix} = \begin{pmatrix} \vec{E}_a \\ \vec{E}_b \end{pmatrix}, \quad (6.2)$$

one recognizes that the drag resistivity, as explained, connects the layers.

To establish an intuitive picture of Coulomb drag we will first discuss it within a Drude picture.

6.1.1 Classical Description

As in the previous Chap. 5 we will start by considering non-relativistic parabolic particles first, making the picture as transparent as possible. In its core Coulomb drag is simple enough to describe it within the previously introduced Drude picture Sec. 5.1.1. We therefore begin with two equations that each have a Drude-like structure:

$$\frac{d}{dt} \vec{v}_a(t) = \frac{q}{m} \vec{E}_a - \frac{1}{\tau} \vec{v}_a(t) + \frac{\vec{v}_b(t) - \vec{v}_a(t)}{\tau_D}, \quad (6.3)$$

$$\frac{d}{dt} \vec{v}_b(t) = \frac{q}{m} \vec{E}_b - \frac{1}{\tau} \vec{v}_b(t) + \frac{\vec{v}_a(t) - \vec{v}_b(t)}{\tau_D}. \quad (6.4)$$

These two equations differ from Eq. (5.1) by an additional contribution proportional to τ_D^{-1} . This additional contribution accounts for differences in the velocity distribution of the two-layers and creates a phenomenological exchange between the layers. At this point we will not specify how such a contribution can arise since this will be part of later discussions (see Chap. 7). Instead we will show how such a phenomenological exchange contribution creates a transresistivity like the Coulomb drag resistivity (see Eq. (6.1)).

To do so, we apply the appropriate conditions to measure the drag. Layer b is assumed to be disconnected which results in a vanishing velocity distribution. in the stationary case this leads to:

$$0 = \frac{q}{m} \vec{E}_b + \frac{\vec{v}_a(t)}{\tau_D}. \quad (6.5)$$

In layer a , the driving layer, we pass a current, which, as discussed in Sec. 5.1.1, leads to a velocity distribution for layer a due to Eq. (5.4). Hence we end up with an equation connecting the electrical field in layer b with the current in layer a :

$$\vec{j}_a = -\frac{nq^2\tau_D}{m} \vec{E}_b. \quad (6.6)$$

What we see in this simplified picture is that the drag is fully determined by the phenomenologically introduced inter-layer scattering rate τ_D . We will show later (see Chap. 7) how such a rate appears from microscopic considerations, but for now we will continue to discuss the Coulomb interaction in two-dimensional electron gases.

6.2 Coulomb Drag in 2DEG

Although from a theoretical point of view Coulomb drag is a rather simple gedanken experiment, the proper experimental realization is far from trivial. The first setting that has been realized was able to see a current to current coupling between a two-dimensional and a three dimensional system [92]. Only a few years later a coupling of two-dimensional systems was achieved [93] for which semiconductor based GaAs heterostructures were used to prepare the experimental setup.

Coulomb drag itself is quite an interesting experiment, since it allows to measure the strength of the Coulomb interaction in a given system, which can become quite crucial in a lot of low dimensional systems (see Sec. 2.2). Of course this is only true if a similar coupling is not created due an effective interaction between the layers caused by phonons [94]. Further some phenomena may alter the Coulomb interaction's influence on the Coulomb drag, such as interlayer condensates [95], or correlated disorder configurations [96].

For Coulomb drag to appear the interlayer scattering rate τ_D^{-1} is crucial. Within the Fermi liquid theory such a scattering rate should have a temperature dependence of T^2 due to the phase space of the electrons. The theories describing Coulomb drag of 2DEGs have become more complicated, e.g. including disorder corrections as well (see Ref. [89, 90]), so that Coulomb drag has become a well-established effect not only in the experimental but also in the theory community. Still, the calculations that have been done for 2DEGs rely on the assumption of a Fermi liquid. As we have seen in Chap. 4 this might not be an appropriate assumption for graphene-based Coulomb drag.

6.2.1 Coulomb Drag in Graphene in Contrast to Coulomb Drag in 2DEG

From an experimental point of view a big advantage of measuring Coulomb drag in graphene is the easily controllable charge carrier concentration that can be tuned from positive charge carriers to negative ones [97, 98]. Further, due to graphene's thickness of only a single atom, it is possible to reach very short distances between the two-layers which allows to explore regimes that could not have been studied before ($dT \ll 1$). So already from an experimental point of view it seems promising to investigate Coulomb drag in graphene.

As we have discussed in Sec. 2.1.4 graphene is quite different when compared to 2DEGs and furthermore we have shown in Chap. 4 that the Coulomb interaction has a quite important effect on graphene. In the previous chapter we have seen in Sec. 5.1.2 that in graphene even the Coulomb interaction can relax a current, creating additional meanderings to the situation of a 2DEG. Nevertheless, if we push the chemical potential high enough, we have seen that it acquires the characteristics of a traditional 2DEG.

We therefore expect Coulomb drag in graphene extends the richness of the Coulomb drag features known in 2DEGs.

6.3 Coulomb Drag in Graphene: a Brief History

Since graphene has been discovered [1, 99] there have been an overwhelming number of publications related to graphene. In this flourishing field many ideas have already been covered, including Coulomb drag [77, 78, 100–104]. But except for one of those works [103], only the rather conventional limit of high doping $\mu \gg T$ has been considered, where graphene starts to obey Fermi liquid behavior. So only the authors of Ref. [103] took interest in the chance, graphene offers to explore also the regime of low doping. Furthermore, all the previous authors have treated Coulomb interaction as a weak perturbation on top of a sufficiently dirty system $\alpha_g^2 T \tau_{\text{dis}} \ll 1$. In many cases this might be the appropriate way to describe the experiments but graphene on boron nitrid offers the chance to explore the ballistic transport regime and beyond as well (see Ref. [10]). This means that within the previous studies in the field of Coulomb drag in graphene there has been a blind spot on the map when it comes to ballistic and hydrodynamic drag in graphene.

The purpose of the next Chap. 7 will be to investigate this blind spot and to, as far as possible, draw the connections to the previous works. Additionally we will in Chap. 8 consider Hall drag, Magnetodrag and further extensions to the Coulomb drag. Before doing so we will summarize some of the previous results and their technique.

6.4 The Perturbative Approach

One of the most complete previous approaches has been published in Ref. [103]. Hence we will take a closer look at their work.

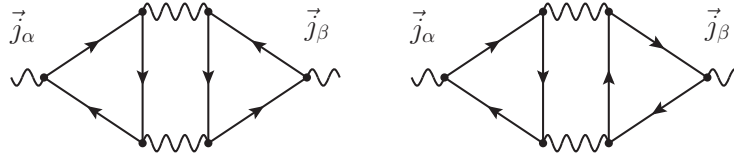


Figure 6.2: *The leading order diagrams causing the Coulomb drag. (Aslamazov Larkin)*

The authors of Ref. [103] have used a perturbative approach. To do so they calculate the conductivity diagrams shown in Fig. 6.2.

The conductivity and the resistivity are related by:

$$\hat{\rho} = \begin{pmatrix} \sigma_{11} & \sigma_{\text{D}} \\ \sigma_{\text{D}} & \sigma_{22} \end{pmatrix}^{-1} = \frac{1}{\sigma_{11}\sigma_{22} - \sigma_{\text{D}}^2} \begin{pmatrix} \sigma_{22} & -\sigma_{\text{D}} \\ -\sigma_{\text{D}} & \sigma_{11} \end{pmatrix}. \quad (6.7)$$

The authors of Ref. [103] assumed further that σ_{ii} is given by Drude conductivity and that the transconductivity σ_{D} is a small parameter, in particular that it is smaller than the Drude conductivity ($\sigma_{\text{D}} \ll \sigma_{ii}$). The drag resistivity in their case is therefore given by:

$$\rho_{\text{D}} \approx \frac{\sigma_{\text{D}}}{\sigma_{11}\sigma_{22}}, \quad (6.8)$$

by omitting the sign due to the definition of the drag resistivity. The drag diagrams (see Fig. 6.2) can now be treated similarly to the perturbative calculation done in Sec. 5.4, except that one needs to do

the calculations away from the Dirac point since at the charge neutral point the diagrams yield zero drag (see the discussion in Secs. 5.4.1 and 8.3.2). Following their calculation the drag conductivity is given by:

$$\sigma_D = \frac{1}{16\pi T} \sum_{\vec{q}} \int \frac{d\omega}{\sinh^2 \frac{\omega}{2T}} \Gamma_a(\omega, \vec{q}) \Gamma_b(\omega, \vec{q}) |\mathcal{D}_{ab}|^2, \quad (6.9)$$

with the inter-layer interaction \mathcal{D}_{ab} and $\Gamma(\omega, \vec{q})$ being the nonlinear susceptibility. The nonlinear susceptibility is an object we will discover later as well but using a completely different path to obtain it (see App. C.2). The interaction between the layers, when including screening via RPA, is given by:

$$\mathcal{D}^{RPA} = \frac{D_0}{(1+D_0 N_a \Pi_a)(1+D_0 N_b \Pi_b) - e^{-2qd} D_0^2 N_a N_b \Pi_a \Pi_b} \begin{pmatrix} 1+D_0 N_b \Pi_b (1-e^{-2qd}) & e^{-qd} \\ e^{-qd} & 1+D_0 N_a \Pi_a (1-e^{-2qd}) \end{pmatrix}, \quad (6.10)$$

where Π_α is the polarization operator of layer α . The results that have been found by the authors of Ref. [103] are summarized in the Tabs. 6.1 and 6.2.

Parameter region	Drag coefficient
$\mu \ll T$	$\rho_D \sim \mu^2 T^{-2}$
$T \ll \mu \ll \frac{v_F}{d}$	$\rho_D \sim \rho_D \sim \mu^{-2} T^2$
$\frac{v_F}{d} \ll \mu$	$\rho_D \sim \mu^{-6} d^{-4} T^2$

Table 6.1: *The asymptotic expressions for the drag coefficient as obtained by the authors of Ref. [103] in the limit of equal layers and varying the chemical potential throughout different regimes.*

Parameter region	Drag coefficient
$\mu_1, \mu_2 \ll T$	$\rho_D \approx 1.41 \alpha_g^2 \frac{\hbar}{e^2} \frac{\mu_1 \mu_2}{T^2}$
$\mu_1 \ll T \ll \mu_2$	$\rho_D \approx 5.8 \alpha_g^2 \frac{\hbar}{e^2} \frac{\mu_1}{\mu_2}$
$T \ll \mu_1 < \mu_2$	$\rho_D \approx \frac{8\pi^2}{3} \alpha_g^2 \frac{\hbar}{e^2} \frac{T^2}{\mu_1 \mu_2} \ln \frac{\mu_1}{T}$

Table 6.2: *The asymptotic expressions for the drag coefficient as obtained by the authors of Ref. [103] in the limit of weak interlayer interaction and small interlayer spacing.*

Already in the variations of the results and the different parameter regimes it becomes clear that the Coulomb drag in graphene is a rich quantity exhibiting unusual behavior when compared to the Coulomb drag of Fermi liquid systems like 2DEGs. Even so, the calculations done by the authors of Ref. [103] rely on the possibility, that sufficient dirty samples of graphene offer to treat the Coulomb interaction perturbatively. In the next Chap. 7 we will develop a way to access the regime of ultra clean graphene and to investigate the parameter regimes that arise there. It is crucial to notice, that ultra clean in the context of Coulomb drag setups is not at all academic but experimentally real (see Sec. 7.2.3).

7

Chapter 7

Coulomb Drag in Graphene: The Kinetic Equation Approach

The design of this Memoir is to deduce strictly from a few principles, obtained chiefly by experiment, the rationale of those electrical phenomena which are produced by the mutual contact of two or more bodies, and which have been termed galvanic; its aim is attained if by means of it the variety of facts be presented as unity to the mind.

Georg Simon Ohm, The Galvanic Circuit Investigated Mathematically

In this chapter we will apply the single layer kinetic equation approach introduced in Sec. 5.2 to gain a better comprehension of Coulomb drag in graphene. We will focus on the clean limit, in which the Coulomb interaction is the dominant contribution for the inter-layer scattering rate. We will start with the kinetic equation for two-layers and build up the machinery to treat Coulomb drag [105]. We will then proceed to extend the machinery towards multilayer drag and Hall drag. Finally we are going to expand the ideas to incorporate a hydrodynamic description and higher-order corrections to drag.

For simplicity we will, whenever we are dealing with exactly two-layers, use the convention $-a$ to indicate the corresponding other layer, in the sense that $-a = b$ and vice versa.

7.1 The Two Layer Kinetic Equation

For clarity we will not begin with the most general case and calculate all the relevant quantities at once. Instead we start with the most simple case and go through the calculation explicitly to gain the greatest possible insight into the technique before extending it towards multiple layers and magnetic fields.

7.1.1 Formulation of the Two Layer Kinetic Equation

In the previous Chap. 6 we have considered a simple Drude picture based description of Coulomb drag. In analogy to Eq. (6.3) we write the kinetic equation, we introduced in Sec. 2.5, for the static homogeneous case with an external force and a small amount of disorder scattering within the relaxation time ansatz introduced in Sec. 5.1.1. Graphene's intrinsic back scattering suppression, changes the impurity scattering rate of isotropic scatterers as shown by the authors of Ref. [106] (the difference is a factor of 2). But considering the relaxation time as the effective transport related relaxation we

arrive at:

$$\begin{aligned}
e\vec{E}^a \frac{\partial \epsilon(\vec{p})}{\partial \vec{p}} \frac{\partial}{\partial \epsilon} n^a(\epsilon, \vec{p}) &= -\frac{n^a(\epsilon, \vec{p}) - \langle n^a(\epsilon, \vec{p}) \rangle_\varphi}{\tau_{\text{dis}}^a} - N_a I_{\text{coll}}^{aa}[n^a] - N_b I_{\text{coll}}^{ab}[n^a, n^b] \\
e\vec{E}^b \frac{\partial \epsilon(\vec{p})}{\partial \vec{p}} \frac{\partial}{\partial \epsilon} n^b(\epsilon, \vec{p}) &= -\frac{n^b(\epsilon, \vec{p}) - \langle n^b(\epsilon, \vec{p}) \rangle_\varphi}{\tau_{\text{dis}}^b} - N_a I_{\text{coll}}^{ba}[n^a, n^b] - N_b I_{\text{coll}}^{bb}[n^b].
\end{aligned} \tag{7.1}$$

Here each layer has its distribution function $n^\alpha(t, \epsilon, \vec{p})$ and its external fields \vec{E}^α . The collisions between the particles take place within the same layer, referred to as intra layer scattering, and between different layers, denoted inter-layer processes. The collision kernel involving intra-layer and inter-layer processes is given by:

$$\begin{aligned}
I_{\text{coll}}^{\alpha\beta}[n^\alpha, n^\beta] &= \frac{1}{\nu(\epsilon_1)} \int d\{x_i\}_{i \in \{2, 1', 2'\}} K^{\alpha\beta}(\{x_i\}) \times \\
&\times \left\{ n^\alpha(x_1)[1 - n^\alpha(x_2)]n^\beta(x_{1'})[1 - n^\beta(x_{2'})] - [1 - n^\alpha(x_1)]n^\alpha(x_2)[1 - n^\beta(x_{1'})]n^\beta(x_{2'}) \right\},
\end{aligned} \tag{7.2}$$

using the notation of ϵ and \vec{v} introduced in Sec. 5.2 (see Eq. (5.11)) for brevity. The integral kernel for the collision integral reads similar to Eq. (5.13):

$$\begin{aligned}
K^{\alpha\beta}(\{x_i\}) &= 2\pi\delta(\epsilon_1 - \epsilon_2 + \epsilon_{1'} - \epsilon_{2'}) (2\pi)^2 \delta(\epsilon_1 \vec{v}_1 - \epsilon_2 \vec{v}_2 + \epsilon_{1'} \vec{v}_{1'} - \epsilon_{2'} \vec{v}_{2'}) \times \\
&\times |\langle x_1, x_2 | U^{\alpha\beta} | x_{1'}, x_{2'} \rangle|^2 \nu(\epsilon_1) \nu(\epsilon_2) \nu(\epsilon_{1'}) \nu(\epsilon_{2'}).
\end{aligned} \tag{7.3}$$

The matrix element is, analogous to Eq. (5.14), given by:

$$|\langle x_1, x_2 | U^{\alpha\beta} | x_{1'}, x_{2'} \rangle|^2 = |D^{\alpha\beta}(q)|^2 \theta_{1,2} \theta_{1',2'}. \tag{7.4}$$

The RPA screened interaction propagator for two-layers has been derived previously and is given by Eq. (6.10). Except for the discussions on the regularization of divergent integrals (see App. C.2.2) and the asymptotics of integrals (see App. C.3.2) we will consider the interaction to be in its bare form, reading:

$$D_{\text{bare}}^{\alpha\beta}(q, d) = D_0(q) e^{-qd\delta_{\alpha,-\beta}} = \frac{2\pi\alpha_g}{q} e^{-qd\delta_{\alpha,-\beta}}, \tag{7.5}$$

Since Coulomb drag is, as is the conductivity, a linear response function, we will linearize the kinetic equation according to

$$n^\alpha(x) = n_F^\alpha(\epsilon) - T \frac{\partial n_F^\alpha(\epsilon)}{\partial \epsilon} h^a(x). \tag{7.6}$$

The linearized collision kernel reads:

$$\delta I_{\text{coll}}^{\alpha\beta} = \frac{1}{\nu(\epsilon_1)} \int d\{x_i\}_{i \in \{2, 1', 2'\}} W^{\alpha\beta}(\{x_i\}) \left\{ h^\alpha(x_1) - h^\alpha(x_2) + h^\beta(x_{1'}) - h^\beta(x_{2'}) \right\} \quad \text{with} \tag{7.7}$$

$$\begin{aligned}
W^{\alpha\beta}(\{x_i\}) &= 2\pi\delta(\epsilon_1 - \epsilon_2 + \epsilon_{1'} - \epsilon_{2'}) (2\pi)^2 \delta(\epsilon_1 \vec{v}_1 - \epsilon_2 \vec{v}_2 + \epsilon_{1'} \vec{v}_{1'} - \epsilon_{2'} \vec{v}_{2'}) \times \\
&\times \frac{|\langle x_1, x_2 | U^{\alpha\beta} | x_{1'}, x_{2'} \rangle|^2 \nu(\epsilon_1) \nu(\epsilon_2) \nu(\epsilon_{1'}) \nu(\epsilon_{2'})}{16 \cosh\left(\frac{\epsilon_1 - \mu_\alpha}{2T}\right) \cosh\left(\frac{\epsilon_2 - \mu_\alpha}{2T}\right) \cosh\left(\frac{\epsilon_{1'} - \mu_\beta}{2T}\right) \cosh\left(\frac{\epsilon_{2'} - \mu_\beta}{2T}\right)},
\end{aligned} \tag{7.8}$$

which forms the linearized kinetic equation in analogy to 5.2:

$$e\vec{E}^\alpha\vec{v}\frac{\partial n_F^\alpha(\epsilon)}{\partial\epsilon} = T\frac{\partial n_F^\alpha(\epsilon)}{\partial\epsilon}\frac{h^\alpha(x) - \langle h^\alpha(x) \rangle_\varphi}{\tau_{\text{dis}}^\alpha} - \sum_\beta N_\beta\delta I_{\text{coll}}^{\alpha\beta}. \quad (7.9)$$

When one compares the linearized collision kernel from Eq. (7.8) with the one from Eq. (7.7) one will notice that in comparison to the symmetries discussed in Sec. 5.2.2 the collision kernel in presence of the additional layer index only obeys the hermiticity relation. The simultaneous exchange of 1 with 1' and 2 with 2' corresponds to an interchanging of the layers. This is an useful observation we will make use of later.

We have now the kinetic equation we will deal with to determine the Coulomb drag. Using the functional approach introduced in Sec. 5.2.2 we can rewrite the kinetic equation into a functional of the form:

$$\begin{aligned} F(h_a, h_b) &= N_a \int dx \nu(\epsilon) \frac{\partial n_F^a(\epsilon)}{\partial\epsilon} h^a(x) \left[e \frac{\vec{E}^a \vec{v}}{T^2} - \frac{h^a(x)}{2T\tau_{\text{dis}}^a} \right] + N_b \int dx \nu(\epsilon) \frac{\partial n_F^b(\epsilon)}{\partial\epsilon} h^b(x) \left[e \frac{\vec{E}^b \vec{v}}{T^2} - \frac{h^b(x)}{2T\tau_{\text{dis}}^b} \right] \\ &+ \frac{N_a^2}{8T^2} \int d\{x_i\} W^{a,a}(\{x_i\}) \left[h^a(x_1) - h^a(x_2) + h^a(x_3) - h^a(x_4) \right]^2 \\ &+ \frac{N_b^2}{8T^2} \int d\{x_i\} W^{b,b}(\{x_i\}) \left[h^b(x_1) - h^b(x_2) + h^b(x_3) - h^b(x_4) \right]^2 \\ &+ \frac{N_a N_b}{4T^2} \int d\{x_i\} W^{a,b}(\{x_i\}) \left[h^a(x_1) - h^a(x_2) + h^b(x_3) - h^b(x_4) \right]^2. \end{aligned} \quad (7.10)$$

7.1.2 The Ansatz for the Two Layer System

In Sec. 5.2 we have discussed the analytic structure of the kernel and as a consequence what kind of appropriate ansatz could solve the equation. The changes within the integral kernel do not affect the conclusion we have drawn in Sec. 5.2. We therefore need to use the very same ansatz to continue. Still, we would like to emphasize that there is a different possible point of view regarding the ansatz given by Eq. (5.23). To gain a better understanding of the phenomena related to the ansatz (5.23), which has been used for the integral kernel chosen in Sec. 5.2, we will try to argue more physically about the system's behavior.

Let us regard this from a different perspective by thinking about the changes that can appear in our system by switching on a weak homogeneous external electrical field. We first recall very briefly how one would think about this situation in an usual Fermi liquid. An attempt there would be to assume that an external field accelerates the total momentum of the Fermi ball. Taking into account a relaxation mechanism this means that there is a relaxation rate such that in the stationary case the overall shift of the Fermi ball is given by $\vec{p} \rightarrow \vec{p} + e\vec{E}\tau$. If the shift is small enough this changes the equilibrium distribution only by a little so that we can describe the situation by changing the distribution using the simple transformation $n_F(\epsilon) \rightarrow n_F(\epsilon + e\vec{v}\vec{E}\tau)$.

For graphene it is still a reasonable assumption that an external electrical field will create a direction dependent shift of the chemical potential $\mu_\alpha(\vec{v}) = \mu_\alpha + \delta\mu_\alpha(\vec{v})$ similar to Fermi liquid case. Additionally we have seen in the discussion of the kinetic equation for a single layer in Sec. 5.2.2 that the Coulomb interaction leads to the specific choice of two relevant modes that do not relax quickly. This means that maybe not only the chemical potential, respectively the particle relaxation, can depend on the direction but also the temperature, corresponding to energy relaxation, can depend on direction, $T \rightarrow T + \delta T(\vec{v})$,

which constitutes the argument given in Ref. [73]. For small deviations from equilibrium we will formulate these ideas as:

$$n^\alpha(x) \approx n_F^\alpha(\epsilon) - \frac{\partial n_F^\alpha(\epsilon)}{\partial \epsilon} \left(\delta\mu_\alpha(\vec{v}) + \frac{\epsilon - \mu_\alpha}{T} \delta T_\alpha(\vec{v}) \right). \quad (7.11)$$

Since we are only interested in the linear response to the external field the structure of the scalar functions $\delta T(\vec{v})$ and $\delta\mu(\vec{x})$ is fixed to be proportional to $\vec{v}\vec{E}$ (they need to vanish in the absence of the external field). Our ansatz for the two-layer system in the presence of two electrical fields yields

$$h^\alpha(x_i) = \sum_\gamma \left(\chi_v^{\alpha,\gamma} + \chi_p^{\alpha,\gamma} \frac{\epsilon_i}{T} \right) e \frac{\vec{E}_\gamma \vec{v}_i}{T^2}, \quad (7.12)$$

where $\chi_v^{\alpha,\gamma}$ and $\chi_p^{\alpha,\gamma}$ are constants. If one compares the two modes entering this ansatz with the previous discussion in Sec. 5.1.1 one recognizes that the part coming with $\chi_p^{\alpha,\gamma}$ has the form of the momentum conserving zero mode and the one coming with $\chi_v^{\alpha,\gamma}$ corresponds to the velocity mode. In this notation one can see that δT leads to contributions to $\chi_p^{\alpha,\gamma}$ and $\chi_v^{\alpha,\gamma}$ indicating that temperature variations belong to both classes of variations. The Mode that does not at all relax due to Coulomb interaction (the momentum conserving mode) and the one that does slowly relax like variations of the chemical potential do (the velocity mode). In this sense the ansatz (7.12) provides us with a useful interpretation of the physics that governs transport in graphene.

This ansatz is a direct consequence of the forward scattering resonance first introduced in Sec. 2.1.4 and 3.1.2. We have recognized already earlier (see Sec. 4.2) that this resonance created traces of the physics related to Luttinger liquids which is based on a dimensionally enforced forward scattering resonance. Already in Sec. 2.1.4 we have interpreted this as a direct consequence of the relativistic spectrum, which not only distinguishes between velocity and momentum but also keeps the absolute value of the velocity constant. In this view it is not very surprising that the proper ansatz for this system is not given by a local equilibrium approximation as it is done in most text books for usual Fermi-liquids (like [52]) but by a direction dependent equilibrium as sketched in Fig. 7.1.

Extensibility of Applicability

In Sec. 5.1.1 we have argued that the selected ansatz is a proper description of the system as long as Ω (now τ_{dis}^{-1} , which appears equivalently) is much smaller than $\alpha_g^2 T$, which is the very same for the two-layer system. However, there is a very curious point to make: the opposite case of negligible Coulomb interaction compared to τ_{dis}^{-1} specifically $\tau_{\text{dis}}^{-1} \gg \alpha_g T$ is given by a kinetic equation of the form of a relaxation time approach as seen in Eq. (5.7). This implies that the most relevant mode for the opposite situation has been taken into account already namely the velocity mode (applying above ansatz one obtains $\chi_v^\alpha = T\tau_{\text{dis}}^\alpha$ at the Dirac point). So as a conclusion it turns out that within the chosen ansatz we should be able to describe the Coulomb dominated regime as well as the disorder dominated regime (in the relaxation time approximation). A more detailed discussion on the applicability will be provided in Sec. 7.2.2, when we have a more thorough view on the problem.

7.1.3 The Effective Kinetic Equations and Thermalization

Since the equations we are dealing with are linear, we can treat the two cases $\vec{E}^a \neq 0$ but $\vec{E}^b = 0$ and $\vec{E}^a = 0$ but $\vec{E}^b \neq 0$ separately, while still gaining the full solution. Applying the ansatz with

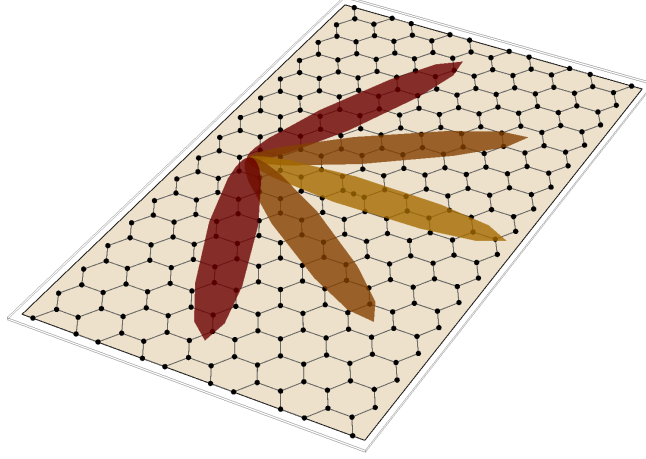


Figure 7.1: A sketch of the direction dependent equilibrium in graphene. The temperature of the particle changes as it changes the direction it looks in (illustrated by the hot color yellow and cooler color red). The kinetic equation involving the direction dependent thermalization approach describes scattering between different equilibria (directions).

the functional we gain the effective kinetic equation for our system (see Sec. 5.2.2 for details on this calculation). One ends up with a functional $F(\chi_v^a, \chi_v^b, \chi_p^a, \chi_p^b)$ as given in Eq. (C.4) (see App. C.1), from which we obtain the effective kinetic equation. Using the following short forms

$$\begin{aligned}
 I_{\text{Intra}}^\alpha &= \frac{1}{4T^3} \int d\{x_i\} W^{\alpha,\alpha}(\{x_i\}) (\vec{v}_1 - \vec{v}_2 + \vec{v}_3 - \vec{v}_4)^2, & I_{\text{Inter}}^{\alpha\beta} \stackrel{\alpha \neq \beta}{=} \frac{1}{2T^3} \int d\{x_i\} W^{\alpha,\beta}(\{x_i\}) (\vec{v}_1 - \vec{v}_2)^2, \\
 I_{\text{D}} &= -\frac{1}{2T^3} \int d\{x_i\} W^{a,b}(\{x_i\}) (\vec{v}_1 - \vec{v}_2) (\vec{v}_3 - \vec{v}_4), & I_{\text{Th}}^{\alpha\beta} \stackrel{\alpha \neq \beta}{=} \frac{1}{2T^4} \int d\{x_i\} W^{\alpha,\beta}(\{x_i\}) (\vec{v}_1 - \vec{v}_2) \vec{q}, \\
 I_{\text{Tr}}^\alpha &= I_{\text{Intra}}^\alpha + \sum_{\beta \neq \alpha} \frac{N_\beta}{N_a} I_{\text{Inter}}^{a,\beta}, & I_{\text{E}} &= \frac{1}{2T^5} \int d\{x_i\} W^{ab}(\{x_i\}) \vec{q}^2 \quad \text{and} \quad A_n^a = - \int dx \frac{\nu(\epsilon)}{T} \frac{\partial n_F^\alpha(\epsilon)}{\partial \epsilon} \left(\frac{\epsilon}{T} \right)^n,
 \end{aligned} \tag{7.13}$$

for integrals that naturally appear while finding the new saddle point, this allows us to write the kinetic equation as done in Eq. (C.5).

When one glances at the short forms given in Eq. (7.13) one may recognize a peculiarity of the energy relaxation related integral I_{E} . As explained in Sec. 5.2.2 all modes are quickly relaxed except for the zero mode and the velocity mode. That is the reason for the appearance of the $\vec{v}_i - \vec{v}_j$ -terms in all the integrals except for one. Within App. C.2.2 we explain in more detail that this causes a divergence, formally sending I_{E} to infinity if no regularization via RPA or a logarithmically curved spectrum is taken into account. But even within RPA or the logarithmically curved spectrum the energy relaxation rate is parametrically enhanced as is explained in Chap. 4. In App. C.3 we estimate the energy relaxation rate for each regime assuming that the energy relaxation is larger than the thermal rates I_{Th}^α .

By rotating within the two-dimensional subspace of χ_p^a and χ_p^b one manages to reach one equation where only in the diagonal element the energy relaxation rate appears. We arrive at $(z_\alpha T \tau_{\text{dis}}^\alpha = 1,$

$N_a = N_b = 1$ for simplicity):

$$\begin{pmatrix} A_0^a \\ 0 \\ A_1^a \\ A_1^a \end{pmatrix} = \begin{pmatrix} I_{\text{Tr}}^a + z_a A_0^a & -I_{\text{D}} & z_a A_1^a & I_{\text{Th}}^a + z_a A_1^a \\ -I_{\text{D}} & I_{\text{Tr}}^b + z_b A_0^b & z_b A_1^b & -2I_{\text{Th}}^b - z_b A_1^b \\ z_a A_1^a & z_b A_1^b & z_a A_2^a + z_b A_2^b & z_a A_2^a - z_b A_2^b \\ 2I_{\text{Th}}^a + z_a A_1^a & -2I_{\text{Th}}^b - z_b A_1^b & z_a A_2^a - z_b A_2^b & 4I_{\text{E}} + z_a A_2^a + z_b A_2^b \end{pmatrix} \begin{pmatrix} \chi_\mu^a \\ \chi_\mu^b \\ \chi_T^s \\ \chi_T^d \end{pmatrix}. \quad (7.14)$$

Since this means, that the mode corresponding to I_{E} becomes irrelevant as long as the off diagonal elements within the same row or column stay much smaller (for example in the clean limit), we can reduce the number of modes to deal with down to three modes only. Formally this parametrically enhanced energy relaxation leads to inter-layer thermalization enforcing $\chi_p^a = \chi_p^b$. Introducing $\chi_p = \chi_p^a = \chi_p^b$ we are able to simplify Eq. (7.14) even more ($z_\alpha T \tau_{\text{dis}}^\alpha = 1$):

$$\vec{c} = \begin{pmatrix} A_0^a & 0 \\ 0 & A_0^b \\ N_a A_1^a & N_b A_1^b \end{pmatrix} = \begin{pmatrix} N_a I_{\text{Tr}}^a + A_0^a z_a & -N_b I_{\text{D}} & A_1^a z_a \\ -N_a I_{\text{D}} & N_b I_{\text{Tr}}^b + A_0^b z_b & A_1^b z_b \\ N_a A_1^a z_a & N_b A_1^b z_b & N_a A_2^a z_a + N_b A_2^b z_b \end{pmatrix} \begin{pmatrix} \chi_v^{a,\text{I}} & \chi_v^{a,\text{II}} \\ \chi_v^{b,\text{I}} & \chi_v^{b,\text{II}} \\ \chi_p^{\text{I}} & \chi_p^{\text{II}} \end{pmatrix} = M \vec{\chi}. \quad (7.15)$$

The distinction I and II is introduced to allow more compact notation and refers to the two situations of only an electric field in layer a or in layer b , respectively.

7.2 The Coulomb Drag Resistivity in Graphene

With Eq. (7.15) we now have the possibility to solve the kinetic equation and hence to calculate the conductivity in close analogy to Eq. (5.29), where the current is given by:

$$\vec{j}_\alpha = e N_\alpha \int \frac{d^2 p}{(2\pi)^2} \vec{v} n_F^\alpha(x) = \frac{e^2}{2} N_\alpha \sum_{\gamma \in \{\text{I,II}\}} \left(A_0^\alpha \chi_v^{\alpha,\gamma} + A_1^\alpha \chi_p^\gamma \right) \vec{E}^\gamma, \quad (7.16)$$

and the definition of a vector (generalized vector involving both cases I and II)

$$\vec{d}^T = \begin{pmatrix} N_a A_0^a & 0 & N_a A_1^a \\ 0 & N_b A_0^b & N_b A_1^b \end{pmatrix} \quad (7.17)$$

enables us to write the conductivity of the two-layer system as:

$$\hat{\sigma} = \frac{e^2}{2} \vec{d}^T \vec{\chi} = \frac{e^2}{2} \vec{d}^T M^{-1} \vec{c}. \quad (7.18)$$

To convince oneself of the proper symmetry $\hat{\sigma}$ needs to obey, one can consider a rescaling of the form $N_\alpha \chi_v^\alpha \rightarrow \tilde{\chi}_v^\alpha$ which makes \tilde{M} explicitly symmetric and transforms \vec{c} such that it equals the definition of \vec{d} .

A proper evaluation of the conductivity can be found in App. C.1.2. The inverse of this tensor is the resistivity tensor defined in Eq. (6.2). Inverting $\hat{\sigma}$ one will observe reoccurring patterns motivating the following choice of short forms that significantly enhance the readability (see Eq. (C.10)):

$$A_0^\alpha = B_0^\alpha, \quad B_1^\alpha = N_\alpha \frac{A_1^\alpha}{A_0^\alpha}, \quad B_2^\alpha = N_\alpha A_2^\alpha - A_1^\alpha B_1^\alpha \quad \text{and} \quad (7.19)$$

$$(T\tau_0)^{-1} = \frac{1}{B_2^a + B_2^b} \left[(B_1^a)^2 I_{\text{Tr}}^a + (B_1^b)^2 I_{\text{Tr}}^b - 2B_1^a B_1^b I_D \right] = \frac{B_1^a I_G^a + B_1^b I_G^b}{B_2^a + B_2^b}. \quad (7.20)$$

The last equation appears to be a combination of interaction induced scattering rates that form together an effective rate measuring the relevance of Coulomb interaction in the system. Furthermore a generalized scattering rate of the form:

$$I_G^\alpha = B_1^\alpha I_{\text{Tr}}^\alpha - B_1^{-\alpha} I_D, \quad (7.21)$$

as well as an effective averaged scattering rate defined as

$$\frac{B_2^a + B_2^b}{T\tau_{\text{ad}}} = \frac{B_2^a}{T\tau_{\text{dis}}^a} + \frac{B_2^b}{T\tau_{\text{dis}}^b} \quad (7.22)$$

will turn out to be quite useful in determining a closed form of the drag resistivity:

$$\rho_D = \frac{2}{e^2} \frac{I_D}{B_0^a B_0^b} \left[1 + \frac{I_G^a I_G^b}{I_D (B_2^a + B_2^b) [(T\tau_0)^{-1} + (T\tau_{\text{ad}})^{-1}]} \right], \quad (7.23)$$

$$\rho_{\alpha\alpha} = \frac{2}{e^2} \frac{1}{N_\alpha B_0^\alpha} \left[\frac{1}{T\tau_{\text{dis}}^\alpha} + \frac{N_\alpha I_{\text{Tr}}^\alpha}{B_0^\alpha} - \frac{N_\alpha (I_G^\alpha)^2}{B_0^\alpha (B_2^a + B_2^b) [(T\tau_0)^{-1} + (T\tau_{\text{ad}})^{-1}]} \right]. \quad (7.24)$$

It is worth to notice, that the effective Coulomb interaction rate Eq. (7.20) appears as a competing rate to the averaged disorder scattering rate Eq. (7.22), a fact, which supports the relevance of these rates for the purpose of understanding the physics governing the Coulomb drag.

The B_n^α s we have introduced obey an interesting relation that may help to make their appearance more transparent. Interpreting the definitions of the A_n^α s in Eq. (7.13) in a slightly different way we can use:

$$Z_\alpha = -\frac{1}{T} \int d\epsilon \nu(\epsilon) \frac{\partial n_F}{\partial \epsilon}, \quad \langle f(\epsilon) \rangle_\alpha = -\frac{1}{TZ_\alpha} \int d\epsilon \nu(\epsilon) \frac{\partial n_F}{\partial \epsilon} f(\epsilon), \quad \text{to write} \quad (7.25)$$

$$A_0^\alpha = Z_\alpha, \quad A_n^\alpha = Z_\alpha \left\langle \left(\frac{\epsilon}{T} \right)^n \right\rangle_\alpha. \quad (7.26)$$

In this language the introduced short form B_n^α appears to read:

$$B_0^\alpha = Z_\alpha \quad B_1^\alpha = N_\alpha \left\langle \frac{\epsilon}{T} \right\rangle_\alpha \quad B_2^\alpha = N_\alpha Z_\alpha \left\langle \frac{(\Delta\epsilon)^2}{T^2} \right\rangle_\alpha = N_\alpha B_0^\alpha \left\langle \frac{\epsilon^2}{T^2} - \left\langle \frac{\epsilon}{T} \right\rangle_\alpha^2 \right\rangle_\alpha. \quad (7.27)$$

If one compares Z_α with the total particle number one recognizes that there is only the additional derivative acting on the distribution function that differs. Hence Z_α is a dimensionless quantity related to the number of states that can scatter. In these terms the B_n^α s represent moments of the scattering phase-space distribution. This interpretation is related to the measure the functional provides us with, which we have discussed in the end of Sec. 5.2.3.

7.2.1 Asymptotics of the Resistivity and its Numerical Evaluation

We will now investigate the different limits our approach allows for, starting with the known result available by perturbation theory as has been done in Ref. [103] (see Sec. 6.4) and then continue with the lesser known regimes. We hereby use the following convention:

- $T \ll \tau_{\text{dis}}^{-1}$ is the diffusive limit where one needs to incorporate the diffusive modes due to coherent impurity scattering. In this regime the result (7.23) is not applicable.
- $\alpha_g^2 T^2 \ll \tau_{\text{dis}}^{-1} \ll T$ corresponds to the ballistic regime since scattering with impurities causes particles to lose their quantum nature (coherence) but the length scale, in which the interaction is relevant is still much longer than the mean free path of the quasi-particles.
- $\tau_{\text{dis}}^{-1} \ll \alpha_g^2 T^2$ is the ultra-ballistic or hydrodynamic phase, where the interaction between the particles take place on a shorter length scale than the mean free path induced by impurities.

We will explain in Sec. 7.2.2 why we are able to consider not only the hydrodynamic regime, which the formalism was developed for, but also the ballistic regime, where a comparison to former work is possible (see Sec. 6.4).

Ballistic Regime

In Sec. 7.1.2 we have first discussed the applicability of our Coulomb drag result (7.23) and have concluded that we should be able to describe the ballistic regime. In Sec. 7.2.2 a detailed discussion is given. Either way we can always try to do the calculation for the ballistic limit and compare them to previous results. In the ballistic regime $(T\tau_{\text{ad}})^{-1}$ is not only by far bigger than $(T\tau_0)^{-1}$, it also wins out compared to the Coulomb induced scattering rates of the individual layers. Therefore we may rewrite Eq. (7.23): the contribution in the big brackets disappears except for unity. Hence the drag resistivity reads:

$$\rho_{\text{D}} = \frac{2}{e^2} \frac{I_{\text{D}}}{B_0^a B_0^b} \quad (7.28)$$

The determination of I_{D} for different regimes can be found in App. C.3 from Eq. (C.47) (large distance (C.51) and (C.52)) we can reach the $\mu \ll T$ limit whereas the intermediate scale $T \ll \mu \ll (2d\alpha_g N)^{-1}$ can be found from Eq. (C.63) (large distance (C.65)), and finally the large scale $(2d\alpha_g N)^{-1} \ll \mu$ can be found by Eq. (C.73) (large distance (C.75)). The mixed situation $\mu_a \ll T \ll \mu_b \ll \frac{1}{2dT\alpha_g N}$ follows from Eq. (C.80). This way we obtain Tab. 7.1, which shows perfect agreement with Tab. 6.2. These results again support the statement that the calculation we have done, although focused on the clean case, is applicable to the ballistic regime as well.

To obtain the asymptotics discussed in App. C.3 we used some generalized integrals (I_{GD} and I_{Gtr}) defined in App. C.2. These generalized integrals allow us to consider a numerical treatment as well as the asymptotics discussed in Tab. 7.1. In the case of effectively zero distance $d \cdot T \approx 0$ the drag resistivity is completely determined by μ/T , which allows us to give the full dependency as shown on the left hand side of Fig. 7.2.

Further we can consider a comparison to the asymptotics discussed for the case of the disordered regime. To do so we consider a cross section of the left hand side of Fig. 7.2 in such away that the

Parameter region	Drag resistivity for $dT \ll 1$	Drag resistivity for $dT \gg 1$
$\mu_a, \mu_b \ll T$	$\rho_D \approx 1.41 \alpha_g^2 \frac{\hbar}{e^2} \frac{\mu_a \mu_b}{T^2}$	$\rho_D \sim \alpha_g^2 \frac{\hbar}{e^2} \frac{\mu_a \mu_b}{T^2} (dT)^{-\eta}$
$\mu_a \ll T \ll \mu_b \ll \frac{1}{2dT\alpha_g N}$	$\rho_D \approx 5.8 \alpha_g^2 \frac{\hbar}{e^2} \frac{\mu_a}{\mu_b}$	
$T \ll \mu_a < \mu_b \ll \frac{1}{2dT\alpha_g N}$	$\rho_D \approx \frac{8\pi^2}{3} \alpha_g^2 \frac{\hbar}{e^2} \frac{T^2 \ln \frac{\Lambda_{ab}}{\lambda_{ab}}}{\mu_a \mu_b}$	$\rho_D \approx 4 \alpha_g^2 \frac{\hbar}{e^2} \frac{T}{\mu_a \mu_b d}$
$\frac{1}{2dT\alpha_g N} \ll \mu_a, \mu_b$	$\rho_D \approx \frac{(4\pi)^2 \zeta(3)}{(\alpha_g N_a N_b)^2} \frac{\hbar}{e^2} \frac{T^2}{\mu_a^3 \mu_b^3 d^4}$	$\rho_D \approx \frac{(4\pi)^2}{15(\alpha_g N_a N_b)^2} \frac{\hbar}{e^2} \frac{T}{\mu_a^3 \mu_b^3 d^5}$

Table 7.1: The asymptotic expressions for the drag coefficient obtained in App. C.3. The cutoffs are given by $\Lambda_{\alpha\beta} = \min(|\mu_\alpha|, |\mu_\beta|, 1/(2d\delta_{\alpha,-\beta}))$ and $\lambda_{\alpha\beta} = \max(\alpha_g N_\alpha |\mu_\alpha|, \alpha_g N_\beta |\mu_\beta|, T)$. The coefficient η is one for $\alpha_g N d T \ll 1$ to be one and three for $\alpha_g N d T \gg 1$.

chemical potential of both layers is the same everywhere ($\mu_a = \mu_b$). Such a cross section is shown in the right hand side of Fig. 7.2, supporting the consistency of the asymptotics with the numerics.

Now that we have verified the known results within the kinetic equation approach we can proceed to determine the behavior of the drag resistivity in the clean situation.

The hydrodynamic phase (approaching the clean limit)

The case that the Coulomb interaction governs transport phenomena is a somewhat unknown limit. In graphene, as explained earlier in Sec. 6.2.1, we are fortunately in the position that a system governed by the Coulomb interaction is not only thinkable but it might as well be within range of experimental realization, as explained in Chap. 6. In the pure Coulomb interaction limit we treat the disorder induced rate $(T\tau_{\text{ad}})^{-1}$ as the smallest scale in the system or put it even to zero.

In contrast to the disordered regime it may happen that in the equation for the resistivity Eq. (7.23) the 1 within the big brackets becomes negligible. Such a situation is given if, for example, the relation $I_D \ll I_{\text{tr}}$ for the dimensionless scattering rates holds true. In such a situation the drag rate I_D may disappear completely from our expressions which indicates that our simple Drude picture of drag (see Sec. 6.1.1) is no longer applicable. In such a situation the drag rate resistivity reads:

$$\rho_D = \frac{2}{e^2} \frac{B_1^a B_1^b}{B_0^a B_0^b} \frac{I_{\text{Tr}}^a I_{\text{Tr}}^b}{\left(B_1^a\right)^2 I_{\text{Tr}}^a + \left(B_1^b\right)^2 I_{\text{Tr}}^b + \frac{B_2^a}{T\tau_{\text{dis}}^a} + \frac{B_2^b}{T\tau_{\text{dis}}^b}}. \quad (7.29)$$

The reason for a drag resistivity in such a situation is purely due to the inter-layer thermalization which leads to the three modes approximation (see for comparison Ref. [105]). We then have transfer between the layers only due to the thermalization constraint $\chi_p^a = \chi_p^b$ as introduced in Sec. 7.1.3. Further details on this thermalization are found in Sec. 7.2.2.

For a small chemical potential $\mu \ll T$ we have exactly the situation described above, which leads to

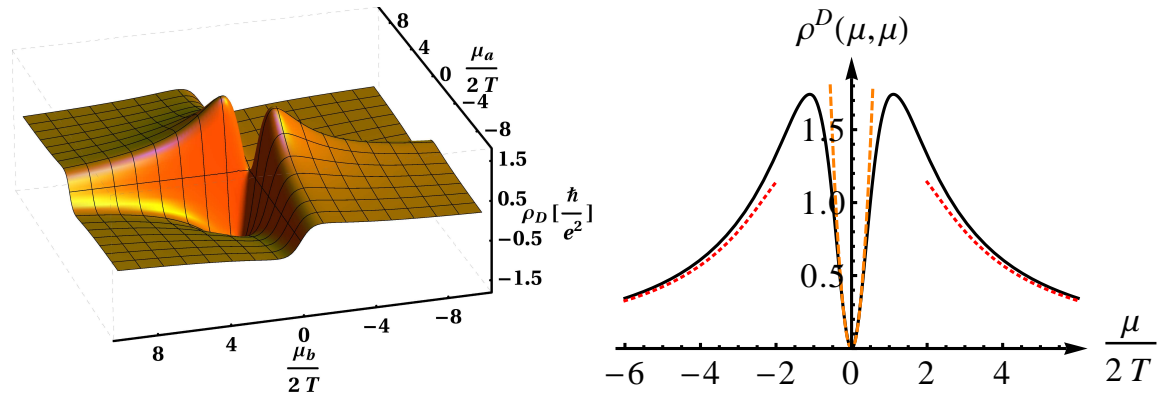


Figure 7.2: *Left:* The drag resistivity in units of $\alpha_g^2 \frac{\hbar}{e^2}$ plotted over $\frac{\mu_\alpha}{2T}$ of the two-layers for disorder scattering rate of order $\tau_{\text{dis}}^{-1} \sim 100\alpha_g^2 T$ and with zero distance ($N = 1$). *Right:* A cross section of the drag resistivity in units of $\alpha_g^2 \frac{\hbar}{e^2}$ plotted over $\frac{\mu_\alpha}{2T}$ of the two equal layers for disorder scattering rate of order $\tau_{\text{dis}}^{-1} \sim 100\alpha_g^2 T$ and with zero distance. In orange dashed lines the asymptotics given in Tab. 7.1 for the case of $\mu_a = \mu_b \ll T$ and in red dotted lines from the same table the regime $T \ll \mu_a = \mu_b \ll \frac{1}{2dT\alpha_g N}$ ($N = 1$).

a drag resistivity given by:

$$\rho_D(\hat{\mu}_a, \hat{\mu}_b) \approx 9.01 \frac{1}{e^2} \alpha_g^2 \frac{\hat{\mu}_a \hat{\mu}_b (N_a + N_b)}{N_a \hat{\mu}_a^2 + N_b \hat{\mu}_b^2 + z} \stackrel{N_a=N_b}{z=0} \approx 18 \frac{1}{e^2} \alpha_g^2 \frac{\mu_a \mu_b}{\mu_a^2 + \mu_b^2}. \quad (7.30)$$

with $z = \frac{9\zeta(3)}{32\pi} \frac{(T\tau_{\text{ad}})^{-1}}{\alpha_g^2 C_{\text{Tr}}}$ (see Eq. (C.49) for details). The remarkable clean limit of this equation unveils, that depending on the way one approaches the Dirac point of both layers, the necessity to vanish at the Dirac point disappears (see discussion in Sec. 8.3). As shown in Eqs. (C.51) and (C.52) this behavior is kept even when considering larger distances $1 \ll dT$ although we have no control of the prefactors. This unintuitive statement will be explained in more detail in Sec. 7.2.2 and is shown in terms of numerical data in Fig. 7.5.

In the intermediate case $T \ll \mu \ll (2d\alpha_g N)^{-1}$ a cancellation between contributions, the intra-layer scattering integrals consist of, happens to appear. This causes the drag rate I_D to be bigger than the interaction induced transport scattering rate I_{tr} . There the clean limit causes no additional contribution since the perturbative obtained drag resistivity stays unchanged.

When we come to the case of a very large chemical potential $(2d\alpha_g N)^{-1} \ll \mu$ we have additional static screening for the interlayer rates in contrast to the previous case, which causes the drag rate to be again much smaller than the intra-layer scattering rates $I_D \ll I_{\text{tr}}$. We also have a cancellation of the drag rate and we obtain the following drag resistivity from Eq. (C.73):

$$\rho_D(\hat{\mu}_a, \hat{\mu}_b) \approx 0.211 \frac{\alpha_g^2 \text{sign}(\mu_a \mu_b) N_a N_b T^2}{e^2} \frac{\ln\left(\frac{|\mu_a|}{2T\lambda_a}\right) \ln\left(\frac{|\mu_b|}{2T\lambda_b}\right)}{(N_a^2 \ln\left(\frac{|\mu_a|}{2T\lambda_a}\right) + N_b^2 \ln\left(\frac{|\mu_b|}{2T\lambda_b}\right))} \quad (7.31)$$

with $\lambda_\alpha = \max(\alpha_g N_\alpha |\mu_\alpha|, \alpha_g N_\beta |\mu_\beta|, T)$ as in App. C.3. For the case of large distances small deviations

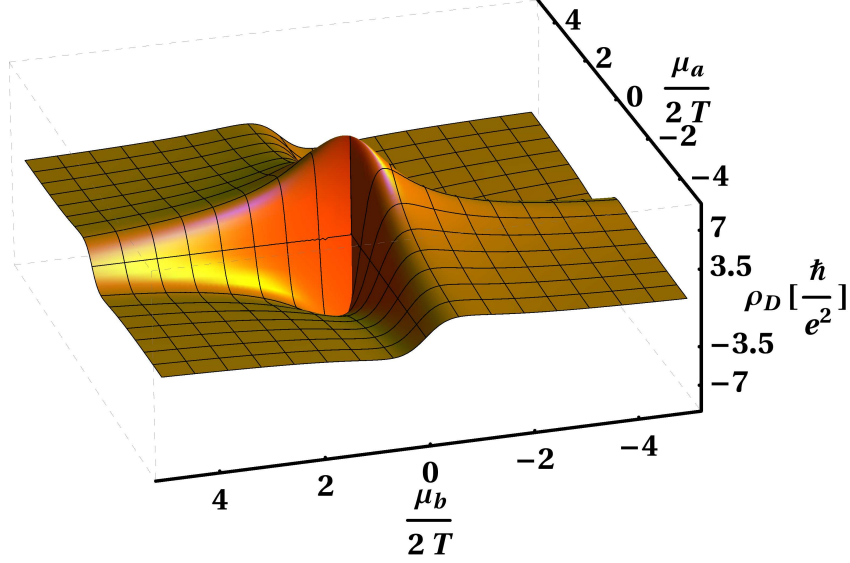


Figure 7.3: The drag resistivity in units of $\alpha_g^2 \frac{\hbar}{e^2}$ plotted over $\frac{\mu_a}{2T}$ of the two-layers for the clean case and with zero distance ($N = 1$). The emphasis is on the non analytic feature at the Dirac point where the exact value is determined by the way one approaches it, see Eq. (7.30) and Fig. 7.4 for further details.

appear due to a slightly changed appearance of the cut-off. The resulting resistivity can be determined from Eq. (C.65). Still one has to be careful, since the three-mode calculation breaks down as soon as the disorder strength becomes big enough to fulfill $\mu^2/\tau_{\text{dis}} \sim I_E$. This does not endanger the clean limit result but tells us that an experimental setting, designed for clean limit measurements in the large μ limit, is harder to achieve than in the small μ limit since disorder is weighted with the chemical potential by the A_1 contributions (see the matrix elements in Eq. (7.14)). Again a more detailed discussion about the validity of the Eq. (7.31) can be found in Sec. 7.2.2

In analogy to the ballistic regime we can use the integrals defined in App. C.2 to obtain numerical values for the generalized integrals at zero distance, which allows us to obtain the full dependency of the drag resistivity for the clean case. This way one obtains Fig. 7.3, in which one can recognize the nontrivial behavior at the Dirac point that is described by Eq. (7.30).

The approximated result is separately shown on the right hand side of Fig. 7.4, illustrating further the non-analytic behavior at the origin by emphasizing two different paths passing through the origin which are parametrized by the corresponding approximation (7.30). The paths are given by:

$$\Gamma_\gamma(t) = (t \sin \gamma, t \cos \gamma, 18 \sin \gamma \cos \gamma). \quad (7.32)$$

One finds on the left hand side of Fig. 7.4 a cross section at small but non-vanishing disorder scattering rate illustrating the applicability of Eq. (7.30) even for small disorder scattering rates.

A very interesting fact is observable when considering equal layers in the clean case. The drag resistivity Eq. (7.23) in this case simplifies ($b \rightarrow a$) and we arrive at:

$$\rho_D = \frac{2}{e^2} \left[\frac{I_D}{(B_0^a)^2} + \frac{I_G^a}{2B_1^a (B_0^a)^2} \right] = \frac{1}{e^2} \left[\frac{I_D}{(B_0^a)^2} + \frac{I_{\text{tr}}^a}{(B_0^a)^2} \right]. \quad (7.33)$$

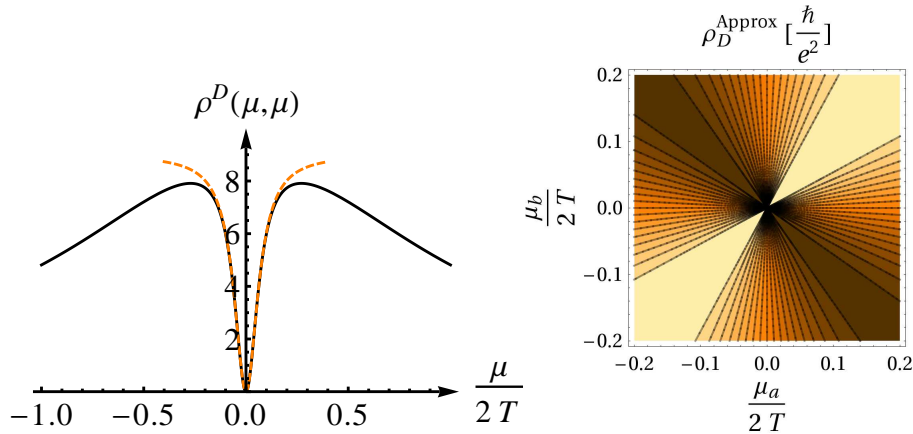


Figure 7.4: *Left:* A cross section of the drag resistivity in units of $\alpha_g^2 \frac{\hbar}{e^2}$ plotted over $\frac{\mu_\alpha}{2T}$ of the two-layers for the case very weak disorder $\tau_{\text{dis}}^{-1} \sim 0.02\alpha_g^2 T$ and with zero distance ($N = 1$). *Right:* Eq. (7.30) plotted in units of $\alpha_g^2 \frac{\hbar}{e^2}$ plotted over $\frac{\mu_\alpha}{2T}$ ($N = 1$). The emphasis of this figure is in the fact that all equirestivity (“equipotential-like”) lines pass straight through the Dirac point of both layers, indicating the non-analytic behavior there. These equirestivity lines are parametrized by Eq. (7.32) and correspond to different cross sections of Eq. (7.30).

This equation suggests that in analogy to the simple Drude consideration of Sec. 6.3 we have a resistivity determined by a drag rate $\tau_D^{-1} \sim I_D/B_0^2$ and a transport scattering rate induced by electron-electron interaction $\tau_{ee}^{-1} \sim I_{\text{tr}}/B_0^2$. For different layers such a simple analogy is much harder and the unambiguous definition of scattering rates becomes less clear. This is the reason for us to work with the integrals I_D and I_{tr} , which correspond, as seen in Eq. (7.33), to interaction induced scattering rates but appear to be not equivalent to the conventional definitions for equal layers.

7.2.2 Discussion of the Results and Their Validity

We now have reached a point where we have seen sufficient effects and physical consequences to stop for a moment to try to more thoroughly understand their meaning and implications. We start by questioning the thermalization approximation and continue with discussing the applicability in the ballistic regime and an overview of all possible regimes.

One of the main reasons for the particular simple form of Eq. (7.23) is that we could reduce the effective four-mode kinetic Eq. (7.14) (or Eq. (C.5)) down to an effective three-mode kinetic Eq. (7.15). This way we managed to get rid of the energy relaxation rate I_E , which drove the inter-layer thermalization, but we also managed to avoid the need to deal with the thermalization rates $I_{\text{Th}}^{\alpha\beta}$. The deeper reason for the inter-layer thermalization is in its foundation, the same one we discussed in Sec. 7.1.2 when we argued for the ansatz and even earlier when we were discussing the structure of the collision kernel in the single layer case (see Sec. 5.2.2): it is the fast forward scattering resonance we came across in Sec. 2.1.4; this time, however it appears as a resonance between the layers. This way the observation in App. C.3, that the energy relaxation is always larger than the thermalization rates, is none other than the statement that in clean graphene we gain a thermalization between the two-layers due to the forward scattering resonance. Thermalization in this context means that their scattering

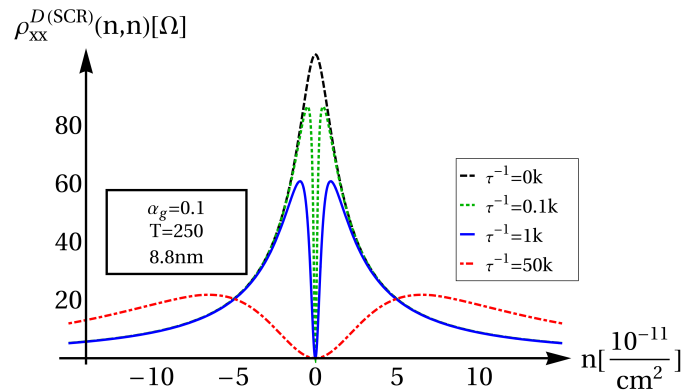


Figure 7.5: Plot of drag resistivity (7.23) with numerical evaluation of the corresponding integrals. The emphasis is in the way the system approaches the clean limit.

rates will be strongly correlated, $\chi_p^a = \chi_p^b$. The remarkable thing here is that this happens for arbitrary distances as long as the graphene sheets do not have any scattering rate except for the Coulomb interaction induced ones (not even the inverse Thouless time). Of course, this may at first sight seem quite counter-intuitive but the explanation is rather simple. Coulomb interaction is a long-range interaction, meaning that the low energy modes, given enough time, will always feel the other layer as long as system size (via Thouless time) or impurities (via scattering rates) do not prevent them from feeling the forward scattering resonance in the system. This is the statement that has already been discussed along the lines of Eq. (7.14). The criterion for thermalization was that the diagonal entry containing the energy relaxation rate in Eq. (7.14) was larger than any off-diagonal one within the same column or row. Since the thermalization rates $I_{\text{Th}}^{\alpha\beta}$ are always smaller than the energy relaxation rate I_E (see App. C.3) the inter-layer thermalization is effective as long as the off diagonal contributions of the type $A_n^\alpha/(T\tau_{\text{dis}}^\alpha)$ stay small. Close to the Dirac point this is basically always true (if the disorder scattering rates do not differ too much) since all A_n^α with odd n disappear, a manifestation of the fact that the two modes χ_v and χ_p are orthogonal at the Dirac point, as explained in the end of Sec. 5.2.3.

When it comes to the applicability of the kinetic equation approach used in Eq. (7.1) with respect to the ballistic regime we need to question the effectiveness of the forward scattering resonance in general. In Sec. 5.2.2 and Sec. 7.1.2 we have argued via the forward scattering resonance that the ansatz (7.12) is the right choice to treat the problem. This way the ansatz is the approximation separating relevant (slow) from irrelevant (fast) modes which has been studied by Ref. [73]. On the other hand we have noticed a curiosity in Sec. 7.1.2, allowing us to go beyond the ultra-ballistic limit. The reason for this extensibility is that the ansatz (7.12) turns out to include the mode governing the solution of the relaxation time ansatz (5.7), namely the velocity mode. This way we manage to use the results obtained by a direction-dependent ansatz for the ballistic regime as well. This is fully supported by the perfect agreements between the results of Tab. 7.1 and those of Tab. 6.2, which have been obtained earlier via a perturbative approach [103]. For the regime $\tau_{\text{dis}}^{-1} \ll \alpha_g^2 T$ and for the regime $\alpha_g^2 T \ll \tau_{\text{dis}}^{-1} \ll T$ Eq. (7.23), which is derived from the thermalized effective kinetic Eq. (7.15), is therefore a suited description of Coulomb drag in graphene. In between the two regimes, for disorder strength of order $\tau_{\text{dis}}^{-1} \sim \alpha_g^2 T$, the thermalization arguments and the pure relaxation time descriptions

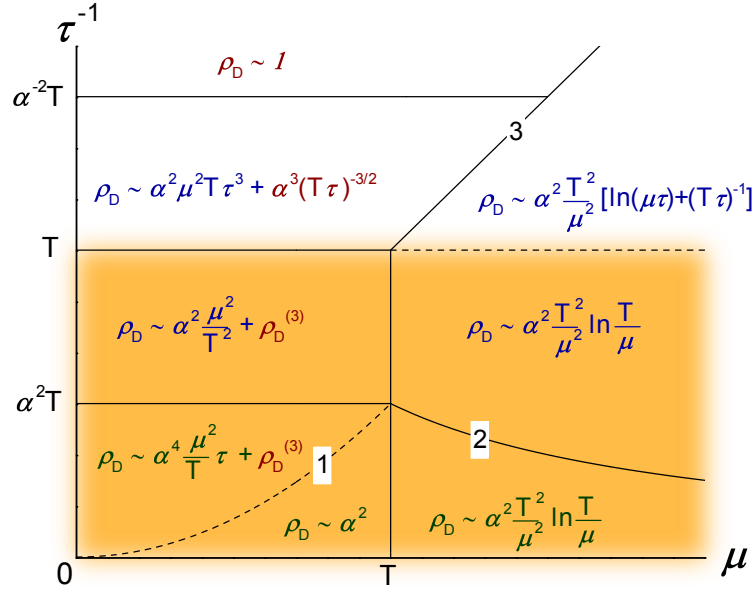


Figure 7.6: The drag coefficients in the case of identical layers in different parameter regimes for $\mu \ll \min(T/\alpha_g, 1/d)$. The orange part ($\tau_{\text{dis}}^{-1} \ll T$) is the regime the kinetic equation is applicable. The regime $\alpha_g^2 T \ll \tau_{\text{dis}}^{-1} \ll T$ is where perturbative (see Ref. [103]) and kinetic equation approach coincide, whereas the regime $\tau_{\text{dis}}^{-1} \ll \alpha_g^2 T$ is obtained by kinetic equation only. The upper regime $T \ll \tau_{\text{dis}}^{-1}$ corresponds to the diffusive regime, where the relaxation time ansatz fails to describe the disorder contributions; this is the regime that has been studied by previous authors [77, 78, 100–104], see Sec. 6.3 for details.

are not well founded. Still, we claim, since above and below the theory applies properly, that the relevant physics for the intermediate case is taken into account and therefore making Eq. (7.23) a well founded approximation.

To gain an overview of the possible regimes including the regimes the previous works have considered, (see Sec. 6.3), Fig. 7.6 provides a collection of the results for the case of equal layers. The orange part of Fig. 7.6 is the regime where Eq. (7.23) is applicable. This part corresponds to the ballistic limit $T\tau_{\text{dis}} \gg 1 \gg \alpha_g^2 T\tau_{\text{dis}}$ whereas $T\tau_{\text{dis}} \ll 1$ (the upper part) corresponds to the diffusive limit. Due to the nature of the collision kernels we take into account (the relaxation time ansatz as well as the Coulomb kernel), diffusive modes like diffusons and cooperons have not been considered, which prohibits us to discuss the diffusive limit properly within the kinetic equation of the two-layer system we started from (Eq. (7.1)). The regime we are actually focused on, the hydrodynamic regime, $\alpha_g T\tau_{\text{dis}} \gg 1$, shows several interesting features. For small chemical potentials around the line 1 we have the situation described by Eq. (7.30) the impurity scattering rate distinguishes the two asymptotics. For large chemical potentials the behavior seems to be quite universal, only the sub-leading correction separates the results there, shown by line 2.

For small chemical potentials there are several highlighted contributions $\rho_D^{(3)}$ in Fig. 7.6. Except for the diffusive regime they are unknown. These contributions correspond to higher-order corrections within the drag rate I_D . Due to symmetry reasons the leading order drag disappears at the Dirac

point, paving the way for possible sub-leading corrections to govern the behavior at charge neutrality (see Sec. 8.3). It is known [91] that this can happen in the diffusive limit. Further details on the higher order contributions can be found in Sec. 8.3.

A discussion of the obvious odd symmetry with respect to the axes is provided later in Sec. 8.3.1, since this symmetry will be crucial there. There is one additional point to make about the symmetries, namely that for all kind of transresistivities it has to be irrelevant if we exchange μ_a with μ_b (if we do the same with τ_{dis}^α). This implies that the transresistivities must behave as even functions with respect to the line $\mu_a = \mu_b$.

7.2.3 Comparison to Experiment

Within the last year the experimental techniques to deal with graphene have developed enormously. Thus, we are in the fortunate position to compare our theoretical considerations with experiments. So far, two experimental groups managed to measure the Coulomb drag resistivity of graphene-based two-layer setups [107, 108]. The two experimental realizations differ in the substrate, the graphene sample is deposited on, and in the material they use to separate the two graphene layers.

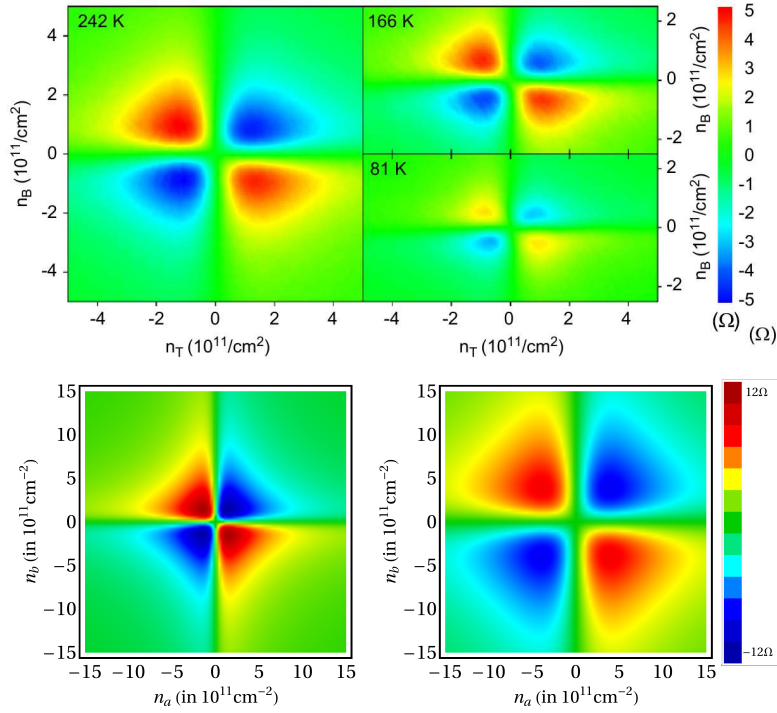


Figure 7.7: Comparison of our data for the drag resistivity (below) with the experimental data (above) from the authors of Ref. [108]. The deviation in the total scale comes from different parameter regimes. Our data is plotted for temperatures $T = 200\text{K}$, coupling strength $\alpha_g = 0.08$ and layer distance $d = 11\text{nm}$ the left figure shows the data for impurity strength $\tau_{\text{dis}}^{-1} = 5\text{K}$ whereas the right shows it for $\tau_{\text{dis}}^{-1} = 25\text{K}$

The experimental data for the resistivity is in both cases given as a function of the charge carrier concentration of each layer. We use a simple relation interpolating the two different regimes introduced

by Ref. [103] to express the resistivity in terms of concentration n_c ,

$$\frac{\mu}{2T} = \frac{\pi n_c}{\sqrt{\pi |n_c| + (T\tau_{\text{dis}})^{-2}}}. \quad (7.34)$$

We further note that the layer distance within our considerations appear as an exponential suppression restricting the momentum, able to contribute to drag. Therefore when considering dimensionless units the quantity $d \cdot T$ determines the value of the integrals. Thus, in our data a change in the temperature always comes along with a change of the distance. This is not a problem a priori but relies on the fact that more numerical data from the evaluation of the integrals would be needed to compensate this taint.

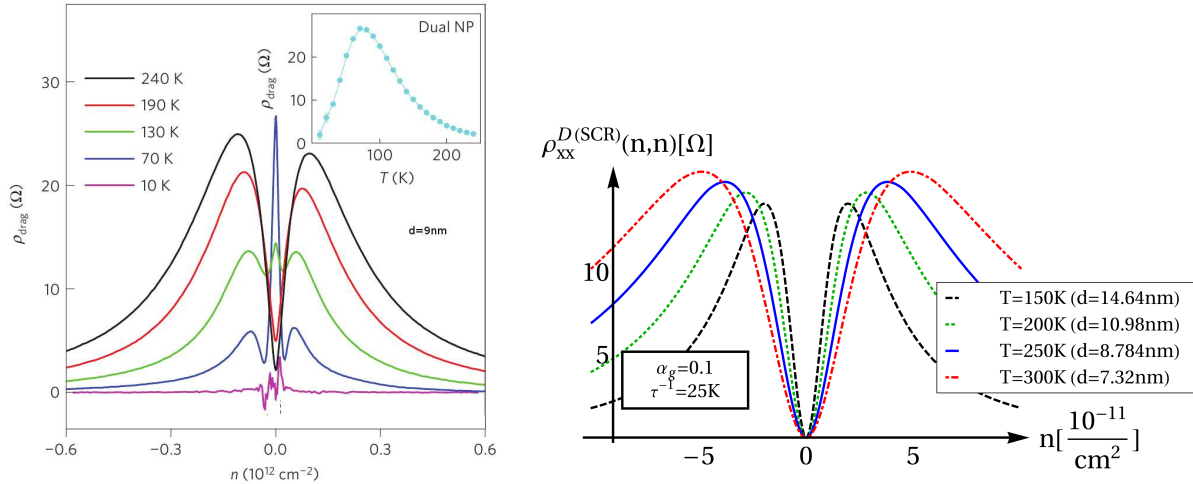


Figure 7.8: Comparison of the cross-section of equal layers of our data (right) for the drag resistivity with the experimental data (left) from the authors of Ref. [107].

The experimental data of Ref. [107] contain drag resistivity measurements varying the concentrations of both layers. They see the symmetry arising from the sign change of a single layer and a peaked structure along lines of equal chemical potential (or equal up to a sign). Thus the qualitative agreement with our theory is quite good as one can determine from Fig.7.7.

One recognizes that the shape of the high resistive pockets (in absolute values) differs slightly but yields better agreement for higher impurity strength. Thus the different shape may arise from contributions coming from the diffusive regime.

A comparison with the data provided by the authors of Ref. [108] can be performed by means of cross-section through the previous data. The experimental data provided allows to compare the temperature trends as well. Since so far temperature variation correspond to distance variations we need to be careful in the comparison with the experiment shown in Fig. 7.8.

The tendencies as a function of temperature are rather good. We see the translation of the peak towards the origin as well as the height change caused by temperature. The latter is not as pronounced as in the experiment since in our case the distance varies as well.

In total the qualitative agreement with the experiments is surprisingly good and supports the general picture we have presented so far. In the experiments one recognizes a feature at the Dirac point which is not present in our data. An explanation for this and possible phenomena related to this are given in Sec. 8.3

8

Chapter 8

Coulomb Drag in Graphene: Generalizations and Further Developments

To explain all nature is too difficult a task for any one man or even for any one age. 'Tis much better to do a little with certainty, & leave the rest for others that come after you, than to explain all things by conjecture without making sure of any thing.

Isaac Newton, quoted in *Never at Rest: A Biography of Isaac Newton*

This chapter is dedicated to further extensions of the approach introduced in the previous Chap. 7 for Coulomb drag. We will show how to generalize the formulation to cover multi-layer systems and how to include a magnetic field yielding Hall drag and magneto drag. We then, proceed by extending the formalism itself to describe higher-order drag and to gain Drude-like equations for the drag setup in graphene.

8.1 Multilayer Drag

When we started to derive the Coulomb drag of two-layers in Sec. 7.1.1 we were focused on the Coulomb drag of a two-layer system. We did not bother thinking about the extensibility of the treatment but focused on making the derivation as clear as possible. Now we can consider possible extensions. The simplest one seems to be adding a layer. Glancing at Eq. (7.1) we see that the consequences of adding a layer would be an additional equation on the one hand and two additional collision integrals connecting all of them on the other hand. Following the logic of our calculation for two-layers we gain a three-layer functional similar to Eq. (7.10):

$$\begin{aligned} F_{3L}(h_a, h_b, h_c) = & F(h_a, h_b) + N_c \int dx \nu(\epsilon) \frac{\partial n_F^c(\epsilon)}{\partial \epsilon} h^c(x) \left[e \frac{\vec{E}^c \vec{v}}{T^2} - \frac{h^c(x)}{2T\tau_{\text{dis}}^c} \right] \\ & + \frac{N_c^2}{8T^2} \int d\{x_i\} W^{c,c}(\{x_i\}) \left[h^c(x_1) - h^c(x_2) + h^c(x_3) - h^c(x_4) \right]^2 \\ & + \frac{N_b N_c}{4T^2} \int d\{x_i\} W^{b,c}(\{x_i\}) \left[h^b(x_1) - h^b(x_2) + h^c(x_3) - h^c(x_4) \right]^2 \\ & + \frac{N_a N_c}{4T^2} \int d\{x_i\} W^{a,c}(\{x_i\}) \left[h^a(x_1) - h^a(x_2) + h^c(x_3) - h^c(x_4) \right]^2. \end{aligned} \quad (8.1)$$

Along the lines of the arguments for the ansatz (7.12) we see no need to restrict them to two-layers only. This way we can derive very analogous an effective three-layer kinetic equation including six modes as it is shown in App. C.1.3. The main difference is in the more lengthy expressions that appear during the calculation.

In Sec. 7.1.3 we noticed a correlation appearing between the two-layers which we referred to as thermalization (see Sec. 7.2.2). In App. C.1.3 we show that the same arguments apply for the three-layer case leading to an effective three-layer thermalization. The detailed calculation is only sketched in App. C.1.3, since it turns out to be too lengthy. Nonetheless it is a straight-forward calculation following the steps in the spirit of the two-layer case.

By solving the thermalized kinetic Eq. (C.11) analogous to Sec. 7.1 we obtain the drag resistivity for the three-layer case to be:

$$\rho_D^{\alpha\beta} = \frac{2}{e^2} \frac{I_D^{\alpha\beta}}{B_0^\alpha B_0^\beta} \left[1 - \frac{I_G^\alpha I_G^\beta}{I_D^{\alpha\beta} \left(\sum_\gamma B_2^\gamma \right) \left(\frac{1}{T\tau_0} + \frac{1}{T\tau_{ad}} \right)} \right], \quad (8.2)$$

$$\rho_{\alpha\alpha} = \frac{2}{e^2} \frac{1}{N_\alpha B_0^\alpha} \left[\frac{1}{T\tau_{dis}^\alpha} + \frac{N_\alpha I_{tr}^\alpha}{B_0^\alpha} - \frac{N_\alpha \left(I_G^\alpha \right)^2}{B_0^\alpha \left(\sum_\gamma B_2^\gamma \right) \left[(T\tau_0)^{-1} + (T\tau_{ad})^{-1} \right]} \right]. \quad (8.3)$$

with the short forms, as previously, given by Eq. (7.13). The generalized rate is given by:

$$I_G^\alpha = B_1^\alpha I_{tr}^\alpha - \sum_{\gamma \neq \alpha} B_1^\gamma I_D^{\alpha\gamma} \quad (8.4)$$

and the characteristic scattering rate for the Coulomb drag is of the form:

$$\frac{1}{T\tau_0} = \frac{\sum_\gamma B_1^\gamma I_G^\gamma}{\sum_\gamma B_2^\gamma} = \frac{1}{\sum_\gamma B_2^\gamma} \left(\sum_\gamma \left(B_1^\gamma \right)^2 I_{tr}^\gamma - \sum_{\substack{\gamma, \delta \\ \gamma \neq \delta}} B_1^\gamma B_1^\delta I_D^{\gamma\delta} \right). \quad (8.5)$$

The averaged disorder scattering rate reads:

$$\frac{\sum_\gamma B_2^\gamma}{T\tau_{ad}} = \sum_\gamma \frac{B_2^\gamma}{T\tau_{dis}^\gamma}. \quad (8.6)$$

Eq. (8.2) is fully downward compatible since reducing the number of flavors $N_\gamma \rightarrow 0$ of the corresponding layers gets rid of the corresponding B_1^γ 's and B_2^γ 's and therefore effectively reduces the possible summations. On the other hand setting the chemical potential of some layers to zero is different from this procedure. It only sets the corresponding $I_D^{\alpha\gamma}$'s and B_1^γ 's to zero which leaves traces within the equation in form of the averaged disorder scattering rate and the characteristic scattering rate for the Coulomb drag. These two multilayer quantities know about the additional layers even if they are at the Dirac point.

Since the Eq. (8.2) reflects the physical properties of a multi-layer system very well, it is expected that this result holds for more than three layers.

The multi-layer setup becomes naturally important if the layer degeneracy is lifted. This is the case if we apply an in-plane magnetic field to the Coulomb drag setup. The electronic spins, so far treated

as degeneracy, will become spin polarized. Furthermore via the Zeeman splitting two different chemical potentials arise, one for each species of spin polarized electrons. Thus, a two layer setup transforms into a four layer setup, since each of the physical layers of graphene counts now as effectively two layers of spin polarized graphene. Coulomb drag in such a setup will cause drag between spin polarized electrons, which via their effective chemical potentials can be controlled. Similar setups are known for conventional systems [109, 110] and 1D setups [111]. A detailed analysis of the Spin drag in graphene-based setups remains as a future work (see outlook Sec. 9).

8.2 The Hall Drag and Magnetodrag

We will return now to the case of two-layers. We now alter the system by including a magnetic field. Before we can continue to modify our machinery to the new setup we need to understand how the system will change due to the changed circumstances.

8.2.1 Applicability of the Kinetic Equation

One of the most studied phenomena in condensed matter physics is the quantum Hall effect (QHE). The quantum Hall effect is observable at very low temperatures in very strong magnetic fields and is based on the change of the electronic structure of the material under these circumstances. The electrons in the quantum Hall phase appear to occupy degenerated quantized energy levels, so-called Landau levels. The formulation we have used so far has depended on the electronic structure in graphene in absence of a magnetic field. Our purpose now is to investigate whether or not we can keep this picture in the presence of a magnetic field. For details of the quantum Hall effect in graphene we refer to the general overview given in Ref. [20].

The question we face in our attempt to deal with Hall drag is: what are the limitations when we want to describe the system with help of the unchanged electronic structure. In case of disordered graphene it is known that there is an interplay of mean free path l_{dis} and magnetic length l_{B} (see for example Ref. [112]). But how is the situation for clean graphene? In Sec. 4.2 we have shown that even for clean graphene at the Dirac point there is an interaction induced lifetime for finite temperatures. Hence we need to determine in a self-consistent manner if such a finite lifetime, which broadens the energy levels, can compete with the tendency of a magnetic field to quantize the electronic structure. The energy levels in graphene that are induced by a magnetic field behave as $\epsilon_n = \omega_c \sqrt{n}$, where the cyclotron frequency is given by $\omega_c = v_F \sqrt{2eB}$ (see Ref. [20]). We look now for the condition:

$$\epsilon_{n+1} - \epsilon_n = \frac{\omega_c^2}{\epsilon_n + \epsilon_{n+1}} < \frac{1}{\tau_q}. \quad (8.7)$$

One important observation is that with higher energies the condition (8.7) becomes more likely to be fulfilled, since the energy appears in the denominator. Following this logic there is an energy ϵ^* at which the broadening is bigger than the distance between the Landau levels hence restoring the linear spectrum of graphene as illustrated in Fig. 8.1.

The quasi-particle broadening is induced due to Coulomb interaction and disorder scattering:

$$\frac{1}{\tau_q} = \frac{1}{\tau_q^{\text{dis}}} + \frac{1}{\tau_q^{\text{ee}}}, \quad (8.8)$$

for the following considerations we will assume the clean setup, where impurity scattering is absent. Let us now assume that the energy scale at which the broadening is bigger than the distance between

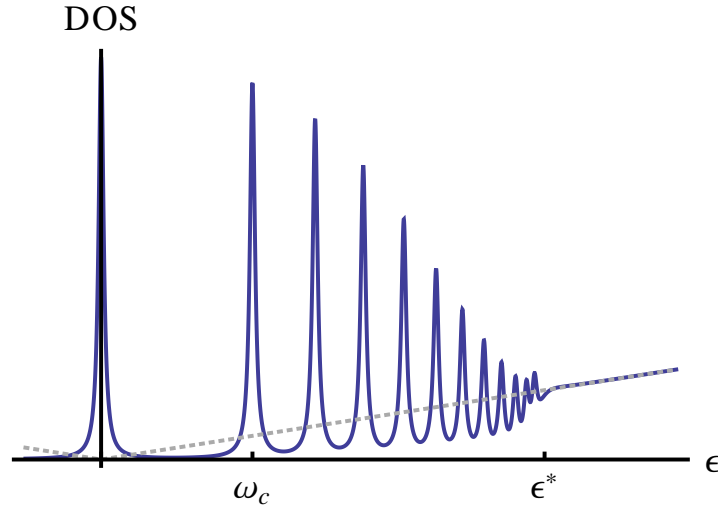


Figure 8.1: Sketch of the density of states (DOS) in the cross over between the regime of Landau level quantization and the recovery of the electronic structure of graphene. The dotted gray line corresponds to the DOS of the system without magnetic field.

the Landau levels fulfills $\epsilon^* \gg \omega_c$, then the condition (8.7) reduces to

$$\frac{\omega_c^2}{2\epsilon} < \frac{1}{\tau_q} \sim \begin{cases} \frac{T}{N} \sqrt{\frac{\epsilon}{T}} & \epsilon < \alpha_g^2 NT \\ \alpha_g T & \epsilon > \alpha_g^2 NT \end{cases}, \quad (8.9)$$

using the result from Eq. (4.21). We see that for large energies $\epsilon > \alpha_g^2 NT$ we need to have $\epsilon > \epsilon^* = \omega_c^2 / (\alpha_g T)$. Since $\omega_c = \sqrt{2} v_F / l_B$ defines the magnetic length we can, with the help of the definition of the screening length (4.5), reformulate this to gain $\epsilon > \epsilon^* = 4 \ln(2) N v_F l_{\text{scr}} / l_B^2$.

There is also the situation that the magnetic field is so weak that the critical energy becomes smaller than the energy scale defined by the magnetic field $\epsilon^* \ll \omega_c$. In such a situation the energy difference changes towards $\epsilon_1 - \epsilon_0 = \omega_c$, which implies that if the condition $\omega_c < \alpha_g T$ holds the complete electronic structure appears to be unchanged by the magnetic field. This condition corresponds to the case that the length scales obey $l_{\text{scr}} < l_B$, it is therefore a natural limit in switching off the magnetic field.

We see that one can easily find situations in which one can deal with the linear electronic structure of graphene in the presence of a weak magnetic field. In all of above discussion we need to remember that $\omega_c \ll T$ must hold for us to be able to treat the system within the kinetic equation approach.

8.2.2 The Kinetic Equation in the Presence of a Magnetic Field

In order to deal with the two-layer system in the presence of a magnetic field we still need to discuss how a weak magnetic field manifests itself in the language of the kinetic equation. A reasonable way to proceed is to look back at the derivation of the electric field in the Liouvillian as done in Sec. 2.5.1 and follow the analogous route with a magnetic field instead. For simplicity we will argue more physically by the usage of the Boltzmann equation. In the Boltzmann theory (see [49, 50, 52]) the way the electric field appears is generalized as a force acting on the distribution function $\vec{F} \nabla_{\vec{p}}$. In presence

of a magnetic field ($\vec{B} = B\vec{e}_z$) we will consider the Lorentz force $\vec{F} = e(\vec{E} + \vec{v} \times \vec{B})$ which alters the Liouville operator [73–75] towards $(\nabla_{\vec{p}} = \vec{v}\partial_\epsilon + \partial_{\vec{v}}$ with $\partial_{\vec{v}} = v_F^{-1}\vec{e}_\phi\partial_\phi$):

$$\mathcal{L}n = \left(\partial_T + \vec{v}\nabla_R + e\vec{E}\vec{v}\partial_\epsilon + \frac{\omega_c^2}{2v_F\epsilon}\partial_\phi \right) n, \quad (8.10)$$

using $\vec{v}(\vec{e}_z \times \partial_{\vec{v}}) = \epsilon^{-1}v_F\partial_\phi$. Hence we obtain now a mixing of directions caused by the magnetic field. Since we have this mixing we need to be more careful with the ansatz (7.12). We will still keep the form of the ansatz but we replace the directions the ansatz can point to by \vec{e}_α . The modified ansatz reads:

$$h^\alpha(x_i) = \sum_\mu \left(\chi_v^{\alpha\mu} + \frac{\epsilon}{T}\chi_p^{\alpha\mu} \right) \vec{v}\vec{e}_\mu. \quad (8.11)$$

The changed Liouvillian induces alterations in the functional (7.10), which read:

$$F_{\text{mod}}(h^a, h^b) = F(h^a, h^b) - \int dx\nu(\epsilon) \frac{\partial n_F^a}{\partial \epsilon} \left(\frac{\omega_c}{2T} \right)^2 \frac{2T}{\epsilon} \partial_\phi \left(h^a(x) \right)^2 - \int dx\nu(\epsilon) \frac{\partial n_F^b}{\partial \epsilon} \left(\frac{\omega_c}{2T} \right)^2 \frac{2T}{\epsilon} \partial_\phi \left(h^b(x) \right)^2. \quad (8.12)$$

Using the ansatz we arrive at the effective kinetic equation for the case of a weak applied magnetic field. The details of the functional variation can be found in App. C.1.4. The effective kinetic equation is expressed in Eq. (C.17). As for the case of no magnetic field a thermalization between the layers appears again (see Sec. 7.1.3), which for each direction separately reduces the modes needed to deal with the system. With the help of the definition from the rotated effective kinetic Eq. (7.15) for M we can write:

$$\begin{pmatrix} A_0^a & 0 \\ 0 & A_0^b \\ N_a A_1^a & N_b A_1^b \\ 0 & 0 \\ 0 & 0 \\ 0 & 0 \end{pmatrix} = \begin{pmatrix} M & yL \\ yL & M \end{pmatrix} \begin{pmatrix} \chi_v^{ax,I} & \chi_v^{ax,II} \\ \chi_v^{bx,I} & \chi_v^{bx,II} \\ \chi_p^{x,I} & \chi_p^{x,II} \\ \chi_v^{ay,I} & \chi_v^{ay,II} \\ \chi_v^{by,I} & \chi_v^{by,II} \\ \chi_p^{y,I} & \chi_p^{y,II} \end{pmatrix} \quad \text{with } L = \begin{pmatrix} A_{-1}^a & 0 & A_0^a \\ 0 & A_{-1}^b & A_0^b \\ N_a A_0^a & N_b A_0^b & N_a A_1^a + N_b A_1^b \end{pmatrix} \quad (8.13)$$

for the rotated system ($(2T)^2 y = 2\omega_c^2$). We have used here that the ansatz is again oriented in such a way that the χ_{\bullet}^{xy} parts do not see the electric field ($b_{\bullet y} = 0$), for further details we refer to App. C.1.4. The current in the additional directions is given by:

$$\vec{j}_\mu^\alpha = eN_\alpha \int \frac{d^2p}{(2\pi)^2} \vec{v} n_F^\alpha(x) = \frac{e^2}{2} N_\alpha \sum_{\substack{\mu \in \{x,y\} \\ \gamma \in \{I,II\}}} \vec{e}_\mu^\gamma \left(A_0^\alpha \chi_v^{\alpha\mu\gamma} + A_1^\alpha \chi_p^{\mu\gamma} \right). \quad (8.14)$$

These equations create an explicit anisotropy, meaning that the conductivity has the structure $\hat{\sigma} = \mathbb{1}\sigma^{xx} + \varepsilon\sigma^{xy}$ (ε being the completely antisymmetric tensor of rank two) which allows us to write:

$$\begin{pmatrix} \vec{j}_x^a \\ \vec{j}_x^b \\ \vec{j}_y^a \\ \vec{j}_y^b \end{pmatrix} = \begin{pmatrix} \hat{\sigma}^{xx} & -\hat{\sigma}^{xy} \\ \hat{\sigma}^{xy} & \hat{\sigma}^{xx} \end{pmatrix} \begin{pmatrix} \vec{E}_x^a \\ \vec{E}_x^b \\ \vec{E}_y^a \\ \vec{E}_y^b \end{pmatrix} = \begin{pmatrix} \sigma_{aa}^{xx} & \sigma_{ab}^{xx} & -\sigma_{aa}^{xy} & -\sigma_{ab}^{xy} \\ \sigma_{ab}^{xx} & \sigma_{bb}^{xx} & -\sigma_{ab}^{xy} & -\sigma_{bb}^{xy} \\ \sigma_{aa}^{xy} & \sigma_{ab}^{xy} & \sigma_{aa}^{xx} & \sigma_{ab}^{xx} \\ \sigma_{ab}^{xy} & \sigma_{bb}^{xy} & \sigma_{ab}^{xx} & \sigma_{bb}^{xx} \end{pmatrix} \begin{pmatrix} \vec{E}_x^a \\ \vec{E}_x^b \\ \vec{E}_y^a \\ \vec{E}_y^b \end{pmatrix} \quad (8.15)$$

Again we use vectors to project the solution of the effective kinetic equation

$$\vec{d}^T = \begin{pmatrix} N_a A_0^a & 0 & N_a A_1^a \\ 0 & N_b A_0^b & N_b A_1^b \end{pmatrix} \quad \text{and} \quad \vec{b} = \begin{pmatrix} A_0^a & 0 \\ 0 & A_0^b \\ N_a A_1^a & N_b A_1^b \end{pmatrix}, \quad (8.16)$$

to write the conductivity in the presence of a magnetic field as:

$$\hat{\sigma}_{xx} = \frac{e^2}{2} \vec{d}^T \left[\begin{pmatrix} M & yL \\ yL & M \end{pmatrix}^{-1} \right]_{11} \vec{b} = \frac{e^2}{2} \vec{d}^T (M - y^2 LM^{-1}L)^{-1} \vec{b} \approx \frac{e^2}{2} \vec{d}^T M^{-1} \vec{b}, \quad (8.17)$$

$$\hat{\sigma}_{xy} = \frac{e^2}{2} \vec{d}^T \left[\begin{pmatrix} M & yL \\ yL & M \end{pmatrix}^{-1} \right]_{21} \vec{b} = y \frac{e^2}{2} \vec{d}^T (M - y^2 LM^{-1}L)^{-1} LM^{-1} \vec{b} \approx y \frac{e^2}{2} \vec{d}^T M^{-1} LM^{-1} \vec{b}. \quad (8.18)$$

One clearly sees that in the limit of weak magnetic fields $\hat{\sigma}_{xx}$ equals Eq. (7.18) and we hence recover the results obtained in the beginning of Sec. 7.2. In the very same way we see that $\hat{\sigma}_{xy}$ for weak magnetic field is proportional to y (which itself is proportional to \vec{B}). The resistivity for this case involves the inversion of the conductivity matrix introduced in Eq. (8.15). The complete discussion is only valid for weak magnetic fields (see Sec. 8.2.1), which is why the expansion of Eq. (8.17) is valid in the regime we are looking for Hall physics. The resistivity reads:

$$\hat{\rho}_{xx} = \left(\hat{\sigma}_{xx} + \hat{\sigma}_{xy} \hat{\sigma}_{xx}^{-1} \hat{\sigma}_{xy} \right)^{-1} \approx \hat{\sigma}_{xx}^{-1} \quad (8.19)$$

$$\hat{\rho}_{xy} = \left(\hat{\sigma}_{xx} + \hat{\sigma}_{xy} \hat{\sigma}_{xx}^{-1} \hat{\sigma}_{xy} \right)^{-1} \hat{\sigma}_{xy} \hat{\sigma}_{xx}^{-1} \approx \hat{\sigma}_{xx}^{-1} \hat{\sigma}_{xy} \hat{\sigma}_{xx}^{-1} \quad (8.20)$$

where the expansion for small y again corresponds to the regime where we can describe the magnetic field in the kinetic equation approach. Doing the matrix multiplications straightforwardly the familiar short forms (7.19) and (7.20) reappear together with

$$C^\alpha = B_0^\alpha - A_{-1}^\alpha B_1^\alpha / N_\alpha, \quad (8.21)$$

which allows us to express the Hall resistivity and the Hall drag as:

$$\rho_{xy}^D = \frac{2}{e^2} \frac{y}{B_0^a B_0^b} \left(\frac{C^a I_G^b + C^b I_G^a}{(B_2^a + B_2^b)[(T\tau_0)^{-1} + (T\tau_{ad})^{-1}]} - \frac{(B_1^a C^a + B_1^b C^b) I_G^a I_G^b}{(B_2^a + B_2^b)^2 [(T\tau_0)^{-1} + (T\tau_{ad})^{-1}]^2} \right), \quad (8.22)$$

$$\rho_{xy}^{\alpha\alpha} = \frac{2}{e^2} \frac{y}{(B_0^\alpha)^2} \left(\frac{B_0^\alpha - C^\alpha}{B_1^\alpha} + \frac{2C^\alpha I_G^\alpha}{(B_2^a + B_2^b)[(T\tau_0)^{-1} + (T\tau_{ad})^{-1}]} - \frac{(B_1^\alpha C^\alpha + B_1^{-\alpha} C^{-\alpha})(I_G^\alpha)^2}{(B_2^a + B_2^b)^2 [(T\tau_0)^{-1} + (T\tau_{ad})^{-1}]^2} \right), \quad (8.23)$$

also using the generalized rate we have introduced in Eq. (7.21) defined as $I_G^\alpha = B_1^\alpha I_{Tr}^\alpha - B_1^{-\alpha} I_D$, the effective Coulomb interaction rate:

$$(T\tau_0)^{-1} = \frac{1}{B_2^a + B_2^b} \left[(B_1^a)^2 I_{Tr}^a + (B_1^b)^2 I_{Tr}^b - 2B_1^a B_1^b I_D \right] = \frac{B_1^a I_G^a + B_1^b I_G^b}{B_2^a + B_2^b}, \quad (8.24)$$

and the averaged disorder scattering rate:

$$\frac{B_2^a + B_2^b}{T\tau_{ad}} = \frac{B_2^a}{T\tau_{dis}^a} + \frac{B_2^b}{T\tau_{dis}^b}. \quad (8.25)$$

8.2.3 Asymptotics of the Hall Drag

In analogy to Sec. 7.2.1 we consider the asymptotic behavior of the Hall drag in several regimes. To do so we follow the same notation of ballistic and ultra-ballistic/hydrodynamic we have defined and used in the case of the Coulomb drag resistivity.

The ballistic regime

When the Coulomb interaction can be considered to be much smaller than the relaxation rate the discussion in Sec. 7.2.1 unveiled that $(T\tau_0)^{-1} + (T\tau_{\text{ad}})^{-1} \approx (T\tau_{\text{ad}})^{-1}$ is the factor suppressing the results that go beyond the perturbative calculation of Ref. [103]. If we do the very same for the Hall drag (8.22) we obtain:

$$\rho_{xy}^{\text{D}} = 0 + O(\alpha_g^2 T \tau_{\text{dis}}), \quad (8.26)$$

where the coefficient of the leading non-vanishing contribution is not accessible, since in the ballistic regime the magnetic field requires additional modes that have not taken into account. This result is not too surprising since a glance at the Drude picture already gives us this result.

We start with a modification of the two-layer Drude Eq. (6.3) taken in the stationary case:

$$0 = \frac{q}{m} \vec{E}_a - \frac{1}{\tau} \vec{v}_a + \frac{\vec{v}_b - \vec{v}_a}{\tau_{\text{D}}} + \frac{q}{m} \vec{v}_a \times \vec{B}, \quad (8.27)$$

$$0 = \frac{q}{m} \vec{E}_b - \frac{1}{\tau} \vec{v}_b + \frac{\vec{v}_a - \vec{v}_b}{\tau_{\text{D}}} + \frac{q}{m} \vec{v}_b \times \vec{B}. \quad (8.28)$$

Driving a current in layer a ($\vec{j}_a = nq\vec{v}_a$) and keeping the second layer untouched, i.e. not connected to leads to prevent the second layer from developing a current (\vec{v}_b), we see that the magnetic field drops from the equation since no current appears in layer b . Hence the equation for layer b reduces to the Drude drag Eq. (6.5) showing no Hall drag features. In this view the result of Eq. (8.26) comes at no surprise. Nevertheless even in this Drude-like picture one may obtain a Hall drag at the cost of incorporating the magnetic field's influence into the quasi-particle kinetics in the collision kernel [113, 114].

From the modified two-layer Drude Eq. (8.27) we gain the Hall resistivity by disregarding the second layer and sending the current in \vec{e}_x direction through the layer a . Having the magnetic field in \vec{e}_z direction one reads for the \vec{e}_y part of the equation:

$$0 = \frac{q}{m} \vec{E} \vec{e}_y + \frac{\vec{j} \vec{e}_x B}{n} (\vec{e}_x \times \vec{e}_z) \vec{y}. \quad (8.29)$$

The drag resistivity appears as

$$\rho^H = B/(qn) \quad (8.30)$$

in these terms.

Within the kinetic equation approach we obtained the Hall resistivity in Eq. (8.23), which in the ballistic limit reduces to:

$$\rho_{xy}^{\alpha\alpha} = y \frac{2}{e^2} \frac{A_{-1}^{\alpha}}{N_{\alpha} (B_0^{\alpha})^2} = y \frac{\pi}{e^2} \frac{\tanh \hat{\mu}_{\alpha}}{N_{\alpha} \ln^2(2 \cosh \hat{\mu}_{\alpha})} = \frac{1}{e^2} \frac{eB}{T^2} \frac{\pi \tanh\left(\frac{\mu_{\alpha}}{2T}\right)}{N_{\alpha} \ln^2\left[2 \cosh\left(\frac{\mu_{\alpha}}{2T}\right)\right]}. \quad (8.31)$$

In the limit of large chemical potentials this result agrees with the Drude picture Eq. (8.30) since the concentration for this case is given by $n = N\mu^2/(4\pi)$. For small chemical potentials the resistivity deviates from Eq. (8.30), implying that using the Hall resistivity to get the concentration in graphene becomes unsuitable for small chemical potentials.

The hydrodynamic phase (the clean case)

When the Coulomb interaction dominates the processes within graphene we see quite unusual physics appear in the kinetic equation. In this situation it is worth rewriting Eq. (8.22) into the following form, getting rid of some cancellations explicitly:

$$\rho_{xy}^D = \frac{2}{e^2} \frac{y}{B_0^a B_0^b} \frac{x \left(C^a I_G^b + C^b I_G^a \right) + C^a B_1^b \left(I_G^b \right)^2 + C^b B_1^a \left(I_G^a \right)^2}{\left(B_1^a I_G^a + B_1^b I_G^b + x \right)^2} \quad \text{with } x = \frac{B_2^a + B_2^b}{T\tau_{\text{ad}}}. \quad (8.32)$$

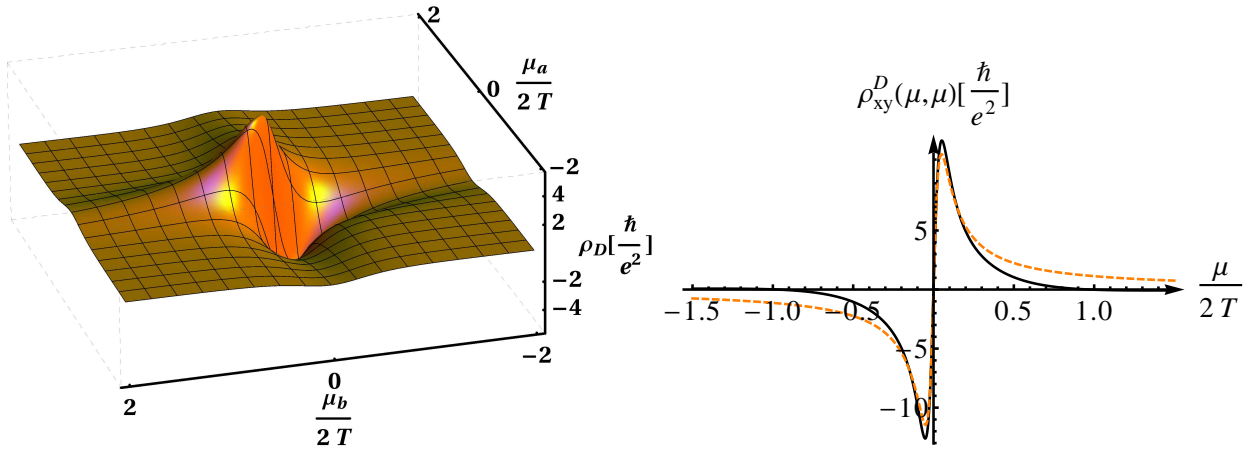


Figure 8.2: *Left:* The Hall drag resistivity in units of $\frac{\hbar}{e^2} \frac{eB}{T^2}$ plotted over $\frac{\mu_a}{2T}$ of the two-layers for disorder scattering rate of order $\tau_{\text{dis}}^{-1} \sim 0.1\alpha_g^2 T$ with $d \cdot T \ll 1$ and for simplicity $N_a = N_b = 1$. *Right:* A cross section of the drag resistivity in units of $\frac{\hbar}{e^2} \frac{eB}{T^2}$ plotted over $\frac{\mu_a}{2T}$ for disorder scattering rate of order $\tau_{\text{dis}}^{-1} \sim 0.02\alpha_g^2 T$ and with $d \cdot T \ll 1$. Note the sign change of the resistivity for $\mu/(2T) \sim 1$ see Sec. 8.2.6 for more details. Further in orange dashed the small μ -asymptotics for the hydrodynamic regime is given in Eq. (8.33) for simplicity again with $N_a = N_b = 1$.

In the case of a small chemical potential we can again use the asymptotics of the involved integrals derived in App. C.3 to arrive at a particularly simple equation for the Hall drag resistivity:

$$\rho_{xy}^D = \frac{2\pi}{e^2} \frac{y}{\ln 2} \frac{N_a \hat{\mu}_a + N_b \hat{\mu}_b}{8 \left[(N_a \hat{\mu}_a)^2 + (N_b \hat{\mu}_b)^2 \right] + z} \quad \text{with } z = \frac{x}{4\alpha_g^2 C_{\text{Tr}}(dT)} \stackrel{dT=0}{\approx} \frac{7.85}{\alpha_g^2} \left(\frac{N_a}{T\tau_{\text{dis}}^a} + \frac{N_b}{T\tau_{\text{dis}}^b} \right). \quad (8.33)$$

The Hall drag of the clean case has a divergence at the Dirac point of both layers that disappears for any small disorder scattering in the system. The comparison of this approximation to the numerically evaluated integrals is given on the right hand side of Fig. 8.2. The overall shape of the Hall drag is

given on the left hand side of Fig. 8.2, which unveils a dramatic change of the symmetry the Hall drag (8.22) obeys in contrast to the symmetry of the Coulomb drag (7.23). The Coulomb drag behaves as an odd function for each of the axes defined by one chemical potential. The Hall drag in contrast is an odd function with respect to the line $\mu_a + \mu_b = 0$, at which the Hall drag disappears. Therefore the difference is that the Coulomb drag is sensitive to the charge-carrier concentration of each layer, whereas the Hall drag seems to be susceptible to the total concentration of charge carriers. An attempt to arrive at a deeper understanding of this change can be found in Sec. 8.2.4.

8.2.4 Properties and Analysis of the Hall Drag

To understand the qualitative change in the Hall drag as compared to the Coulomb drag we first need to take a look at the influence of the magnetic field in graphene. In Eq. (8.10) we have included the Lorentz force into the kinetic equation. In conventional non-relativistic systems the Lorentz force appears to be “charge over mass” selective. In graphene however, due to massless charge carriers, the Lorentz force becomes energy-selective. This is an important difference since the magnetic field in Eq. (8.13) not only mixes the directions but also the symmetry of the modes. To understand this statement we should again remember the interpretation of the coefficients A_n as scalar products of our modes (see Eq. (5.34)). In this language the influence disorder has on the system is contained in the A_s . The entry A_0 suggests a mixing of a velocity mode with another velocity mode whereas A_2 refers to a mixing of a momentum mode with another momentum mode. The contribution A_1 appears in disorder scattering as a mixing of a velocity with a momentum mode instead. At the Dirac point A_1 vanishes (see the discussion after Eq. (5.34)) which is the reason we could define a conductivity in absence of impurities there (see Sec. 5.2.3). The magnetic field now manifests as an energy weighted mixing of directions that causes a change in this viewpoint by exchanging coefficients A_n to A_{n-1} , seen explicitly in Eq. (C.15). The reduction of the n dramatically changes the symmetry properties of the coefficients A_n in such way that at the Dirac point the magnetic field scatters only between a velocity and a momentum mode not between a momentum and another momentum or respectively a velocity and another velocity mode. To understand this more easily it is helpful to imagine a sketch as it is given in Fig. 8.3. Let us consider the following scenario to gain a clearer picture. We assume that

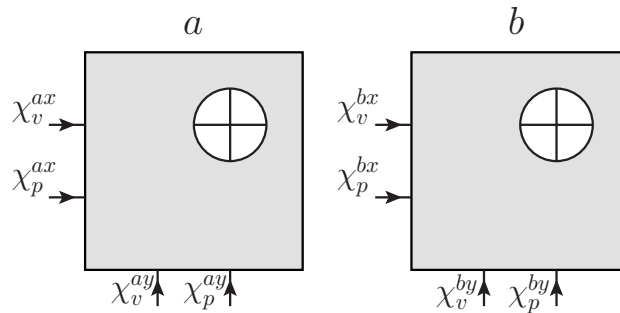


Figure 8.3: A sketch of the possible modes appearing in a magnetic field. The gray region symbolizes the region the magnetic field causes possible mixing of the modes pointing in x direction with those pointing in y direction.

layer b is at the Dirac point. In Fig. 8.3 this implies that the magnetic field allows only for scattering

between χ_v^{bx} and χ_p^{by} and respectively χ_p^{bx} and χ_v^{by} . Also, since layer b resides at the Dirac point the velocity mode does not communicate with the momentum mode. This creates an interesting situation when we consider the electric current Eq. (5.29) and the energy current analogous defined as:

$$\vec{j}_E = N \int \frac{d^2p}{(2\pi)^2} \epsilon \vec{v} n(x) = \frac{e}{2} N (A_1 \chi_0 + A_2 \chi_1) \vec{E}, \quad (8.34)$$

$$\vec{j} = \frac{e^2}{2} N (A_0 \chi_0 + A_1 \chi_1) \vec{E}. \quad (8.35)$$

At the Dirac point χ_v is exclusively responsible for the electrical current whereas χ_p exclusively covers the energy current. An electric field in x direction will create a pure electrical current in x direction. In presence of a magnetic field the electrical current will be scattered into a pure energy current in y direction as one can easily derive from Eq. (C.15). This means that at the Dirac point Eq. (8.23) yields zero since no electrical current is transferred between the directions.

Since the Dirac point apparently provides us with the possibility to more easily understand what processes are going on in the system we will now consider the Hall drag from layer a to layer b in the case that layer b stays at the Dirac point whereas layer a does not. We will consider a current in layer a in x direction which leaves us with seemingly two scenarios to gain an electric field in layer b in y direction:

- The electric current in layer a consisting of χ_v^{ax} and χ_p^{ax} is scattered via the magnetic field to the modes χ_v^{ay} and χ_p^{ay} . Here now the usual Coulomb drag could provide us with a possibility affect layer b , but since layer b is at the Dirac point this is not possible. Note: it would be possible for an energy current but not for an electric current.
- Again we start with the electric current in layer a consisting of χ_v^{ax} and χ_p^{ax} . To directly affect layer b seems impossible since layer b resides at the Dirac point. But we have learned that there is the phenomenon of thermalization (see Sec. 7.1.3), which means that although there will be no current in layer b in x direction there might be an energy current instead. In exactly the way we have previously discussed the single layer case at the Dirac point this energy current will now scatter the χ_v^{by} mode.

After this simple picture it is worth to actually look at the Hall drag result simplified for the case of $\mu_b = 0$:

$$\rho_{xy}^D = \frac{2}{e^2} \frac{y}{B_0^a B_0^b} \frac{C^b I_G^a}{(B_2^a + B_2^b) [(B_1^a I_G^a + (T\tau_{ad})^{-1})]} \quad \text{with } I_G^a = B_1^a I_{tr}^a \quad \text{and } C^b = B_0^b. \quad (8.36)$$

In this expression the nominator corresponds exactly our second pathway since the magnetic field appears via C^b , which knows about the magnetic field of layer b only, B_1^a corresponds to the χ_p^{ax} component of the driving current and I_{tr}^a knows about the collision kernel creating the thermalization.

The symmetry of the drag resistivity (7.23) (see Sec. 7.2.1) looks completely different from that of the Hall drag. But since the Hall drag is a transresistivity it has to obey the even symmetry with respect to the axes $\mu_a = \mu_b$ physically reflecting that the layers can be distinguished only by the layer-dependent parameters we included, μ_α and τ_{dis}^α . To analyze further properties we utilize the following replacement rules:

$$I_G^\alpha \xrightarrow{\mu_\alpha \rightarrow -\mu_\alpha} -I_G^\alpha, \quad I_G^\alpha \xrightarrow{\mu_{-\alpha} \rightarrow -\mu_{-\alpha}} I_G^\alpha, \quad B_n^\alpha \xrightarrow{\mu_\alpha \rightarrow -\mu_\alpha} (-1)^n B_n^\alpha, \quad C^\alpha \xrightarrow{\mu_\alpha \rightarrow -\mu_\alpha} C^\alpha, \quad (8.37)$$

In contrast to the Coulomb drag resistivity (7.23) The Hall drag does not obey any symmetry with respect to the axes, instead it appears to be an odd function under simultaneous sign change of the chemical potential of both layers. Therefore, due to the even symmetry with respect to the axes $\mu_a = \mu_b$, the Hall drag has an odd symmetry with respect to the axes $\mu_a + \mu_b = 0$. The fact that the Hall drag has a different symmetry as compared to the Coulomb drag is somewhat clear, since the magnetic field appears in linear response, causing one single distinct change in the symmetry properties when changing the direction the modes point to. If we focus on the symmetry axis $\mu_a + \mu_b = 0$, around which the Hall drag behaves as an odd function, we might think about the vanishing of the Hall drag as a cancellation of the two pathways we have described earlier. In Fig. 8.3 this vanishing can be understood when we remind ourselves again of the overall symmetry properties of the ingredients. Each layer and collision kernel stays invariant if all energies, momenta and their corresponding chemical potential change sign. This is a manifestation of the fact that the system does not distinguish between hole-like particles and electron-like particles (see the symmetry discussion in Sec. 8.3.1). The magnetic field's influence being energy sensitive forces us to change its direction in this conceptual electron-hole symmetry to keep the invariance. In this sense we can think about the cancellation of the two pathways (via χ^{ay} or via χ^{by} in Fig. 8.3) as a cancellation that comes due to opposite signs of the magnetic field, in an otherwise perfectly symmetric setup.

8.2.5 Magnetic Field Induced Drag at the Dirac Point

A quite beautiful observation can be made in Eq. (8.13), namely the change in the matrices at the Dirac point of both layers. In this situation M becomes diagonal and the only entries left in L are the those that contain A_0^α . Thus the matrices that appear are simple enough to write down in Eq. (8.17), and although the I_D is zero the combination $-y^2 L M^{-1} L$ generates an entry that serves us as an effective drag rate. From these considerations we obtain, using the usual drag resistivity for the ballistic case Eq. (7.28) a magneto drag resistivity at the Dirac point of both layers that reads:

$$\rho_D = -\frac{2}{e^2} \frac{y^2}{B_2^a z_a + B_2^b z_b} = -\frac{2}{T^2} \frac{B^2}{\frac{B_2^a}{T\tau_{\text{dis}}^a} + \frac{B_2^b}{T\tau_{\text{dis}}^b}}, \quad (8.38)$$

with B being the magnetic field. A peculiarity of this feature is its appearance with a negative sign independent of the sign of the magnetic field or the chemical potentials.

In the discussion of the previous Sec. 8.2.4 this feature is easily understood. To do so we will consider both layers at the Dirac point. Driving an electric current in x direction in layer a then corresponds only to the χ_v mode being driven (see Fig. 8.3), in analogy to the previous section the magnetic field scatters this mode into a pure energy current. This energy current going in y direction thermalizes with the second layer, inducing the same energy current there. Subsequently this energy current in y direction in layer b scatters again with the magnetic field into an electric current pointing in x direction. In this scenario a thermalization like mechanism is crucial, and a suited test to verify this can be found by using the non-thermalized equations given in Eq. (C.16). Performing the calculation we obtain a magneto drag resistivity, that reads:

$$\rho_D = -\frac{2}{e^2} \frac{y^2 I_E}{I_E (B_2^a z_a + B_2^b z_b) + \frac{B_2^a B_2^b z_a z_b}{N_a N_b}} \propto -\frac{B^2 \tau_{\text{dis}}}{T^2} \frac{\alpha_g^2 \ln(1/\alpha_g)}{\alpha_g^2 N T \ln(1/\alpha_g) + \tau_{\text{dis}}^{-1}}. \quad (8.39)$$

One sees that depending on the strength of thermalization the result varies. In this regard this result

provides an excellent litmus test for the thermalization hypothesis of an experimental setup. The comparison with experiment given in Fig. 8.4 shows a very good agreement.

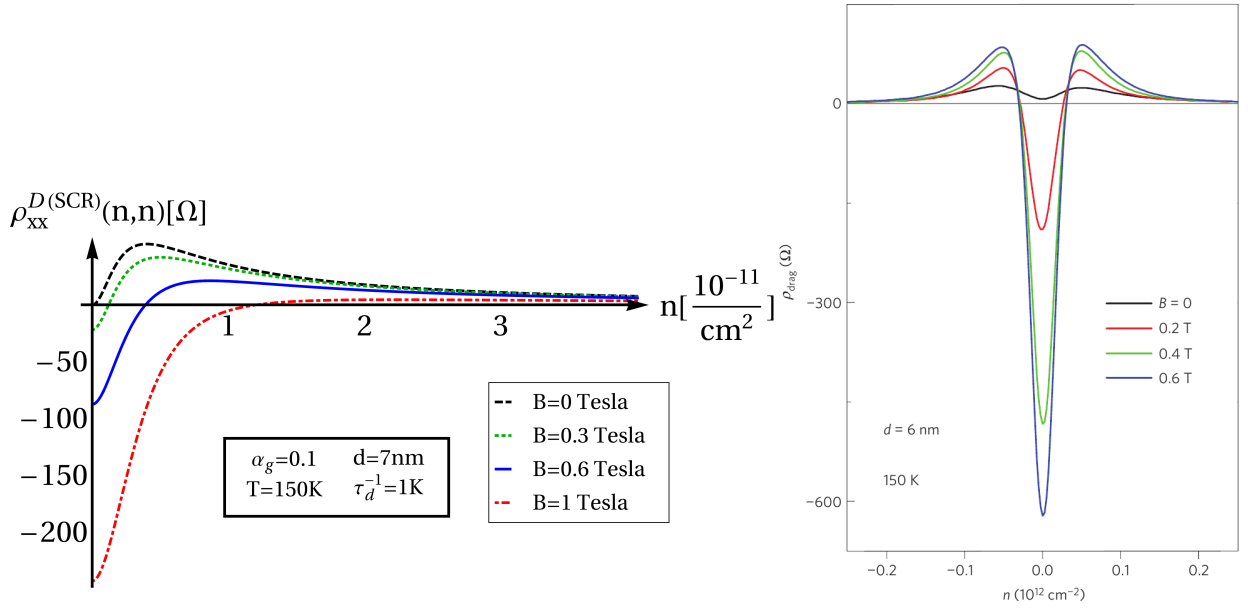


Figure 8.4: *Left:* The magnetodrag resistivity for equal concentration varying the strength of the magnetic field. *Right:* The magneto drag resistivity measured by the authors of Ref. [108]

The peak at the Dirac point is very well described within our theory as one can see in Fig. 8.4. It is worth to note that the experimental data suggests that their measurements are slightly above the field strength we can describe without the need to deal with Landau-levels, since the peak shows already saturation effects. Further the side peaks in the experiment increase in contrast to our estimation. We assume, that this discrepancy arises from the experimental setting being rather in the ballistic than hydrodynamic regime. Thus, the magnetodrag in the hydrodynamic regime seems to differ from the ballistic regime. Further investigation of the interplay of different regimes and comparison with the experiment is needed, which is work in progress (see Chap. 9).

8.2.6 Comparison to Experiment

From private communications with the group of Andre Geim [115] we know that Hall drag measurements are currently in progress which is why we will give here some more detailed data to compare with.

Again we use the relation given in Eq. (7.34) to transform the chemical potential into concentration. For the same reasons, that have been explained in Sec. 7.2.3 we vary distance and temperature simultaneously. The Hall drag resistivity is plotted in the left of Fig. 8.5.

One of the most interesting features shown in our data in the left-hand side of Fig. 8.5 is the sign change that occurs away from the Dirac point. The unpublished data kindly provided by the group of Andre Geim [115] right-hand side of Fig. 8.5 exhibits exactly such a sign change, a strong support of the theory presented here. Furthermore the experiment shows the disappearance of the Hall drag

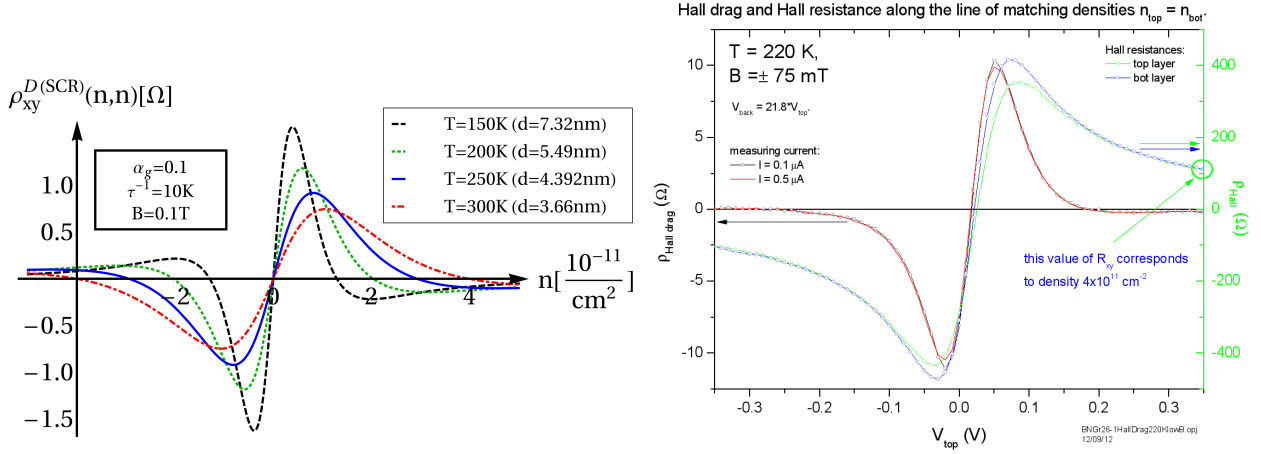


Figure 8.5: *Left:* The Hall drag resistivity for equal concentration varying temperature and distance. *Right:* Unpublished data, a courtesy of the group of Andre Geim, showing measurements of the Hall drag [115].

along the line $n_a + n_b = 0$, when the concentrations equal up to the sign. Thus, the experimental data matches very well with the theory we presented in this work. Nonetheless, further experimental data is needed to perform a complete comparison of theory and experiment, which is left as an ongoing work (see Chap. 9).

8.3 Higher-Order Drag

In the previous Secs. 7.2.3 and 8.2.6 we introduced the first experimental observations on Coulomb drag in graphene. These first experimental measurements have been performed by the authors of Refs. [107, 108]. The overall behavior of the drag is in qualitative agreement with the here presented theory (see Chap. 7.2.3) except of one detail. The authors of Ref. [107] found that at low temperature a non-vanishing, even peaked, Coulomb drag appears at the Dirac point of both layers (see left hand side of Fig. 7.8). This section is devoted to the question of the possible origin of this Coulomb drag at the Dirac point. First we will investigate why the theory presented so far fails to describe the feature at the charge neutrality point. Subsequently we will explain how to overcome this problem.

8.3.1 The Vanishing of the Leading Order

The investigation of the symmetry of the Coulomb drag resistivity is performed using the objects we have derived so far. There are several ways to discuss the symmetries of the leading order Coulomb drag. One example is the diagrammatic language [91, 103]. For consistency we rather study the kinetic equation, in particular the collision kernel. The collision kernel for two-layers Eq. (7.8) has been derived in App. A.2.

We write again the collision kernel from Eq. (7.8):

$$W^{\alpha\beta}(\{x_i\}) = 2\pi\delta(\epsilon_1 - \epsilon_2 + \epsilon_{1'} - \epsilon_{2'}) (2\pi)^2 \delta(\epsilon_1 \vec{v}_1 - \epsilon_2 \vec{v}_2 + \epsilon_{1'} \vec{v}_{1'} - \epsilon_{2'} \vec{v}_{2'}) \times \\ \times \frac{|\langle x_1, x_2 | U^{\alpha\beta} | x_{1'}, x_{2'} \rangle|^2 \nu(\epsilon_1) \nu(\epsilon_2) \nu(\epsilon_{1'}) \nu(\epsilon_{2'})}{16 \cosh(\frac{\epsilon_1 - \mu_\alpha}{2T}) \cosh(\frac{\epsilon_2 - \mu_\alpha}{2T}) \cosh(\frac{\epsilon_{1'} - \mu_\beta}{2T}) \cosh(\frac{\epsilon_{2'} - \mu_\beta}{2T})}, \quad (8.40)$$

The basic symmetry we need to consider within the collision kernel is seen by interchanging $\epsilon_1 \rightarrow -\epsilon_2$, $\epsilon_2 \rightarrow -\epsilon_1$ and $\vec{v}_1 \leftrightarrow \vec{v}_2$. The energy and momentum conservation, via the delta constraints, and the density of states stay unchanged. The matrix element Eq. (A.19) contains the Berry phase and the interaction propagator. The Berry phase (see Eq. (5.15) for the representation in terms of \vec{v}_1 and \vec{v}_2) stays as well unchanged and since the interaction is a function of $\vec{q} = \epsilon_1 \vec{v}_1 - \epsilon_2 \vec{v}_2$ and $\omega = \epsilon_1 - \epsilon_2$ the propagator is also unchanged. The only place in the collision integral where something changes is within the hyperbolic cosines that originate from the Fermi distribution function (see App. A.3). Since the hyperbolic cosine is an even function, the interchanges result in the mapping $\mu_\alpha \rightarrow -\mu_\alpha$. The transformation behavior of the collision kernel could have been guessed since the symmetry operation corresponds to an inversion of the spectrum. Which due to electron-hole symmetry of the spectrum leaves naturally the collision kernel invariant except for the distribution functions. The crucial observation is now that the collision kernel is invariant with respect of the transformation $\epsilon_1 \rightarrow -\epsilon_2$, $\epsilon_2 \rightarrow -\epsilon_1$ and $\vec{v}_1 \leftrightarrow \vec{v}_2$ if the chemical potential is zero, $\mu_\alpha = 0$. The analog argument can be performed using the primed coordinates in all symmetry operations. This way the discussion affects μ_β instead of μ_α .

So far we identified a possible symmetry of the integral kernel if one layer is tuned to the Dirac point. What needs to be resolved is how this symmetry effects the drag resistivity if one of the layers reaches the Dirac point. The drag resistivity (7.23) simplifies substantially in the ballistic case, Eq. (7.28). In this limit the resistivity is determined by the coefficients B_0 given in Eq. (7.19) and I_D . The coefficients B_0 have neither zeros nor singularities. Hence, we have to analyze the drag rate related integral I_D which is defined in Eq. (7.13) but for convenience given again:

$$I_D = -\frac{1}{2T^3} \int d\{x_i\} W^{a,b}(\{x_i\}) (\vec{v}_1 - \vec{v}_2) (\vec{v}_{1'} - \vec{v}_{2'}). \quad (8.41)$$

Within this integral again we encounter the integral kernel (7.8). However, I_D involves additionally $\vec{v}_1 - \vec{v}_2$ (and the primed version) that describes the velocity transfer between the layers. In case that one of the layers e.g. layer a , is at the Dirac point the replacements $\epsilon_1 \rightarrow -\epsilon_2$, $\epsilon_2 \rightarrow -\epsilon_1$ and $\vec{v}_1 \leftrightarrow \vec{v}_2$ keep the integral kernel $W^{\alpha\beta}(\{x_i\})$ invariant but it interchanges the velocities $\vec{v}_2 - \vec{v}_1$, which creates a sign change indicating that the integral in its entirety is zero. The vanishing of the velocity transfer rate is due to the electron hole symmetry at the Dirac point [91, 103].

Alternatively one may study the diagrams that are related to the Coulomb drag. In App. A.2 we derive the collision integral from Keldysh diagrammatics which allows us to identify the these related diagrams. It turns out that the ansatz (7.12) leads to vertices within the diagrammatic formulation. With these vertices we can rewrite I_D into the expressions given in Eq. (C.24) where the appearing Γ s correspond to the triangles shown in Fig. 8.6. The reason for this diagram to vanish is the same as for the collision kernel but can be applied for each vertex Γ separately (see Eq. (C.22)). Still it is worth having the analogy to the diagrammatic language in mind since we will use it in the next section.

When we consider the hydrodynamic limit we get an additional contribution, which led to the drag

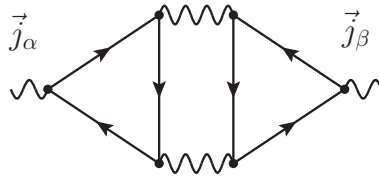


Figure 8.6: *The lowest order drag diagram also known as Aslamazov Larkin diagram.*

resistivity (7.29) that does not necessary involve I_D :

$$\rho_D = \frac{2}{e^2} \frac{B_1^a I_{\text{Tr}}^a B_1^b I_{\text{Tr}}^b}{B_0^a B_0^b \left[(B_1^a)^2 I_{\text{Tr}}^a + (B_1^b)^2 I_{\text{Tr}}^b + \frac{B_2^a + B_2^b}{T \tau_{\text{ad}}} \right]}. \quad (8.42)$$

The crucial point here is that at the Dirac point the coefficients B_1 vanish as well. The reason for this is rather simple and lies in the fact that firstly the coefficients $B_1 \sim A_1$ and secondly as we showed in Eq. (5.34) the coefficients A_1 describes to the overlap of the velocity mode with the zero mode. However, at the Dirac point the two modes are orthogonal (see Sec. 5.2.3) which means that the additional contribution disappears as long as some impurity scattering is present.

In total this means that at the Dirac point of either one of the layers the Coulomb drag is zero due to the inability of the system to transfer velocity between the layers (electron hole symmetry) and due to the fact that velocity and zero mode are orthogonal to each other (see Sec. 7.2.1 for the exception to this in the clean case). The latter means that the electrical current is then purely given by the velocity mode and although we have thermalization, meaning that the zero modes of the layers stay connected, they do not influence the electronic properties.

With this understanding of the symmetry of the Coulomb drag resistivity we will now continue to investigate higher-order corrections.

8.3.2 The Changes Due to Higher Order-Drag

In Sec. 8.3.1 we discussed why we are not able to see anything but zero transresistivity at the Dirac point of both layers in absence of the magnetic field (except for the clean limit discussed in Sec. 7.2.1). In the experiment reported in Ref. [107], this feature appeared for small temperatures which, before we even start to speculate about its origin, means that, if we can describe this feature within the developed technique, it is more likely to be described in the ballistic regime then inside the hydrodynamic one. So utilizing the discussion of the previous Sec. 8.3.1, we know that in the ballistic limit the Coulomb drag resistivity gains its sign changes from the drag rate related integral I_D . For this integral we showed explicitly that the particle hole symmetry causes it to vanish at the Dirac point. Hence sub-leading terms become important, which is why we need to consider corrections to the drag related integral that break this particle hole symmetry.

The most straightforward approach to this problem is to look for higher order corrections in the Coulomb interaction. For this purpose we consider a higher order self-energy that is able to provide a contribution to the drag rate related integral i.e. to have a closed bubble that could belong to a different layer see Fig. A.4. In App. A.2.2 we determine the Keldysh self-energy of such a diagram and show how to form a collision kernel out of it. The calculations for this are straightforward but

lengthy and therefore performed completely in the appendix. The main result of these considerations are found in Eq. (A.41) which explains how the previous matrix element within the collision kernel changes by adding higher order contributions.

The collision integral we discussed previously is altered now compared to the higher-order collision kernel in the matrix element $|\mathcal{M}_0|^2 \rightarrow |\mathcal{M}_0|^2 + \mathcal{M}_0\mathcal{M}_1^* + \mathcal{M}_0^*\mathcal{M}_1$ implying that we can adapt the complete discussion from the previous section except that we need to test the matrix element for particle hole symmetry. For this reason we write explicitly the matrix element from Eq. (A.41)

$$\begin{aligned}
 & \mathcal{M}_0\mathcal{M}_1^* + \mathcal{M}_0^*\mathcal{M}_1 \\
 &= \frac{-\pi}{4^2} D_0(\vec{q}_1) \sum_{\lambda_3\lambda_{3'}} \int \frac{d^2q_2}{(2\pi)^2} \frac{d\omega_2}{2\pi} \left[1 + \vec{v}_1\vec{v}_2 + (\vec{v}_1 + \vec{v}_2) \lambda_3 \frac{\vec{p}_3}{|\vec{p}_3|} \right] \left[1 + \vec{v}_{1'}\vec{v}_{2'} + (\vec{v}_{1'} + \vec{v}_{2'}) \lambda_{3'} \frac{\vec{p}_{3'}}{|\vec{p}_{3'}|} \right] \times \\
 & \times D_0(\vec{q}_2 - \vec{q}_1) D_0(-\vec{q}_2) \left[\delta(\epsilon_3 - \lambda_3|\vec{p}_3|) \mathbb{P} \frac{\tanh\left(\frac{\epsilon_3 - \mu_\alpha}{2T}\right)}{\epsilon_{3'} - \lambda_{3'}|\vec{p}_{3'}|} + \delta(\epsilon_{3'} - \lambda_{3'}|\vec{p}_{3'}|) \mathbb{P} \frac{\tanh\left(\frac{\epsilon_{3'} - \mu_\beta}{2T}\right)}{\epsilon_3 - \lambda_3|\vec{p}_3|} \right] \quad (8.43)
 \end{aligned}$$

where the energies obey $\epsilon_3 = \epsilon_1 - \omega_2$ and $\epsilon_{3'} = \epsilon_{1'} + \omega_2$ and the momenta $\vec{p}_3 = \epsilon_1\vec{v}_1 - \vec{q}_2$ and $\vec{p}_{3'} = \epsilon_{1'}\vec{v}_{1'} + \vec{q}_2$ and for brevity $\lambda_\alpha = \text{sign}(\epsilon_\alpha)$. Further \mathbb{P} indicates the principal value integral. A detailed analysis of this matrix element has not yet been done but is not necessary for investigating its particle hole symmetry properties. Again we consider the exchange $\epsilon_1 \rightarrow -\epsilon_2$, $\epsilon_2 \rightarrow -\epsilon_1$ and $\vec{v}_1 \leftrightarrow \vec{v}_2$ as before. The transferred momentum \vec{q}_1 stays invariant but the energies change like $\epsilon_3 = -\epsilon_2 - \omega_2 = -\epsilon_1 + \omega_1 - \omega_2$ and $\epsilon_{3'} = -\epsilon_{1'} - \omega_1 + \omega_2$ and the momenta transform correspondingly. Each try to avoid the additional contributions fails due to the total energy $\epsilon_1 + \epsilon_{1'}$ or the corresponding total momentum $\vec{p}_1 + \vec{p}_{1'}$ that enters the process. The total energy flowing through the matrix element can be understood more easily by means of the diagrammatic language in the right hand side of Fig. 8.7. If the total momentum and

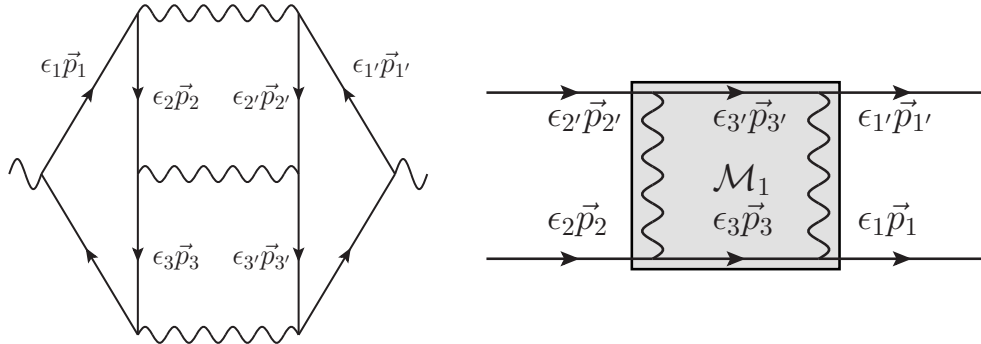


Figure 8.7: *Left:* Higher order Coulomb drag diagram with the corresponding energy and momenta labeling. *Right:* The matrix element that appears within the higher order kinetic equation.

energy is zero, we have $\epsilon_3 = -\epsilon_{3'}$ and $\vec{p}_3 = -\vec{p}_{3'}$. If we perform the integral substitution in the latter case we in dead see that the matrix element stays invariant. On the other hand, in this situation the matrix element can diverge, a possible indication of an exciton condensation. Nevertheless the matrix element from Eq. (A.41) allows contributions to I_D that do not vanish at the Dirac point. If we assume

to be close to the Dirac point we read

$$I_D = C_D \alpha_g^2 \frac{\mu_a \mu_b}{(2T)^2} + C_{\text{hoD}} \alpha_g^3 \quad (8.44)$$

which affects the drag resistivity (see Eq. (7.23)) such that for $\mu \ll \alpha_g^{1/2} T$ and $1 \gg T \tau_{\text{dis}}$ we read:

$$\rho_D \propto \frac{1}{e^2} \frac{\tilde{C}_{\text{hoD}} \alpha_g^3 T + \tilde{C}_1 \alpha_g^4 \mu_a \mu_b \tau_{\text{dis}} N}{T + \tilde{C}_2 \alpha_g^2 \mu_a \mu_b \tau_{\text{dis}} N}. \quad (8.45)$$

Exactly at the Dirac point this yields:

$$\rho_D \propto \frac{\alpha_g^3}{e^2} \quad (8.46)$$

This changes the phase diagram we introduced previously as shown in Fig. 8.8. Thus, the higher order contribution allows for a drag resistivity at the Dirac point. Away from the Dirac point one notes, that as shown in Fig. 8.8 approaching the clean limit thermalization takes over and overcomes completely the contributions from I_D and therefore replacing the α_g^3 contribution by α_g^2 .

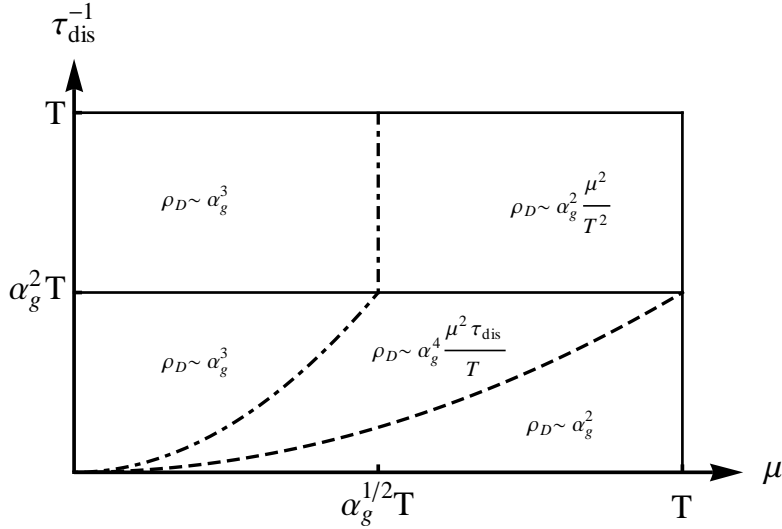


Figure 8.8: The drag coefficients in case of identical layers considering the higher order drag contribution from Coulomb interaction. The dash-dotted line separates the previous results (see Fig. 7.6) from the higher order drag.

Diffusive Regime

Throughout this work we focused on the limit $T \tau_{\text{dis}} \gg 1$ and even more $\alpha_g^2 T \tau_{\text{dis}} \gg 1$ where we found the thermalization between the layers. Since the resistivity peak at the Dirac point is seen experimentally we will qualitatively discuss the consequence for the peak expected from the diffusive regime.

For stronger disorder or at low temperatures $T \tau_{\text{dis}} \ll 1$, the electron motion becomes diffusive. In this regime, the standard perturbative approach is applicable. The lowest-order perturbative calculation [89] amounts to evaluation of the Aslamasov-Larkin-type diagram (see Fig. 8.6) for the drag

conductivity given by

$$\sigma_D^{\alpha\beta} = \frac{1}{16\pi T} \sum_{\vec{q}} \int \frac{d\omega}{\sinh^2 \frac{\omega}{2T}} \Gamma_1^\beta(\omega, \vec{q}) \Gamma_2^\alpha(\omega, \vec{q}) |D^R|^2, \quad (8.47)$$

where D^R is the retarded propagator of the inter-layer interaction Eq. (6.10) (not necessarily screened) and $\Gamma_a^\alpha(\omega, \vec{q})$ is the non-linear susceptibility (similar to Eq. (C.22)) [in fact, all previous studies of the Coulomb drag in graphene [63, 101, 103, 104, 116, 117] focused on Eq. (8.47)]. In the diffusive regime, $\Gamma_a^\alpha(\omega, \vec{q})$ can be found using the Ohm's law and the continuity equation [118] $\vec{\Gamma} = e\vec{q}(\partial\sigma/\partial n)\text{Im}\Pi^R$. All microscopic details are now encoded in the diffusion coefficient and the density dependence of the single-layer conductivity σ . Close to the Dirac point $\mu \ll T \ll \tau_{\text{dis}}^{-1}$ the derivative $\partial\sigma/\partial n \sim nv_F^4\tau_{\text{dis}}^4$ (independently of the precise nature of impurities). After this the evaluation of Eq. (8.47) is rather standard (except that, in contrast to Ref. [89], the Thomas-Fermi screening length is much longer than the inter-layer spacing $\kappa d \ll 1$) and yields

$$\rho_D^{(2)}(\mu_i \ll T \ll \tau_{\text{dis}}^{-1}) \sim (h/e^2)\alpha^2\mu_1\mu_2 T\tau_{\text{dis}}^3, \quad (8.48)$$

vanishing at $\mu_i = 0$ due to the electron-hole symmetry.

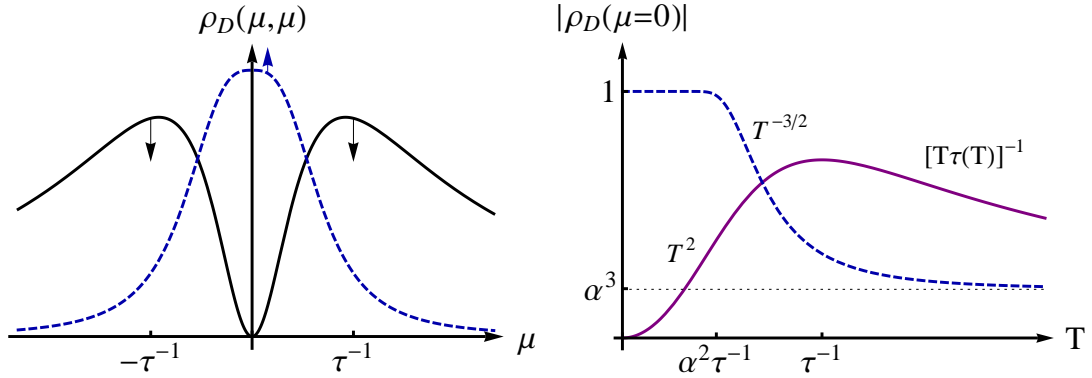


Figure 8.9: Schematic view of the drag coefficient at low temperatures. **Left:** $\rho_D^{(2)}(\mu)$ (solid line) and $\rho_D^{(3)}(\mu)$ (blue dashed line). The arrows indicate the tendency of the two terms with the decrease of temperature $T \rightarrow 0$. **Right:** $\rho_D^{(3)}(\mu = 0)$ and $\rho_D^{\text{corr}}(\mu = 0)$ (solid line) as functions of T .

The importance of the electron-hole asymmetry for $\rho_D^{(2)}$ follows from Eq. (8.47): the non-linear susceptibility can be thought of as a measure of the asymmetry. But $\rho_D^{(2)}$ dominates the observable effect only under standard assumptions of the Fermi-liquid behavior in the two layers ($\mu \gg v_F/d \gg T$, $\mu\tau \gg 1$). On the contrary, in the vicinity of the Dirac point in graphene, the next-order contribution $\rho_D^{(3)}$ [91] as well as disorder correlations [96] (see App. D) become important and yield non-zero drag at $\mu_i = 0$.

The explicit results of Ref. [91] were obtained in the usual limit $\kappa d \gg 1$. Extending these calculations to the opposite case $\kappa d \ll 1$ we find close to the Dirac point

$$\rho_D^{(3)}(\mu_i \ll T \ll \tau_{\text{dis}}^{-1} \ll \alpha^{-2}T) \sim (h/e^2)\alpha^3(T\tau_{\text{dis}})^{-3/2}, \quad (8.49)$$

and $\rho_D^{(3)} \sim h/e^2$ for $\tau_{\text{dis}}^{-1} \gg \alpha^{-2}T$. Away from the Dirac point this contribution decays as a function of the chemical potential $\rho_D^{(3)}(\mu\tau_{\text{dis}} \gg \max[1, \alpha^{-1}(T\tau_{\text{dis}})^{1/2}]) \sim (h/e^2)(\mu\tau_{\text{dis}})^{-3}$ and rapidly becomes subleading. As a result, $\rho_D^{(3)}$ is only detectable at low T and μ , see Fig. 8.9.

While estimating $\rho_D^{(3)}(\mu_i = 0)$, we assume the single-layer conductivity $\sigma \sim e^2/h$ discarding localization effects. Indeed, experiments on high-quality samples show T -independent σ down to $T = 30$ mK [119], that can be explained by the specific character of disorder in graphene [84, 120, 121].

Although this estimation unveiled interesting and experimentally relevant dependencies the considerations done here are not complete. A detailed analysis of the interplay of the effects governing the resistivity at the Dirac point remain to be performed and promises rich physics to investigate (see outlook Sec. 9).

8.4 Drude-Like Picture for Drag

We have seen the kinetic equation as an effective approach to graphene-based drag setups. Using the modes, the ansatz (7.12) provided us with, we have written the effective kinetic equations in a compact and elegant way (see Eqs. (7.15) and (8.13)). Nonetheless with help of the currents Eq. (5.42) we might rotate our equations, written in terms of χ modes towards an equation involving only currents. In the thermalized case we can use:

$$\begin{pmatrix} \vec{j}^{a\beta} \\ \vec{j}^{b\beta} \\ \vec{j}_E^\beta \end{pmatrix} = \begin{pmatrix} \frac{e^2}{2} N_a A_0^a & 0 & \frac{e^2}{2} N_a A_1^a \\ 0 & \frac{e^2}{2} N_b A_0^b & \frac{e^2}{2} N_b A_1^b \\ \frac{eT}{2} N_a A_1^a & \frac{eT}{2} N_b A_1^b & \frac{eT}{2} (N_a A_2^a + N_b A_2^b) \end{pmatrix} \begin{pmatrix} \chi_v^{a\beta} \\ \chi_v^{b\beta} \\ \chi_p^\beta \end{pmatrix}. \quad (8.50)$$

Performing the rotation does not affect the physics we described. It also will not help in calculating the drag resistivity or Hall drag resistivity. What it will allow us though, is to express the effective kinetic equations in terms of currents. On the level of an effective equation such a formulation is clearly more natural and fits nicely into the Drude picture introduced in Sec. 6.1.1, although it is equivalent to the compact equations we introduced in Eqs. (7.15) and (8.13).

The Drude-like Drag

The rotation introduced in Eq. (8.50) will provide us a formulation in terms of constant currents. From the point of view of hydrodynamic fields (5.42) we consider the current to constant effectively decoupling current from the continuity equations. Performing the Rotation one obtains:

$$\frac{e^2}{2} B_0^a \vec{E}_a + \frac{e}{T} \vec{j}_E \frac{I_G^a}{B_2^a + B_2^b} = \vec{j}^a \left(\frac{I_{\text{tr}}^a}{B_0^a} + \frac{B_1^a I_G^a}{N_a (B_2^a + B_2^b)} + \frac{z_a}{N_a} \right) + \vec{j}^b \left(\frac{I_D}{B_0^b} + \frac{B_1^b I_G^a}{N_b (B_2^a + B_2^b)} \right) \quad (8.51)$$

$$\frac{e^2}{2} B_0^b \vec{E}_b + \frac{e}{T} \vec{j}_E \frac{I_G^b}{B_2^a + B_2^b} = \vec{j}^a \left(\frac{I_D}{B_0^a} + \frac{B_1^a I_G^b}{N_a (B_2^a + B_2^b)} \right) + \vec{j}^b \left(\frac{I_{\text{tr}}^b}{B_0^b} + \frac{B_1^b I_G^b}{N_b (B_2^a + B_2^b)} + \frac{z_b}{N_b} \right) \quad (8.52)$$

$$\frac{eT}{2} B_0^a B_1^a \vec{E}_a + \frac{eT}{2} B_0^b B_1^b \vec{E}_b = \frac{T}{e} \frac{B_1^a B_2^b (z_a - z_b)}{B_2^a + B_2^b} \left(\frac{\vec{j}^a}{N_a} - \frac{\vec{j}^b}{N_b} \right) + \vec{j}_E \frac{B_2^a z_a + B_2^b z_b}{B_2^a + B_2^b}. \quad (8.53)$$

Where we used the short-hand notation introduced for the drag resistivity in Eq. (7.13), further we use Eqs. (7.19), (7.21) and $z_\alpha T \tau_{\text{dis}}^\alpha = 1$ for further simplifications. For orientation we will repeat the short-hand notations starting with the integrals:

$$\begin{aligned}
I_{\text{Intra}}^\alpha &= \frac{1}{4T^3} \int d\{x_i\} W^{\alpha,\alpha}(\{x_i\}) (\vec{v}_1 - \vec{v}_2 + \vec{v}_3 - \vec{v}_4)^2, & I_{\text{Inter}}^{\alpha\beta} &\stackrel{\alpha \neq \beta}{=} \frac{1}{2T^3} \int d\{x_i\} W^{\alpha,\beta}(\{x_i\}) (\vec{v}_1 - \vec{v}_2)^2, \\
I_{\text{D}} &= -\frac{1}{2T^3} \int d\{x_i\} W^{a,b}(\{x_i\}) (\vec{v}_1 - \vec{v}_2) (\vec{v}_3 - \vec{v}_4), & I_{\text{Th}}^{\alpha\beta} &\stackrel{\alpha \neq \beta}{=} \frac{1}{2T^4} \int d\{x_i\} W^{\alpha,\beta}(\{x_i\}) (\vec{v}_1 - \vec{v}_2) \vec{q}, \\
I_{\text{Tr}}^\alpha &= I_{\text{Intra}}^\alpha + \sum_{\beta \neq \alpha} \frac{N_\beta}{N_\alpha} I_{\text{Inter}}^{\alpha\beta}, & I_{\text{E}} &= \frac{1}{2T^5} \int d\{x_i\} W^{ab}(\{x_i\}) \vec{q}^2 \quad \text{and} \quad A_n^a = - \int dx \frac{\nu(\epsilon)}{T} \frac{\partial n_F^\alpha(\epsilon)}{\partial \epsilon} \left(\frac{\epsilon}{T} \right)^n,
\end{aligned} \tag{8.54}$$

the scattering phase-space moments (see end of Sec. 7.2)

$$A_0^\alpha = B_0^\alpha, \quad B_1^\alpha = N_\alpha \frac{A_1^\alpha}{A_0^\alpha}, \quad B_2^\alpha = N_\alpha A_2^\alpha - A_1^\alpha B_1^\alpha \quad \text{and} \tag{8.55}$$

the averaged impurity scattering rate

$$\frac{B_2^a + B_2^b}{T \tau_{\text{ad}}} = \frac{B_2^a}{T \tau_{\text{dis}}^a} + \frac{B_2^b}{T \tau_{\text{dis}}^b} \tag{8.56}$$

and the effective Coulomb scattering rate

$$(T \tau_0)^{-1} = \frac{1}{B_2^a + B_2^b} \left[(B_1^a)^2 I_{\text{Tr}}^a + (B_1^b)^2 I_{\text{Tr}}^b - 2B_1^a B_1^b I_{\text{D}} \right] = \frac{B_1^a I_{\text{G}}^a + B_1^b I_{\text{G}}^b}{B_2^a + B_2^b}. \tag{8.57}$$

Finally the generalized rate, which is given by

$$I_{\text{G}}^\alpha = B_1^\alpha I_{\text{Tr}}^\alpha - B_1^{-\alpha} I_{\text{D}}. \tag{8.58}$$

A comparison with Eq. (6.3) unveils that the main difference arises from the total energy current that corresponds to an independent degree of freedom mixing the currents and creates contributions beyond I_{D} . In this sense this Drude-like equation for the two-layer system summarizes in a very compact way the complete physical picture that governs transport in two graphene layers. Further we see on the level of the Drude-like equation (8.51) already that, in comparison to usual Drude picture, the thermalization creates additional contributions to the drag, since I_{D} appears not exclusively as interlayer coupling.

The Drude-like Hall Drag

Analogous to the previous section we can perform the same rotation for the x and the y direction in presence of a magnetic field. Thus collecting all the ingredients we arrive at:

$$\begin{aligned}
\frac{e^2}{2} B_0^a \vec{E}_a + \frac{e}{T} \vec{j}_E \frac{I_{\text{G}}^a}{B_2^a + B_2^b} &= \vec{j}^a \left(\frac{I_{\text{tr}}^a}{B_0^a} + \frac{B_1^a I_{\text{G}}^a}{N_a (B_2^a + B_2^b)} + \frac{z_a}{N_a} \right) + \vec{j}^b \left(\frac{I_{\text{D}}}{B_0^b} + \frac{B_1^b I_{\text{G}}^a}{N_b (B_2^a + B_2^b)} \right) \\
&+ \frac{\vec{B}}{T^2} \times \left[e \vec{j}^a \left(\frac{B_0^a - C^a}{B_0^a B_1^a} - \frac{B_1^a C^a}{N_a (B_2^a + B_2^b)} \right) - e \vec{j}^b \frac{B_1^a C^a}{N_b (B_2^a + B_2^b)} + \frac{e^2 \vec{j}_E}{T} \frac{C^a}{B_2^a + B_2^b} \right], \tag{8.59}
\end{aligned}$$

$$\begin{aligned} \frac{e^2}{2} B_0^b \vec{E}_b + \frac{e}{T} \vec{j}_E \frac{I_G^b}{B_2^a + B_2^b} &= \vec{j}^a \left(\frac{I_D}{B_0^a} + \frac{B_1^a I_G^b}{N_a (B_2^a + B_2^b)} \right) + \vec{j}^b \left(\frac{I_{\text{tr}}^b}{B_0^b} + \frac{B_1^b I_G^b}{N_b (B_2^a + B_2^b)} + \frac{z_b}{N_b} \right) \\ &+ \frac{\vec{B}}{T^2} \times \left[-e \vec{j}^a \frac{B_1^b C^b}{N_a (B_2^a + B_2^b)} + e \vec{j}^b \left(\frac{B_0^b - C^b}{B_0^b B_1^b} - \frac{B_1^b C^b}{N_b (B_2^a + B_2^b)} \right) + \frac{e^2}{T} \vec{j}_E \frac{C^b}{B_2^a + B_2^b} \right], \end{aligned} \quad (8.60)$$

$$\frac{eT}{2} B_0^a B_1^a \vec{E}_a + \frac{eT}{2} B_0^b B_1^b \vec{E}_b = \frac{T}{e} \frac{B_1^a B_1^b (z_a - z_b)}{B_2^a + B_2^b} \left(\frac{\vec{j}^a}{N_a} - \frac{\vec{j}^b}{N_b} \right) + \vec{j}_E \frac{B_2^a z_a + B_2^b z_b}{B_2^a + B_2^b} + \frac{\vec{B}}{T} \times [\vec{j}^a + \vec{j}^b]. \quad (8.61)$$

In addition to the short-hand notations Eqs. (7.13), (7.19) and (7.21), which have been used in the previous section we employ further the relation (8.21) which reads

$$C^\alpha = B_0^\alpha - A_{-1}^\alpha B_1^\alpha / N_\alpha. \quad (8.62)$$

Again the benefit of these equations is their simple Drude-like form. We observe in Eq. (8.61) that at the Dirac point the energy current and the electric current are orthogonal. This underlines again the independence of the two currents in graphene and the need to deal with both when investigating transport properties in graphene.

With these equations we managed now to regain equations in the spirit of Eqs. (6.3) and (5.1) with which we started the transport journey.

9

Chapter 9

Conclusion

In this thesis we have performed an analysis of the interplay of the Coulomb interaction with the electronic structure in graphene and its consequences for the transport properties. This chapter will summarize the results and add conclusions to this work.

Although the Coulomb interaction might be strong in graphene, we assumed that screening, e.g. due to the substrate, allows for a perturbative treatment. Furthermore, finite temperature allowed us to deal with the Coulomb interaction properly, a fact we used to investigate graphene's electronic properties at the Dirac point. Finally the kinetic equation approach enabled us to describe transport in graphene and double layer structures of graphene, which we studied towards the end.

In **Chapter 4**, we tamed the Coulomb interaction, i.e. we reformulated the problem by introducing finite temperature, which made the calculation controllable. This allowed us to treat the Coulomb interaction properly at finite temperature within the random phase approximation (RPA). We found that RPA provides an excellent way to deal with the forward scattering resonance (FSR), which at finite temperature is even more pronounced. We found the dispersion relation of plasmons, which turn out to be rather good quasi-particles, and we found that the temperature itself gives rise to static screening with a screening length of order $l_{\text{scr}} \propto (\alpha_g NT)^{-1}$. We found that due to the forward scattering resonance (FSR) the quasi-particle lifetime is substantially reduced, classifying graphene effectively as a marginal Fermi-liquid. As a consequence, close to the Dirac point (for energies $\epsilon \ll \alpha_g^2 NT$) the conceptual separation between electron-like and hole-like particles fails. On this basis, we determined the energy relaxation rate, which is logarithmically enhanced by the FSR, similarly to the quasi-particle lifetime. The quasi-particle scattering rate, the dephasing rate and the energy relaxation rate obey a non-trivial, non-monotonous behavior as a function of energy.

In **Chapter 5**, we carried out calculations for transport in graphene within the language of the kinetic equation including only the bare Coulomb interaction. We emphasized the importance of the choice of ansatz, which, based on the forward scattering resonance (FSR), corresponds to a direction dependent equilibrium, and showed how this ansatz allows for an analytic solution of the kinetic equation. We then, in the case that the chemical potential is at the Dirac point, treat the transport within the RPA in clean graphene without utilizing the ansatz. We obtained the transport scattering rate, which shows a non-monotonous energy behavior, but turned out to be smaller than the energy relaxation rate. This made it necessary to perform a thermal average of the transport scattering rate, which agreed with the previously obtained rate and conductivity obtained via the kinetic equation approach including only the bare Coulomb interaction. We finished this chapter by introducing the hydrodynamic formulation of transport in graphene and possible extensions of it.

In **Chapter 7**, we started to use the kinetic equation approach to describe Coulomb drag in a two layer graphene setup. We found the phenomenon of directional thermalization between the layers, which simplifies the direction dependent equilibria ansatz of a two layer setup. We solved the kinetic equation analytically and obtained the Coulomb drag for the hydrodynamic (ultra-ballistic) as well as for the ballistic regime, where we have a perfect agreement with previous works. We found in these equations a non-trivial interplay of velocity and momentum transfer between the layers, which led in the ultra clean limit to a non-analytic expression for the drag resistivity at the Dirac point.

Finally, in **Chapter 8**, we extended the description of the Coulomb drag in graphene. We determined the multilayer drag and the Hall drag. In the latter, the magnetic field acts as an energy selective scatterer. It thus led to interesting phenomena in the Hall resistivity, the Hall drag and even to a non-vanishing magneto-drag at the Dirac point. Towards the end of this chapter, we showed how to extend the formulation towards higher order drag and its close connection to a Drude-like formulation, which allows for a more intuitive understanding of the phenomena presented in this chapter.

The experimental developments of the last years are astonishing and support the relevance of our calculations. These include the measurements performed to determine the relaxation of hot electrons [70], which is closely related to the calculations performed in Sec. 4.2.3, as well as conductivity measurements performed on suspended graphene [86] (see Sec. 5.4.4). Furthermore, we have been very fortunate that within the last year Coulomb drag measurements with graphene have become experimentally accessible [107, 108]. In Sec. 7.2.3 we presented a comparison of our theory with experiments showing a very good agreement. A Short time after the first Coulomb drag experiments, the interplay with a magnetic field was also studied [107]. In Sec. 8.2.5, we showed that our theory is capable of explaining one of the open questions of the experimental data [107], namely the strong magnetodrag at the Dirac point. Finally in Sec. 8.2.6, we compared our result with unpublished data, courtesy of the group of Andre Geim [115], supporting very well our theory of the Hall drag.

The work that has been presented here allows for many further directions of research, of which some are already underway and publications are planned. Publication is planned for:

- the Hall drag, that has been introduced in Sec. 8.2. Since in recent times experiments started to measure the Hall drag (see Sec. 8.2.6) we aspire towards a publication with experimentalists, allowing for a detailed comparison of theory and experiment.
- the magnetodrag presented in Sec. 8.2.5 was puzzling experimentalists since their observation of the effect. A joint publication with experimentalists would again allow for a more detailed comparison of theory and experiment.
- the spin drag explained in the context of the multi-layer drag in Sec. 8.1, which promises to provide additional utilizations for graphene in the field of spintronics.

This list involves only the most advanced projects we wish to complete soon. But there are many more promising extensions we wish to study, this includes, e.g.:

- the Navier Stokes equations of graphene, which is sketched in Sec. 5.3. It will provide us with many further follow-ups. Particular interesting examples are: the possibility to analytically investigate finite system setups and to study consequences of applying non-equilibrium conditions to the system.
- a detailed investigation of the different mechanisms that govern drag at the Dirac point and the regimes they apply to (see Sec. 8.3). This is very important to understand the experimental observation at the Dirac point [108].

-
- the magnetodrag drag in the regime of Landau-level quantization.
 - drag setups involving the Dirac Fermions of 3D topological insulators.

This is of course an incomplete list of possible projects including only those we are particular interested in. The formulation presented in this work is powerful enough that we expect many more projects to arise, which crucially depend on the insights provided by this work.

In conclusion, we found that the Coulomb interaction, although treatable perturbatively, affects graphene substantially. We have seen the appearance of the forward scattering resonance (FSR), which leads to rich behavior at the Dirac point and moreover creates the direction dependent equilibrium as a general equilibration scheme to external directed perturbations of the system. In the drag setup this direction dependent equilibration caused an interplay between the layers leading to an effective thermalization of two parallel layers of graphene. Because of this direction dependent equilibration, the description of the system simplified enormously, resembling graphene specific Drude-like equations. In this sense, the FSR led to a particular elegant and simple formulation allowing us to access even rather complex graphene-based setups like the drag resistivity and the Hall drag in graphene. Already the mere fact that experiments have been performed, measuring Coulomb drag in graphene, strongly supports the relevance of this theoretical work to the field of transport in graphene. With our contribution, we have proven that complex setups can appear to be controllable and even more can be treated relatively simple by employing particular effects unique to graphene. The dynamics and the speed of the current developments in graphene suggest that the theoretical considerations we presented in this work could become relevant in multi-layered clean graphene-based applications. Furthermore, graphene's intrinsic properties that are both discovered or not yet discovered, promise that graphene research will remain an exciting and fascinating field.

A Keldysh Objects and the Kinetic Equation

A.1 Keldysh Self-energy and Keldysh Polarization Operator

In this section we provide the structural details of the Keldysh objects we use within the diagrammatic calculation. Most of the details and techniques are useful as well for the kinetic equation we consider later.

A.1.1 The Keldysh Self-energy in Lowest Order

In the beginning in Sec. 2.4.1 we faced first time the self-energy. In lowest order it appears in two possibilities namely the Hartree (left in Fig. A.1) and the Fock diagram (right in Fig. A.1). Since Hartree is usually considered to be canceled out by the ionic background of the system the contribution we will look for is the Fock diagram.



Figure A.1: The Feynman diagram for the Hartree (left) and the Fock (right) contribution to self-energy

The Self-energy reads in lowest order reads:

$$\check{\Sigma} = \langle \check{\phi}_1 \check{G}_2 \check{\phi}_2 \rangle_\phi \quad (\text{A.1})$$

with the Greens function as defined in Eq. (2.26) and the Hubbard Stratonovich field as given in Eq. (2.27). Using the correlation as they are given by Eq. (2.28) we gain:

$$\check{\Sigma} = \frac{i}{2} \begin{pmatrix} D^K G^R + D^R G^K & D^R G^R + D^K G^K + D^A G^A \\ D^A G^R + D^R G^A \stackrel{!}{=} 0 & D^A G^K + D^K G^A \end{pmatrix} \quad (\text{A.2})$$

The interaction here has been kept quite general but since we want to deal with the Coulomb interaction we need the polarization operator or a related object to gain a less singular structure of the interaction.

A.1.2 The Keldysh Polarization Operator

In analogy to the self-energy the first time the polarization operator is presented is in Sec. 2.4.1. Its appearance corresponds to the interaction propagator in the very same way the self-energy corresponds to the Green's function. Its Feynman graph can be seen in Fig. A.2. The main difference is that, the



Figure A.2: The Feynman diagram of the polarization operator

interactions we deal with have no sublattice or valley structure. Thus these degrees of freedom will be traced out. We read:

$$\begin{aligned} \text{Tr} \left[\check{G}_1 \check{\phi}_1 \check{G}_2 \check{\phi}_2 \right] &= \phi_1^c \phi_2^c \text{Tr} \left[G_1^A G_2^A + G_1^R G_2^R \right] + \phi_1^c \phi_2^q \text{Tr} \left[G_1^K G_2^A + G_1^R G_2^K \right] \\ &+ \phi_1^q \phi_2^c \text{Tr} \left[G_1^A G_2^K + G_1^K G_2^R \right] + \phi_1^q \phi_2^q \text{Tr} \left[G_1^R G_2^A + G_1^A G_2^R + G_1^K G_2^K \right], \end{aligned} \quad (\text{A.3})$$

which then forms the corresponding bosonic Keldysh polarization operator:

$$\check{\Pi} = \frac{i}{2} \begin{pmatrix} G_1^A G_2^A + G_1^R G_2^R \stackrel{!}{=} 0 & G_1^A G_2^K + G_1^K G_2^R = \Pi^A \\ G_1^K G_2^A + G_1^R G_2^K = \Pi^R & G_1^R G_2^A + G_1^A G_2^R + G_1^K G_2^K = \Pi^K \end{pmatrix}. \quad (\text{A.4})$$

Within this definition of the polarization operator we gain now

$$\check{D} = \check{D}_0 - \check{D}_0 \check{\Pi} \check{D}, \quad (\text{A.5})$$

analogous to the Dyson equation of the self-energy given in Eq. (2.32). But with the Keldysh structure of the interaction following the bosonic structure:

$$\check{D} = \begin{pmatrix} D^K & D^R \\ D^A & 0 \end{pmatrix} \quad (\text{A.6})$$

A.2 The Collision Integral

We introduced in Sec. 2.5 the formalism of the kinetic equation. We will now report on the details needed to match the kinetic equation approach with the field theoretical description. In Sec. 2.5 we derived the Liouvillian and introduced formally the collision kernel as a abstract object that reads

$$\text{LG}^K = i \left((G^R - G^A) \Sigma^K - G^K (\Sigma^R - \Sigma^A) \right). \quad (\text{A.7})$$

In Sec. 2.5 we showed how integration over either momentum or energy gives the Eilenberger or Boltzmann equation. But for the purpose of studying the integral kernel it is more useful to consider the general object on the right hand side of Eq. (A.7).

A.2.1 Coulomb interaction: Lowest Order

In equation(A.7) the appearing Greens functions are of fermionic type and have the Keldysh rotation following Larkin and Ovchinnikov (see Eq. (2.26)). The first thing to do, is therefore to find the self-energy of the system we are looking for. Within the notation $\check{\phi} = \phi_{c1}\mathbb{1} + \phi_q\sigma_1$ for the Hubbardt Stratonovich field the lowest order diagram able to create a four particle scattering process between the layers is the one forming the following self-energy illustrated in Fig. A.3:

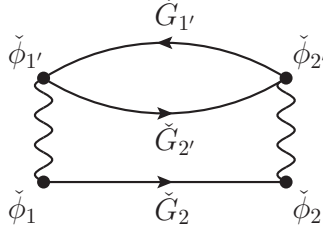


Figure A.3: Coulomb interaction correction we take into account for the drag.

$$\check{\Sigma} = - \langle \check{\phi}_1 \check{G}_2 \check{\phi}_2 \text{Tr} [\check{G}_{1'} \check{\phi}_{1'} \check{G}_{2'} \check{\phi}_{2'}] \rangle_{\phi} \quad (\text{A.8})$$

with a minus sign due to the fermionic loop.

Since we need some details on the Keldysh structure we do some straightforward matrix multiplications that will be instructive for the further treatment (see Eq. (A.3) as well).

$$\check{\phi}_1 \check{G}_2 \check{\phi}_2 = \begin{pmatrix} \phi_1^q G_2^A \phi_2^q + \phi_1^c G_2^R \phi_2^c + \phi_1^c G_2^K \phi_2^q & \phi_1^q G_2^A \phi_2^c + \phi_1^c G_2^R \phi_2^q + \phi_1^c G_2^K \phi_2^c \\ \phi_1^c G_2^A \phi_2^q + \phi_1^q G_2^R \phi_2^c + \phi_1^q G_2^K \phi_2^q & \phi_1^q G_2^A \phi_2^c + \phi_1^c G_2^R \phi_2^q + \phi_1^q G_2^K \phi_2^c \end{pmatrix} \quad (\text{A.9})$$

$$[\check{\phi}_1 \check{G}_2 \check{\phi}_2]^R - [\check{\phi}_1 \check{G}_2 \check{\phi}_2]^A = (G_2^R - G_2^A) (\phi_1^c \phi_2^c - \phi_1^q \phi_2^q) + G_2^K (\phi_1^c \phi_2^q - \phi_1^q \phi_2^c) \quad (\text{A.10})$$

$$[\check{\phi}_1 \check{G}_2 \check{\phi}_2]^K = [\check{\phi}_1 \check{G}_2 \check{\phi}_2]^K - [\check{\phi}_1 \check{G}_2 \check{\phi}_2]^Q = (G_2^R - G_2^A) (\phi_1^c \phi_2^q - \phi_1^q \phi_2^c) + G_2^K (\phi_1^c \phi_2^c - \phi_1^q \phi_2^q) \quad (\text{A.11})$$

In lowest order of the interaction the Hubbardt-Stratonovich fields obey $\langle \phi_1^\alpha \phi_{1'}^\beta \rangle_{\phi} = D_0(\vec{p}_1 - \vec{p}_{1'})\delta_{\alpha,-\beta}i/2$. We obtain therefore:

$$\begin{aligned} \Sigma^R - \Sigma^A &= \left(\frac{i}{2}\right)^2 D_0^2 \left\{ (G_2^R - G_2^A) \text{Tr} \left[G_{1'}^K G_{2'}^K - (G_{1'}^R - G_{1'}^A) (G_{2'}^R - G_{2'}^A) \right] \right. \\ &\quad \left. - G_{2'}^K \text{Tr} \left[(G_{1'}^R - G_{1'}^A) G_{2'}^K - G_{1'}^K (G_{2'}^R - G_{2'}^A) \right] \right\} \end{aligned} \quad (\text{A.12})$$

$$\begin{aligned} \Sigma^K = \Sigma^K - \Sigma^Q &= \left(\frac{i}{2}\right)^2 D_0^2 \left\{ G_2^K \text{Tr} \left[G_{1'}^K G_{2'}^K - (G_{1'}^R - G_{1'}^A) (G_{2'}^R - G_{2'}^A) \right] \right. \\ &\quad \left. - (G_2^R - G_2^A) \text{Tr} \left[(G_{1'}^R - G_{1'}^A) G_{2'}^K - G_{1'}^K (G_{2'}^R - G_{2'}^A) \right] \right\}. \end{aligned} \quad (\text{A.13})$$

The contraction between ϕ_1^α and $\phi_{2'}^\alpha$ is due to symmetry reasons given by the same expressions and is topological not distinguishable which means that already the integration over the internal variables will take into account other contractions.

We can now express the collision kernel in terms of Green's functions to gain the following kinetic equation:

$$\begin{aligned} \mathcal{L}G^K = & -i \left(\frac{i}{2}\right)^2 D_0^2 \left\{ \left[(G_1^R - G_1^A) G_2^K - G_1^K (G_2^R - G_2^A) \right] \text{Tr} \left[G_{1'}^K G_{2'}^K - (G_{1'}^R - G_{1'}^A) (G_{2'}^R - G_{2'}^A) \right] \right. \\ & \left. + \left[G_2^K G_1^K - (G_1^R - G_1^A) (G_2^R - G_2^A) \right] \text{Tr} \left[(G_{1'}^R - G_{1'}^A) G_{2'}^K - G_{1'}^K (G_{2'}^R - G_{2'}^A) \right] \right\} \end{aligned}$$

Note that still everything is convoluted although not explicitly written. An interesting observation is that we can reduce the complexity of the equations to deal with by introducing $2T_i^\alpha = G_i^K + \alpha (G_i^R - G_i^A)$. A vigilant observer may notice the construction of the T_i as a rotation in Keldysh space. Thus the collision kernel simplifies to:

$$\mathcal{L}G^K = -4i \left(\frac{i}{2}\right)^2 D_0^2 \left\{ [T_1^+ T_2^- - T_1^- T_2^+] \text{Tr} [T_{1'}^+ T_{2'}^- + T_{1'}^- T_{2'}^+] + [T_1^+ T_2^- + T_1^- T_2^+] \text{Tr} [T_{1'}^+ T_{2'}^- - T_{1'}^- T_{2'}^+] \right\}. \quad (\text{A.14})$$

In equilibrium we can rewrite $G_i^K = f_i (G_i^R - G_i^A) = 2if_i \mathcal{A}_i$ with the spectral weight $\mathcal{A}_i = (2i)^{-1} (G_i^R - G_i^A)$. Further due to its form the T_i^α is always on mass shell and in equilibrium we read: $T_i^\alpha = i\mathcal{A}_i (f_i + \alpha)$. Utilizing this observation we might write:

$$2i\mathcal{L}(1 - 2n_1)\mathcal{A}_1 = 8i \left(\frac{i}{2}\right)^2 D_0^2 (2i)^4 \mathcal{A}_1 \mathcal{A}_2 \text{Tr} [\mathcal{A}_{1'} \mathcal{A}_{2'}] (n_1 n_{-2} n_{1'} n_{-4} - n_{-1} n_2 n_{-1'} n_4). \quad (\text{A.15})$$

since

$$\begin{aligned} & \left\{ \left[\frac{f_1 + 1}{2} \frac{f_2 - 1}{2} - \frac{f_1 - 1}{2} \frac{f_2 + 1}{2} \right] \left[\frac{f_{1'} + 1}{2} \frac{f_{2'} - 1}{2} + \frac{f_{1'} - 1}{2} \frac{f_{2'} + 1}{2} \right] \right. \\ & \quad \left. + \left[\frac{f_1 + 1}{2} \frac{f_2 - 1}{2} + \frac{f_1 - 1}{2} \frac{f_2 + 1}{2} \right] \left[\frac{f_{1'} + 1}{2} \frac{f_{2'} - 1}{2} - \frac{f_{1'} - 1}{2} \frac{f_{2'} + 1}{2} \right] \right\} \\ & = \left\{ [n_{-1} n_2 - n_1 n_{-2}] [n_{-1'} n_{2'} + n_{1'} n_{-2'}] + [n_{-1} n_2 + n_1 n_{-2}] [n_{-1'} n_{2'} - n_{1'} n_{-2'}] \right\} \\ & = -2 (n_1 n_{-2} n_{1'} n_{-4} - n_{-1} n_2 n_{-1'} n_4) \quad (\text{A.16}) \end{aligned}$$

where we used $f_i = 1 - 2n_i$, $n_{-i} = 1 - n_i$ and n_i being the Fermi distribution of particle i . One can make use of the relation $(f_i + \alpha)/2 = \alpha n_{-\alpha i}$. We see that Eq. (A.15) has already the proper form of distribution functions to gain the usual collision integral. To make this more manifest we reintroduce the needed integrations and write explicitly

$$\begin{aligned}
& (\partial_T + \gamma \tilde{v}_F \vec{n}_{p_1} \nabla_R) n(\epsilon_1 = \gamma_1 v_F p_1) \\
&= 8N \int \frac{d^2 q}{(2\pi)^2} \frac{d^2 p_3}{(2\pi)^2} \frac{d\omega}{2\pi} \frac{d\epsilon_3}{2\pi} D_0^2(q) (-\pi)^3 \delta(\epsilon_2 - \gamma_2 v_F p_2) \delta(\epsilon_3 - \gamma_3 v_F p_3) \delta(\epsilon_4 - \gamma_4 v_F p_4) \\
&\quad \times \theta_{\gamma_1, \gamma_2} \theta_{\gamma_3, \gamma_4} \left[n(\epsilon_1) n(-\epsilon_2) n(\epsilon_3) n(-\epsilon_4) - n(-\epsilon_1) n(\epsilon_2) n(-\epsilon_3) n(\epsilon_4) \right] \\
&= -N \int \frac{d^2 p_2}{(2\pi)^2} \frac{d^2 p_3}{(2\pi)^2} \frac{d^2 p_4}{(2\pi)^2} (2\pi) \delta(\epsilon_1 - \epsilon_2 + \epsilon_3 - \epsilon_4) (2\pi)^2 \delta(\vec{p}_1 - \vec{p}_2 + \vec{p}_3 - \vec{p}_4) D_0^2(q) \\
&\quad \times \theta_{\gamma_1, \gamma_2} \theta_{\gamma_3, \gamma_4} \left[n(\epsilon_1) n(-\epsilon_2) n(\epsilon_3) n(-\epsilon_4) - n(-\epsilon_1) n(\epsilon_2) n(-\epsilon_3) n(\epsilon_4) \right] \\
&= - \int \frac{d^2 p_2}{(2\pi)^2} \frac{d^2 p_3}{(2\pi)^2} \frac{d^2 p_4}{(2\pi)^2} \mathcal{K}_B(\vec{p}_1, \vec{p}_2, \vec{p}_3, \vec{p}_4) \left[n(\epsilon_1) n(-\epsilon_2) n(\epsilon_3) n(-\epsilon_4) \right. \\
&\quad \left. - n(-\epsilon_1) n(\epsilon_2) n(-\epsilon_3) n(\epsilon_4) \right] \quad (\text{A.17})
\end{aligned}$$

With the collision integral kernel \mathcal{K}_B in Boltzmann-form given by

$$\mathcal{K}_B(\vec{p}_1, \vec{p}_2, \vec{p}_3, \vec{p}_4) = (2\pi) \delta(\epsilon_1 - \epsilon_2 + \epsilon_3 - \epsilon_4) (2\pi)^2 \delta(\vec{p}_1 - \vec{p}_2 + \vec{p}_3 - \vec{p}_4) |\mathcal{M}_0|^2, \quad (\text{A.18})$$

With the leading order matrix element of the collision kernel to be:

$$|\mathcal{M}_0|^2 = N \theta_{\gamma_1, \gamma_2} \theta_{\gamma_3, \gamma_4} D_0^2(q). \quad (\text{A.19})$$

Hereby the object $\theta_{\gamma_1, \gamma_2}$ is defined as:

$$\theta_{\gamma_1, \gamma_2} = \text{Tr} \left[\mathcal{P}_{\gamma_1}(\vec{p}_1) \mathcal{P}_{\gamma_2}(\vec{p}_2) \right] = \frac{1}{2} [1 + \gamma_1 \gamma_2 \hat{p}_1 \hat{p}_2], \quad (\text{A.20})$$

which is the Dirac factor that appears when projecting on the chiral basis. (see Sec. 5.15)

A.2.2 Coulomb Interaction: Sub-leading Contributions

We will follow the very same line as in the leading order case except that we will start with a diagram of higher order shown in Fig. A.4. Since the contributions that appear in higher order tend to be more complex some needed details will appear slightly smaller than others.

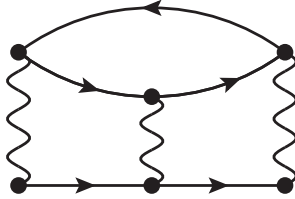


Figure A.4: Coulomb interaction correction we take into account for the higher order drag.

We start with the self-energy given by:

$$\check{\Sigma} = - \langle \check{\phi}_1 \check{G}_2 \check{\phi}_2 \check{G}_3 \check{\phi}_3 \text{Tr} \left[\check{G}_1' \check{\phi}_1' \check{G}_2' \check{\phi}_2' \check{G}_3' \check{\phi}_3' \right] \rangle_{\phi}. \quad (\text{A.21})$$

As done previously we look for the combinations we will need for the collision integral.

$$\begin{aligned}
& \left[\check{\phi}_1 \check{G}_2 \check{\phi}_2 \check{G}_3 \check{\phi}_3 \right]^R - \left[\check{\phi}_1 \check{G}_2 \check{\phi}_2 \check{G}_3 \check{\phi}_3 \right]^A \\
&= \left(\phi_1^c \phi_2^c \phi_3^c - \phi_1^q \phi_2^c \phi_3^q \right) \left(G_2^R G_3^R - G_2^A G_3^A \right) + \left(\phi_1^c \phi_2^c \phi_3^q - \phi_1^q \phi_2^c \phi_3^c \right) \left(G_2^K G_3^A + G_2^R G_3^K \right) \\
&+ \left(\phi_1^c \phi_2^q \phi_3^q - \phi_1^q \phi_2^q \phi_3^c \right) \left(G_2^K G_3^K + G_2^R G_3^A - G_2^A G_3^R \right) + \left(\phi_1^c \phi_2^q \phi_3^c - \phi_1^q \phi_2^q \phi_3^q \right) \left(G_2^K G_3^R - G_2^A G_3^K \right) \quad (\text{A.22})
\end{aligned}$$

$$\begin{aligned}
& \left[\check{\phi}_1 \check{G}_2 \check{\phi}_2 \check{G}_3 \check{\phi}_3 \right]^K - \left[\check{\phi}_1 \check{G}_2 \check{\phi}_2 \check{G}_3 \check{\phi}_3 \right]^Q \\
&= \left(\phi_1^c \phi_2^c \phi_3^c - \phi_1^q \phi_2^c \phi_3^q \right) \left(G_2^K G_3^A + G_2^R G_3^K \right) + \left(\phi_1^c \phi_2^c \phi_3^q - \phi_1^q \phi_2^c \phi_3^c \right) \left(G_2^R G_3^R - G_2^A G_3^A \right) \\
&+ \left(\phi_1^c \phi_2^q \phi_3^q - \phi_1^q \phi_2^q \phi_3^c \right) \left(G_2^K G_3^K - G_2^A G_3^K \right) + \left(\phi_1^c \phi_2^q \phi_3^c - \phi_1^q \phi_2^q \phi_3^q \right) \left(G_2^K G_3^K + G_2^R G_3^A - G_2^A G_3^R \right) \quad (\text{A.23})
\end{aligned}$$

In the very same way we gain the higher order polarization operator:

$$\begin{aligned}
\text{Tr} \left[\check{G}_{1'} \check{\phi}_{1'} \check{G}_{2'} \check{\phi}_{2'} \check{G}_{3'} \check{\phi}_{3'} \right] &= \phi_{1'}^c \phi_{2'}^c \phi_{3'}^c \left(G_{1'}^A G_{2'}^A G_{3'}^A + G_{1'}^R G_{2'}^R G_{3'}^R \right) + \phi_{1'}^q \phi_{2'}^c \phi_{3'}^c \left(G_{1'}^A G_{2'}^K G_{3'}^A + G_{1'}^A G_{2'}^R G_{3'}^K + G_{1'}^K G_{2'}^R G_{3'}^R \right) \\
&+ \phi_{1'}^c \phi_{2'}^q \phi_{3'}^c \left(G_{1'}^A G_{2'}^A G_{3'}^K + G_{1'}^K G_{2'}^A G_{3'}^R + G_{1'}^R G_{2'}^K G_{3'}^R \right) + \phi_{1'}^q \phi_{2'}^q \phi_{3'}^c \left(G_{1'}^A G_{2'}^R G_{3'}^A + G_{1'}^R G_{2'}^A G_{3'}^R + G_{1'}^A G_{2'}^K G_{3'}^K + G_{1'}^K G_{2'}^K G_{3'}^R \right) \\
&+ \phi_{1'}^c \phi_{2'}^c \phi_{3'}^q \left(G_{1'}^K G_{2'}^A G_{3'}^A + G_{1'}^R G_{2'}^K G_{3'}^A + G_{1'}^R G_{2'}^R G_{3'}^K \right) + \phi_{1'}^q \phi_{2'}^c \phi_{3'}^q \left(G_{1'}^R G_{2'}^A G_{3'}^A + G_{1'}^A G_{2'}^R G_{3'}^R + G_{1'}^K G_{2'}^K G_{3'}^A + G_{1'}^K G_{2'}^R G_{3'}^K \right) \\
&+ \phi_{1'}^c \phi_{2'}^q \phi_{3'}^q \left(G_{1'}^R G_{2'}^R G_{3'}^A + G_{1'}^A G_{2'}^A G_{3'}^R + G_{1'}^K G_{2'}^A G_{3'}^K + G_{1'}^R G_{2'}^K G_{3'}^K \right) \\
&+ \phi_{1'}^q \phi_{2'}^q \phi_{3'}^q \left(G_{1'}^R G_{2'}^A G_{3'}^K + G_{1'}^K G_{2'}^R G_{3'}^A + G_{1'}^A G_{2'}^K G_{3'}^R + G_{1'}^K G_{2'}^K G_{3'}^K \right) \quad (\text{A.24})
\end{aligned}$$

It helps to look at certain combinations for which it appears to be helpful to use the short-hand notation $\mathbb{I}\mathbb{I} = \text{Tr} \left[\check{G}_{1'} \check{\phi}_{1'} \check{G}_{2'} \check{\phi}_{2'} \check{G}_{3'} \check{\phi}_{3'} \right]$ as a generalization of the polarization operator from the previous section. We then read:

$$\begin{aligned}
\langle \left(\phi_1^c \phi_2^c \phi_3^c - \phi_1^q \phi_2^c \phi_3^q \right) \mathbb{I}\mathbb{I} \rangle_\phi &= \left(\frac{i}{2} \right)^3 D_0^3 \text{Tr} \left[G_{1'}^K \left(G_{2'}^K G_{3'}^K + G_{2'}^R G_{3'}^A - G_{2'}^A G_{3'}^R \right) - \left(G_{1'}^R - G_{1'}^A \right) \left(G_{2'}^K G_{3'}^R - G_{2'}^A G_{3'}^K \right) \right] \\
\langle \left(\phi_1^c \phi_2^c \phi_3^q - \phi_1^q \phi_2^c \phi_3^c \right) \mathbb{I}\mathbb{I} \rangle_\phi &= \left(\frac{i}{2} \right)^3 D_0^3 \text{Tr} \left[G_{1'}^K \left(G_{2'}^K G_{3'}^R - G_{2'}^A G_{3'}^K \right) - \left(G_{1'}^R - G_{1'}^A \right) \left(G_{2'}^K G_{3'}^K + G_{2'}^R G_{3'}^A - G_{2'}^A G_{3'}^R \right) \right] \\
\langle \left(\phi_1^c \phi_2^q \phi_3^q - \phi_1^q \phi_2^q \phi_3^c \right) \mathbb{I}\mathbb{I} \rangle_\phi &= \left(\frac{i}{2} \right)^3 D_0^3 \text{Tr} \left[G_{1'}^K \left(G_{2'}^R G_{3'}^R - G_{2'}^A G_{3'}^A \right) - \left(G_{1'}^R - G_{1'}^A \right) \left(G_{2'}^R G_{3'}^K + G_{2'}^K G_{3'}^A \right) \right] \\
\langle \left(\phi_1^c \phi_2^q \phi_3^c - \phi_1^q \phi_2^q \phi_3^q \right) \mathbb{I}\mathbb{I} \rangle_\phi &= \left(\frac{i}{2} \right)^3 D_0^3 \text{Tr} \left[G_{1'}^K \left(G_{2'}^K G_{3'}^A + G_{2'}^R G_{3'}^K \right) - \left(G_{1'}^R - G_{1'}^A \right) \left(G_{2'}^R G_{3'}^R - G_{2'}^A G_{3'}^A \right) \right] \quad (\text{A.25})
\end{aligned}$$

where for simplicity we use D_0^3 although the momenta of the interaction propagator differs.

The polarization operator is per construction cyclic which means that taking into account all possible contractions we can differ between the cyclic ones and the ones odd in total number of transpositions. So we gain finally a degeneracy of three by connecting only $1 \rightarrow 1'$, $2 \rightarrow 2'$ and $3 \rightarrow 3'$ setting the

self-energy to be:

$$\Sigma^R - \Sigma^A = \left(\frac{i}{2}\right)^3 D_0^3 \quad (\text{A.26})$$

$$\begin{aligned} & \times \left\{ \left(G_2^R G_3^R - G_2^A G_3^A \right) \text{Tr} \left[G_{1'}^K \left(G_{2'}^K G_{3'}^K + G_{2'}^R G_{3'}^A - G_{2'}^A G_{3'}^R \right) - \left(G_{1'}^R - G_{1'}^A \right) \left(G_{2'}^K G_{3'}^R - G_{2'}^A G_{3'}^K \right) \right] \right. \\ & + \left(G_2^K G_3^A + G_2^R G_3^K \right) \text{Tr} \left[G_{1'}^K \left(G_{2'}^K G_{3'}^R - G_{2'}^A G_{3'}^K \right) - \left(G_{1'}^R - G_{1'}^A \right) \left(G_{2'}^K G_{3'}^K + G_{2'}^R G_{3'}^A - G_{2'}^A G_{3'}^R \right) \right] \\ & + \left(G_2^K G_3^K + G_2^R G_3^A - G_2^A G_3^R \right) \text{Tr} \left[G_{1'}^K \left(G_{2'}^R G_{3'}^R - G_{2'}^A G_{3'}^A \right) - \left(G_{1'}^R - G_{1'}^A \right) \left(G_{2'}^R G_{3'}^K + G_{2'}^K G_{3'}^A \right) \right] \\ & \left. + \left(G_2^K G_3^R - G_2^A G_3^K \right) \text{Tr} \left[G_{1'}^K \left(G_{2'}^K G_{3'}^A + G_{2'}^R G_{3'}^K \right) - \left(G_{1'}^R - G_{1'}^A \right) \left(G_{2'}^R G_{3'}^R - G_{2'}^A G_{3'}^A \right) \right] \right\} \quad (\text{A.27}) \end{aligned}$$

$$\Sigma^K = \left(\frac{i}{2}\right)^3 D_0^3 \quad (\text{A.28})$$

$$\begin{aligned} & \times \left\{ \left(G_2^K G_3^A + G_2^R G_3^K \right) \text{Tr} \left[G_{1'}^K \left(G_{2'}^K G_{3'}^K + G_{2'}^R G_{3'}^A - G_{2'}^A G_{3'}^R \right) - \left(G_{1'}^R - G_{1'}^A \right) \left(G_{2'}^K G_{3'}^R - G_{2'}^A G_{3'}^K \right) \right] \right. \\ & + \left(G_2^R G_3^R - G_2^A G_3^A \right) \text{Tr} \left[G_{1'}^K \left(G_{2'}^K G_{3'}^R - G_{2'}^A G_{3'}^K \right) - \left(G_{1'}^R - G_{1'}^A \right) \left(G_{2'}^K G_{3'}^K + G_{2'}^R G_{3'}^A - G_{2'}^A G_{3'}^R \right) \right] \\ & + \left(G_2^K G_3^R - G_2^A G_3^K \right) \text{Tr} \left[G_{1'}^K \left(G_{2'}^R G_{3'}^R - G_{2'}^A G_{3'}^A \right) - \left(G_{1'}^R - G_{1'}^A \right) \left(G_{2'}^R G_{3'}^K + G_{2'}^K G_{3'}^A \right) \right] \\ & \left. + \left(G_2^K G_3^K + G_2^R G_3^A - G_2^A G_3^R \right) \text{Tr} \left[G_{1'}^K \left(G_{2'}^K G_{3'}^A + G_{2'}^R G_{3'}^K \right) - \left(G_{1'}^R - G_{1'}^A \right) \left(G_{2'}^R G_{3'}^R - G_{2'}^A G_{3'}^A \right) \right] \right\} \quad (\text{A.29}) \end{aligned}$$

The kinetic equation looks for the higher order collision kernel as follows:

$$\begin{aligned} \mathcal{L}G^K &= -i \left(\frac{i}{2}\right)^3 D_0^3 \left\{ \left[\left(G_{1'}^R - G_{1'}^A \right) \left(G_{2'}^R G_{3'}^K + G_{2'}^K G_{3'}^A \right) - G_{1'}^K \left(G_{2'}^R G_{3'}^R - G_{2'}^A G_{3'}^A \right) \right] \times \right. \\ & \times \text{Tr} \left[G_{1'}^K \left(G_{2'}^K G_{3'}^K + G_{2'}^R G_{3'}^A - G_{2'}^A G_{3'}^R \right) + \left(G_{1'}^R - G_{1'}^A \right) \left(G_{2'}^A G_{3'}^K - G_{2'}^K G_{3'}^R \right) \right] \\ & + \left[G_{1'}^K \left(G_{2'}^K G_{3'}^A + G_{2'}^R G_{3'}^K \right) - \left(G_{1'}^R - G_{1'}^A \right) \left(G_{2'}^R G_{3'}^R - G_{2'}^A G_{3'}^A \right) \right] \times \\ & \times \text{Tr} \left[G_{1'}^K \left(G_{2'}^K G_{3'}^R - G_{2'}^A G_{3'}^K \right) - \left(G_{1'}^R - G_{1'}^A \right) \left(G_{2'}^K G_{3'}^K + G_{2'}^R G_{3'}^A - G_{2'}^A G_{3'}^R \right) \right] \\ & + \left[G_{1'}^K \left(G_{2'}^K G_{3'}^K + G_{2'}^R G_{3'}^A - G_{2'}^A G_{3'}^R \right) + \left(G_{1'}^R - G_{1'}^A \right) \left(G_{2'}^A G_{3'}^K - G_{2'}^K G_{3'}^R \right) \right] \times \\ & \times \text{Tr} \left[G_{1'}^K \left(G_{2'}^R G_{3'}^R - G_{2'}^A G_{3'}^A \right) - \left(G_{1'}^R - G_{1'}^A \right) \left(G_{2'}^R G_{3'}^K + G_{2'}^K G_{3'}^A \right) \right] \\ & + \left[\left(G_{1'}^R - G_{1'}^A \right) \left(G_{2'}^K G_{3'}^K + G_{2'}^R G_{3'}^A - G_{2'}^A G_{3'}^R \right) - G_{1'}^K \left(G_{2'}^K G_{3'}^R - G_{2'}^A G_{3'}^K \right) \right] \times \\ & \left. \times \text{Tr} \left[G_{1'}^K \left(G_{2'}^K G_{3'}^A + G_{2'}^R G_{3'}^K \right) - \left(G_{1'}^R - G_{1'}^A \right) \left(G_{2'}^R G_{3'}^R - G_{2'}^A G_{3'}^A \right) \right] \right\} \quad (\text{A.30}) \end{aligned}$$

So far only one class of diagrams is included. Gaining the other diagrams one needs to exchange e.g. 1 and 3, which is only a sign change for $\langle (\phi_1^c \phi_2^q \phi_3^q - \phi_1^q \phi_2^q \phi_3^c) \Pi \rangle_\phi$ and $\langle (\phi_1^c \phi_2^c \phi_3^q - \phi_1^q \phi_2^c \phi_3^c) \Pi \rangle_\phi$.

Further we will introduce again T_i^α that led to a compactified notation in the previous section. Additionally to the T_i^α we need as well the $2M_i^\alpha = G_i^K + \alpha (G_i^R + G_i^A)$ which yields:

$$G_2^K G_3^K + G_2^R G_3^A - G_2^A G_3^R = (T_2^+ M_3^+ + T_2^- M_3^- + M_2^- T_3^+ + M_2^+ T_3^-) \quad (\text{A.31})$$

$$G_2^R G_3^R - G_2^A G_3^A = (T_2^+ M_3^+ + T_2^- M_3^- - M_2^- T_3^+ - M_2^+ T_3^-) \quad (\text{A.32})$$

$$G_2^R G_3^K + G_2^K G_3^A = (T_2^+ M_3^+ - T_2^- M_3^- - M_2^- T_3^+ + M_2^+ T_3^-) \quad (\text{A.33})$$

$$G_2^K G_3^R - G_2^A G_3^K = (T_2^+ M_3^+ - T_2^- M_3^- + M_2^- T_3^+ - M_2^+ T_3^-). \quad (\text{A.34})$$

We simplify the collision kernel towards:

$$\begin{aligned} \mathcal{L}G^K &= -i \left(\frac{i}{2}\right)^3 D_0^3 \times \\ &\times \left\{ \left[T_1^+ (M_2^+ T_3^- - T_2^- M_3^-) + T_1^- (M_2^- T_3^+ - T_2^+ M_3^+) \right] \text{Tr} \left[T_{1'}^+ (M_{2'}^+ T_{3'}^- + T_{2'}^- M_{3'}^-) + T_{1'}^- (M_{2'}^- T_{3'}^+ + T_{2'}^+ M_{3'}^+) \right] \right. \\ &- \left[T_1^+ (M_2^+ T_3^- - T_2^- M_3^-) - T_1^- (M_2^- T_3^+ - T_2^+ M_3^+) \right] \text{Tr} \left[T_{1'}^+ (M_{2'}^+ T_{3'}^- + T_{2'}^- M_{3'}^-) - T_{1'}^- (M_{2'}^- T_{3'}^+ + T_{2'}^+ M_{3'}^+) \right] \\ &- \left[T_1^+ (M_2^+ T_3^- + T_2^- M_3^-) + T_1^- (M_2^- T_3^+ + T_2^+ M_3^+) \right] \text{Tr} \left[T_{1'}^+ (M_{2'}^+ T_{3'}^- - T_{2'}^- M_{3'}^-) + T_{1'}^- (M_{2'}^- T_{3'}^+ - T_{2'}^+ M_{3'}^+) \right] \\ &\left. + \left[T_1^+ (M_2^+ T_3^- + T_2^- M_3^-) - T_1^- (M_2^- T_3^+ + T_2^+ M_3^+) \right] \text{Tr} \left[T_{1'}^+ (M_{2'}^+ T_{3'}^- - T_{2'}^- M_{3'}^-) - T_{1'}^- (M_{2'}^- T_{3'}^+ - T_{2'}^+ M_{3'}^+) \right] \right\} \\ &= -4i \left(\frac{i}{2}\right)^3 D_0^3 \left\{ T_1^- M_2^- T_3^+ \text{Tr} \left[T_{1'}^+ T_{2'}^- M_{3'}^- \right] - T_1^+ T_2^- M_3^- \text{Tr} \left[T_{1'}^- M_{2'}^- T_{3'}^+ \right] \right. \\ &\quad \left. + T_1^+ M_2^+ T_3^- \text{Tr} \left[T_{1'}^- T_{2'}^+ M_{3'}^+ \right] - T_1^- T_2^+ M_3^+ \text{Tr} \left[T_{1'}^+ M_{2'}^+ T_{3'}^- \right] \right\} \quad (\text{A.35}) \end{aligned}$$

and the diagram with crossed lines forms:

$$\begin{aligned} \mathcal{L}G^K &= -i \left(\frac{i}{2}\right)^3 D_0^3 \times \\ &\times \left\{ \left[T_1^+ (M_2^+ T_3^- - T_2^- M_3^-) + T_1^- (M_2^- T_3^+ - T_2^+ M_3^+) \right] \text{Tr} \left[T_{1'}^+ (M_{2'}^+ T_{3'}^- + T_{2'}^- M_{3'}^-) + T_{1'}^- (M_{2'}^- T_{3'}^+ + T_{2'}^+ M_{3'}^+) \right] \right. \\ &+ \left[T_1^+ (M_2^+ T_3^- - T_2^- M_3^-) - T_1^- (M_2^- T_3^+ - T_2^+ M_3^+) \right] \text{Tr} \left[T_{1'}^+ (M_{2'}^+ T_{3'}^- + T_{2'}^- M_{3'}^-) - T_{1'}^- (M_{2'}^- T_{3'}^+ + T_{2'}^+ M_{3'}^+) \right] \\ &+ \left[T_1^+ (M_2^+ T_3^- + T_2^- M_3^-) + T_1^- (M_2^- T_3^+ + T_2^+ M_3^+) \right] \text{Tr} \left[T_{1'}^+ (M_{2'}^+ T_{3'}^- - T_{2'}^- M_{3'}^-) + T_{1'}^- (M_{2'}^- T_{3'}^+ - T_{2'}^+ M_{3'}^+) \right] \\ &\left. + \left[T_1^+ (M_2^+ T_3^- + T_2^- M_3^-) - T_1^- (M_2^- T_3^+ + T_2^+ M_3^+) \right] \text{Tr} \left[T_{1'}^+ (M_{2'}^+ T_{3'}^- - T_{2'}^- M_{3'}^-) - T_{1'}^- (M_{2'}^- T_{3'}^+ - T_{2'}^+ M_{3'}^+) \right] \right\} \\ &= -4i \left(\frac{i}{2}\right)^3 D_0^3 \left\{ T_1^+ M_2^+ T_3^- \text{Tr} \left[T_{1'}^+ M_{2'}^+ T_{3'}^- \right] - T_1^+ T_2^- M_3^- \text{Tr} \left[T_{1'}^+ T_{2'}^- M_{3'}^- \right] \right. \\ &\quad \left. + T_1^- M_2^- T_3^+ \text{Tr} \left[T_{1'}^- M_{2'}^- T_{3'}^+ \right] - T_1^- T_2^+ M_3^+ \text{Tr} \left[T_{1'}^- T_{2'}^+ M_{3'}^+ \right] \right\} \quad (\text{A.36}) \end{aligned}$$

One recognizes within this notation that each term has four Green's functions on mass shell which means that we deal, as it should be, with a two particle scattering process.

To identify the proper matrix element we will continue exploring the structure of the collision kernel in the vicinity of equilibrium where we can make again use of $T_i^\alpha = i\mathcal{A}_i(f_i + \alpha) = i\mathcal{A}_i 2n_{-\alpha i}$ gaining:

$$\begin{aligned} \mathcal{L}G^K &= -2i \left(\frac{i}{2}\right)^3 D_0^3 (2i)^4 \\ &\times \left\{ \mathcal{A}_1 M_2^+ \mathcal{A}_3 \text{Tr} \left[\mathcal{A}_{1'} M_{2'}^+ \mathcal{A}_{3'} \right] n_1 n_{-3} n_{1'} n_{-3'} + \mathcal{A}_1 M_2^- \mathcal{A}_3 \text{Tr} \left[\mathcal{A}_{1'} M_{2'}^- \mathcal{A}_{3'} \right] n_{-1} n_3 n_{-1'} n_{3'} \right. \\ &\quad \left. - \mathcal{A}_1 \mathcal{A}_2 M_3^+ \text{Tr} \left[\mathcal{A}_{1'} \mathcal{A}_{2'} M_{3'}^+ \right] n_{-1} n_2 n_{-1'} n_{2'} - \mathcal{A}_1 \mathcal{A}_2 M_3^- \text{Tr} \left[\mathcal{A}_{1'} \mathcal{A}_{2'} M_{3'}^- \right] n_1 n_{-2} n_{1'} n_{-2'} \right\} \quad (\text{A.37}) \end{aligned}$$

Still we need to work a bit to gain the proper form of Fermi distributions. To do so one needs to make use of the symmetries of the Kernel. We need to map partially 2 to 3 and respectively 2' to 3'. Note that this is only a renaming since there is always a integration over all primed, 2 and 3. To make the next step very clear one should look for the projected states meaning that the collision kernel will be projected on the chiral basis of the incoming particle. With the projection \mathbb{P}_λ we read:

$$\text{Tr} \left[\mathcal{A}_{1'} \mathcal{A}_{2'} M_{3'}^+ \right] = \mathcal{A}_{1' \lambda'_1} \mathcal{A}_{2' \lambda'_2} M_{3' \lambda'_3}^+ \text{Tr} \left[\mathbb{P}_{\lambda'_1} \mathbb{P}_{\lambda'_2} \mathbb{P}_{\lambda'_3} \right] = \mathcal{A}_{1' \lambda'_1} \mathcal{A}_{2' \lambda'_2} M_{3' \lambda'_3}^+ \Theta_{\lambda'_1 \lambda'_2 \lambda'_3} \quad (\text{A.38})$$

where

$$\Theta_{\lambda'_1 \lambda'_2 \lambda'_3} = \frac{1}{4} \left(1 + \lambda'_1 \lambda'_2 \hat{p}_{1'} \hat{p}_{2'} + \lambda'_1 \lambda'_3 \hat{p}_{1'} \hat{p}_{3'} + \lambda'_2 \lambda'_3 \hat{p}_{2'} \hat{p}_{3'} \right) \quad (\text{A.39})$$

is responsible for the Dirac factors within the three leg polarization. Projecting the kinetic equation and exchanging the energies as discussed we gain:

$$\begin{aligned} \mathcal{L}G_{1\lambda_1}^K &= 8i \left(\frac{i}{2}\right)^2 (2i)^4 \mathcal{A}_{1\lambda_1} \mathcal{A}_{2\lambda_2} \mathcal{A}_{1'\lambda_{1'}} \mathcal{A}_{2'\lambda_{2'}} \left(n_1 n_{-2} n_{1'} n_{-2'} - n_{-1} n_2 n_{-1'} n_{2'} \right) \times \\ &\quad \times \frac{-i}{4} D_0^3 \Theta_{\lambda_1 \lambda_2 \lambda_3} \Theta_{\lambda_{1'} \lambda_{2'} \lambda_{3'}} \left[M_{3\lambda_3}^+ M_{3'\lambda_{3'}}^+ - M_{3\lambda_3}^- M_{3'\lambda_{3'}}^- \right] \quad (\text{A.40}) \end{aligned}$$

The matrix element reads now:

$$\mathcal{M}_0^* \mathcal{M}_1 + \mathcal{M}_0 \mathcal{M}_1^* = \frac{1}{4} D_0^3 \Theta_{\lambda_1 \lambda_2 \lambda_3} \Theta_{\lambda_{1'} \lambda_{2'} \lambda_{3'}} \left[\frac{1}{i} G_{3\lambda_3}^K \left(G_{3'\lambda_{3'}}^R + G_{3'\lambda_{3'}}^A \right) + \left(G_{3\lambda_3}^R + G_{3\lambda_3}^A \right) \frac{1}{i} G_{3'\lambda_{3'}}^K \right]. \quad (\text{A.41})$$

Some of the properties of this matrix element will be discussed in Sec. 8.3.2

A.3 The Linearized Collision Kernel

In this section we will derive the the linearized collision kernel for the case of small deviations from equilibrium that will be parametrized by $n(\epsilon, t) = n_F(\epsilon) + (4T \cosh^2 \epsilon / (2T))^{-1} h(\epsilon, t)$. We will start

with the quantum kinetic equation written in Eq. (A.17) Hence we have the following collision integral:

$$I_{\text{Coll}} = \sum_{\gamma_2, \gamma_3, \gamma_4} \int \frac{d^2 p_2}{(2\pi)^2} \frac{d^2 p_3}{(2\pi)^2} \frac{d^2 p_4}{(2\pi)^2} \mathcal{K}_B(\vec{p}_1, \vec{p}_2, \vec{p}_3, \vec{p}_4) \left[n(\epsilon_1) n(-\epsilon_2) n(\epsilon_3) n(-\epsilon_4) \right. \\ \left. - n(-\epsilon_1) n(\epsilon_2) n(-\epsilon_3) n(\epsilon_4) \right] \quad (\text{A.42})$$

with $(\epsilon_i = \gamma_i v_F |\vec{p}_i|)$

$$\mathcal{K}_B(\vec{p}_1, \vec{p}_2, \vec{p}_3, \vec{p}_4) = (2\pi) \delta(\epsilon_1 - \epsilon_2 + \epsilon_3 - \epsilon_4) (2\pi)^2 \delta(\vec{p}_1 - \vec{p}_2 + \vec{p}_3 - \vec{p}_4) |\mathcal{M}|^2 \quad (\text{A.43})$$

as already defined before. By plugging in the parametrization for $n(\epsilon, t)$ and throwing away all non-linear contributions in h_F we will end up with combinations of distribution functions given by:

$$\frac{h_F(\epsilon_1)}{4T \cosh^2 \frac{\epsilon_1}{2t}} \left[n_F(-\epsilon_2) n_F(\epsilon_3) n_F(-\epsilon_4) + n_F(\epsilon_2) n_F(-\epsilon_3) n_F(\epsilon_4) \right] \\ + \frac{h_F(\epsilon_2)}{4T \cosh^2 \frac{\epsilon_2}{2t}} \left[n_F(\epsilon_1) n_F(\epsilon_3) n_F(-\epsilon_4) + n_F(-\epsilon_1) n_F(-\epsilon_3) n_F(\epsilon_4) \right] \\ + \frac{h_F(\epsilon_3)}{4T \cosh^2 \frac{\epsilon_3}{2t}} \left[n_F(\epsilon_1) n_F(-\epsilon_2) n_F(-\epsilon_4) + n_F(-\epsilon_1) n_F(\epsilon_2) n_F(\epsilon_4) \right] \\ + \frac{h_F(\epsilon_4)}{4T \cosh^2 \frac{\epsilon_4}{2t}} \left[n_F(\epsilon_1) n_F(-\epsilon_2) n_F(\epsilon_3) + n_F(-\epsilon_1) n_F(\epsilon_2) n_F(-\epsilon_3) \right] \quad (\text{A.44})$$

We used the relation $[4T \cosh(x/2T)]^{-1} = T^{-1} n_F(x) n_F(-x)$ and $\frac{n_F(1) n_F(2)}{n_F(-1) n_F(-2)} = \frac{n_F(3) n_F(4)}{n_F(-3) n_F(-4)}$ to get for the distribution functions:

$$\underbrace{\frac{1}{T} n_F(\epsilon_1) n_F(-\epsilon_2) n_F(\epsilon_3) n_F(-\epsilon_4)}_{\left[16T \cosh\left(\frac{\epsilon_1}{2T}\right) \cosh\left(\frac{\epsilon_2}{2T}\right) \cosh\left(\frac{\epsilon_3}{2T}\right) \cosh\left(\frac{\epsilon_4}{2T}\right) \right]^{-1}} \left[h(\epsilon_1) - h(\epsilon_2) + h(\epsilon_3) - h(\epsilon_4) \right] \quad (\text{A.45})$$

With the following integral weight

$$\mathcal{W}_B(\vec{p}_1, \vec{p}_2, \vec{p}_3, \vec{p}_4) = \mathcal{K}_B(\vec{p}_1, \vec{p}_2, \vec{p}_3, \vec{p}_4) \\ = \frac{(2\pi) \delta(\epsilon_1 - \epsilon_2 + \epsilon_3 - \epsilon_4) (2\pi)^2 \delta(\vec{p}_1 - \vec{p}_2 + \vec{p}_3 - \vec{p}_4) |\mathcal{M}|^2}{16T \cosh\left(\frac{\epsilon_1}{2T}\right) \cosh\left(\frac{\epsilon_2}{2T}\right) \cosh\left(\frac{\epsilon_3}{2T}\right) \cosh\left(\frac{\epsilon_4}{2T}\right)} \quad (\text{A.46})$$

the linearized collision integral is writable as

$$\delta I = \sum_{\gamma_2, \gamma_3, \gamma_4} \int \frac{d^2 p_2}{(2\pi)^2} \frac{d^2 p_3}{(2\pi)^2} \frac{d^2 p_4}{(2\pi)^2} \mathcal{W}_B(\vec{p}_1, \vec{p}_2, \vec{p}_3, \vec{p}_4) \left[h_F(\epsilon_1) - h_F(\epsilon_2) + h_F(\epsilon_3) - h_F(\epsilon_4) \right] \quad (\text{A.47})$$

B

Appendix B

Polarization and Rates

B.1 Polarization Operator

In this Appendix we evaluate the polarization operator, Eq. (3.12), at finite temperature. In a scattering process with emitting a photon, three different momenta are involved which form in two dimensions triangles as shown in Fig. B.1. Specifically, if an electron before scattering has the momentum \vec{p} and the emitted photon carries momentum \vec{q} , the electron that is left over has to carry $\vec{p} - \vec{q}$. The angular integration over the transferred momentum \vec{q} becomes complicated. To proceed further it is convenient to choose elliptic coordinates defined by $\xi = p + |\vec{p} - \vec{q}|$ and $\eta = p - |\vec{p} - \vec{q}|$. The corresponding coordinate system is shown in Fig. B.1. Using the elliptic coordinates, the expressions for the imaginary and real parts of the polarization bubble take the form

$$\text{Im } \Pi^R = \frac{\sinh(Q\beta)}{2\pi} \text{Re} \left[\frac{Q}{\sqrt{\beta^2 - 1}} \int_0^1 d\eta \frac{\sqrt{1 - \eta^2}}{\cosh(Q\beta) + \cosh(\eta Q)} + \frac{Q}{\sqrt{1 - \beta^2}} \int_1^\infty d\xi \frac{\sqrt{\xi^2 - 1}}{\cosh(Q\beta) + \cosh(\xi Q)} \right], \quad (\text{B.1})$$

$$\text{Re } \Pi^R = -\frac{Q}{\pi^2} \int_1^\infty d\xi \int_0^1 d\eta \frac{\sinh(\xi Q) \sqrt{\frac{1 - \eta^2}{\xi^2 - 1}} \frac{\xi}{\beta^2 - \xi^2} + \sinh(\eta Q) \sqrt{\frac{\xi^2 - 1}{1 - \eta^2}} \frac{\eta}{\beta^2 - \eta^2}}{\cosh(\xi Q) + \cosh(\eta Q)}. \quad (\text{B.2})$$

Here and below we introduce the notation $\beta = \Omega/Q$ to decouple expansions in small or large Q from the behavior at the singularity $Q = \Omega$. For simplicity we set $v_F = 1$ and $T = 1$. The integrals in Eqs. (B.1) and (B.2) are evaluated separately in the four regions shown in Fig. 4.1.

Region 1

In region 1 the condition $Q \ll 1$ and $\beta > 1$ hold, which means that in Eq. (B.1) only the part with the η -integral is left. Expanding the integrands in small $\eta Q \ll 1$, we get

$$\text{Im } \Pi^R \simeq \frac{Q \sinh(Q\beta)}{2\pi\sqrt{\beta^2 - 1}} \int_0^1 d\eta \frac{\sqrt{1 - \eta^2}}{\cosh(Q\beta) + 1} = \frac{Q \tanh(Q\beta/2)}{8\sqrt{\beta^2 - 1}} \quad (\text{B.3})$$

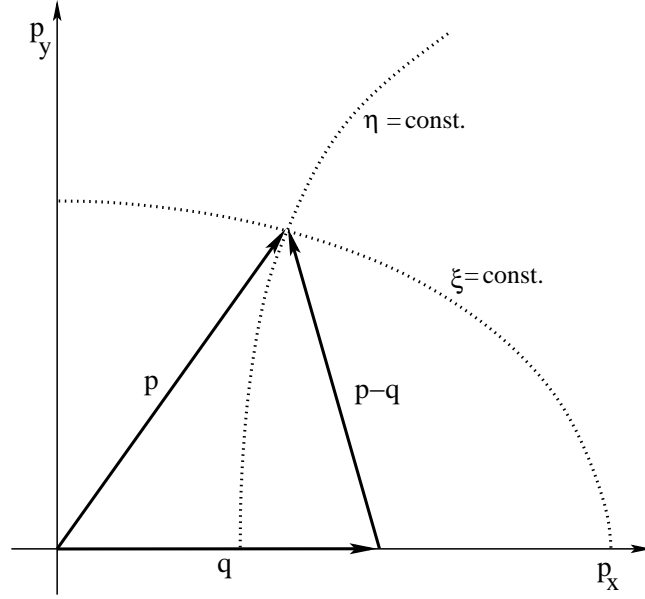


Figure B.1: Sketch of elliptic coordinates

for imaginary part and

$$\text{Re } \Pi^R \simeq \frac{-Q}{\pi^2} \underbrace{\int_0^1 \frac{d\eta}{\sqrt{1-\eta^2}} \frac{Q\eta^2}{\beta^2-\eta^2}}_{\simeq \frac{\pi Q}{2} \left(\frac{\beta}{\sqrt{\beta^2-1}} - 1 \right)} \underbrace{\int_1^\infty \frac{d\xi}{\cosh(\xi Q) + 1} \frac{\sqrt{\xi^2-1}}{\cosh(\xi Q) + 1}}_{\simeq \frac{2 \ln 2}{Q^2}} \simeq -\frac{\ln 2}{\pi} \left(\frac{|\beta|}{\sqrt{\beta^2-1}} - 1 \right) \quad (\text{B.4})$$

for the real part of Π^R . The term $\propto \sinh(\xi Q)$ in Eq. (B.2) yields a contribution of the order of $\sim Q^2$. The second term $\propto \sinh(\eta Q)$ results in Eq. (B.4).

Region 2

In region 2, we have $Q \gg 1$ and $\beta > 1$. In Eq. (B.1) again only the η -integral is left and by neglecting $\cosh(\eta Q)$ and expanding in large Q we get

$$\text{Im } \Pi^R \simeq \frac{1}{2\pi} \frac{\sinh(Q\beta)}{\sqrt{\beta^2-1}} \int_0^1 d\eta \frac{\sqrt{1-\eta^2}}{\cosh(Q\beta)} = \frac{1}{8} \frac{Q \text{sign } \beta}{\sqrt{\beta^2-1}}. \quad (\text{B.5})$$

By expanding Eq. (B.2) in large Q and resolving exponentials in the denominator by a geometric series, we see that the leading contribution comes from $\eta \simeq 1$ ($y = \xi - 1 \simeq 0$). A competition of Q and $\Omega^2 - Q^2$ arises and the limit $\Omega^2 - Q^2 \ll Q$ gives the relevant contribution. The corresponding principal value integral reads:

$$\text{Re } \Pi^R \simeq -Q^{-1/2} \sum_{n=1}^{\infty} \frac{(-1)^n}{(n\pi)^{3/2}} \underbrace{\int_0^\infty \frac{d\sqrt{2y} \sqrt{2y^2} e^{-Qn\sqrt{2y^2}/2}}{(\beta^2-1)^2 - \sqrt{2y^4}}}_{\simeq -\frac{\pi}{4} \frac{1}{\sqrt{\beta^2-1}}} \simeq -\frac{1}{4\sqrt{\pi}} \frac{1}{\sqrt{Q(\beta^2-1)}} \sum_{n=1}^{\infty} \frac{(-1)^{n+1}}{n^{3/2}} \quad (\text{B.6})$$

Region 3

Region 3 is characterized by the conditions $Q \ll 1$ and $\beta < 1$. In this region, only the ξ -integral contributes to Eq. (B.1). By expanding the integrand in small $Q\beta$ we get

$$\text{Im } \Pi^R \simeq \frac{Q\beta}{2\pi} \frac{Q}{\sqrt{1-\beta^2}} \int_1^\infty d\xi \overbrace{\frac{\sqrt{\xi^2-1}}{1+\cosh(\xi Q)}}^{\simeq \frac{2\ln 2}{Q^2}} \simeq \frac{\ln 2}{\pi} \text{Re} \frac{\beta}{\sqrt{1-\beta^2}}. \quad (\text{B.7})$$

The simplification of Eq. (B.2) in region 3 is similar to that leading to Eq. (B.4). The contribution of the first term in Eq. (B.2) is of order $Q \ln Q$, yielding

$$\text{Re } \Pi^R \simeq -\frac{Q}{\pi^2} \int_0^1 \frac{d\eta}{\sqrt{1-\eta^2}} \overbrace{\frac{Q\eta^2}{\beta^2-\eta^2}}^{=-\frac{\pi Q}{2}} \int_1^\infty d\xi \overbrace{\frac{\sqrt{\xi^2-1}}{\cosh(\xi Q)+1}}^{\simeq \frac{2\ln 2}{Q^2}} \simeq \frac{\ln 2}{\pi}. \quad (\text{B.8})$$

Region 4

Finally, in region 4 the conditions $Q \gg 1$ and $\beta < 1$ are fulfilled. In Eq. (B.1) only the ξ -integral contributes and by neglecting $\cosh(Q\beta)$ and expanding the integrand in large $Q\xi$ we get

$$\text{Im } \Pi^R \simeq \frac{\sinh(Q\beta)}{\pi} \frac{Q}{\sqrt{1-\beta^2}} \int_1^\infty d\xi \underbrace{\sqrt{\xi^2-1} e^{-Q\xi}}_{\simeq e^{-Q} \frac{1}{Q^{3/2}} \sqrt{\frac{\pi}{2}}} \simeq \frac{\sinh(Q\beta)}{\sqrt{\beta^2-1}} \frac{e^{-Q}}{\sqrt{2\pi Q}}. \quad (\text{B.9})$$

In region 4 the simplification of Eq. (B.2) differs from that in region 2 in one important point. By neglecting $\cosh(Q\eta)$ in comparison to $\cosh(Q\xi)$, the first term [$\propto \sinh(Q\xi)$] yields no principle value integral, while β is smaller 1. This results in

$$\text{Re } \Pi^R \simeq -\frac{Q}{\pi^2} \int_1^\infty d\xi \frac{\xi}{\sqrt{\xi^2-1}(\beta^2-\xi^2)} \int_0^1 d\eta \sqrt{1-\eta^2} = \frac{1}{8} \frac{Q}{\sqrt{1-\beta^2}}. \quad (\text{B.10})$$

B.2 Calculating the Rates

In this Appendix we calculate the integrals for inelastic scattering rates.

B.2.1 Definitions of the Rates

The rates we are interested in are defined by inserting the kernel \mathcal{K}_j into the integrand for the imaginary part of the total self-energy, Eq. (4.15) ($j = q, +, E, \text{tr}$):

- Total quantum scattering-rate ($j = q$):

$$\mathcal{K}_q = 1;$$

- Energy relaxation-rate ($j = E$):

$$\mathcal{K}_E = \frac{\omega^2}{T^2};$$

- Transport scattering-rate ($j = \text{tr}$):

$$\mathcal{K}_{\text{tr}} = \frac{1}{2} \sin^2 \theta = \frac{1}{2} \frac{q^2 \sin^2 \gamma}{\epsilon^2 + q^2 - 2\epsilon q \cos \gamma}.$$

Here θ is the angle between incoming particle and outgoing particle and γ is the angle between \vec{q} and \vec{p} . The origin of \mathcal{K}_{tr} is explained in Sec. 5.4.1. The kernel for the chiral scattering rate τ_{\pm}^{-1} depends on the scattering channel. In particular, for + chirality at $\epsilon > 0$ the electron-electron scattering kernel contains $\cos^2(\theta/2)$ and the electron-hole scattering kernel contains $\sin^2(\theta/2)$ due to Dirac factors.

It is convenient to introduce the dimensionless energy $y = \epsilon/2T$. The integrals we have to handle are of the following form:

$$\tau_j^{-1}(y) = -\frac{2T^2}{v_F^2} \int_0^\infty \frac{dQ}{2\pi} Q \int_0^{2\pi} \frac{d\gamma}{2\pi} \sum_{\Omega=y \pm \sqrt{y^2 + Q^2 - 2Qy \cos \gamma}} \left[\mathcal{K}_j(\Omega, Q, y) \text{Im} D_{\text{RPA}}^R(\Omega, Q) \left[\coth(\Omega) + \tanh(y - \Omega) \right] \right]. \quad (\text{B.11})$$

Since the combinations $y \pm \sqrt{y^2 + Q^2 - 2Qy \cos \gamma}$ lead to complicated integrands, we split the integrals into the parts corresponding to $Q \ll y$ and $y \ll Q$. Here γ is the angle between the transferred momentum \vec{q} and the initial momentum \vec{p} .

B.2.2 Simplifying the Integrand

The imaginary part of the interaction propagator is given by

$$\text{Im} D_{\text{RPA}}^R(\Omega, Q) = -\frac{D_0^2(Q) N \text{Im} \Pi(\Omega, Q)}{\left[1 + D_0(Q) N \text{Re} \Pi(\Omega, Q)\right]^2 + \left[D_0(Q) N \text{Im} \Pi(\Omega, Q)\right]^2}, \quad (\text{B.12})$$

where

$$D_0(Q) = \frac{v_F^2 \alpha_g \pi}{T Q} \quad (\text{B.13})$$

is the bare Coulomb interaction.

The splitting of the Q integral leads to the following simplification:

$$\Omega \simeq y \pm \begin{cases} y - Q \cos \gamma & Q \ll y \\ Q - y \cos \gamma & y \ll Q \end{cases}, \quad \sqrt{|Q^2 - \Omega^2|} \simeq \begin{cases} 2y & + \\ Q |\sin \gamma| & - \\ 2\sqrt{yQ} \left| \sin \frac{\gamma}{2} \right| & + \\ 2\sqrt{yQ} \left| \cos \frac{\gamma}{2} \right| & - \end{cases} \quad \begin{matrix} Q \ll y \\ y \ll Q \end{matrix} \quad (\text{B.14})$$

Here +, - correspond to the two possible values for Ω that appear in Eq. (B.11). These signs reflect the separation of integration domains into the parts above and below the mass-shell line $Q = \Omega$: + corresponds to $\Omega > Q$ and - corresponds to $\Omega < Q$. Below we simplify the integrands $\mathcal{I} = [g + f] \mathcal{K}_j \text{Im} D_{\text{RPA}}^R$ separately in each to the region in the Q vs Ω plane.

Region 1

In region 1, the dominant contribution to all the rates comes from the domain $y \ll Q$. Using the simplified polarization operator, Eq. (4.2), we obtain

$$\mathcal{I}_{1,2}^j(y, Q, \gamma) \simeq \frac{v_F^2}{T} \frac{1}{N} \frac{\pi^2}{8} \frac{\sqrt{yQ} \left| \sin \frac{\gamma}{2} \right|}{\left(\frac{2\sqrt{y}\sqrt{Q}}{\alpha_g N} \left| \sin \frac{\gamma}{2} \right| - \ln 2 \right)^2 + \left(\frac{\pi}{16} Q^2 \right)^2} \times \begin{cases} 1, & j = q \\ 2 \cos^2 \frac{\gamma}{2}, & j = + \\ 4Q^2, & j = E \\ \frac{1}{2} \sin^2 \gamma, & j = \text{tr} \end{cases} \quad (\text{B.15})$$

Here and below the first digit in the subscript of the function \mathcal{I} denotes the region in the Q vs Ω plane, while the second digit is 1 for $Q \ll y$ and 2 for $Q \gg y$.

Region 2

The contribution to all the rates coming from the region 2 is exponentially small in Regime IV. In other Regimes, it contains at least an extra α_g as compared to the contributions of region 3, except for the situations when results for the rate are determined by momenta q of order T/v_F . In this situations, it turns out that the asymptotics produced by region 2 is the same as the asymptotics of region 3. We remind the reader that finding the numerical value of the prefactor is beyond our analytical approach when integrals are dominated by $q \sim T/v_F$. Therefore, there is no case where we need to calculate the contribution of region 2.

Region 3

Region 3 appears to be the most important region because most of the final results for the rates are determined by this region. In this region both small and large y compared to Q are important:

- $y \gg Q$:

$$\mathcal{I}_{3,1}^j(y, Q, \gamma) \simeq \frac{v_F^2}{NT} \frac{\pi}{\ln 2} \frac{|\sin \gamma| Q^{-1}}{\left[\left(\frac{Q}{\alpha_g N \ln 2} + 1 \right)^2 - 1 \right] \sin^2 \gamma + 1} \times \begin{cases} 1, & j = q \\ 2, & j = + \\ 4Q^2 \cos^2 \gamma, & j = E \\ \frac{1}{2} \frac{Q^2}{y^2} \sin^2 \gamma, & j = \text{tr} \end{cases} ; \quad (\text{B.16})$$

- $y \ll Q$:

$$\mathcal{I}_{3,2}^j(y, Q, \gamma) \simeq \frac{v_F^2}{T} \frac{1}{N} \frac{2\pi}{\ln 2} \sqrt{y} \frac{Q^{-3/2} \cos \frac{\gamma}{2}}{\frac{4y}{Q} \left(\frac{Q}{\alpha_g N \ln 2} + 1 \right)^2 \cos^2 \frac{\gamma}{2} + 1} \times \begin{cases} 1, & j = q \\ 2 \sin^2 \frac{\gamma}{2}, & j = + \\ 4Q^2, & j = E \\ \frac{1}{2} \sin^2 \gamma, & j = \text{tr} \end{cases} \quad (\text{B.17})$$

Region 4

This region is only important for the energy relaxation rate ($j = E$). The corresponding contribution is governed by $Q \ll y$, so that only the energy range $y \gg 1$ is of interest, where

$$\mathcal{I}_{4,1}^E(y, Q, \gamma) \simeq \frac{v_F^2 \alpha_g^2 \pi^2 4N}{T \sqrt{2\pi Q}} \frac{\sin \gamma \cos^2 \gamma}{\left(\sin \gamma + \frac{\alpha_g \pi N}{8}\right)^2} \quad (\text{B.18})$$

B.2.3 Results for the Rates

Finally we estimate the rates in the Regimes I, II, III, and IV as defined in Fig. 4.4, using the simplified integrands of the previous part.

Region 1

The contributions of Region 1 to the quantum and transport scattering rates are only relevant for energies in Regime II for $y \ll Q$, where we have:

$$\tau_j^{-1}(y) = \frac{2T^2}{v_F^2} \int_{\min(y,1)}^1 \frac{dQ}{2\pi} Q \int_0^{2\pi} \frac{d\gamma}{2\pi} \mathcal{I}_{1,2}^j(y, Q, \gamma). \quad (\text{B.19})$$

Performing first the angular integration over γ , we obtain the quantum scattering rate:

$$\tau_q^{-1}(y) \simeq 4\alpha_g T \int_0^1 da \frac{1}{\sqrt{1-a^2}} \simeq 2\pi\alpha_g T, \quad (\text{B.20})$$

the chiral scattering rate:

$$\tau_+^{-1}(y) \simeq 4\alpha_g T \int_0^1 da \sqrt{1-a^2} \simeq \pi\alpha_g T, \quad (\text{B.21})$$

and the transport scattering rate:

$$\tau_{\text{tr}}^{-1}(y) \simeq 8\alpha_g T \int_0^1 da a^2 \sqrt{1-a^2} \simeq \frac{\pi}{2} \alpha_g T. \quad (\text{B.22})$$

Here the integrals over the variable $a = \alpha_g N \ln 2 / \sqrt{4yQ}$ correspond to the Q integration.

Regime	$\tau_q^{-1}(y)$	Q	Ω	γ	θ
II	$\simeq 2\pi\alpha_g T$	$\alpha_g^2 N^2 / y$	Q	$0 \leq \gamma \leq \pi$	$0 \leq \theta \leq \pi$

Table B.1: Contribution of region 1 to the total quantum scattering rate τ_q^{-1} in Regime II and the characteristic values of the transferred momentum Q , transferred frequency Ω , the angle γ between momenta \vec{p} and \vec{q} , and the scattering angle θ (the results here and in tables below are symmetric with respect to $\gamma \rightarrow -\gamma$ and $\theta \rightarrow -\theta$).

Regime	$\tau_+^{-1}(y)$	Q	Ω	γ	θ
II	$\simeq 2\pi\alpha_g T$	$\alpha_g^2 N^2 / y$	Q	$0 < \gamma < \pi$	$0 < \theta < \pi$

Table B.2: Contribution of region 1 to the chiral quantum scattering rate τ_+^{-1} in Regime II and the characteristic values of Q, Ω , γ , and θ dominating this contribution.

Regime	$\tau_{\text{tr}}^{-1}(y)$	Q	Ω	γ	θ
II	$\simeq \pi\alpha_g T / 2$	$\alpha_g^2 N^2 / y$	Q	$0 < \gamma < \pi$	$0 < \theta < \pi$

Table B.3: Contribution of region 1 to the transport scattering rate τ_{tr}^{-1} in Regime II and the characteristic values of Q, Ω , γ , and θ dominating this contribution.

In all the regimes, the contribution of region 1 to the energy relaxation rate is parametrically the same as that of other regions. Since the numerical prefactor is not accessible within our calculation (the integrals are dominated by $qv_F \sim T$), we have chosen to present only the calculation of the contribution of region 3.

Region 2

There is no important contribution from region 2 (see Sec. B.2.2 above).

Region 3

This is the most important region for all the rates in most of the Regimes. The corresponding integrals are expressed through the kernels $\mathcal{I}_{3,i}^j$ introduced in Sec. B.2.2 as follows:

$$\tau_j^{-1}(y) = \frac{2T^2}{v_F^2} \int_0^{\min(y,1)} \frac{dQ}{2\pi} Q \int_0^{2\pi} \frac{d\gamma}{2\pi} \mathcal{I}_{3,1}^j(y, Q, \gamma) + \frac{2T^2}{v_F^2} \int_{\min(y,1)}^1 \frac{dQ}{2\pi} Q \int_0^{2\pi} \frac{d\gamma}{2\pi} \mathcal{I}_{3,2}^j(y, Q, \gamma) \quad (\text{B.23})$$

Using the short-hand notations

$$x' = \frac{1}{\alpha_g N \ln 2}, \quad y' = \frac{y}{\alpha_g N \ln 2},$$

we obtain the following result for the contribution of region 3 to the quantum scattering rate:

$$\tau_q^{-1}(y) \simeq \frac{\alpha_g T}{\pi} \left\{ \int_0^{\min(x',y')} dx \frac{\text{arsinh}[\sqrt{x(x+2)}]}{\sqrt{x(x+2)}(x+1)} + \int_{\min(x',y')}^{x'} dx \frac{\text{arsinh}\left[\sqrt{4y'}\left(\sqrt{x+\frac{1}{x}}\right)\right]}{(1+x)\sqrt{1+4y'\left(\sqrt{x+\frac{1}{x}}\right)^2}} \right\}. \quad (\text{B.24})$$

Regime	$\tau_q^{-1}(y)$	Q	Ω	γ	θ
I	$\sim \frac{\sqrt{y}}{N}T$	1	$-Q$	$0 < \gamma < \pi$	$0 < \theta < \pi$
II	$\simeq \pi\alpha_g T$	$\alpha_g^2 N^2/y$	$-Q$	$0 < \gamma < \pi$	$0 < \theta < \pi$
III	$\simeq \frac{4\beta(2)}{\pi}\alpha_g T$	$\alpha_g NT$	$Q \cos \gamma$	$0 < \gamma < \pi$	$\theta \lesssim \frac{\alpha_g N}{y} \ll 1$
IV	$\simeq \frac{4\beta(2)}{\pi}\alpha_g T$	$\alpha_g NT$	$Q \cos \gamma$	$0 < \gamma < \pi$	$\theta \lesssim \frac{\alpha_g N}{y} \ll 1$

Table B.4: Contribution of region 3 to the total quantum scattering rate τ_q^{-1} in all energy domains and the corresponding characteristic values of the transferred momentum Q, transferred frequency Ω , the angle γ between momenta \vec{p} and \vec{q} , and the scattering angle θ .

For the contribution of region 3 to the chiral scattering rate we get:

$$\tau_+^{-1}(y) \simeq \frac{\alpha_g T}{\pi} \left\{ \int_0^{\min(x', y')} dx \frac{\operatorname{arsinh}[\sqrt{x(x+2)}]}{\sqrt{x(x+2)}(x+1)} + \int_{\min(x', y')}^{x'} dx \frac{\sqrt{1 + 4y' \left(\sqrt{x} + \frac{1}{\sqrt{x}}\right)^2} \operatorname{arsinh} \left[\sqrt{4y' \left(\sqrt{x} + \frac{1}{\sqrt{x}}\right)} \right] - \sqrt{4y' \left(\sqrt{x} + \frac{1}{\sqrt{x}}\right)}}{(1+x)^2 \frac{4y'}{x}} \right\} \quad (\text{B.25})$$

Regime	$\tau_+^{-1}(y)$	Q	Ω	γ	θ
I	$\sim \frac{\sqrt{y}}{N}T$	1	$-Q$	$0 < \gamma < \pi$	$0 < \theta < \pi$
II	$\simeq \pi\alpha_g T$	$\alpha_g^2 N^2/y$	$-Q$	$0 < \gamma < \pi$	$0 < \theta < \pi$
III	$\simeq \frac{8\beta(2)}{\pi}\alpha_g T$	$\alpha_g NT$	$Q \cos \gamma$	$0 < \gamma < \pi$	$\theta \lesssim \frac{\alpha_g N}{y} \ll 1$
IV	$\simeq \frac{8\beta(2)}{\pi}\alpha_g T$	$\alpha_g NT$	$Q \cos \gamma$	$0 < \gamma < \pi$	$\theta \lesssim \frac{\alpha_g N}{y} \ll 1$

Table B.5: Contribution of region 3 to the chiral quantum scattering rate τ_+^{-1} in all energy domains and the corresponding characteristic values of Q, Ω , γ , and θ .

The contribution of region 3 to the energy relaxation rate reads:

$$\tau_E^{-1}(y) \simeq \frac{\alpha_g}{\pi(x')^2} T \left\{ \int_0^{\min(x', y')} dx \frac{x}{x+2} \left[\frac{\operatorname{arsinh}(\sqrt{x(x+2)})}{(x+1)^{-1} \sqrt{x(x+2)}} - 1 \right] + \int_{\min(x', y')}^{x'} dx \frac{x^2 \operatorname{arsinh} \left[\sqrt{4y' \left(\sqrt{x} + \frac{1}{\sqrt{x}} \right)} \right]}{(1+x) \sqrt{1+4y' \left(\sqrt{x} + \frac{1}{\sqrt{x}} \right)^2}} \right\}. \quad (\text{B.26})$$

Regime	$\tau_E^{-1}(y)$	Q	Ω	γ	θ
I	$\sim \frac{\sqrt{y}}{N} T$	1	$-Q$	$0 < \gamma < \pi$	$0 < \theta < \pi$
II	$\sim \alpha_g^2 T \frac{N}{\sqrt{y}} \ln \left(\frac{y}{\alpha_g^2 N^2} \right)$	1	$-Q$	$\pi - \frac{\alpha_g N}{\sqrt{y}}$	$\frac{\alpha_g N}{\sqrt{y}} \ll 1$
III	$\sim \alpha_g^2 T \frac{N}{\sqrt{y}} \ln \left(\frac{y}{\alpha_g^2 N^2} \right)$	1	$-Q$	$\pi - \frac{\alpha_g N}{\sqrt{y}}$	$\frac{\alpha_g N}{\sqrt{y}} \ll 1$
IV	$\sim \alpha_g^2 N T \ln \left(\frac{1}{\alpha_g^2 N^2} \right)$	1	$-Q$	$\pi - \frac{\alpha_g N}{\sqrt{y}}$	$\theta \lesssim \frac{\alpha_g N}{y} \ll 1$

Table B.6: Contribution of region 3 to the energy relaxation rate τ_E^{-1} obtained in all energy domains within the energy-diffusion approximation and the corresponding characteristic values of Q , Ω , γ , and θ . Since in all energy domains the result is dominated by $Q \sim 1$, the numerical prefactors can not be obtained from the asymptotics at $Q \ll 1$ and $Q \gg 1$.

Finally, region 3 yields the following result for τ_{tr}^{-1} :

$$\tau_{\text{tr}}^{-1}(y) \simeq \frac{\alpha_g}{2\pi y'^2} T \int_0^{\min(x', y')} dx \frac{x}{x+2} \left[1 - \frac{\operatorname{arsinh}(\sqrt{x(x+2)})}{(x+1)\sqrt{x(x+2)}} \right] + \frac{4}{\pi} \alpha_g T \int_{\min(x', y')}^{x'} dx \sqrt{\frac{y'}{x}} \left[\frac{z^2 + 3}{3z^4} - \frac{\operatorname{arsinh} z}{z^5 (1+z^2)^{-1/2}} \right]_{z=\sqrt{4y' \left(\sqrt{x} + \frac{1}{\sqrt{x}} \right)}}. \quad (\text{B.27})$$

Regime	$\tau_{\text{tr}}^{-1}(y)$	Q	Ω	γ	θ
I	$\sim \frac{\sqrt{y}}{N} T$	1	$-Q$	$0 < \gamma < \pi$	$0 < \theta < \pi$
II	$\simeq \frac{\pi}{4} \alpha_g T$	$\frac{\alpha_g^2 N^2}{y}$	$-Q$	$\pi - \frac{\alpha_g N}{\sqrt{y}}$	$\frac{\alpha_g N}{\sqrt{y}} \ll 1$
III	$\sim \frac{N}{y} \alpha_g^2 T$	y	$y(1 - 2 \sin \frac{\gamma}{2})$	$\frac{\alpha_g N}{y} \ \& \ \pi - \frac{\alpha_g N}{y}$	$\theta \lesssim \frac{\alpha_g N}{y} \ll 1$
IV	$\sim \frac{N}{y^2} \alpha_g^2 T$	1	$Q \cos \gamma$	$\frac{\alpha_g N}{y}$	$\theta \lesssim \frac{\alpha_g N}{y} \ll 1$

Table B.7: Contribution of region 3 to the transport scattering rate τ_{tr}^{-1} in all energy domains and the corresponding characteristic values of Q , Ω , γ , and θ . Since in energy domains I and IV the result is dominated by $Q \sim 1$, the numerical prefactors in these domains are beyond the accuracy of our approximations. Furthermore, since in Regime III the integral is dominated by $Q \sim y$, the splitting of the integrand according Eqs. (B.16) and (B.17) does not reproduce the correct prefactor.

Region 4

This region is only relevant for the energy relaxation rate in Regime IV, where the main contribution comes from $Q \ll y$, yielding

$$\tau_{\text{E}}^{-1}(y) = \frac{8T^2}{v_F^2} \int_1^{\max(y,1)} \frac{dQ}{2\pi} Q \int_0^{\frac{\pi}{2} - \frac{1}{Q}} \frac{d\gamma}{2\pi} \mathcal{I}_{4,1}^{\text{E}, \gamma \ll \frac{\pi}{2} - \frac{1}{Q}}(y, Q, \gamma) \approx \frac{12N}{\sqrt{2\pi}} \alpha_g^2 T y^{3/2} \ln\left(\frac{16}{N\pi\alpha_g\sqrt{y}}\right). \quad (\text{B.28})$$

Since the result is determined by $Q \sim \Omega \sim y \gg 1$, the energy-diffusion model is, in fact, not applicable in this Regime.

B.3 Scattering Rates from the Generalized Golden Rule

In this Appendix we analyze the Golden Rule (GR) approach to calculating quantum and transport scattering rates. The quantum scattering rate for electrons was introduced in Eq. (4.16). Using the imaginary part of the self energy Eq. (24), we obtain

$$\begin{aligned} \tau_+^{-1}(\epsilon) &\propto \int d\vec{q} \int d\omega \left| D_{\text{RPA}}(q, \omega) \right|^2 [1 - n_F(\epsilon - \omega)] \int d\vec{p} \text{Tr} \left[\mathcal{P}_+(\vec{p}) \delta(\epsilon - v_{\text{FP}}) \mathcal{A}_0(\epsilon - \omega, \vec{p} - \vec{q}) \right] \\ &\times \int dE \left[n_F(E - \omega/2) - n_F(E + \omega/2) \right] \int d\vec{k} \text{Tr} \left[\mathcal{A}_0(E - \omega/2, \vec{k} - \vec{q}/2) \mathcal{A}_0(E + \omega/2, \vec{k} + \vec{q}/2) \right]. \end{aligned} \quad (\text{B.29})$$

The spectral weights \mathcal{A}_0 are defined in Eq. (2.19). Equation (B.29) is completely equivalent to Eq. (46) of the main text.

We can regard the quantum scattering rate as the probability (per unit time) of the electron decay with emitting an electron-hole pair. The amplitude of this decay process is given by the “half” of the self-energy diagram shown in Fig. B.2. The incoming and outgoing particles in this diagram are taken at the mass shell. Equation (B.29) has the form of the Fermi golden rule with the amplitude determined by the RPA-screened interaction.

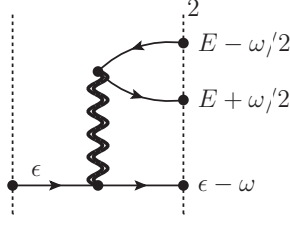


Figure B.2: Diagram for the “elementary” inelastic scattering amplitude.

We now apply the GR to calculate the transport scattering rate. This amounts to including an extra transport factor $[\vec{v}_i \cdot (\vec{v}_i - \vec{v}_f)]/v_F^2$ accounting for the change of the current due to scattering, in the integrand of Eq. (B.29). Here \vec{v}_i and \vec{v}_f are total velocities of incoming and outgoing particles. For the linear electronic dispersion the velocities of individual quasi-particles are determined by the relation

$$\vec{v} = \frac{\partial \epsilon}{\partial \vec{p}} = \frac{v_F^2 \vec{p}}{\epsilon} \quad (\text{B.30})$$

This results in the following transport factor:

$$\frac{\vec{v}_i \cdot (\vec{v}_i - \vec{v}_f)}{v_F^2} = v_F^2 \frac{\vec{p}}{\epsilon} \left(\frac{\vec{p}}{\epsilon} - \frac{\vec{p} - \vec{q}}{\epsilon - \omega} - \frac{\vec{k} + \vec{q}/2}{E + \omega/2} + \frac{\vec{k} - \vec{q}/2}{E - \omega/2} \right), \quad (\text{B.31})$$

Note that in the conventional case of massive particles with the quadratic electronic dispersion, $\vec{v} = \vec{p}/m$ and hence $\vec{v}_i - \vec{v}_f \propto \vec{p} - (\vec{p} - \vec{q}) - (\vec{k} + \vec{q}/2) + (\vec{k} - \vec{q}/2) = 0$, which reflects the fact that because of the total momentum conservation there is no current relaxation in conventional metals due to the electron-electron interaction.

We now make use of the particle-hole symmetry of the graphene spectrum in order to simplify the expression for transport scattering rate. Let us reverse the integration variables in the second line of Eq. (B.29): $(E, \vec{k}) \mapsto (-E, -\vec{k})$. Using the symmetry $\mathcal{A}_0(\epsilon, \vec{p}) = \mathcal{A}_0(-\epsilon, -\vec{p})$, we see that the trace in the integrand is not changed. The difference of two equilibrium distribution functions in the second line of Eq. (B.29) is also independent of the sign of E . Thus the contribution of particle-hole pair into the current relaxation vanishes, which corresponds to the absence of the Coulomb-drag contribution to the conductivity in undoped graphene (Fig. 5.7f). This allows us to keep only the part of the transport factor Eq. (B.31) which is even under reversing E and \vec{k} ,

$$v_F^2 \frac{\vec{p}}{\epsilon} \left(\frac{\vec{p}}{\epsilon} - \frac{\vec{p} - \vec{q}}{\epsilon - \omega} \right) = 1 - \text{sign}(\epsilon - \omega) \cos \theta, \quad (\text{B.32})$$

where θ is the scattering angle. Inserting this reduced transport factor into the first line of Eq. (B.29) and calculating the trace of projection operators, we obtain

$$\begin{aligned} & [1 - \text{sign}(\epsilon - \omega) \cos \theta] \text{Tr} \left[\mathcal{P}_+(\vec{p}) \mathcal{A}_0(\epsilon - \omega, \vec{p} - \vec{q}) \right] \\ &= -\frac{\pi}{2} [1 - \text{sign}(\epsilon - \omega) \cos \theta] \left[(1 + \cos \theta) \delta(\epsilon - \omega - v_F |\vec{p} - \vec{q}|) + (1 - \cos \theta) \delta(\epsilon - \omega + v_F |\vec{p} - \vec{q}|) \right] \\ &= \frac{1}{2} (1 - \cos^2 \theta) \left[\mathcal{A}_{0,+}(\epsilon - \omega, \vec{p} - \vec{q}) + \mathcal{A}_{0,-}(\epsilon - \omega, \vec{p} - \vec{q}) \right]. \quad (\text{B.33}) \end{aligned}$$

This way the transport factor $1 - \cos^2 \theta$ appears for Dirac fermions.

The GR calculation of the transport scattering rate reproduces the result obtained from the Drude conductivity Eq. (5.58). Note that an additional broadening δ was not used in this calculation. This shows that our result for τ_{tr}^{-1} can be actually applied in the limit $\tau_{\text{tr}}^{-1} \gg \delta$ as we argued in Sec. 5.4.3.

C

Effective Kinetic Equations and Collision Integrals

C.1 Solution of the Effective Kinetic Equation

In this appendix we will provide additional details to follow more easily the calculation and the arguments drawn in Sec. 5.2 and 7.1. Although we provide details for Chap. 5 we keep for generality the labels of the layers as they are used starting with Chap. 6.

C.1.1 The Functional Approach

In Sec. 5.2.2 we introduced the functional technique to find the proper effective kinetic equations. As discussed in Sec. 5.2.2 the crucial part of this technique is the ansatz (7.12). To discuss some kind of general treatment we will consider an easy case with several directions given. We consider two orthogonal directions to begin with. Note that if only one direction is relevant the discussion simplifies a lot by choosing this direction as the one the ansatz points to.

To do so we will consider the functional that corresponds to the relaxation time ansatz. Proceeding with linearization we might write down a functional in analogy to Eq. (5.21):

$$F(h) = \int dx_1 \nu(\epsilon_1) \frac{\partial n_F}{\partial \epsilon_1} \left[\frac{e\vec{E}\vec{v}_1}{T^2} h_1 - \frac{1}{2T\tau_{\text{dis}}} h_1^2 \right]. \quad (\text{C.1})$$

If we plug in an ansatz of the type $h = \sum_{\beta} \chi_v^{\beta} \vec{v} \vec{e}_{\beta}$ where \vec{e}_{β} corresponds to a unity vector, $\beta \in \{x, y\}$ and $\vec{e}_x \vec{e}_y = 0$.

To continue let us firstly consider the situation of having two physical directions \vec{A} and \vec{B} . If we assume that the absolute orientation in space does not matter and only the relative orientation of \vec{A} and \vec{B} affects the system we can rewrite expressions of the type

$$\begin{aligned} \langle (\vec{A}\vec{v}) (\vec{B}\vec{v}) \rangle_{\varphi} &= ABv^2 \int_0^{2\pi} \frac{d\varphi}{2\pi} \cos(\varphi_A - \varphi) \cos(\varphi_B - \varphi) \\ &= ABv^2 \int_{0-\varphi_A}^{2\pi-\varphi_A} \frac{d\bar{\varphi}}{2\pi} \cos(\bar{\varphi}) \left[\cos(\bar{\varphi}) \cos(\varphi_A - \varphi_B) - \sin(\bar{\varphi}) \sin(\varphi_A - \varphi_B) \right] \\ &= \frac{1}{2} ABv^2 \cos(\varphi_A - \varphi_B) = \frac{v^2}{2} \vec{A}\vec{B} \quad (\text{C.2}) \end{aligned}$$

Using this observation we can rewrite Eq. (C.1) within the assumption $\vec{e}_x \vec{e}_y = 0$ to gain:

$$\begin{aligned}
F(\chi_v^\beta, \chi_p^\beta) &= \sum_\beta \int d\epsilon_1 \nu(\epsilon_1) \frac{\partial n_F}{\partial \epsilon_1} \left[\frac{1}{2T^2} e \vec{E} \vec{e}_\beta \chi_v^\beta - \frac{1}{4T\tau_{\text{dis}}} (\chi_v^\beta)^2 \right] \\
&= \sum_\beta \frac{1}{2} \left[\frac{e \vec{E} \vec{e}_\beta}{T^2} A_0 \chi_v^\beta - \frac{1}{2T\tau_{\text{dis}}} (A_0 (\chi_v^\beta)^2) \right], \quad (\text{C.3})
\end{aligned}$$

where we used the A s according to definition (5.25). We see that within this schematics we gain $\chi_v^\beta = e\tau_{\text{dis}} \vec{E} \vec{e}_\beta / T$ which gives the proper direction \vec{E} for the current, since $\sum_\beta (\vec{E} \vec{e}_\beta) (\vec{v} \vec{e}_\beta) = \sum_\beta \vec{E} (\vec{e}_\beta \otimes \vec{e}_\beta) \vec{v} = \vec{v} \vec{E}$ if used in Eq. (5.29).

C.1.2 Derivation of the Effective Kinetic Equation for Coulomb Drag of Two Layers

With help of the functional method introduced in Sec. 5.2.2 we will calculate the effective kinetic equation for the two layer case following the one layer calculation given in Sec. 5.2.2. To do so we use the two layer functional (7.10) derived in Sec. 7.1.1 We therefore use the functional obtained in Eq. (7.10) to proceed as in Sec. 7.1 and apply the ansatz (7.12) to it. Since in each layer, the direction is given by the external electric field we skip the direction splitting introduced in Sec. C.1.1. We gain four kinetic equations of an algebraic structure by taking the derivative of $F[h_a(\chi_v^{aa}, \chi_p^{aa}), h_b(\chi_v^{ba}, \chi_p^{ba})]$ with respect to $\chi_v^{aa}, \chi_v^{ba}, \chi_p^{aa}$ and χ_p^{ba} . For brevity we use $z_\alpha T \tau_{\text{dis}}^\alpha = 1$ and get the conditions:

$$\begin{aligned}
0 &= \frac{\delta F}{\delta \chi_v^{aa}} = \int dx \nu(\epsilon) \frac{\partial n_F^a(\epsilon)}{\partial \epsilon} \left(e \frac{\vec{E}_a}{T^2} \vec{v} \right)^2 \left[1 - z_a \left(\chi_v^{aa} + \chi_p^{aa} \frac{\epsilon}{T} \right) \right] + \frac{N_a \chi_v^{aa}}{4T^2} \int d\{x_i\} W^{aa}(\{x_i\}) \left[(\vec{v}_1 - \vec{v}_2 + \vec{v}_3 - \vec{v}_4) \frac{e \vec{E}_a}{T^2} \right]^2 \\
&\quad + \frac{N_b}{2T^2} \int d\{x_i\} W^{ab}(\{x_i\}) \left\{ \left[\chi_v^{aa} (\vec{v}_1 - \vec{v}_2) + \chi_v^{ba} (\vec{v}_3 - \vec{v}_4) + \frac{\vec{q}}{T} (\chi_p^{aa} - \chi_p^{ba}) \right] e \frac{\vec{E}_a}{T^2} \right\} (\vec{v}_1 - \vec{v}_2) e \frac{\vec{E}_a}{T^2}, \\
0 &= \frac{\delta F}{\delta \chi_p^{aa}} = \int dx \nu(\epsilon) \frac{\partial n_F^a(\epsilon)}{\partial \epsilon} \left(e \frac{\vec{E}_a}{T^2} \vec{v} \right)^2 \frac{\epsilon}{T} \left[1 - z_a \left(\chi_v^{aa} + \chi_p^{aa} \frac{\epsilon}{T} \right) \right] \\
&\quad + \frac{N_b}{2T^2} \int d\{x_i\} W^{ab}(\{x_i\}) \left\{ \left[\chi_v^{aa} (\vec{v}_1 - \vec{v}_2) + \chi_v^{ba} (\vec{v}_3 - \vec{v}_4) + \frac{\vec{q}}{T} (\chi_p^{aa} - \chi_p^{ba}) \right] e \frac{\vec{E}_a}{T^2} \right\} \frac{\vec{q}}{T} e \frac{\vec{E}_a}{T^2}, \\
0 &= \frac{\delta F}{\delta \chi_p^{ba}} = - \int dx \nu(\epsilon) \frac{\partial n_F^b(\epsilon)}{\partial \epsilon} \left(e \frac{\vec{E}_a}{T^2} \vec{v} \right)^2 \frac{\epsilon}{T} z_b \left(\chi_v^{ba} + \chi_p^{ba} \frac{\epsilon}{T} \right) \\
&\quad + \frac{N_a}{2T^2} \int d\{x_i\} W^{ab}(\{x_i\}) \left\{ \left[\chi_v^{aa} (\vec{v}_1 - \vec{v}_2) + \chi_v^{ba} (\vec{v}_3 - \vec{v}_4) + \frac{\vec{q}}{T} (\chi_p^{aa} - \chi_p^{ba}) \right] e \frac{\vec{E}_a}{T^2} \right\} \frac{\vec{q}}{T} e \frac{\vec{E}_a}{T^2}, \\
0 &= \frac{\delta F}{\delta \chi_v^{ba}} = - \int dx \nu(\epsilon) \frac{\partial n_F^b(\epsilon)}{\partial \epsilon} \left(e \frac{\vec{E}_a}{T^2} \vec{v} \right)^2 z_b \left(\chi_v^{ba} + \chi_p^{ba} \frac{\epsilon}{T} \right) + \frac{N_b \chi_v^{ba}}{4T^2} \int d\{x_i\} W^{bb}(\{x_i\}) \left[(\vec{v}_1 - \vec{v}_2 + \vec{v}_3 - \vec{v}_4) \frac{e \vec{E}_a}{T^2} \right]^2 \\
&\quad + \frac{N_a}{2T^2} \int d\{x_i\} W^{ab}(\{x_i\}) \left\{ \left[\chi_v^{aa} (\vec{v}_1 - \vec{v}_2) + \chi_v^{ba} (\vec{v}_3 - \vec{v}_4) + \frac{\vec{q}}{T} (\chi_p^{aa} - \chi_p^{ba}) \right] e \frac{\vec{E}_a}{T^2} \right\} (\vec{v}_3 - \vec{v}_4) e \frac{\vec{E}_a}{T^2}.
\end{aligned} \tag{C.4}$$

we also used the fact that the system obeys no anisotropy meaning that as explained in Eq. (C.2) we can use the following identity $2(\vec{v}_i \vec{E})(\vec{v}_j \vec{E}) = \vec{v}_i \vec{v}_j \vec{E}^2$. For simplicity we drop the indices that indicate the electric field the modes are directed to. Further more we replaced $\epsilon_1 \vec{v}_1 - \epsilon_2 \vec{v}_2$ with \vec{q} for brevity. Doing so one gets:

$$\begin{pmatrix} A_0^a & 0 \\ 0 & A_0^b \\ A_1^a & 0 \\ 0 & A_1^b \end{pmatrix} = \begin{pmatrix} N_a I_{\text{Tr}}^a + z_a A_0^a & -N_b I_{\text{D}} & N_b I_{\text{Th}}^{ab} + z_a A_1^a & -N_b I_{\text{Th}}^{ab} \\ -N_a I_{\text{D}} & N_b I_{\text{Tr}}^b + z_b A_0^b & -N_a I_{\text{Th}}^{ba} & N_a I_{\text{Th}}^{ba} + z_b A_1^b \\ N_b I_{\text{Th}}^{ab} + z_a A_1^a & -N_b I_{\text{Th}}^{ba} & N_b I_{\text{E}} + z_a A_2^a & -N_b I_{\text{E}} \\ -N_a I_{\text{Th}}^{ab} & N_a I_{\text{Th}}^{ba} + z_b A_1^b & -N_a I_{\text{E}} & N_a I_{\text{E}} + z_b A_2^b \end{pmatrix} \begin{pmatrix} \chi_v^a \\ \chi_v^b \\ \chi_p^a \\ \chi_p^b \end{pmatrix}. \quad (\text{C.5})$$

with the usage of the short-hand notation defined in Eq. (7.13).

Conductivity and Resistivity for Three Modes

By inverting M (see Eq. (7.15)) it is a straight forward task to obtain the conductivity σ with the entries (for even more brevity $A_n(\mu_\alpha) = A_n^a$ further $N_a = N_b = N$ and $z_a = z_b = z$ later restored for resistivity):

$$\sigma_{aa} = \frac{e^2 N^2 v_F^2}{2} \frac{1}{\text{Det}(M)} \left\{ 2z A_0^a A_1^a A_1^b I_{\text{D}} + z (A_0^a)^2 \left[(A_2^a + A_2^b) (I_{\text{Tr}}^b + z A_0^b) - z (A_1^b)^2 \right] \right. \\ \left. - (A_1^a)^2 \left[(I_{\text{Tr}}^a + z A_0^a) (I_{\text{Tr}}^b + z A_0^b) + I_{\text{D}}^2 \right] \right\}, \quad (\text{C.6})$$

$$\sigma_{bb} = \frac{e^2 N^2 v_F^2}{2} \frac{1}{\text{Det}(M)} \left\{ 2z A_0^b A_1^a A_1^b I_{\text{D}} + z (A_0^b)^2 \left[(A_2^a + A_2^b) (I_{\text{Tr}}^a + z A_0^a) - z (A_1^a)^2 \right] \right. \\ \left. - (A_1^b)^2 \left[(I_{\text{Tr}}^a + z A_0^a) (I_{\text{Tr}}^b + z A_0^b) + I_{\text{D}}^2 \right] \right\}, \quad (\text{C.7})$$

$$\sigma_{\text{D}} = \sigma_{ba} = \sigma_{ab} = \frac{e^2 N^2 v_F^2}{2} \frac{-1}{\text{Det}(M)} \left\{ A_1^a A_1^b (I_{\text{Tr}}^a I_{\text{Tr}}^b - I_{\text{D}}^2) \right. \\ \left. + z I_{\text{D}} \left[A_0^a (A_1^b)^2 + A_0^b (A_1^a)^2 - A_0^a A_0^b (A_2^a + A_2^b) \right] \right\}, \quad (\text{C.8})$$

where the determinant of the matrix M is given by

$$\text{Det}(M) = z \left\{ 2z A_1^a A_1^b I_{\text{D}} + (A_2^a + A_2^b) \left[(I_{\text{Tr}}^a + z A_0^a) (I_{\text{Tr}}^b + z A_0^b) - I_{\text{D}}^2 \right] \right. \\ \left. - z \left[(A_1^b)^2 (I_{\text{Tr}}^a + z A_0^a) + (A_1^a)^2 (I_{\text{Tr}}^b + z A_0^b) \right] \right\}. \quad (\text{C.9})$$

If one applies the relation of drag resistivity with conductivity given in Eq. (6.7) (the non-approximated version) one ends up with

$$\rho_D = \frac{-2}{e^2 N v_F^2} \frac{\frac{A_1^a A_1^b}{A_0^a A_0^b} (I_D^2 - I_{\text{Tr}}^a I_{\text{Tr}}^b) + z I_D \left[A_2^a + A_2^b - A_1^a \frac{A_1^a}{A_0^a} - A_1^b \frac{A_1^b}{A_0^b} \right]}{A_0^b \frac{(A_1^a)^2}{A_0^a} I_{\text{Tr}}^a + A_0^a \frac{(A_1^b)^2}{A_0^b} I_{\text{Tr}}^b + 2 A_1^a A_1^b I_D + z A_0^a A_0^b \left[A_2^a + A_2^b - A_1^a \frac{A_1^a}{A_0^a} - A_1^b \frac{A_1^b}{A_0^b} \right]} \quad (\text{C.10})$$

where one recognizes repetitive patterns that indicate a simplification by introducing new shortening objects as they are given in equations (7.19) and (7.20)

C.1.3 The Effective Kinetic Equation for Three Layers

In Sec. C.1.2 we showed how to get the effective kinetic equation out of the functional (7.10) with help of the ansatz (7.12). In this ansatz we did not need to limit ourselves to two layers only as explained in Sec. 8.1. Hence we can consider the more complicated case of three layers. The functional for three layers involves additional distribution functions and collision integrals which surely make the derivation of the effective kinetic equation for three layers more lengthy. For this reason we will not give all the details but refer to the essential steps. Writing down the functional and determining the new saddle point equations (see the discussion in Sec. 5.2.2) is a lengthy but straight forward task. The result needs to be of the following form:

$$\begin{pmatrix} A_0^a & 0 & 0 \\ 0 & A_0^b & 0 \\ 0 & 0 & A_0^c \\ A_1^a & 0 & 0 \\ 0 & A_1^b & 0 \\ 0 & 0 & A_1^c \end{pmatrix} = (\hat{I} + \hat{A}) \begin{pmatrix} \chi_v^{aI} & \chi_v^{aII} & \chi_v^{aIII} \\ \chi_v^{bI} & \chi_v^{bII} & \chi_v^{bIII} \\ \chi_v^{cI} & \chi_v^{cII} & \chi_v^{cIII} \\ \chi_p^{aI} & \chi_p^{aII} & \chi_p^{aIII} \\ \chi_p^{bI} & \chi_p^{bII} & \chi_p^{bIII} \\ \chi_p^{cI} & \chi_p^{cII} & \chi_p^{cIII} \end{pmatrix}. \quad (\text{C.11})$$

Since the three layer situation involves bigger matrices we separated the matrix that comes from the relaxation time collision kernel

$$\hat{A} = \begin{pmatrix} x_a A_0^a & 0 & 0 & x_a A_1^a & 0 & 0 \\ 0 & x_b A_0^b & 0 & 0 & x_b A_1^b & 0 \\ 0 & 0 & x_c A_0^c & 0 & 0 & x_c A_1^c \\ x_a A_1^a & 0 & 0 & x_a A_2^a & 0 & 0 \\ 0 & x_b A_1^b & 0 & 0 & x_b A_2^b & 0 \\ 0 & 0 & x_c A_1^c & 0 & 0 & x_c A_2^c \end{pmatrix}, \quad (\text{C.12})$$

from the matrix that is determined by the coulomb collision kernel.

$$\hat{I} = \begin{pmatrix} N_a I_{\text{Tr}}^a & -N_b I_{\text{D}}^{ab} & -N_c I_{\text{D}}^{ac} & \sum_{\alpha \neq a} N_\alpha I_{\text{Th}}^{a\alpha} & -N_b I_{\text{Th}}^{ab} & -N_c I_{\text{Th}}^{ac} \\ -N_a I_{\text{D}}^{ba} & N_b I_{\text{Tr}}^b & -N_c I_{\text{D}}^{bc} & -N_a I_{\text{Th}}^{ba} & \sum_{\alpha \neq b} N_\alpha I_{\text{Th}}^{b\alpha} & -N_c I_{\text{Th}}^{bc} \\ -N_a I_{\text{D}}^{ca} & -N_b I_{\text{D}}^{cb} & N_c I_{\text{Tr}}^c & -N_a I_{\text{Th}}^{ca} & -N_b I_{\text{Th}}^{cb} & \sum_{\alpha \neq c} N_\alpha I_{\text{Th}}^{c\alpha} \\ \sum_{\alpha \neq a} N_\alpha I_{\text{Th}}^{a\alpha} & -N_b I_{\text{Th}}^{ba} & -N_c I_{\text{Th}}^{ca} & \sum_{\alpha \neq a} N_\alpha I_{\text{E}}^{a\alpha} & -N_b I_{\text{E}}^{ab} & -N_c I_{\text{E}}^{ac} \\ -N_a I_{\text{Th}}^{ab} & \sum_{\alpha \neq b} N_\alpha I_{\text{Th}}^{b\alpha} & -N_c I_{\text{Th}}^{cb} & -N_a I_{\text{E}}^{ab} & \sum_{\alpha \neq b} N_\alpha I_{\text{E}}^{b\alpha} & -N_c I_{\text{E}}^{cb} \\ -N_a I_{\text{Th}}^{ac} & -N_b I_{\text{Th}}^{bc} & \sum_{\alpha \neq c} N_\alpha I_{\text{Th}}^{c\alpha} & -N_a I_{\text{E}}^{ac} & -N_b I_{\text{E}}^{bc} & \sum_{\alpha \neq c} N_\alpha I_{\text{E}}^{c\alpha} \end{pmatrix}. \quad (\text{C.13})$$

In the right bottom three by three block of the definition (C.13) we see, similar to Eq. (C.5), the appearance of the energy relaxation rates $I_{\text{E}}^{\alpha\beta}$ which are in the same way divergent as we discussed it in Sec. 7.1 for the two layer case. The idea is again to diagonalize this block which again has one obvious eigenvalue 0 by adding up the rows or columns (the columns need some ratio of N_α s involved). The mode that turns out to be unaffected by the interlayer thermalization is $\chi_p(N_a + N_b + N_c) = N_a \chi_p^a + N_b \chi_p^b + N_c \chi_p^c$ and again all orthogonal modes get suppressed leading to an effective three layer thermalization. Although the calculation is more involved this time one can explicitly show that except for the case of switching of one layer $N_\alpha \rightarrow 0$ the diagonal element after rotation is always proportional to the energy relaxation rate I_{E} .

To think, that the same idea works in case of a multilayer setup has not been proven strictly so far since the analytic diagonalization becomes quite complicated which means that the multilayer thermalization is the weak point to argue about. Still per construction it is clear that $\chi_p \sum_\beta N_\beta = \sum_\beta N_\beta \chi_p^\beta$ is the mode with zero eigenvalue for arbitrary layers.

What is left to do is the procedure, that as has been done in the previous Sec. C.1.2 namely solving the matrix equation and find the the conductivity tensor whose inverse leads to the resistivity tensor. Again this calculation is lengthy but not very complicated and its result can be found in Eq. (8.2).

C.1.4 The Effective Kinetic Equation in Presence of a Magnetic Field

The magnetic field mixes different directions requesting us to do a proper multi-direction treatment as exemplary introduced in Sec. C.1.1. In the Liouville operator defined in Eq. (8.10) we see the way the magnetic field comes into play. An important observation is to understand the action of ∂_ϕ more properly. Which is why we consider:

$$\langle (\vec{A}\vec{v})\partial_\phi(\vec{B}\vec{v}) \rangle_{\vec{v}} = ABv^2 \int_0^{2\pi} \frac{d\varphi}{2\pi} \cos(\varphi_A - \varphi) \sin(\varphi_B - \varphi) = \frac{v^2}{2} |\vec{A} \times \vec{B}|. \quad (\text{C.14})$$

This way we gain with the modified ansatz (8.11), the altered functional (8.12) and the short forms introduced in Eq. (7.13) the following modified functional:

$$\begin{aligned}
F_{\text{mod}}(\chi_v^{\alpha\mu}, \chi_p^{\alpha\mu}) = & \frac{T}{2} \sum_{\gamma \in \{a,b\}} N_\gamma \left[\frac{1}{2T\tau_{\text{dis}}^\gamma} \sum_{\mu \in \{x,y\}} \left(A_0^\gamma (\chi_v^{\gamma\mu})^2 + 2A_1^\gamma \chi_v^{\gamma\mu} \chi_p^{\gamma\mu} + A_2^\gamma (\chi_p^{\gamma\mu})^2 \right) + N_\gamma I_{\text{Intra}}^\gamma \frac{1}{2} \sum_{\mu \in \{x,y\}} (\chi_v^{\gamma\mu})^2 \right. \\
& \left. - \sum_{\mu \in \{x,y\}} \left(A_0^\gamma \chi_v^{\gamma\mu} + A_1^\gamma \chi_p^{\gamma\mu} \right) \frac{e}{T^2} \vec{E}^\gamma \vec{e}_\mu + 2 \left(\frac{\omega_c}{2T} \right)^2 \left(A_{-1}^\gamma \chi_v^{\gamma x} \chi_v^{\gamma y} + A_0^\gamma (\chi_v^{\gamma x} \chi_p^{\gamma y} + \chi_p^{\gamma x} \chi_v^{\gamma y}) + A_1^\gamma \chi_p^{\gamma x} \chi_p^{\gamma y} \right) \right] \\
+ \frac{T}{2} N_a N_b \sum_{\mu \in \{x,y\}} & \left[\frac{1}{2} I_{\text{Inter}}^{ab} (\chi_v^{a\mu})^2 + \frac{1}{2} I_{\text{Inter}}^{ba} (\chi_v^{b\mu})^2 - I_D \chi_v^{a\mu} \chi_v^{b\mu} + \left(I_{\text{Th}}^{ab} \chi_v^{a\mu} + I_{\text{Th}}^{ba} \chi_v^{b\mu} \right) (\chi_p^{a\mu} - \chi_p^{b\mu}) + \frac{1}{2} I_E (\chi_p^{a\mu} - \chi_p^{b\mu})^2 \right].
\end{aligned} \tag{C.15}$$

Already in this form we recognize that the second direction we took into account does not mix and behaves as in the case without magnetic field except for the magnetic field, which couples the two directions. With $b_{\gamma\mu} = e\vec{E}_\gamma \vec{e}_\mu / T^2$, $(2T)^2 y = 2\omega_c^2$ and as previously $T\tau_{\text{dis}}^\alpha z_\alpha = 1$ we define the following short forms for the effective kinetic equation:

$$\hat{N} = \begin{pmatrix} N_a I_{\text{Tr}}^a + z_a A_0^a & -N_b I_D & N_b I_{\text{Th}}^{ab} + z_a A_1^a & -N_b I_{\text{Th}}^{ab} \\ -N_a I_D & N_b I_{\text{Tr}}^b + z_b A_0^b & -N_a I_{\text{Th}}^{ba} & N_a I_{\text{Th}}^{ba} + z_b A_1^b \\ N_b I_{\text{Th}}^{ab} + z_a A_1^a & -N_b I_{\text{Th}}^{ba} & N_b I_E + z_a A_2^a & -N_b I_E \\ -N_a I_{\text{Th}}^{ba} & N_a I_{\text{Th}}^{ba} + z_b A_1^b & -N_a I_E & N_a I_E + z_b A_2^b \end{pmatrix}, \quad \hat{K} = \begin{pmatrix} A_{-1}^a & 0 & A_0^a & 0 \\ 0 & A_{-1}^b & 0 & A_0^b \\ A_0^a & 0 & A_1^a & 0 \\ 0 & A_0^b & 0 & A_1^b \end{pmatrix}, \tag{C.16}$$

which allows us to write:

$$\begin{pmatrix} A_0^a b_{ax} & 0 \\ 0 & A_0^b b_{bx} \\ A_1^a b_{ax} & 0 \\ 0 & A_1^b b_{bx} \\ A_0^a b_{ay} & 0 \\ 0 & A_0^b b_{by} \\ A_1^a b_{ay} & 0 \\ 0 & A_1^b b_{by} \end{pmatrix} = \begin{pmatrix} \hat{N} & y\hat{K} \\ y\hat{K} & \hat{N} \end{pmatrix} \begin{pmatrix} \chi_v^{axI} & \chi_v^{axII} \\ \chi_v^{bxI} & \chi_v^{bxII} \\ \chi_p^{axI} & \chi_p^{axII} \\ \chi_p^{bxI} & \chi_p^{bxII} \\ \chi_v^{ayI} & \chi_v^{ayII} \\ \chi_v^{byI} & \chi_v^{byII} \\ \chi_p^{ayI} & \chi_p^{ayII} \\ \chi_p^{byI} & \chi_p^{byII} \end{pmatrix} \tag{C.17}$$

Hereby the matrix \hat{N} has been introduced in Eq. (C.5) and we see that without the magnetic field $y \rightarrow 0$ the directions decouple and by choosing the ansatz to point in the direction of the electric field we further gain $b_{ay} = 0$ which was exactly the system of equation we treated in Sec. 7.1.3. To proceed with Eq. (C.17) we need to consider the thermalization which is explained in Sec. 8.2.2 and is performed in Eq. (8.13).

C.2 The Integrals Appearing within the Effective Kinetic Equation

In this section we want to investigate the integrals that appear within the derivation of the kinetic equation. Their structure not only unveils the forward scattering resonance but shows close connections to the diagrammatic analysis we have performed in Chap. 4.

The A_n^α are exactly solvable by using the polylogarithm Li. The thermal factors read then:

$$A_n^\alpha = A_n(\mu_\alpha = 2Tx) = -\frac{1}{2\pi}(n+1)! \left[\text{Li}_{n+1}(-e^{2x}) + (-1)^n \text{Li}_{n+1}(-e^{-2x}) \right]. \quad (\text{C.18})$$

The asymptotics of the polylogarithm will be discussed in the later Sec. C.3.

The integrals specified by I_{Intra}^α , I_{Inter}^α and I_{D} as defined in Eq. (7.13) need a more involved treatment to gain insights. One realizes that all these integrals can be described by two kinds of generalized integrals namely an integral related to the drag rate $I_{\text{GD}}(\mu_\alpha, \mu_\beta)$ and one related to transport rate $I_{\text{Gtr}}(\mu_\alpha, \mu_\beta)$.

$$I_{\text{GD}}(\mu_\alpha, \mu_\beta) = -\frac{1}{2T^3} \int d\{x_i\} W^{\alpha\beta}(\{x_i\}) (\vec{v}_1 - \vec{v}_2) (\vec{v}_3 - \vec{v}_4) \quad (\text{C.19})$$

$$I_{\text{Gtr}}(\mu_\alpha, \mu_\beta) = \frac{1}{2T^3} \int d\{x_i\} W^{\alpha\beta}(\{x_i\}) (\vec{v}_1 - \vec{v}_2)^2 \quad (\text{C.20})$$

Gaining the following connections to the integrals given in Eq. (7.13)

$$I_{\text{Intra}}^\alpha = I_{\text{Gtr}}(\mu_\alpha, \mu_\alpha) - I_{\text{GD}}(\mu_\alpha, \mu_\alpha) \quad I_{\text{Inter}}^\alpha = I_{\text{Gtr}}(\mu_\alpha, \mu_{-\alpha}) \quad I_{\text{D}} = I_{\text{GD}}(\mu_a, \mu_b) \quad (\text{C.21})$$

To handle these generalized rates in a more reasonable way and to draw the connection to a perturbative approach we will introduce the generalized vertex functions (**GVF**):

$$\tilde{\Gamma}_{i,j}^n(\omega, \vec{q}, \mu) = \int d\epsilon_i d\epsilon_j 2\pi \frac{\nu(\epsilon_i)\nu(\epsilon_j)\delta(\epsilon_i - \epsilon_j - \omega)}{4 \cosh\left(\frac{\epsilon_i - \mu}{2T}\right) \cosh\left(\frac{\epsilon_j - \mu}{2T}\right)} \int d\hat{v}_i d\hat{v}_j \theta_{\gamma_i, \gamma_j} (\vec{v}_i - \vec{v}_j)^n (2\pi)^2 \delta(\epsilon_i \vec{v}_i - \epsilon_j \vec{v}_j - \vec{q}) \quad (\text{C.22})$$

with $2\theta_{\gamma_i, \gamma_j} = 1 + \vec{v}_i \vec{v}_j$ being the Dirac factor as introduced in Eq. (A.20) (And discussed in Sec. 4.2.1). One recognizes the different symmetries that arise by varying n from even to odd. To compensate this symmetry change we project the odd case onto \vec{q} which is the only direction $\tilde{\Gamma}_{i,j}^n$ can point to.

$$\Gamma_{i,j}^n(\omega, \vec{q}, \mu) = \begin{cases} \tilde{\Gamma}_{i,j}^n(\omega, \vec{q}, \mu) & n = 0 \bmod 2 \\ \hat{q} \tilde{\Gamma}_{i,j}^n(\omega, \vec{q}, \mu) & n = 1 \bmod 2 \end{cases} \quad (\text{C.23})$$

The generalized rates read

$$I_{\text{GD}}(\mu_\alpha, \mu_\beta) = \frac{1}{2T^3} \int \frac{d^2q}{(2\pi)^2} \int \frac{d\omega}{2\pi} |D_{\alpha\beta}|^2 \Gamma_{1,2}^1(\omega, \vec{q}, \mu_\alpha) \Gamma_{3,4}^1(\omega, \vec{q}, \mu_\beta), \quad (\text{C.24})$$

$$I_{\text{Gtr}}(\mu_\alpha, \mu_\beta) = \frac{1}{2T^3} \int \frac{d^2q}{(2\pi)^2} \int \frac{d\omega}{2\pi} |D_{\alpha\beta}|^2 \Gamma_{1,2}^2(\omega, \vec{q}, \mu_\alpha) \Gamma_{3,4}^0(\omega, \vec{q}, \mu_\beta), \quad (\text{C.25})$$

with help of the generalized vertex functions. Note that the sign change of I_{GD} comes due to the fact that the $\tilde{\Gamma}_{i,j}^1$ for the two cases have to point in opposite directions.

C.2.1 Simplification of the Generalized Vertex Functions (GVF)

The generalized vertex functions can be simplified by decomposing the delta distribution that provides the momentum conservation. The GVFs that have an odd power of $(\vec{v}_i - \vec{v}_j)^n$ would be vectorial but

have been projected to \hat{q} since there is no other direction they can point to (see Eq. (C.23)). We continue considering only the angle dependent part:

$$\begin{aligned} & \int d\hat{v}_i d\hat{v}_j \theta_{\gamma_i, \gamma_j} (\vec{v}_i - \vec{v}_j)^n (2\pi)^2 \delta(\epsilon_i \vec{v}_i - \epsilon_j \vec{v}_j - \vec{q}) \\ &= \int d\hat{v}_i d\hat{v}_j \frac{1}{2} (1 + \vec{v}_i \vec{v}_j) \left[2(1 - \vec{v}_i \vec{v}_j) \right]^{\lfloor \frac{n}{2} \rfloor} \left[\hat{q} (\vec{v}_i - \vec{v}_j) \right]^{n \bmod 2} \times \\ & \quad \times \frac{(2\pi)^2}{q} \delta(|\epsilon_i \vec{v}_i - \epsilon_j \vec{v}_j| - |\vec{q}|) \delta\left(\frac{\epsilon_i \vec{v}_i - \epsilon_j \vec{v}_j}{|\epsilon_i \vec{v}_i - \epsilon_j \vec{v}_j|} - \hat{q}\right) \end{aligned} \quad (\text{C.26})$$

averaging over the directions of \vec{q} shows that only $\vec{v}_i \vec{v}_j = \cos(\phi)$ will be relevant for further calculation implying that the velocity integral reduces to:

$$\begin{aligned} & \int d\hat{v}_i d\hat{v}_j \frac{1}{2} (1 + \vec{v}_i \vec{v}_j) (\vec{v}_i - \vec{v}_j)^n (2\pi)^2 \delta(\epsilon_i \vec{v}_i - \epsilon_j \vec{v}_j - \vec{q}) \\ &= \frac{2}{q} \int_0^\pi d\phi \sin^2 \phi \left[2(1 - \cos \phi) \right]^{\lfloor \frac{n}{2} \rfloor - 1} \left(\frac{\epsilon_i + \epsilon_j}{2q} \right)^{n \bmod 2} \delta(|\epsilon_i \vec{v}_i - \epsilon_j \vec{v}_j| - |\vec{q}|) \\ &= \text{Re} \sqrt{(q^2 - (\epsilon_i - \epsilon_j)^2) ((\epsilon_i + \epsilon_j)^2 - q^2)} \frac{1}{\epsilon_i^2 \epsilon_j^2} \left(\frac{q^2 - (\epsilon_i - \epsilon_j)^2}{\epsilon_i \epsilon_j} \right)^{\lfloor \frac{n}{2} \rfloor - 1} \left(\frac{\epsilon_i + \epsilon_j}{2q} \right)^{n \bmod 2}. \end{aligned} \quad (\text{C.27})$$

The GVF can now be written by introducing the coordinate $E = \epsilon_i + \epsilon_j$, decomposing the cosine hyperbolic in the denominator and symmetrizing the E -integral allowing to write:

$$\begin{aligned} \Gamma^n(\omega, \vec{q}, \mu) &= \frac{1}{4\pi} \int_0^\infty dE \frac{\text{Re} \sqrt{(q^2 - \omega^2)(E^2 - q^2)}}{|E^2 - \omega^2| \sinh\left(\frac{\omega}{2T}\right)} \left(4 \frac{q^2 - \omega^2}{E^2 - \omega^2} \right)^{\lfloor \frac{n}{2} \rfloor - 1} \left(\frac{E}{2q} \right)^{n \bmod 2} \times \\ & \times \left[\tanh\left(\frac{E + \omega - 2\mu}{4T}\right) - \tanh\left(\frac{E - \omega - 2\mu}{4T}\right) + (-1)^{n \bmod 2} \left(\tanh\left(\frac{E + \omega + 2\mu}{4T}\right) - \tanh\left(\frac{E - \omega + 2\mu}{4T}\right) \right) \right], \end{aligned} \quad (\text{C.28})$$

which has the advantage that one can easily recognize the confinement $\omega \lesssim T$. This notation is a good starting point to gain deeper insights into the structure of the collision kernel.

C.2.2 Insights to the Collision Kernel

We will now look more closely at the analytic structure of the collision kernel to legitimate the ansatz we have chosen in sections 5.2.2 and 7.1.2. The language developed so far allows us to rewrite the collision kernel reading:

$$\int d\{x_i\} W^{\alpha, \beta}(\{x_i\}) = \int \frac{d^2 q}{(2\pi)^2} \int \frac{d\omega}{2\pi} |D_{\alpha\beta}|^2 \Gamma_{1,2}^0(-\omega, -\vec{q}, \mu_\alpha) \Gamma_{3,4}^0(\omega, \vec{q}, \mu_\beta). \quad (\text{C.29})$$

Taking a look at Eq. (C.28) one realizes that since every Γ^0 comes with $(q^2 - \omega^2)^{-1/2}$ the collision kernel will diverge if considered $D_{\alpha\beta}$ as bare Coulomb interaction as defined in Eq. (2.23). As explained

in Chap. 4 the divergence at $q^2 = \omega^2$ corresponds to forward scattering. We also showed that a RPA screened interaction will compensate this even at the Dirac point as long as the temperature stays finite. The bigness of the above divergence is then to be seen as enhancement ($\sim \alpha_g T$) compared to a usual golden rule calculation ($\sim \alpha_g^2 T$).

To convince one self that we need no other modes to take into account we will briefly look at more general GVF taking into account arbitrary modes of the form: $(\epsilon/T)^n \vec{v} \vec{E}$. Considering the same kind of decoupling we will get modified $\Gamma^{n,m}$ reading:

$$\Gamma_{i,j}^{n,m}(\omega, \vec{q}, \mu) = \frac{1}{T^m} \int d\epsilon_i d\epsilon_j 2\pi \frac{\nu(\epsilon_i)\nu(\epsilon_j)\delta(\epsilon_i - \epsilon_j + \omega)}{4 \cosh\left(\frac{\epsilon_i - \mu}{2T}\right) \cosh\left(\frac{\epsilon_j - \mu}{2T}\right)} \times \\ \times \int d\hat{v}_i d\hat{v}_j \theta_{\gamma_i, \gamma_j} \left(\epsilon_i^m \vec{v}_i - \epsilon_j^m \vec{v}_j\right)^n (2\pi)^2 \delta\left(\epsilon_i \vec{v}_i - \epsilon_j \vec{v}_j + \vec{q}\right). \quad (\text{C.30})$$

In an similar way as shown in appendix C.2.1 we integrate out the angle degree of freedom gaining $(q^2 - (\epsilon_i - \epsilon_j)^2)^{-1/2}$ and a term of the type:

$$\left(\epsilon_i^m \vec{v}_i - \epsilon_j^m \vec{v}_j\right)^n = \left(\epsilon_i^{2m} + \epsilon_j^{2m} - 2(\epsilon_i \epsilon_j)^m \vec{v}_i \vec{v}_j\right)^{n/2} = \left(\epsilon_i^{2m} + \epsilon_j^{2m} - (\epsilon_i \epsilon_j)^{m-1} (\epsilon_i^2 + \epsilon_j^2 - q^2)\right)^{n/2}. \quad (\text{C.31})$$

This term is not able to cancel $(q^2 - (\epsilon_i - \epsilon_j)^2)^{-1/2}$ which will cause the forward scattering divergence. Even if one considers large chemical potential ($\epsilon_i \approx \mu + \delta_i$) above equation changes to $\mu^{2m-2}(q^2 + (m^2 - 1)(\delta_i - \delta_j)^2)$ indicating that only the velocity modes are resistant to fast relaxation (except non-analytic modes see Secs. 5.2.4 and C.2.3). So again one has to take into account the RPA screened interaction to regularize the corresponding integral hence enhancing the resulting scattering weight.

Note changes in the interaction due to the second layer (see Eq. (6.10)) does not change this discussion since dynamic screening is responsible for these effects.

C.2.3 The Collision Kernels Involving the Imbalance Mode

In Sec. 5.2.4 we have seen that there is one additional mode, which avoided the discussion above by being non-analytic. In analogy to Eqs. (C.19) and (C.20) we can define rates involving the third mode χ_s . Which means that we need to consider as well some GVFs related to the third mode

$$\tilde{\Gamma}_{s;i,j}^n(\omega, \vec{q}, \mu) = \int d\epsilon_i d\epsilon_j 2\pi \frac{\nu(\epsilon_i)\nu(\epsilon_j)\delta(\epsilon_i - \epsilon_j - \omega)}{4 \cosh\left(\frac{\epsilon_i - \mu}{2T}\right) \cosh\left(\frac{\epsilon_j - \mu}{2T}\right)} \\ \int d\hat{v}_i d\hat{v}_j \theta_{\gamma_i, \gamma_j} \left(\text{sign}(\epsilon_i) \vec{v}_i - \text{sign}(\epsilon_j) \vec{v}_j\right)^n (2\pi)^2 \delta\left(\epsilon_i \vec{v}_i - \epsilon_j \vec{v}_j - \vec{q}\right) \quad (\text{C.32})$$

which can be similarly analyzed and simplified as the Γ s of the previous sections. Simplification leads to:

$$\Gamma_s^n(\omega, \vec{q}, \mu) = \frac{1}{4\pi} \int_{|\omega|}^{\infty} dE \frac{\text{Re} \sqrt{(q^2 - \omega^2)(E^2 - q^2)}}{|E^2 - \omega^2| \sinh\left(\frac{\omega}{2T}\right)} \left(4 \frac{q^2 - \omega^2}{E^2 - \omega^2}\right)^{\lceil \frac{n}{2} \rceil - 1} \left(\frac{E}{2q}\right)^{n \bmod 2} F_n(\omega, \mu, E) \\ - \frac{1}{16\pi} \int_0^{|\omega|} dE \frac{F_0(\omega, \mu, E)}{\sinh\left(\frac{\omega}{2T}\right)} \text{Re} \sqrt{\frac{E^2 - q^2}{q^2 - \omega^2}} \left(4 \frac{E^2 - q^2}{E^2 - \omega^2}\right)^{\lceil \frac{n}{2} \rceil} \left(\frac{\omega}{2q}\right)^{n \bmod 2} \quad (\text{C.33})$$

with

$$F_n(\omega, \mu, E) = \left[\tanh\left(\frac{E + \omega - 2\mu}{4T}\right) - \tanh\left(\frac{E - \omega - 2\mu}{4T}\right) + (-1)^{n \bmod 2} \left(\tanh\left(\frac{E + \omega + 2\mu}{4T}\right) - \tanh\left(\frac{E - \omega + 2\mu}{4T}\right) \right) \right] \quad (\text{C.34})$$

Although it looks like Γ_s^n could be divergent it turns out that this part cancels when putting everything together. But within this representation the appearance of being divergent is somewhat natural since the decomposition has performed in such a way that that the cancellation is not yet apparent. Still this form is useful to understand that if one would perform the calculation for two or more layers there would appear a thermalization of the third mode between the layers.

To see the cancellation more clearly we put together the ingredients needed for I_s (see Sec. 5.2.4) and obtain for the critical part only:

$$I_{s,\text{crit}} = \frac{1}{4T^3} \int \frac{dq}{(2\pi)^2} \int \frac{d\omega}{2\pi} D_0^2 \frac{1}{(16\pi)^2} \int_0^{|\omega|} dE \int_0^{|\omega|} dE' \frac{F_0(\omega, \mu, E) F_0(\omega, \mu, E')}{\sinh^2\left(\frac{\omega}{2T}\right)} \frac{\text{Re} \sqrt{(E^2 - q^2)(E'^2 - q^2)}}{q^2 - \omega^2} \left(4 \frac{q^2 - \omega^2}{q^2} \frac{E^2(E'^2 - q^2) + E'^2(E^2 - q^2)}{(E^2 - \omega^2)(E'^2 - \omega^2)} \right) \quad (\text{C.35})$$

where one clearly sees the cancellation of $q^2 - \omega^2$ verifying the third mode to be not quickly relaxed by forward scattering.

The peculiar A_{sn} s that appear within the third mode calculation can be explicitly evaluated and yield:

$$A_{sn}(x) = \frac{1}{2\pi} \begin{cases} 2x & n = 0 \\ \frac{\pi^2}{3} + (2x)^2 & n = 1 \\ \pi^2(2x) + (2x)^3 & n = 2 \end{cases} \quad (\text{C.36})$$

C.3 The Asymptotics

The final purpose of this section is to provide all ingredients needed to discuss the asymptotics of the drag resistivity. We will, therefore start with objects that appear most often namely the coefficients A_n . Their asymptotics is given by:

$$A_n(x \ll 1) = \frac{1}{\pi} \begin{cases} \ln(2) & n = 0 \\ 4x \ln(2) & n = 1 \\ \frac{9}{2} \zeta(3) & n = 2 \end{cases} \quad A_n(|x| \gg 1) = \frac{\text{sign}(x)}{2\pi} \begin{cases} 2x + 2e^{-2x} & n = 0 \\ (2x)^2 + \frac{\pi^2}{3} - 4e^{-2x} & n = 1 \\ (2x)^3 + 2x\pi^2 + 12e^{-2x} & n = 2 \end{cases} , \quad (\text{C.37})$$

and the coefficient appearing in magnetic field reads $A_{-1}(x) = \tanh(x)/(2\pi)$. Immediately we gain the asymptotics of the B_n by:

$$B_n(x \ll 1) = \begin{cases} \ln(2)/\pi & n = 0 \\ 4Nx & n = 1 \\ \frac{9N}{2\pi} \zeta(3) & n = 2 \end{cases} \quad B_n(x \gg 1) = \begin{cases} |x|/\pi & n = 0 \\ 2Nx + \frac{N\pi^2}{6x} & n = 1 \\ \pi N|x|/3 & n = 2 \end{cases} . \quad (\text{C.38})$$

And hence the objects needed for Hall drag (see Eq. (8.21)):

$$C^\alpha(x \ll 1) \approx \frac{\ln 2}{\pi} \qquad C^\alpha(x \gg 1) \approx -\frac{\pi^2}{12x} \quad (\text{C.39})$$

The next step will be to simplify the GVFs to obtain the asymptotics of the rates.

C.3.1 The Limit of Small Chemical Potential

When we are in the situation that $\mu\alpha \ll T$ for both layers this means that screening is done by temperature only. Since we consider to have the same temperature in our layers this means basically that $\Pi_a \approx \Pi_b$. The RPA screened interaction as it is given in Eq. (6.10) simplifies then and for the purpose of gaining only parametrics can be thought of being the one layer interaction with an additional degeneracy. This is surely only appropriate if $q < d^{-1}$ hence not allowing to gain any numerical prefactors.

This strong assumption allows us to use a powerful mapping to the rates we have obtained in Secs. 4 and B.2.3. As one has seen in appendix C.2.2 the bare interaction kernel is given as $\Gamma^0 \Gamma^0$ combination. For the single layer case we provided in App. B.2.3 closed expressions for the corresponding rates. The bare kernel in this sense corresponds to the rate $\tau_\pm(\epsilon)$ of Sec. 4.

Our aim is therefore to express the integral kernels of the GVFs in terms of the one of Γ^0 . It turns out that only $\omega < q$ (region 3) is relevant. By comparison we identify:

$$\Gamma^n \approx \frac{\omega}{\sinh(\frac{\omega}{2T})} \operatorname{Re} \frac{1}{\sqrt{q^2 - \omega^2}} \int_q^\infty dE \frac{\sqrt{E^2 - q^2}}{\cosh^2(\frac{E}{4T})} \times \underbrace{\frac{1}{2} \left(1 + (-1)^n + \frac{\mu}{T} \frac{E}{4T} (1 - (-1)^n) \right) \left(4 \frac{q^2 - \omega^2}{E^2 - \omega^2} \right)^{\lceil \frac{n}{2} \rceil} \left(\frac{E}{2q} \right)^{n \bmod 2}}_{K_n}. \quad (\text{C.40})$$

The kernels we will actually need are $K_{\text{tr}} = K_0 K_2$, $K_{\text{D}} = K_1 K_1$, $K_{\text{Th}} = K_0 K_1 q$ and $K_{\text{E}} = K_0 K_0 q^2$. In our Sec. 4.2.1 (especially appendix B.2) we described everything using momentum q and angle γ between \vec{q} and \vec{p}_1 . In the case of $\omega < q$ we read then:

$$\begin{aligned} K_{\text{tr}} &= \frac{q^2}{\epsilon^2} \sin^2(\gamma) & K_{\text{D}} &= \frac{\mu_a \mu_b}{T^2} \frac{q^2}{T^2} \sin^4(\gamma) \\ K_{\text{Th}\alpha} &= \frac{\mu_\alpha}{T} \frac{q^2}{T^2} \sin^2(\gamma) & K_{\text{E}} &= q^2 \end{aligned} \quad (\text{C.41})$$

with the equations given in appendix B.2 we can estimate the behavior of the rates.

Small Distance

The first thing we learn already from the mapping is that. For $dT \ll 1$ there will be no change to the system parametrically speaking. This is due to the fact that especially after energy averaging above rates will be determined by $q \sim T$. The dependence of the chemical potential can be seen already by expanding the definition of the GVFs. One reads:

$$\Gamma_{\mu \ll T}^0(\omega, \vec{q}, \mu) \approx \frac{1}{4\pi} \int_0^\infty dE \frac{\sqrt{(q^2 - \omega^2)(E^2 - q^2)}}{|E^2 - \omega^2| \sinh(\frac{\omega}{2T})} \left(4 \frac{q^2 - \omega^2}{E^2 - \omega^2} \right)^{-1} \left[\tanh\left(\frac{E + \omega}{4T}\right) - \tanh\left(\frac{E - \omega}{4T}\right) \right], \quad (\text{C.42})$$

$$\Gamma_{\mu \ll T}^1(\omega, \vec{q}, \mu) \approx \frac{\mu}{4\pi T} \int_0^\infty dE \frac{\sqrt{(q^2 - \omega^2)(E^2 - q^2)}}{|E^2 - \omega^2| \sinh\left(\frac{\omega}{2T}\right)} \left(\frac{E}{2q}\right) \left[\frac{1}{\cosh^2\left(\frac{E-\omega}{4T}\right)} - \frac{1}{\cosh^2\left(\frac{E+\omega}{4T}\right)} \right], \quad (\text{C.43})$$

$$\Gamma_{\mu \ll T}^2(\omega, \vec{q}, \mu) \approx \frac{1}{4\pi} \int_0^\infty dE \frac{\sqrt{(q^2 - \omega^2)(E^2 - q^2)}}{|E^2 - \omega^2| \sinh\left(\frac{\omega}{2T}\right)} 2 \left[\tanh\left(\frac{E+\omega}{4T}\right) - \tanh\left(\frac{E-\omega}{4T}\right) \right]. \quad (\text{C.44})$$

The rates can be obtained numerically with coefficients $C_D(dT)$ and $C_{\text{tr}}(dT)$ that are slowly varying:

$$\begin{aligned} I_{\text{GD}}(\mu_\alpha \ll T, \mu_\beta \ll T) &= \frac{1}{2T^3} \int \frac{d^2q}{(2\pi)^2} \int \frac{d\omega}{2\pi} \left(D_{\alpha\beta}^{\text{bare}}\right)^2 \Gamma_{\mu \ll T}^1(-\omega, -\vec{q}, \mu_\alpha) \Gamma_{\mu \ll T}^1(\omega, \vec{q}, \mu_\beta) \\ &\approx \alpha_g^2 C_D(dT) \frac{\mu_\alpha \mu_\beta}{(2T)^2} \end{aligned} \quad (\text{C.45})$$

$$\begin{aligned} I_{\text{Gtr}}(\mu_\alpha \ll T, \mu_\beta \ll T) &= \frac{1}{2T^3} \int \frac{d^2q}{(2\pi)^2} \int \frac{d\omega}{2\pi} \left(D_{\alpha\beta}^{\text{bare}}\right)^2 \Gamma_{\mu \ll T}^2(-\omega, -\vec{q}, \mu_\alpha) \Gamma_{\mu \ll T}^0(\omega, \vec{q}, \mu_\beta) \\ &\approx \alpha_g^2 C_{\text{Tr}}(dT) \end{aligned} \quad (\text{C.46})$$

For zero distance those coefficients are given by $C_D(dT = 0) \approx 0.1374$ and $C_{\text{Tr}}(dT = 0) \approx 0.2193$. In Sec. 5.4 it is shown that energy relaxation is logarithmically larger than transport related quantities like $I_{\text{Th}\alpha}$. Therefore energy relaxation is fast enough to treat only the kinetic equation with three modes. We have now everything one needs to get the drag resistivity for small chemical potential:

$$\rho_D(\hat{\mu}_a, \hat{\mu}_b) \approx \frac{1}{e^2} \frac{\alpha_g^2 2\pi^2}{\ln^2 2} C_D(dT) \hat{\mu}_a \hat{\mu}_b \left[1 + \frac{32\pi}{9\zeta(3)} \frac{\alpha_g^2 C_{\text{Tr}}^2(dT)}{C_D(dT)} \frac{N_a + N_b}{(T\tau_0)^{-1} + (T\tau_{\text{ad}})^{-1}} \right]. \quad (\text{C.47})$$

Where the effective drag rate is given by:

$$(T\tau_0)^{-1} = \frac{32\pi}{9\zeta(3)} \alpha_g^2 C_{\text{Tr}} \left(N_a \hat{\mu}_a^2 + N_b \hat{\mu}_b^2 \right) \quad (\text{C.48})$$

If now τ_{ad}^{-1} is of order of $\alpha_g^2 T$ we can define $\tilde{\tau}_{\text{ad}}^{-1} = \tau_{\text{ad}}^{-1} \frac{9\zeta(3)}{32\pi} \frac{1}{\alpha_g^2 C_{\text{Tr}}}$ which leads to a simplification if $N_a \hat{\mu}_a^2 + N_b \hat{\mu}_b^2 + \frac{1}{T\tilde{\tau}_{\text{ad}}} \ll (N_a + N_b)^2 C_{\text{Tr}}(dT)/C_D(dT)$ holds. We obtain:

$$\rho_D(\hat{\mu}_a, \hat{\mu}_b) \approx \frac{1}{e^2} \alpha_g^2 \frac{(2\pi)^2}{2 \ln^2 2} C_{\text{Tr}}(dT) \frac{\hat{\mu}_a \hat{\mu}_b (N_a + N_b)}{N_a \hat{\mu}_a^2 + N_b \hat{\mu}_b^2 + \frac{1}{T\tilde{\tau}_{\text{ad}}}}. \quad (\text{C.49})$$

The prefactor is approximately $(2\pi/\ln 2)^2 C_{\text{Tr}}(dT)/2 \approx 9.01$.

Large Distance

In the case that the distance is large $dT \gg 1$ it turns out that we actually need to use the kernels given in Eq. (C.41). By usage of the appendix of our previous article we recognize a additional scale

and get the following behavior for the inter layer rates:

$$I_j \propto \begin{cases} \frac{\alpha_g^2 NT}{dT} \begin{cases} \ln\left(\frac{1}{\alpha_g NdT}\right) & j = E \\ \hat{\mu}_\alpha & j = \text{Th}_\alpha \\ \hat{\mu}_a \hat{\mu}_b & j = D \end{cases} & \alpha_g NdT \ll 1 \\ \frac{T}{N(dT)^3} \begin{cases} 1 & j = E \\ \hat{\mu}_\alpha & j = \text{Th}_\alpha \\ \hat{\mu}_a \hat{\mu}_b & j = D \end{cases} & \alpha_g NdT \gg 1 \end{cases}. \quad (\text{C.50})$$

The intra layer rates are of course not changed. The interesting fact one can see here is that energy relaxation is always faster than thermalization. So in both situations we are allowed to use the kinetic equation for three modes only. Since the inter layer rates are suppressed by distance compared to the intra layer rates we need only to adapt the inter layer rates compared to the zero distance calculation.

For $\alpha_g NdT \ll 1$ we gain the following parametrically behavior for the drag resistivity:

$$\rho_D \propto \frac{\alpha_g^2 \hat{\mu}_a \hat{\mu}_b}{e^2 (dT)} \left[1 + C_1 \frac{\alpha_g^2 N(dT)}{(T\tau_0)^{-1} + (T\tau_{\text{dis}})^{-1}} \right], \quad (\text{C.51})$$

with an unknown constant C_1 . For this regime we have $(T\tau_0)^{-1} \propto \alpha_g^2 N(\hat{\mu}_a^2 + \hat{\mu}_b^2)$. As in the previous case of small distances we see that if $(T\tau_0)^{-1} + z \ll \alpha_g^2 N(dT)$ is fulfilled we will enter a regime that is up to numbers identical to the one discussed in Eq. (C.49).

For $\alpha_g NdT \gg 1$ we follow the very same logic ending up with:

$$\rho_D \propto \frac{\hat{\mu}_a \hat{\mu}_b}{e^2 N^2 (dT)^3} \left[1 + C_2 \frac{\alpha_g (\alpha_g NdT)^3}{(T\tau_0)^{-1} + (T\tau_{\text{dis}})^{-1}} \right], \quad (\text{C.52})$$

and again we do not know C_2 . In this regime $(T\tau_0)^{-1}$ behaves in the very same way as in the previous one leading again to the unusual behavior as given in Eq. (C.49).

C.3.2 The Limit of Large Chemical Potential

We consider now the situation of large chemical potentials namely $\mu \gg T$. In this limit we will choose a different path to gain the rates. Since kinematically suppressed the most important regime is $\omega < q \ll \mu$. In this regime we can actually gain information from the GVs directly by the treatment showed below:

$$\Gamma_{\mu \gg T}^0(\omega, \vec{q}, \mu) \approx \frac{-1}{16\pi\sqrt{q^2 - \omega^2} \sinh\left(\frac{\omega}{2T}\right)} \int_q^\infty dE \left(E\sqrt{E^2 - q^2} - q^2 \ln(E + \sqrt{E^2 - q^2}) \right) \times \\ \times \frac{1}{8T} \left[\frac{1}{\cosh^2\left(\frac{E+\omega-2|\mu|}{4T}\right)} - \frac{1}{\cosh^2\left(\frac{E-\omega-2|\mu|}{4T}\right)} \right] \approx \frac{|\mu|\omega}{2\pi\sqrt{q^2 - \omega^2} \sinh\left(\frac{\omega}{2T}\right)} \left(1 - \frac{q^2}{8\mu^2} \right), \quad (\text{C.53})$$

$$\begin{aligned}
\Gamma_{\mu \gg T}^1(\omega, \vec{q}, \mu) &\approx \frac{\sqrt{q^2 - \omega^2}}{4\pi q \sinh\left(\frac{\omega}{2T}\right)} \int_q^\infty dE \left(\sqrt{E^2 - q^2} - \sqrt{q^2 - \omega^2} \arctan\left(\frac{\sqrt{E^2 - q^2}}{\sqrt{q^2 - \omega^2}}\right) \right) \times \\
&\times \frac{\text{sign}(\mu)}{8T} \left[\frac{1}{\cosh^2\left(\frac{E+\omega-2|\mu|}{4T}\right)} - \frac{1}{\cosh^2\left(\frac{E-\omega-2|\mu|}{4T}\right)} \right] \approx -\frac{\text{sign}(\mu)\omega\sqrt{q^2 - \omega^2}}{2\pi q \sinh\left(\frac{\omega}{2T}\right)} \left(1 - \frac{q^2}{8\mu^2} + \frac{\omega^2}{4\mu^2} \right),
\end{aligned} \tag{C.54}$$

$$\begin{aligned}
\Gamma_{\mu \gg T}^2(\omega, \vec{q}, \mu) &\approx \frac{-\sqrt{q^2 - \omega^2}}{2\pi \sinh\left(\frac{\omega}{2T}\right)} \int_q^\infty dE \left(\ln(E + \sqrt{E^2 - q^2}) + \frac{\sqrt{q^2 - \omega^2}}{\omega} \text{arctanh}\left(\frac{E \sqrt{q^2 - \omega^2}}{\omega \sqrt{E^2 - q^2}}\right) \right) \times \\
&\times \frac{1}{8T} \left[\frac{1}{\cosh^2\left(\frac{E+\omega-2|\mu|}{4T}\right)} - \frac{1}{\cosh^2\left(\frac{E-\omega-2|\mu|}{4T}\right)} \right] \approx \frac{\omega\sqrt{q^2 - \omega^2}}{2\pi|\mu| \sinh\left(\frac{\omega}{2T}\right)} \left(1 - \frac{q^2}{8\mu^2} + \frac{\omega^2}{3\mu^2} + \frac{\pi^2(2T)^2}{12\mu^2} \right).
\end{aligned} \tag{C.55}$$

We used in these relation that for small T we can use $(8T)^{-1} \text{sech}(x/(4T)) \approx \delta(x) + \pi^2(4!)^{-1}(4T)^2 \delta''(x)$ where the last term of this relation is relevant for $\Gamma_{\mu \gg T}^2$.

With these powerful approximations we will continue getting the rates. Note that the definition of transport rate and thermalization rate are very close in this limit since $\Gamma^0 \Gamma^2$ differs from $\Gamma^0 q \Gamma^1$ by a factor of μ .

Intermediate Chemical Potential for Small and Large Distances

The chemical potential will now be assumed to obey the condition $\alpha_g N \mu \ll 1/(2d)$ additionally to $T \ll \mu$. We will consider two cases: the first one $dT \ll 1$ in which we will consider the frequency cut-off to be $\Lambda_\omega = \infty$ since it is restricted by temperature and the second one $dT \gg 1$ where the cut-off

is chosen to be $\Lambda_\omega = q$. We get the following generalized rates for the regime $T \ll |\mu_\alpha| \ll \frac{1}{\alpha_g d}$:

$$I_{\text{GD}}^{\alpha\beta} \approx \frac{1}{2T^3} \int_{\lambda_{\alpha\beta}}^{\min(|\mu_\alpha|, |\mu_\beta|)} \frac{dq}{2\pi} \int_{-\Lambda_\omega}^{\Lambda_\omega} \frac{d\omega}{2\pi} \frac{(2\pi)^2 \alpha_g^2}{q^2} e^{-2qd\delta_{\alpha,-\beta}} \frac{\text{sign}(\mu_\alpha \mu_\beta) \omega^2}{4\pi^2 q^2} \frac{q^2 - \omega^2}{\sinh^2\left(\frac{\omega}{2T}\right)} \left[1 + \left(\frac{\omega^2}{4} - \frac{q^2}{8} \right) \left(\frac{1}{\mu_\alpha^2} + \frac{1}{\mu_\beta^2} \right) \right]$$

$$\approx \frac{\alpha_g^2}{3} \text{sign}(\mu_\alpha \mu_\beta) \begin{cases} \ln\left(\frac{\Lambda_{\alpha\beta}}{\lambda_{\alpha\beta}}\right) + \left(\frac{(2T)^2}{\mu_\alpha^2} + \frac{(2T)^2}{\mu_\beta^2} \right) \left[\frac{\pi^2}{20} \ln\left(\frac{\Lambda_{\alpha\beta}}{\lambda_{\alpha\beta}}\right) - \frac{1}{16} \frac{\Lambda_{\alpha\beta}^2}{(2T)^2} \right] & dT \ll 1 \\ \frac{6}{\pi^2} \frac{\Lambda_{\alpha\beta}}{2T} + \frac{1}{\pi^2} \left(\frac{(2T)^2}{\mu_\alpha^2} + \frac{(2T)^2}{\mu_\beta^2} \right) \left[\frac{1}{6} \frac{\Lambda_{\alpha\beta}^3}{(2T)^3} - \frac{1}{4} \frac{\Lambda_{\alpha\beta}^3}{(2T)^3} \right] & dT \gg 1 \end{cases}, \quad (\text{C.56})$$

$$I_{\text{Gtr}}^{\alpha\beta} \approx \frac{1}{2T^3} \int_{\lambda_{\alpha\beta}}^{\min(\mu_\alpha, \mu_\beta)} \frac{dq}{2\pi} \int_{-\Lambda_\omega}^{\Lambda_\omega} \frac{d\omega}{2\pi} \frac{(2\pi)^2 \alpha_g^2}{q^2} \frac{\omega^2 e^{-2qd\delta_{\alpha,-\beta}}}{4\pi^2 \sinh^2\left(\frac{\omega}{2T}\right)} \frac{|\mu_\beta|}{|\mu_\alpha|} \left[1 - \frac{q^2}{8} \left(\frac{1}{\mu_\alpha^2} + \frac{1}{\mu_\beta^2} \right) + \frac{(2\omega)^2 + (2\pi T)^2}{12\mu_\alpha^2} \right]$$

$$\approx \frac{\alpha_g^2}{3} \frac{|\mu_\beta|}{|\mu_\alpha|} \begin{cases} \ln\left(\frac{\Lambda_{\alpha\beta}}{\lambda_{\alpha\beta}}\right) + \frac{3\pi^2 (2T)^2}{20\mu_\alpha^2} \ln\left(\frac{\Lambda_{\alpha\beta}}{\lambda_{\alpha\beta}}\right) - \frac{1}{16} \left(\frac{(2T)^2}{\mu_\alpha^2} + \frac{(2T)^2}{\mu_\beta^2} \right) \frac{\Lambda_{\alpha\beta}^2}{T^2} & dT \ll 1 \\ \frac{6}{\pi^2} \frac{\Lambda_{\alpha\beta}}{2T} + \frac{1}{2\mu_\alpha^2} (2T)^2 \frac{\Lambda_{\alpha\beta}}{2T} + \frac{2(2T)^2}{9\pi^2 \mu_\alpha^2} \frac{\Lambda_{\alpha\beta}^3}{(2T)^3} - \frac{1}{4\pi^2} \left(\frac{(2T)^2}{\mu_\alpha^2} + \frac{(2T)^2}{\mu_\beta^2} \right) \frac{\Lambda_{\alpha\beta}^3}{(2T)^3} & dT \gg 1 \end{cases} \quad (\text{C.57})$$

where for brevity we used $\Lambda_{\alpha\beta} = \min(|\mu_\alpha|, |\mu_\beta|, 1/(2d\delta_{\alpha,-\beta}))$ and $\lambda_{\alpha\beta} = \max(\alpha_g N_\alpha |\mu_\alpha|, \alpha_g N_\beta |\mu_\beta|, T)$. One recognizes the similarity of the expressions which is why we will look carefully at the following combination that is strongly related to the generalized rate defined in Eq. (7.21):

$$I_{\text{GI}}^{\alpha\beta} = \frac{|\mu_\alpha|}{|\mu_\beta|} I_{\text{Gtr}}^{\alpha\beta} - \frac{I_{\text{GD}}^{\alpha\beta}}{\text{sign}(\mu_\alpha \mu_\beta)} = \frac{\alpha_g^2}{3} \begin{cases} \frac{\pi^2}{20} (2T)^2 \frac{2\mu_\beta^2 - \mu_\alpha^2}{\mu_\alpha^2 \mu_\beta^2} \ln\left(\frac{\Lambda_{\alpha\beta}}{\lambda_{\alpha\beta}}\right) & dT \ll 1 \\ \frac{1}{2} \frac{(2T)^2}{\mu_\alpha^2} \frac{\Lambda_{\alpha\beta}}{2T} + \frac{1}{18\pi^2} (2T)^2 \frac{\mu_\beta^2 - 3\mu_\alpha^2}{\mu_\alpha^2 \mu_\beta^2} \frac{\Lambda_{\alpha\beta}^3}{(2T)^3} & dT \gg 1 \end{cases} \quad (\text{C.58})$$

Where $I_{\text{GI}}^{\alpha\beta}$ is a generalized scattering rate we introduce due to its useful properties, like $I_{\text{GI}}^{\alpha\alpha} = I_{\text{Intra}}^\alpha$ and:

$$I_{\text{G}}^\alpha = B_1^\alpha I_{\text{Tr}}^\alpha - B_1^{-\alpha} I_{\text{D}} \approx \frac{2}{\hat{\mu}_\alpha} \left(\hat{\mu}_\alpha^2 N_\alpha I_{\text{GI}}^{\alpha\alpha} + |\hat{\mu}_{-\alpha} \hat{\mu}_\alpha| N_{-\alpha} I_{\text{GI}}^{\alpha,-\alpha} \right). \quad (\text{C.59})$$

One should remember that the intra layer quantities will be never affected by the large distance case $dT \gg 1$ which means that in the large distance case the cut off is always given by: $\Lambda_{ab} 2d = 1$.

To proceed we need to check the energy relaxation to be still enhanced. The energy relaxation reads:

$$I_{\text{E}} \propto \frac{N \mu_a \mu_b}{T^5} \int_0^{\min(|\mu_\alpha|, |\mu_\beta|)} dq q^3 \int_{-\Lambda_\omega}^{\Lambda_\omega} \frac{\omega^2}{\sinh^2\left(\frac{\omega}{2T}\right)} \frac{|D_{ab}^{\text{RPA}}|^2}{q^2 - \omega^2}. \quad (\text{C.60})$$

For the case of large chemical potential the polarization operator and therefore the screened interaction reads:

$$\Pi_{\mu \gg T}(\omega, q) = \frac{|\mu|}{2\pi} \left(1 + \frac{i\omega}{\sqrt{q^2 - \omega^2}} \right) \frac{|D_{ab}^{\text{RPA}}|^2}{q^2 - \omega^2} \approx \frac{(2\pi)^2 \alpha_g^2 e^{-2qd}}{q[q(q + \alpha_g(|\mu_a| + |\mu_b|))^2 - \omega^2(q + 2\alpha_g(|\mu_a| + |\mu_b|))]} \quad (\text{C.61})$$

Finally we obtain the energy relaxation rate to be enhanced by an factor (μ/T) compared to thermalization rate:

$$I_E \propto \frac{\alpha_g^2 N \mu_a \mu_b}{T^2} \begin{cases} \ln \left(\frac{\Lambda_{\alpha\beta}}{\max(T, \alpha_g(|\mu_a| + |\mu_b|))} \right) & dT \ll 1 \\ \frac{\Lambda_{\alpha\beta}}{T} & dT \gg 1 \end{cases}, \quad (\text{C.62})$$

justifying the usage of the thermalized kinetic equation involving three modes only. The resistivity forms therefore for $dT \ll 1$:

$$\rho_D(\hat{\mu}_a, \hat{\mu}_b) \approx \frac{\alpha_g^2 2\pi^2 \ln \left(\frac{\Lambda_{ab}}{\lambda_{ab}} \right)}{e^2 3 \hat{\mu}_a \hat{\mu}_b} \times \left[1 + \frac{\alpha_g^2 \pi^3 \left(N_a \ln \left(\frac{\Lambda_{aa}}{\lambda_{aa}} \right) + N_b \ln \left(\frac{\Lambda_{ab}}{\lambda_{ab}} \right) \frac{2\hat{\mu}_b^2 - \hat{\mu}_a^2}{|\hat{\mu}_a \hat{\mu}_b|} \right) \left(N_b \ln \left(\frac{\Lambda_{bb}}{\lambda_{bb}} \right) + N_a \ln \left(\frac{\Lambda_{ab}}{\lambda_{ab}} \right) \frac{2\hat{\mu}_a^2 - \hat{\mu}_b^2}{|\hat{\mu}_b \hat{\mu}_a|} \right)}{100 |\hat{\mu}_b \hat{\mu}_a| (N_a |\hat{\mu}_a| + N_b |\hat{\mu}_b|) \ln \left(\frac{\Lambda_{ab}}{\lambda_{ab}} \right) ((T\tau_0)^{-1} + (T\tau_{\text{dis}})^{-1})} \right], \quad (\text{C.63})$$

with the characteristic rate given by:

$$(T\tau_0)^{-1} = \frac{\pi}{5} \frac{\alpha_g^2}{N_a |\hat{\mu}_a| + N_b |\hat{\mu}_b|} \left[N_a^2 \ln \left(\frac{\Lambda_{aa}}{\lambda_{aa}} \right) + N_b^2 \ln \left(\frac{\Lambda_{bb}}{\lambda_{bb}} \right) + N_a N_b \frac{\hat{\mu}_a^2 + \hat{\mu}_b^2}{|\hat{\mu}_a \hat{\mu}_b|} \ln \left(\frac{\Lambda_{ab}}{\lambda_{ab}} \right) \right]. \quad (\text{C.64})$$

For large distances we gain:

$$\rho_D(\hat{\mu}_a, \hat{\mu}_b) \approx \frac{\alpha_g^2}{e^2} \frac{4\Lambda_{ab}}{(2T)\hat{\mu}_a \hat{\mu}_b} \left[1 + \frac{\alpha_g^2 \left(N_a \frac{\pi^2}{10} \ln \left(\frac{\Lambda_{aa}}{\lambda_{aa}} \right) + N_b \frac{|\hat{\mu}_b|}{|\hat{\mu}_a|} \frac{\Lambda_{ab}}{2T} \right) \left(N_a \frac{\pi^2}{10} \ln \left(\frac{\Lambda_{bb}}{\lambda_{bb}} \right) + N_b \frac{|\hat{\mu}_a|}{|\hat{\mu}_b|} \frac{\Lambda_{ab}}{2T} \right)}{\pi |\hat{\mu}_a \hat{\mu}_b| (N_a |\hat{\mu}_a| + N_b |\hat{\mu}_b|) \frac{\Lambda_{ab}}{2T} ((T\tau_0)^{-1} + (T\tau_{\text{dis}})^{-1})} \right], \quad (\text{C.65})$$

with the altered characteristic rate:

$$(T\tau_0)^{-1} = \frac{2}{\pi} \frac{\alpha_g^2}{N_a |\hat{\mu}_a| + N_b |\hat{\mu}_b|} \left[N_a^2 \frac{\pi^2}{10} \ln \left(\frac{\Lambda_{aa}}{\lambda_{aa}} \right) + N_b^2 \frac{\pi^2}{10} \ln \left(\frac{\Lambda_{bb}}{\lambda_{bb}} \right) + N_a N_b \frac{\hat{\mu}_a^2 + \hat{\mu}_b^2}{|\hat{\mu}_a \hat{\mu}_b|} \frac{\Lambda_{ab}}{2T} \right]. \quad (\text{C.66})$$

Where one should remember that $\Lambda_{ab} 2d = 1$.

Large Chemical Potential for Small and Large Distances

This time we assume the chemical potential to be that large ($1/(2d) \ll \alpha_g N \mu$) that static screening comes into play. For this limit we are using

$$\Pi(\omega = 0, q \ll \frac{1}{2d}) \approx \frac{\mu}{2\pi} \quad (\text{C.67})$$

which gains

$$D_{\alpha\beta} = \frac{2\pi\alpha_g}{q} \delta_{\alpha\beta} + \frac{4\pi q}{\alpha_g N_a N_b \mu_a \mu_b \sinh(qd)} \delta_{\alpha-\beta} \quad (\text{C.68})$$

as screened interaction to proceed with. Since the only change that appears in this regime is within the intra layer rates we focus on them. Again we consider the two cases of distance namely $dT \ll 1$

and $dT \gg 1$. The generalized rates for the regime $\frac{1}{\alpha_g d} \ll \mu_\alpha$ taken within the same notation as for Eq. (C.56) forms:

$$I_{\text{GD}}^{\alpha\beta} = \frac{1}{2T^2} \int_{\lambda_{\alpha\beta}}^{\min(|\mu_\alpha|, |\mu_\beta|)} \frac{dq}{2\pi} q \int_{-\Lambda_\omega}^{\Lambda_\omega} \frac{d\omega}{2\pi} |D_{\alpha\beta}|^2 \frac{\text{sign}(\mu_\alpha \mu_\beta) \omega^2}{4\pi^2 \sinh^2\left(\frac{\omega}{2T}\right)} \left[1 + \left(\frac{\omega^2}{4} - \frac{q^2}{8}\right) \left(\frac{1}{\mu_\alpha^2} + \frac{1}{\mu_\beta^2}\right) \right]$$

$$\underset{\alpha \neq \beta}{\approx} \begin{cases} \frac{4 \text{sign}(\hat{\mu}_\alpha \hat{\mu}_\beta)}{\alpha_g^2 N_a^2 N_b^2 (2Td)^4 \hat{\mu}_\alpha^2 \hat{\mu}_\beta^2} \left[\frac{\zeta(3)}{2} + \left(\frac{\pi^2 \zeta(3)}{40} - \frac{5\zeta(5)}{16} \frac{1}{(2Td)^2}\right) \left(\frac{1}{\hat{\mu}_\alpha^2} + \frac{1}{\hat{\mu}_\beta^2}\right) \right] & dT \ll 1 \\ \frac{4 \text{sign}(\hat{\mu}_\alpha \hat{\mu}_\beta)}{\alpha_g^2 N_a^2 N_b^2 (2Td)^5 \hat{\mu}_\alpha^2 \hat{\mu}_\beta^2} \left[\frac{\pi^2}{15} + \frac{1}{(2Td)^2} \left(\frac{\pi^4}{252} - \frac{\pi^4}{168}\right) \left(\frac{1}{\hat{\mu}_\alpha^2} + \frac{1}{\hat{\mu}_\beta^2}\right) \right] & dT \gg 1 \end{cases} \quad (\text{C.69})$$

$$I_{\text{Gtr}}^{\alpha\beta} = \frac{N}{2T^2} \int_{\lambda_{\alpha\beta}}^{\min(|\mu_\alpha|, |\mu_\beta|)} \frac{dq}{2\pi} q \int_{-\Lambda_\omega}^{\Lambda_\omega} \frac{d\omega}{2\pi} |D_{\alpha\beta}|^2 \frac{\omega^2}{4\pi^2 \sinh^2\left(\frac{\omega}{2T}\right)} \frac{|\mu_\beta|}{|\mu_\alpha|} \left[1 - \frac{q^2}{8} \left(\frac{1}{\mu_\alpha^2} + \frac{1}{\mu_\beta^2}\right) + \frac{(2\omega)^2 + (2\pi T)^2}{12\mu_\alpha^2} \right]$$

$$\underset{\alpha \neq \beta}{\approx} \begin{cases} \frac{4}{\alpha_g^2 N_a^2 N_b^2 (2Td)^4 |\hat{\mu}_\alpha^3 \hat{\mu}_\beta|} \left[\frac{\zeta(3)}{2} + \frac{3\pi^2 \zeta(3)}{40} \frac{1}{\hat{\mu}_\alpha^2} - \frac{5\zeta(5)}{16} \frac{1}{(2Td)^2} \left(\frac{1}{\hat{\mu}_\alpha^2} + \frac{1}{\hat{\mu}_\beta^2}\right) \right] & dT \ll 1 \\ \frac{4}{\alpha_g^2 N_a^2 N_b^2 (2Td)^5 |\hat{\mu}_\alpha^3 \hat{\mu}_\beta|} \left[\frac{\pi^2}{15} + \frac{\pi^4}{180} \frac{1}{\hat{\mu}_\alpha^2} + \frac{1}{(2Td)^2} \frac{\pi^4}{189} \frac{1}{\hat{\mu}_\alpha^2} - \frac{\pi^4}{168} \frac{1}{(2Td)^2} \left(\frac{1}{\hat{\mu}_\alpha^2} + \frac{1}{\hat{\mu}_\beta^2}\right) \right] & dT \gg 1 \end{cases} \quad (\text{C.70})$$

We see immediately that as in the $\mu \ll T$ case the inter layer rates are strongly suppressed with large distance. Again we take a look at the following combination:

$$I_{\text{GI}}^{\alpha\beta} = \frac{|\mu_\alpha|}{|\mu_\beta|} I_{\text{Gtr}}^{\alpha\beta} - \frac{I_{\text{GD}}^{\alpha\beta}}{\text{sign}(\mu_\alpha \mu_\beta)} \underset{\alpha \neq \beta}{\approx} \frac{\pi^2}{\alpha_g^2 N_a^2 N_b^2 (2Td)^4 \hat{\mu}_\alpha^2 \hat{\mu}_\beta^2} \begin{cases} \frac{\zeta(3)}{10} \frac{2\hat{\mu}_\beta^2 - \hat{\mu}_\alpha^2}{\hat{\mu}_\alpha^2 \hat{\mu}_\beta^2} & dT \ll 1 \\ \frac{\pi^2}{45} \frac{1}{\hat{\mu}_\alpha^2} \frac{1}{(2Td)} + \frac{\pi^2}{3^{3.7}} \frac{1}{(2Td)^3} \frac{\hat{\mu}_\beta^2 - 3\hat{\mu}_\alpha^2}{\hat{\mu}_\alpha^2 \hat{\mu}_\beta^2} & dT \gg 1 \end{cases} \quad (\text{C.71})$$

To proceed we need to know again what the energy relaxation does for that large chemical potential. Again we start with Eq. (C.60) but using this time a stronger screened interaction we will gain the energy relaxation with an enhancement to the thermalization rate by a factor of (μ/T) :

$$\frac{|D_{ab}^{\text{RPA}}|^2}{q^2 - \omega^2} \approx \frac{(2\pi)^2 e^{-2qd}}{d|\mu_a \mu_b| q (qd\alpha_g^2 |\mu_a \mu_b| - 2\omega^2)} \quad I_{\text{E}} \propto \frac{1}{\alpha_g^2 \mu_a \mu_b} \begin{cases} (dT)^{-4} & dT \ll 1 \\ (dT)^{-5} & dT \gg 1 \end{cases} \quad (\text{C.72})$$

Using the three modes involving drag resistivity we obtain for $dT \ll 1$:

$$\rho_{\text{D}}(\hat{\mu}_a, \hat{\mu}_b) \approx \frac{1}{e^2 \alpha_g^2 N_a^2 N_b^2} \frac{4\pi^2 \zeta(3)}{(2Td)^4 (\hat{\mu}_a \hat{\mu}_b)^3} \left[1 + \frac{\frac{\pi^3 \zeta(3)}{6^{3.5^2}} \alpha_g^6 N_a^3 N_b^3 |\hat{\mu}_a \hat{\mu}_b| (2dT)^4 \ln\left(\frac{\Lambda_{aa}}{\lambda_{aa}}\right) \ln\left(\frac{\Lambda_{bb}}{\lambda_{bb}}\right)}{(N_a |\hat{\mu}_a| + N_b |\hat{\mu}_b|) ((T\tau_0)^{-1} + (T\tau_{\text{dis}})^{-1})} \right] \quad (\text{C.73})$$

where the characteristic Coulomb drag rate is given by:

$$(T\tau_0)^{-1} = \frac{\pi}{5} \frac{\alpha_g^2}{(N_a |\hat{\mu}_a| + N_b |\hat{\mu}_b|)} \left(N_a^2 \ln\left(\frac{\Lambda_{aa}}{\lambda_{aa}}\right) + N_b^2 \ln\left(\frac{\Lambda_{bb}}{\lambda_{bb}}\right) \right) \quad (\text{C.74})$$

And similar the drag resistivity for $dT \gg 1$:

$$\rho_D(\hat{\mu}_a, \hat{\mu}_b) \approx \frac{1}{e^2 \alpha_g^2 N_a^2 N_b^2} \frac{8\pi^2}{15(2Td)^5 (\hat{\mu}_a \hat{\mu}_b)^3} \left[1 - \frac{\frac{4\pi}{45} \alpha_g^6 N_a^3 N_b^3 |\hat{\mu}_a \hat{\mu}_b| (2dT)^5 \Lambda_{aa} \Lambda_{bb}}{(2T)^2 (N_a |\hat{\mu}_a| + N_b |\hat{\mu}_b|) ((T\tau_0)^{-1} + (T\tau_{\text{dis}})^{-1})} \right]. \quad (\text{C.75})$$

where the characteristic Coulomb drag rate is given by:

$$(T\tau_0)^{-1} = \frac{2}{\pi} \frac{\alpha_g^2}{(N_a |\hat{\mu}_a| + N_b |\hat{\mu}_b|)} \frac{1}{2T} (N_a^2 \Lambda_{aa} + N_b^2 \Lambda_{bb}). \quad (\text{C.76})$$

Large and Small Chemical Potential for Small Distances

We introduced in the beginning of this section (see C.3.2) approximations of the GVFs allowing for an analytic treatment of the rates for a large chemical potential. If we like to combine the limit of small chemical potential with the limit of large chemical potential we need to integrate again as it has been done in Sec. C.3.1. For Simplicity we will choose $\mu_a \ll T \ll \mu_b$. Since the intra layer contributions stay unchanged we will focus at the inter layer rates gaining:

$$\begin{aligned} I_{\text{GD}}(\mu_a \ll T \ll \mu_b) &= \frac{1}{2T^3} \int \frac{d^2q}{(2\pi)^2} \int \frac{d\omega}{2\pi} \left(D_{\alpha\beta}^{\text{bare}} \right)^2 \Gamma_{\mu \ll T}^1(-\omega, -\vec{q}, \mu_\alpha) \Gamma_{\mu \gg T}^1(\omega, \vec{q}, \mu_\beta) \\ &\approx \alpha_g^2 C_{\text{D2}}(dT) \frac{\mu_a \text{sign}(\mu_b)}{2T} \end{aligned} \quad (\text{C.77})$$

$$\begin{aligned} I_{\text{Gtr}}(\mu_a \ll T, \mu_b \gg T) &= \frac{1}{2T^3} \int \frac{d^2q}{(2\pi)^2} \int \frac{d\omega}{2\pi} \left(D_{\alpha\beta}^{\text{bare}} \right)^2 \Gamma_{\mu \ll T}^2(-\omega, -\vec{q}, \mu_\alpha) \Gamma_{\mu \gg T}^0(\omega, \vec{q}, \mu_\beta) \\ &\approx \alpha_g^2 C_{\text{Tr(ab)}}(dT) \frac{\mu_b}{2T} \end{aligned} \quad (\text{C.78})$$

$$\begin{aligned} I_{\text{Gtr}}(\mu_b \gg T, \mu_a \ll T) &= \frac{1}{2T^3} \int \frac{d^2q}{(2\pi)^2} \int \frac{d\omega}{2\pi} \left(D_{\alpha\beta}^{\text{bare}} \right)^2 \Gamma_{\mu \gg T}^2(-\omega, -\vec{q}, \mu_\alpha) \Gamma_{\mu \ll T}^0(\omega, \vec{q}, \mu_\beta) \\ &\approx \alpha_g^2 C_{\text{Tr(ba)}}(dT) \frac{2T}{\mu_b} \end{aligned} \quad (\text{C.79})$$

where the C s zero distance limit is $C_{\text{D2}}(dT=0) \approx 0.2035$, $C_{\text{Tr(ab)}}(dT=0) \approx 0.3384$ and $C_{\text{Tr(ba)}}(dT=0) \approx 0.2271$. Due to this artificial asymmetry the transport rate for the layers obeys an interesting behavior. The transport rate of layer b reads: $I_{\text{Tr}}^b \approx \alpha_g^2 C_{\text{Tr(ba)}} |\hat{\mu}_b^{-1}|$ whereas the transport rate of layer a reads: $I_{\text{Tr}}^a \approx \alpha_g^2 C_{\text{Tr(ab)}} |\hat{\mu}_b|$ and is strongly enhanced by the presence of layer b . Hence we are gaining for the drag resistivity:

$$\rho_D \approx \frac{\alpha_g^2}{e^2} C_{\text{D2}} \frac{2\pi^2}{\ln 2} \frac{\mu_a}{\mu_b} \left[1 + \frac{12}{\pi} \alpha_g^2 N \frac{C_{\text{Tr(ba)}}}{C_{\text{D2}}} \frac{(2C_{\text{Tr(ab)}} - C_{\text{D2}})}{(T\tau_0)^{-1} + (T\tau_{\text{dis}})^{-1}} \right] \quad (\text{C.80})$$

With the characteristic rate for the Coulomb drag given by:

$$(T\tau_0)^{-1} \approx \frac{6}{\pi} \alpha_g^2 N C_{\text{Tr(ba)}} \quad (\text{C.81})$$

D

Appendix D

Correlated Disorder and Diffusive Corrections to the Higher-Order Drag

Following the notation introduced by Ref. [91] we will briefly sketch the estimation of drag contributions at the Dirac point. This estimation is of experimental relevance, which is why we exceptionally consider the diffusive regime. We will start with higher-order Coulomb interaction contributions in the diffusive regime and proceed then with correlated disorder contributions.

D.1 Estimation of Diffusive Higher Order-drag

In this section we follow the calculation that has been performed in Ref. [91] but will adapt it towards our situation. The relevant regime for the experimental setup is $N\kappa d \ll 1$, in which we will now use the terminology in analogy to Ref. [91]. Thus, the propagator for the longitudinal vector potential reads:

$$\mathcal{V}_{12}(q, \omega) \simeq \frac{1}{\nu} \frac{\kappa q}{[Dq(q + 2N\kappa) - i\omega][Dq^2 - i\omega]}. \quad (\text{D.1})$$

Substituting this into the third order drag equation given by Ref. [91] we obtain:

$$\begin{aligned} \rho_D^{(3)} &= \frac{\hbar}{e^2} 32T \frac{g^2}{\nu^5} \int_0^\infty d\omega d\Omega \mathcal{F}_1(\omega, \Omega) \mathcal{F}_2(\omega, \Omega) \\ &\times \int \frac{d^2q}{(2\pi)^2} \int \frac{d^2Q}{(2\pi)^2} \text{Im} \left\{ \left[\frac{1}{Dq^2 - i\omega} \right]^2 \frac{\kappa q}{[Dq(q + 2N\kappa) - i\omega][Dq^2 - i\omega]} \right. \\ &\times \frac{\kappa|\mathbf{q}/2 - \mathbf{Q}|}{[D(\mathbf{q}/2 - \mathbf{Q})^2 + 2D|\mathbf{q}/2 - \mathbf{Q}|N\kappa - i(\omega/2 - \Omega)][D(\mathbf{q}/2 - \mathbf{Q})^2 - i(\omega/2 - \Omega)]} \\ &\times \left. \frac{\kappa|\mathbf{q}/2 + \mathbf{Q}|}{[D(\mathbf{q}/2 + \mathbf{Q})^2 + 2D|\mathbf{q}/2 + \mathbf{Q}|N\kappa - i(\omega/2 + \Omega)][D(\mathbf{q}/2 + \mathbf{Q})^2 - i(\omega/2 + \Omega)]} \right\}. \quad (\text{D.2}) \end{aligned}$$

The frequency integrals are dominated by $\omega \sim \Omega \sim T$, whereas the momentum integrals are dominated by $q \sim Q \sim q_T = \sqrt{T/D}$. Therefore, the drag conductivity given by Ref. [91] can be estimated as

$$\begin{aligned} \rho_D^{(3)} &\sim \frac{\hbar T g^2}{e^2 \nu^5} \underbrace{T^2}_{d\omega d\Omega} \underbrace{q_T^4}_{d^2 q d^2 Q} \frac{1}{(Dq_T^2 + T)^5} \frac{\kappa^3 q_T^3}{(Dq_T^2 + T + Dq_T N\kappa)^3} \\ &\sim \frac{\hbar}{e^2} \frac{1}{g^3} \left(\frac{\kappa}{N\kappa + \sqrt{T/D}} \right)^3. \end{aligned} \quad (\text{D.3})$$

Therefore, for $N\kappa \gg \sqrt{T/D}$ we get

$$\rho_D^{(3)} \sim \frac{\hbar}{e^2} \frac{1}{N^3 g^3}, \quad (\text{D.4})$$

while for $N\kappa \ll \sqrt{T/D}$ we find

$$\rho_D^{(3)} \sim \frac{\hbar}{e^2} \frac{1}{g^3} \left(\frac{D\kappa^2}{T} \right)^{3/2}. \quad (\text{D.5})$$

In the first case the expression for the third-order drag coefficient is given by

$$\begin{aligned} \rho_D^{(3)} &= \frac{\hbar}{e^2} 32T \frac{g^2}{\nu^5} \int_0^\infty d\omega d\Omega \mathcal{F}_1(\omega, \Omega) \mathcal{F}_2(\omega, \Omega) \int \frac{d^2 q}{(2\pi)^2} \int \frac{d^2 Q}{(2\pi)^2} \text{Im} \left\{ \left[\frac{1}{Dq^2 - i\omega} \right]^2 \right. \\ &\times \left. \left(\frac{1}{2ND} \right)^3 \frac{1}{Dq^2 - i\omega} \frac{1}{D(\mathbf{q}/2 - \mathbf{Q})^2 - i(\omega/2 - \Omega)} \frac{1}{D(\mathbf{q}/2 + \mathbf{Q})^2 - i(\omega/2 + \Omega)} \right\}. \end{aligned} \quad (\text{D.6})$$

The integrals here are now dimensionless [one measures momenta in units of $(T/D)^{1/2}$ and frequencies in units of T]. In the second case the prefactor is again determined by a dimensionless integral:

$$\begin{aligned} \rho_D^{(3)} &= \frac{\hbar}{e^2} 32T \frac{g^2}{\nu^5} \int_0^\infty d\omega d\Omega \mathcal{F}_1(\omega, \Omega) \mathcal{F}_2(\omega, \Omega) \int \frac{d^2 q}{(2\pi)^2} \int \frac{d^2 Q}{(2\pi)^2} \text{Im} \left\{ \left[\frac{1}{Dq^2 - i\omega} \right]^2 \right. \\ &\times \left. \kappa^3 \frac{q}{[Dq^2 - i\omega]^2} \frac{|\mathbf{q}/2 - \mathbf{Q}|}{[D(\mathbf{q}/2 - \mathbf{Q})^2 - i(\omega/2 - \Omega)]^2} \frac{|\mathbf{q}/2 + \mathbf{Q}|}{[D(\mathbf{q}/2 + \mathbf{Q})^2 - i(\omega/2 + \Omega)]^2} \right\}. \end{aligned} \quad (\text{D.7})$$

For $T\tau \ll 1$ and $\mu\tau \gg 1$, we have

$$\kappa \sim \alpha\mu/v, \quad (\text{D.8})$$

which implies

$$N\kappa = \sqrt{\frac{T}{D}} \leftrightarrow \frac{1}{\tau} = \frac{\alpha^2 N^2 \mu^2}{T}. \quad (\text{D.9})$$

For $\mu\tau \ll 1$, we have

$$\kappa \sim \alpha/v\tau, \quad (\text{D.10})$$

and hence

$$N\kappa = \sqrt{\frac{T}{D}} \leftrightarrow \frac{1}{\tau} = \frac{T}{\alpha^2 N^2}. \quad (\text{D.11})$$

Thus, for

$$\max\{T, \alpha^2 N^2 \mu^2 / T\} \ll 1/\tau \ll T/\alpha^2 N^2$$

the third-order drag resistivity reads:

$$\rho_D^{(3)} \sim \frac{\alpha^3}{(T\tau)^{3/2}}. \quad (\text{D.12})$$

At $T\tau \sim 1$ this result matches the ballistic third-order drag resistivity, Eq. (8.46).

For yet lower $T \ll \alpha^2 N^2 / \tau$ and $\mu\tau \ll 1$ the third-order drag saturates at

$$\rho_D^{(3)} \sim \frac{\hbar}{e^2} \frac{1}{N^3}. \quad (\text{D.13})$$

Finally, for $\mu\tau \gg \max\{1, (T\tau)^{1/2}/\alpha N\}$, the third-order drag behaves as

$$\rho_D^{(3)} \sim \frac{\hbar}{e^2} \frac{1}{(N\mu\tau)^3}. \quad (\text{D.14})$$

D.2 Estimation of Correlated Disorder Contributions

As emphasized in Ref. [122], the correlations between the disorder potentials of the two layers might be especially important in drag experiments on graphene near the Dirac point for the two reasons: (i) similarly to the third-order drag, it does not require [96] the particle-hole symmetry and hence provides finite drag at the charge neutrality point [122]; (ii) in contrast to experiments on conventional semiconducting double wells, the interlayer distance in graphene experiments is rather small, which enhances the disorder correlations between the layers. In what follows, we analyze the two models of correlations: (A) Correlated scattering off common short-range impurities [96] and (B) correlations of large-scale inhomogeneities of the chemical potentials in the layers [122].

D.2.1 A. Short-Range Correlations: Correlated Impurity Scattering

Following Ref. [96], we introduce the matrix of disorder correlators $w_{\hat{\mathbf{v}}\hat{\mathbf{v}}'}^{(ij)} = \langle u^{(i)} u^{(j)} \rangle_{\text{imp}}$. The values of $w^{(ij)}$ at $i \neq j$ differ from zero due to correlations between the impurity potentials $u^{(i)}$ in different layers. The total scattering rates are defined by

$$\frac{1}{\tau_{ij}} = \left\langle w_{\hat{\mathbf{v}}\hat{\mathbf{v}}'}^{ij} \frac{1 + \hat{\mathbf{v}}\hat{\mathbf{v}}'}{2} \right\rangle, \quad (\text{D.15})$$

where the symbol $\langle \dots \rangle$ stands for the angular average. The disorder correlations between the layers are described by the characteristic rate

$$\frac{1}{\tau_g} = \frac{\tau_{12} - \tau}{\tau^2}, \quad (\text{D.16})$$

where $1/\tau = [1/\tau_{11} + 1/\tau_{22}]/2$. The time scale τ_g is a characteristic scale on which carriers in the two layers start “feeling” the difference between the impurity potentials $u^{(1)}$ and $u^{(2)}$. The potentials in the two layers are strongly correlated when $\tau_g \gg \tau$. One might expect that for realistic systems the situation of moderately correlated potentials, $\tau_g \sim \tau \sim \tau_{12}$, is typically realized. Weakly correlated potentials ($\tau_{12} \gg \tau$) yield $\tau_g \ll \tau$. Below we assume that disorder is sufficiently short-ranged and do not distinguish between the total and transport scattering rates for the estimates.

We start from the ballistic regime $T\tau \gg 1$. The correlated disorder affects the drag in a way similar to the third-order drag. With correlated disorder, one can include an interlayer disorder line w_{12} into the inelastic scattering amplitude. In the ballistic $\rho_D^{(3)}$ drag we had one amplitude M_2 with two interaction lines and one with a single wave line (M_1). The corresponding drag rate contains $2\text{Re}[M_1(M_2)^*] \propto \alpha^3$. Now one can form the second-order scattering amplitude M_2 using one interaction line (α) and one interlayer-disorder line, which introduces a factor $(T\tau_{12})^{-1}$. This gives

$$\frac{1}{\tau_D^{\text{corr}}} \sim \alpha^2 T (T\tau_{12})^{-1} = \alpha^2 / \tau_{12}, \quad (\text{D.17})$$

and

$$\rho_D^{\text{corr}} \sim \frac{\alpha^2}{T\tau_{12}}, \quad (\text{D.18})$$

which overcomes the third-order drag $\rho_D^{(3)} \sim \alpha^3$ for $1/\tau_{12} > \alpha T$. This happens in the perturbative regime ($1/\tau > \alpha^2 T$, assuming correlated disorder, $\tau_{12} \sim \tau$), where the correlated-disorder contribution can be calculated diagrammatically. Similarly to $\sigma_D^{(3)}$, the corresponding diagram involves two four-leg vertices (hence finite drag at the Dirac point $\mu = 0$), but now connected in all possible ways by two interaction lines and one disorder line w_{12} .

The general expression for the drag resistivity in the ballistic regime, including both third-order and correlated-disorder drag rates for equal layers has the form:

$$\rho_D \sim \frac{\hbar}{e^2} \frac{1}{NT} \frac{\frac{N}{\tau} \left(\alpha^2 \frac{\mu^2}{T} + \alpha^3 T + \frac{\alpha^2}{\tau_{12}} \right) + \frac{\mu^2 N^2}{T^2} \left[\alpha^4 T^2 - \left(\alpha^2 \frac{\mu^2}{T} + \alpha^3 T + \frac{\alpha^2}{\tau_{12}} \right)^2 \right]}{\frac{1}{\tau} + \frac{\mu^2 N}{T^2} \left[\alpha^2 T + \left(\alpha^2 \frac{\mu^2}{T} + \alpha^3 T + \frac{\alpha^2}{\tau_{12}} \right) \right]} \quad (\text{D.19})$$

Exactly at the Dirac point it reduces to:

$$\rho_D(\mu = 0) \sim \frac{\hbar}{e^2} \alpha^2 \left(\frac{1}{T\tau_{12}} + \alpha \right). \quad (\text{D.20})$$

Let us now analyze the role of correlated disorder in the diffusive regime $T\tau \ll 1$. Again, we assume the absence of localization at the Dirac point (see Section 3). The drag resistivity for the case of correlated disorder was calculated in the diffusive regime in Ref. [96]. It is dominated by the Maki-Thompson diagram with an interlayer Cooper propagator. It is worth noting that any difference in the disorder potentials (as well as in chemical potentials of the layers) leads to a finite gap in these propagators given by $1/\tau_g$. The main result of Ref. [96] is as follows:

$$\rho_D^{\text{corr}} \sim \frac{\hbar}{e^2} \frac{1}{g^2 [\lambda_{21}^{-1} + \ln(\varepsilon_0/T)]^2} \ln \frac{T\tau_\varphi\tau_g}{\tau_\varphi + \tau_g} \quad (\text{D.21})$$

at $\tau_g^{-1} \ll T \ll \tau^{-1}$, and

$$\rho_D^{\text{corr}} \sim \frac{\hbar}{e^2} \frac{(T\tau_g)^2}{g^2 [\lambda_{21}^{-1} + \ln(\varepsilon_0\tau_g)]^2}. \quad (\text{D.22})$$

at lower temperatures $T \ll \tau_g^{-1}$.

In graphene near the Dirac point, for small interlayer distance $\kappa d \ll 1$ the interlayer interaction constant in the Cooper channel is $\lambda_{12} \sim \alpha$. The Cooper channel cutoff energy is $\epsilon_0 = 1/\tau$ (the logarithm in the Cooper channel appears only for a constant density of states; in graphene in the diffusive regime this happens only for energies below $1/\tau$), the dimensionless conductance $g \sim 1$, and $\tau_\phi \sim 1/T$. Substituting these values to Eqs. (D.21) and (D.22), we arrive at

$$\rho_D^{\text{corr}} \sim \frac{\hbar}{e^2} \frac{\alpha^2}{[1 - \alpha \ln(T\tau)]^2}, \quad \tau_g^{-1} \ll T \ll \tau^{-1}, \quad (\text{D.23})$$

$$\rho_D^{\text{corr}} \sim \frac{\hbar}{e^2} \frac{\alpha^2 (T\tau_g)^2}{[1 - \alpha \ln(T\tau)]^2}, \quad T \ll \tau_g^{-1}. \quad (\text{D.24})$$

These results are $\propto \alpha^2$ for realistic temperatures, $T\tau \gg \exp(-1/\alpha)$. For a moderately correlated disorder $\tau_g \sim \tau$, Eqs. (D.18) and (D.24) then lead to

$$\rho_D^{\text{corr}} \sim \frac{\hbar}{e^2} \alpha^2 \begin{cases} (T\tau)^{-1}, & T\tau \gg 1 \\ (T\tau)^2, & T\tau \ll 1 \end{cases}, \quad (\text{D.25})$$

which yields a maximum at $T \sim 1/\tau$ in the temperature dependence of the drag resistivity at the charge neutrality point. For strongly correlated disorder potentials ($\tau_g \gg \tau$), this maximum develops into a plateau between $\tau_g^{-1} \ll T \ll \tau^{-1}$.

D.2.2 B. Long-Range Correlations: Correlated Macroscopic Inhomogeneities

Let us now analyze within our kinetic-equation framework the model of correlated macroscopic spatial fluctuations $\delta\mu_i$ in chemical potentials of the two layers [122], characterized by the correlation function

$$F_{ij}^{(\mu)}(\vec{r} - \vec{r}') = \langle \delta\mu_i(\vec{r}) \delta\mu_j(\vec{r}') \rangle \neq 0. \quad (\text{D.26})$$

We restrict ourselves to the ballistic regime $T\tau \gg 1$. Assuming the spatial scale of the fluctuations to be much larger than all characteristic scales related to the particle scattering, $v\tau_{ee}$, $v\tau_D$, and $v\tau$, we solve the hydrodynamic equations locally, yielding Eq. (7.23) with local values of the chemical potentials encoded in functions $B_1^{a(b)} \sim \mu_{a(b)}/T$, as well as in the local drag rate

$$\frac{1}{\tau_D(\vec{r})} \sim \alpha^2 N \frac{\mu_1(\vec{r}) \mu_2(\vec{r})}{T}.$$

On the other hand, since the coefficients $B_0 \sim 1$ and $B_2 \sim 1$, as well as the transport electron-electron scattering rate $\tau_{ee}^{-1} \sim \alpha^2 T$ are finite at the neutrality point, we can neglect the fluctuations of μ_i in these quantities. Exactly at the Dirac point $\mu_{1,2} = 0$, assuming that the fluctuations of chemical potentials are weak (the precise condition is established below), we can further neglect the B_1 -terms in the denominator of Eq. (7.23), yielding for the ‘‘local resistivity’’

$$\begin{aligned} \rho_D(\vec{r}) &\simeq \frac{\hbar}{e^2} \frac{2B_2\tau}{NB_0^a B_0^b T} \left[\frac{1}{\tau\tau_D(\vec{r})} + \frac{B_1^a(\vec{r})B_1^b(\vec{r})}{\tau_{ee}^a \tau_{ee}^b} \right] \\ &\sim \frac{\hbar}{e^2} \frac{\tau}{NT} \delta\mu_1(\vec{r}) \delta\mu_2(\vec{r}) \left(\frac{\alpha^2 N}{T\tau} + \alpha^4 N^2 \right). \end{aligned} \quad (\text{D.27})$$

Averaging this expression over the small fluctuations of the correlated chemical potentials [122], we arrive at the correction to the universal third-order result, $\rho_D^{(3)}(\mu = 0) \sim (\hbar/e^2)\alpha^3$,

$$\Delta\rho_D(\mu = 0) \sim \frac{\hbar}{e^2} \frac{\alpha^2 F_{12}^{(\mu)}(0)}{T^2} (1 + \alpha^2 NT\tau) \sim \frac{\hbar}{e^2} \frac{F_{12}^{(\mu)}(0)}{T^2} \begin{cases} \alpha^4 NT\tau & \frac{1}{\tau} \ll \alpha^2 NT, \\ \alpha^2 & \alpha^2 NT \ll \frac{1}{\tau} \ll T. \end{cases} \quad (\text{D.28})$$

We see that in the Coulomb-dominated transport regime, this correction is dominated by the fluctuations in B_1 , whereas in the disorder-dominated (perturbative) regime, the main role is played by a locally finite drag rate.

Finally, in the ultraclean limit

$$\frac{1}{\tau} \ll \alpha^2 NF_{ii}^{(0)}/T, \quad (\text{D.29})$$

we can neglect $1/\tau$ in the denominator of the local drag resistivity given by Eq. (7.23), yielding a natural analog of Eq. (7.29):

$$\Delta\rho_D(\mu = 0)(\mathbf{r}) \sim \frac{\hbar}{e^2} \alpha^2 \frac{\delta\mu_1 \delta\mu_2}{\delta\mu_1 \delta\mu_1 + \delta\mu_2 \delta\mu_2}. \quad (\text{D.30})$$

In particular, for perfectly correlated chemical potentials, $\delta\mu_1(\mathbf{r}) = \delta\mu_2(\mathbf{r})$, the fluctuations drops out from Eq. (D.30) and the local resistivity turns out to be independent of \mathbf{r} . In a more general case, the averaging over fluctuations becomes nontrivial, but this can only affect the numerical prefactor in the final result. Thus, the correlated large-scale fluctuations of the chemical potentials in the layers in effect shift the curve 1 in Fig. 7.6 upwards, extending the validity of the fully equilibrated result,

$$\rho_D \sim \frac{\hbar}{e^2} \alpha^2, \quad (\text{D.31})$$

to the case of finite disorder, Eq. (D.29), at the Dirac point. This implies that in the case of correlated inhomogeneities the disorder-induced dip in the lower left panel of Fig. 1 develops only for sufficiently strong disorder.

Acknowledgments

During my wonderful time at the institute of condensed matter theory (TKM) I met a lot of people I would like to thank, this includes technical and physical input, discussions I really enjoyed and everything else that makes life worth living.

I would like to thank my supervisor Alexander Mirlin for showing me the beauty of condensed matter physics and for giving me subsequently the opportunity to work in this field and writing my thesis at this institute. I wish to thank as well Jörg Schmalian for co-refereeing my thesis and for providing me from time to time all kinds of enjoyable food for thoughts.

I would like to thank my advisor Igor Gornyi for his patience and calmness in teaching me physics. He became a guide to me in playing with ideas and concepts. I thank Pavel Ostrovsky for his passion in arguing with me, which was both incredibly helpful and enjoyable.

Further I wish to thank my collaborators Mikhail Titov and Boris Narozhny for all the stimulating discussions and Leonid Ponomarenko for allowing me to use unpublished data.

I wish to thank Lars Fritz and Markus Müller for sharing their insights with me.

I thank Sam Carr, Elio König, Stephan Ngo Dinh and Christian Seiler for the instructional and enjoyable “Book Seminars” and discussions we had in our office. Furthermore I wish to thank Ulf Briskot, Peter Orth and Martin Schneider for all the helpful conversations.

I would like to thank all the members at the TKM institute for the atmosphere and the support they provide, in particular Rose, who not only kept our work going but as well our lives.

List of publications

This dissertation is based on several works both published (below) and not yet published (see outlook in Chap. 9). In this chapter we want to provide the references to these works.

M. Schütt, P. M. and Ostrovsky, I. V. Gornyi, and A. D. Mirlin, Coulomb interaction in graphene: Relaxation rates and transport. *Phys. Rev. B*, **83** 155441 pages 25, (2011)

We analyze the inelastic electron-electron scattering in undoped graphene within the Keldysh diagrammatic approach. We demonstrate that finite temperature strongly affects the screening properties of graphene, which, in turn, influences the inelastic-scattering rates as compared to the zero-temperature case. Focusing on the clean regime, we calculate the quantum scattering rate which is relevant for dephasing interference processes. We identify a hierarchy of regimes arising due to the interplay of a plasmon enhancement of the scattering and finite-temperature screening of the interaction. We further address the energy relaxation and transport scattering rates in graphene. We find a nonmonotonic energy dependence of the inelastic relaxation rates in clean graphene, which is attributed to the resonant excitation of plasmons. Finally, we discuss the temperature dependence of the conductivity at the Dirac point in the presence of both interaction and disorder. Our results complement the kinetic equation and hydrodynamic approaches for the collision-limited conductivity of clean graphene and can be generalized to the treatment of physics of inelastic processes in strongly nonequilibrium setups.

M. Schütt, P. M. Ostrovsky, M. Titov, I. V. Gornyi, B. N. Narozhny, A. D. Mirlin, Coulomb drag in graphene near the Dirac point. Accepted for publication as a Letter in *Physical Review Letters* (2012)

We study Coulomb drag in double-layer graphene near the Dirac point. A particular emphasis is put on the case of clean graphene, with transport properties dominated by the electron-electron interaction. Using the quantum kinetic equation framework, we show that the drag becomes T -independent in the clean limit, $T\tau \rightarrow \infty$, where T is temperature and $1/\tau$ impurity scattering rate. For stronger disorder (or lower temperature), $T\tau \ll 1/\alpha^2$, where α is the interaction strength, the kinetic equation agrees with the leading-order (α^2) perturbative result. At still lower temperatures, $T\tau \ll 1$ (diffusive regime) this contribution gets suppressed, while the next-order (α^3) contribution becomes important; it yields a peak centered at the Dirac point with a magnitude that grows with lowering $T\tau$.

Bibliography

- [1] K. S. Novoselov, A. K. Geim, S. V. Morozov, D. Jiang, Y. Zhang, S. V. Dubonos, I. V. Grigorieva, and A. A. Firsov. Electric field effect in atomically thin carbon films. *Science*, 306:666, 2004. doi: 10.1126/science.1102896.
(Cited on pages 1 and 78.)
- [2] A. K. Geim and K. S. Novoselov. The rise of graphene. *Nature Materials*, 6:183, 2007.
(Cited on pages 1 and 5.)
- [3] R. E. Peierls. Quelques proprietes typiques des corps solides. *Ann. I. H. Poincare*, 5:177, 1935.
(Cited on page 1.)
- [4] L.D. Landau. Zur theorie der phasenumwandlungen ii. *Phys. Z. Sowjetunion*, 11:26, 1937.
(Cited on page 1.)
- [5] Changgu Lee, Xiaoding Wei, Jeffrey W. Kysar, and James Hone. Measurement of the elastic properties and intrinsic strength of monolayer graphene. *Science*, 321:385–388, 2008. doi: 10.1126/science.1157996.
(Cited on page 1.)
- [6] J. Scott Bunch, Scott S. Verbridge, Jonathan S. Alden, Arend M. van der Zande, Jeevak M. Parpia, Harold G. Craighead, and Paul L. McEuen. Impermeable atomic membranes from graphene sheets. *Nano Letters*, 8:2458–2462, 2008. doi: 10.1021/nl801457b.
(Cited on page 1.)
- [7] R. R. Nair, H. A. Wu, P. N. Jayaram, I. V. Grigorieva, and A. K. Geim. Unimpeded permeation of water through helium-leak-tight graphene-based membranes. *Science*, 335:442–444, 2012. doi: 10.1126/science.1211694.
(Cited on page 1.)
- [8] Alexander A. Balandin. Thermal properties of graphene and nanostructured carbon materials. *Nature Materials*.
(Cited on page 1.)
- [9] A. B. Kuzmenko, E. van Heumen, F. Carbone, and D. van der Marel. Universal optical conductance of graphite. *Phys. Rev. Lett.*, 100:117401, 2008. doi: 10.1103/PhysRevLett.100.117401.
(Cited on page 1.)
- [10] Alexander S. Mayorov, Roman V. Gorbachev, Sergey V. Morozov, Liam Britnell, Rashid Jalil, Leonid A. Ponomarenko, Peter Blake, Kostya S. Novoselov, Kenji Watanabe, Takashi Taniguchi, and A. K. Geim. Micrometer-scale ballistic transport in encapsulated graphene at room temperature. *Nano Letters*, 11:2396, 2011. doi: 10.1021/nl200758b.
(Cited on pages 1, 2, and 78.)

- [11] K. S. Novoselov, Z. Jiang, Y. Zhang, S. V. Morozov, H. L. Stormer, U. Zeitler, J. C. Maan, G. S. Boebinger, P. Kim, and A. K. Geim. Room-temperature quantum hall effect in graphene. *Science*, 315:1379, 2007. doi: 10.1126/science.1137201.
(Cited on page 1.)
- [12] K. S. Novoselov, V. I. Fal'ko, L. Colombo, P. R. Gellert, M. G. Schwab, and K. Kim. A roadmap for graphene. *Nature*, 490:192–200, 2012. doi: 10.1038/nature11458.
(Cited on page 1.)
- [13] K. S. et al Novoselov. Two-dimensional gas of massless dirac fermions in graphene. *Nature*, 438:197, 2005.
(Cited on pages 2, 5, and 51.)
- [14] Gordon W. Semenoff. Condensed-matter simulation of a three-dimensional anomaly. *Phys. Rev. Lett.*, 53:2449–2452, 1984. doi: 10.1103/PhysRevLett.53.2449.
(Cited on pages 2 and 7.)
- [15] M. I. Katsnelson. Zitterbewegung, chirality, and minimal conductivity in graphene. *The European Physical Journal B - Condensed Matter and Complex Systems*, 51:157–160, 2006. doi: 10.1140/epjb/e2006-00203-1.
(Cited on page 2.)
- [16] N. Stander, B. Huard, and D. Goldhaber-Gordon. Evidence for klein tunneling in graphene p-n junctions. *Phys. Rev. Lett.*, 102:026807, 2009. doi: 10.1103/PhysRevLett.102.026807.
(Cited on page 2.)
- [17] M.B. Pograbskii. Mutual drag of carriers in a semiconductor-insulator-semiconductor system. *Sov. Phys. Semicond.*, 11:372, 1977.
(Cited on pages 2 and 75.)
- [18] Peter J. Price. Hot electron effects in heterolayers. *Physica B+C*, 117–118,Part 2:750, 1983. doi: 10.1016/0378-4363(83)90642-3.
(Cited on pages 2 and 75.)
- [19] M. I. Katsnelson K. S. Novoselov T. J. Booth Jannik C. Meyer, A. K. Geim and S. Roth. The structure of suspended graphene sheets. *Nature*, 446:60, 2007.
(Cited on page 3.)
- [20] A. H. Castro Neto, F. Guinea, N. M. R. Peres, K. S. Novoselov, and A. K. Geim. The electronic properties of graphene. *Reviews of Modern Physics*, 81:109, 2009. doi: 10.1103/RevModPhys.81.109.
(Cited on pages 5, 70, and 99.)
- [21] H. L. Stormer P. Kim Y. Zhang, Y. W. Tan. Experimental observation of the quantum hall effect and berrys phase in graphene. *Nature*, 438:201, 2005.
(Cited on pages 5 and 51.)
- [22] N.W. Ashcroft and N.D. Mermin. *Solid state physics*. Science: Physics. 1976. ISBN 9780030493461.
(Cited on page 5.)

-
- [23] P. R. Wallace. The band theory of graphite. *Phys. Rev.*, 71:622–634, 1947. doi: 10.1103/PhysRev.71.622.
(Cited on page 7.)
- [24] D. M. Basko. Theory of resonant multiphonon raman scattering in graphene. *Phys. Rev. B*, 78:125418, 2008. doi: 10.1103/PhysRevB.78.125418.
(Cited on page 7.)
- [25] D. M. Basko. Resonant low-energy electron scattering on short-range impurities in graphene. *Phys. Rev. B*, 78:115432, 2008. doi: 10.1103/PhysRevB.78.115432.
(Cited on page 7.)
- [26] Tsuneya Ando, Alan B. Fowler, and Frank Stern. Electronic properties of two-dimensional systems. *Rev. Mod. Phys.*, 54:437–672, 1982. doi: 10.1103/RevModPhys.54.437.
(Cited on page 11.)
- [27] I. V. Gornyi, A. D. Mirlin, and D. G. Polyakov. Electron transport in a disordered luttinger liquid. *Phys. Rev. B*, 75:085421, 2007. doi: 10.1103/PhysRevB.75.085421.
(Cited on pages 11, 41, and 45.)
- [28] A. G. Yashenkin, I. V. Gornyi, A. D. Mirlin, and D. G. Polyakov. Quantum interference and spin-charge separation in a disordered luttinger liquid. *Phys. Rev. B*, 78:205407, 2008. doi: 10.1103/PhysRevB.78.205407.
(Cited on page 45.)
- [29] D. Bagrets, I. Gornyi, A. Mirlin, and D. Polyakov. Relaxation processes in a disordered luttinger liquid. *Semiconductors*, 42:994, 2008. doi: 10.1134/S1063782608080204.
(Not cited.)
- [30] D. A. Bagrets, I. V. Gornyi, and D. G. Polyakov. Publisher’s note: Nonequilibrium kinetics of a disordered luttinger liquid [phys. rev. b 80, 113403 (2009)]. *Phys. Rev. B*, 80:119904, 2009. doi: 10.1103/PhysRevB.80.119904.
(Not cited.)
- [31] Stéphane Ngo Dinh, Dmitry A. Bagrets, and Alexander D. Mirlin. Tunneling into a nonequilibrium luttinger liquid with impurity. *Phys. Rev. B*, 81:081306, 2010. doi: 10.1103/PhysRevB.81.081306.
(Not cited.)
- [32] D. B. Gutman, Yuval Gefen, and A. D. Mirlin. Nonequilibrium luttinger liquid: Zero-bias anomaly and dephasing. *Phys. Rev. Lett.*, 101:126802, 2008. doi: 10.1103/PhysRevLett.101.126802.
(Cited on page 46.)
- [33] D. B. Gutman, Yuval Gefen, and A. D. Mirlin. Tunneling spectroscopy of luttinger-liquid structures far from equilibrium. *Phys. Rev. B*, 80:045106, 2009. doi: 10.1103/PhysRevB.80.045106.
(Cited on pages 11, 41, and 46.)
- [34] D. Pines and P. Nozieres. *The Theory of Quantum Liquids: Normal Fermi liquids*. The Theory of Quantum Liquids. 1966.
(Cited on page 11.)
-

- [35] Jörg Schmalian. Privat communications. 2012.
(Cited on page 11.)
- [36] M. P. Mink, H. T. C. Stoof, R. A. Duine, Marco Polini, and G. Vignale. Probing the topological exciton condensate via coulomb drag. *Phys. Rev. Lett.*, 108:186402, 2012. doi: 10.1103/PhysRevLett.108.186402.
(Cited on page 11.)
- [37] I. L. Aleiner, D. E. Kharzeev, and A. M. Tsvelik. Spontaneous symmetry breaking in graphene subjected to an in-plane magnetic field. *Phys. Rev. B*, 76:195415, 2007. doi: 10.1103/PhysRevB.76.195415.
(Not cited.)
- [38] Maxim Yu. Kharitonov and Konstantin B. Efetov. Electron screening and excitonic condensation in double-layer graphene systems. *Phys. Rev. B*, 78:241401, 2008. doi: 10.1103/PhysRevB.78.241401.
(Cited on page 11.)
- [39] L.D. Landau, E.M. Lifshitz, and L.P. Pitaevskii. *Statistical Physics*. Number Teil 2. 1980. ISBN 9780750626361.
(Cited on pages 12 and 16.)
- [40] A.A. Abrikosov, I.E. Dzyaloshinskii, and L.P. Gor'kov. *Quantum Field Theoretical Methods in Statistical Physics*. 1965.
(Cited on page 12.)
- [41] Andrey V. Chubukov and Dmitrii L. Maslov. Singular corrections to the fermi-liquid theory. *Phys. Rev. B*, 69:121102, 2004. doi: 10.1103/PhysRevB.69.121102.
(Cited on page 12.)
- [42] J. Gonzalez, F. Guinea, and M. A. H. Vozmediano. Marginal-fermi-liquid behavior from two-dimensional coulomb interaction. *Physical Review B (Condensed Matter and Materials Physics)*, 59:R2474, 2008.
(Cited on pages 12, 27, and 29.)
- [43] B. L. Altshuler and A. G. Aronov. *Electron-electron interaction in disordered conductors*. Elsevier Science Publisher, 1985.
(Cited on pages 12 and 41.)
- [44] I. L. Aleiner, B. L. Altshuler, and M. E. Gershenson. Interaction effects and phase relaxation in disordered systems. *Waves in Random and Complex Media*, 9:201, 1999.
(Cited on pages 12 and 66.)
- [45] A. Altland and Simons B. *Codensed Matter Field Theory*. Cambridge, 2007.
(Cited on pages 12 and 16.)
- [46] G. D. Mahan. *Many-Particle Physics*. Plenum, 1990.
(Not cited.)
- [47] J. W. Negele and H. Orland. *Quantum Many-Particle Systems*. Addison-Wesley, 1988.
(Cited on pages 12 and 16.)

-
- [48] L. V. Keldysh. Ionization in the field of a strong electromagnetic wave. *J. Exptl. Theoret. Phys.*, 47:1945, 1964.
(Cited on page 14.)
- [49] J. Rammer and H. Smith. Quantum field-theoretical methods in transport theory of metals. *Reviews of Modern Physics*, 58:323, 1986. doi: 10.1103/RevModPhys.58.323.
(Cited on pages 14, 15, 18, 19, and 100.)
- [50] A. Kamenev. *Field Theory of Non-Equilibrium Systems*. 2011. ISBN 9780521760829.
(Cited on pages 14, 15, 16, 18, and 100.)
- [51] Yu.N. Ovchinnikov A.I. Larkin. *Vortex Motion in Semiconductors, In: Nonequilibrium Superconductivity*. Modern problems in condensed matter sciences, Vol. 12. Elsevier, 1986. ISBN 0-444-86943-3.
(Cited on page 15.)
- [52] L.P. Pitaevskii and E.M. Lifshitz. *Physical Kinetics*. 1981. ISBN 9780750626354.
(Cited on pages 18, 25, 84, and 100.)
- [53] C. Gorini, P. Schwab, R. Raimondi, and A. L. Shelankov. Non-abelian gauge fields in the gradient expansion: Generalized boltzmann and eilenberger equations. *Phys. Rev. B*, 82:195316, 2010. doi: 10.1103/PhysRevB.82.195316.
(Cited on page 19.)
- [54] J. M. Ziman. *Electrons and Phonons (Chapter 7: Formal Transport Theory)*. Oxford University Press, 1960. ISBN 0198507798.
(Cited on page 21.)
- [55] J. M. Luttinger. Theory of thermal transport coefficients. *Phys. Rev.*, 135:A1505, 1964. doi: 10.1103/PhysRev.135.A1505.
(Cited on page 22.)
- [56] Karen Michaeli and Alexander M. Finkel'stein. Quantum kinetic approach for studying thermal transport in the presence of electron-electron interactions and disorder. *Phys. Rev. B*, 80:115111, 2009. doi: 10.1103/PhysRevB.80.115111.
(Cited on page 22.)
- [57] G.E. Uhlenbeck and G.W. Ford. *Lectures in statistical mechanics*. Lectures in applied mathematics. American Mathematical Society, 1974.
(Cited on pages 22, 24, and 25.)
- [58] L.D. Landau and E.M. Lifshitz. *Course of Theoretical Physics. Vol. 6: Fluid Mechanics*. Oxford, 1987.
(Cited on pages 22, 24, and 25.)
- [59] M. S. Foster and I. L. Aleiner. Graphene via large n i: Renormalization. *Physical Review B (Condensed Matter and Materials Physics)*, 77:195413, 2008. doi: 10.1103/PhysRevB.77.195413.
(Cited on pages 27, 29, and 72.)
-

- [60] J. González, F. Guinea, and M.A.H. Vozmediano. Non-fermi liquid behavior of electrons in the half-filled honeycomb lattice (a renormalization group approach). *Nuclear Physics B*, 424:595–618, 1994. doi: 10.1016/0550-3213(94)90410-3.
(Cited on pages 27, 28, 30, and 33.)
- [61] J. González, F. Guinea, and M. A. H. Vozmediano. Unconventional quasiparticle lifetime in graphite. *Phys. Rev. Lett.*, 77:3589–3592, 1996. doi: 10.1103/PhysRevLett.77.3589.
(Cited on pages 30, 32, 33, and 57.)
- [62] M. S. Foster and I. L. Aleiner. Slow imbalance relaxation and thermoelectric transport in graphene. *Physical Review B (Condensed Matter and Materials Physics)*, 79:085415, 2008.
(Cited on pages 30, 33, 43, 62, 70, and 71.)
- [63] E. H. Hwang, Ben Yu-Kuang Hu, and S. Das Sarma. Inelastic carrier lifetime in graphene. *Phys. Rev. B*, 76:115434, 2007. doi: 10.1103/PhysRevB.76.115434.
(Cited on pages 32 and 114.)
- [64] I. L. Aleiner and Ya. M. Blanter. Inelastic scattering time for conductance fluctuations. *Phys. Rev. B*, 65:115317, 2002. doi: 10.1103/PhysRevB.65.115317.
(Cited on page 41.)
- [65] B. N. Narozhny, Gábor Zala, and I. L. Aleiner. Interaction corrections at intermediate temperatures: Dephasing time. *Phys. Rev. B*, 65:180202, 2002. doi: 10.1103/PhysRevB.65.180202.
(Cited on pages 42 and 46.)
- [66] F. V. Tikhonenko, A. A. Kozikov, A. K. Savchenko, and R. V. Gorbachev. Transition between electron localization and antilocalization in graphene. *Phys. Rev. Lett.*, 103:226801, 2009. doi: 10.1103/PhysRevLett.103.226801.
(Cited on pages 46 and 74.)
- [67] V.F. Gantmakher and I.B. Levinson. *Carrier scattering in metals and semiconductors*. Modern problems in condensed matter sciences. 1987.
(Cited on page 47.)
- [68] J. Voutilainen, A. Fay, P. Häkkinen, J. K. Viljas, T. T. Heikkilä, and P. J. Hakonen. Energy relaxation in graphene and its measurement with supercurrent. *Phys. Rev. B*, 84:045419, 2011. doi: 10.1103/PhysRevB.84.045419.
(Cited on page 48.)
- [69] Steve Gilbertson, Tomasz Durakiewicz, Jian-Xin Zhu, Aditya D. Mohite, Andrew Dattelbaum, and George Rodriguez. Direct measurement of quasiparticle lifetimes in graphene using time-resolved photoemission. *Journal of Vacuum Science and Technology B: Microelectronics and Nanometer Structures*, 30:03D116, 2012. doi: 10.1116/1.4715440.
(Cited on page 48.)
- [70] K. J. Tielrooij, J. C. W. Song, S. A. Jensen, A. Centeno, A. Pesquera, A. Zurutuza Elorza, M. Bonn, L. S. Levitov, and F. H. L. Koppens. Photo-excitation cascade and multiple carrier generation in graphene. *ArXiv e-prints*, 2012.
(Cited on pages 48 and 120.)

-
- [71] L. Fritz, J. Schmalian, M. Müller, and S. Sachdev. Quantum critical transport in clean graphene. *Physical Review B (Condensed Matter and Materials Physics)*, 78:085416, 2008.
(Cited on pages 53, 54, 56, 57, 59, 70, and 71.)
- [72] A. B. Kashuba. Conductivity of defectless graphene. *Physical Review B (Condensed Matter and Materials Physics)*, 78:085415, 2008.
(Cited on pages 53, 54, 56, 57, 59, 70, and 71.)
- [73] M. Müller, L. Fritz, and S. Sachdev. Quantum-critical relativistic magnetotransport in graphene. *Physical Review B (Condensed Matter and Materials Physics)*, 78:115406, 2008.
(Cited on pages 58, 62, 70, 71, 84, 93, and 101.)
- [74] M. Müller, L. Fritz, S. Sachdev, and J. Schmalian. Relativistic magnetotransport in graphene. *AIP Conference Proceedings*, 1134:170, 2009.
(Cited on pages 60 and 70.)
- [75] M. Müller and S. Sachdev. Collective cyclotron motion of the relativistic plasma in graphene. *Physical Review B (Condensed Matter and Materials Physics)*, 78:115419, 2008.
(Cited on page 101.)
- [76] Markus Müller, Jörg Schmalian, and Lars Fritz. Graphene: A nearly perfect fluid. *Phys. Rev. Lett.*, 103:025301, 2009. doi: 10.1103/PhysRevLett.103.025301.
(Cited on pages 62, 70, and 71.)
- [77] B. N. Narozhny. Coulomb drag as a measure of trigonal warping in doped graphene. *Phys. Rev. B*, 76:153409, 2007. doi: 10.1103/PhysRevB.76.153409.
(Cited on pages 67, 78, and 94.)
- [78] Wang-Kong Tse, Ben Yu-Kuang Hu, and S. Das Sarma. Theory of coulomb drag in graphene. *Phys. Rev. B*, 76:081401, 2007. doi: 10.1103/PhysRevB.76.081401.
(Cited on pages 67, 78, and 94.)
- [79] A. Schuessler, P. M. Ostrovsky, I. V. Gornyi, and A. D. Mirlin. Analytic theory of ballistic transport in disordered graphene. *Phys. Rev. B*, 79:075405, 2009. doi: 10.1103/PhysRevB.79.075405.
(Cited on page 72.)
- [80] M. Titov, P. M. Ostrovsky, I. V. Gornyi, A. Schuessler, and A. D. Mirlin. Charge transport in graphene with resonant scatterers. *Phys. Rev. Lett.*, 104:076802, 2010. doi: 10.1103/PhysRevLett.104.076802.
(Not cited.)
- [81] A. Schuessler, P. M. Ostrovsky, I. V. Gornyi, and A. D. Mirlin. Full counting statistics in disordered graphene at the dirac point: From ballistics to diffusion. *Phys. Rev. B*, 82:085419, 2010. doi: 10.1103/PhysRevB.82.085419.
(Not cited.)
- [82] P. M. Ostrovsky, M. Titov, S. Bera, I. V. Gornyi, and A. D. Mirlin. Diffusion and criticality in undoped graphene with resonant scatterers. *Phys. Rev. Lett.*, 105:266803, 2010. doi: 10.1103/PhysRevLett.105.266803.
(Cited on page 72.)
-

- [83] P. M. Ostrovsky, I. V. Gornyi, and A. D. Mirlin. Quantum criticality and minimal conductivity in graphene with long-range disorder. *Phys. Rev. Lett.*, 98:256801, 2007. doi: 10.1103/PhysRevLett.98.256801.
(Cited on page 74.)
- [84] P. M. Ostrovsky, I. V. Gornyi, and A. D. Mirlin. Electron transport in disordered graphene. *Phys. Rev. B*, 74:235443, 2006. doi: 10.1103/PhysRevB.74.235443.
(Cited on page 115.)
- [85] A. D. Mirlin, F. Evers, I. V. Gornyi, and P. M. Ostrovsky. Anderson transitions: Criticality, symmetries and topologies. *International Journal of Modern Physics B*, 24:1577, 2010. doi: 10.1142/S0217979210064526.
(Cited on page 74.)
- [86] K. I. Bolotin, K. J. Sikes, J. Hone, H. L. Stormer, and P. Kim. Temperature-dependent transport in suspended graphene. *Phys. Rev. Lett.*, 101:096802, 2008. doi: 10.1103/PhysRevLett.101.096802.
(Cited on pages 74 and 120.)
- [87] I. V. Gornyi, V. Yu. Kachorovskii, and A. D. Mirlin. Conductivity of suspended graphene at the dirac point. *Phys. Rev. B*, 86:165413, 2012. doi: 10.1103/PhysRevB.86.165413.
(Cited on page 74.)
- [88] Antti-Pekka Jauho and Henrik Smith. Coulomb drag between parallel two-dimensional electron systems. *Phys. Rev. B*, 47:4420, 1993. doi: 10.1103/PhysRevB.47.4420.
(Cited on page 75.)
- [89] Alex Kamenev and Yuval Oreg. Coulomb drag in normal metals and superconductors: Diagrammatic approach. *Phys. Rev. B*, 52:7516, 1995. doi: 10.1103/PhysRevB.52.7516.
(Cited on pages 77, 113, and 114.)
- [90] Karsten Flensberg, Ben Yu-Kuang Hu, Antti-Pekka Jauho, and Jari M. Kinaret. Linear-response theory of coulomb drag in coupled electron systems. *Phys. Rev. B*, 52:14761, 1995. doi: 10.1103/PhysRevB.52.14761.
(Cited on page 77.)
- [91] Alex Levchenko and Alex Kamenev. Coulomb drag at zero temperature. *Phys. Rev. Lett.*, 100:026805, 2008. doi: 10.1103/PhysRevLett.100.026805.
(Cited on pages 75, 95, 109, 110, 114, 163, and 164.)
- [92] P. M. Solomon, P. J. Price, D. J. Frank, and D. C. La Tulipe. New phenomena in coupled transport between 2d and 3d electron-gas layers. *Phys. Rev. Lett.*, 63:2508, 1989. doi: 10.1103/PhysRevLett.63.2508.
(Cited on page 77.)
- [93] T. J. Gramila, J. P. Eisenstein, A. H. MacDonald, L. N. Pfeiffer, and K. W. West. Mutual friction between parallel two-dimensional electron systems. *Phys. Rev. Lett.*, 66:1216, 1991. doi: 10.1103/PhysRevLett.66.1216.
(Cited on page 77.)

-
- [94] Martin Chr. Bønsager, Karsten Flensberg, Ben Yu-Kuang Hu, and A. H. MacDonald. Frictional drag between quantum wells mediated by phonon exchange. *Phys. Rev. B*, 57:7085–7102, 1998. doi: 10.1103/PhysRevB.57.7085.
(Cited on page 77.)
- [95] J. P. Eisenstein L. N. Pfeiffer D. Nandi, A. D. K. Finck and K. W. West. Exciton condensation and perfect coulomb drag. *Nature*, 488:481, 2012. doi: 10.1038/nature11302.
(Cited on page 77.)
- [96] I. V. Gornyi, A. G. Yashenkin, and D. V. Khveshchenko. Coulomb drag in double layers with correlated disorder. *Phys. Rev. Lett.*, 83:152, 1999. doi: 10.1103/PhysRevLett.83.152.
(Cited on pages 77, 114, 165, and 166.)
- [97] E. Tutuc S. Kim. Coulomb drag and magnetotransport in graphene double layers. *Solid States Communications*, 152:1283, 2012. doi: 10.1016/j.ssc.2012.04.032.
(Cited on page 77.)
- [98] M. I. Katsnelson K. S. Novoselov T. Tudorovskiy I. V. Grigorieva A. H. MacDonald S. V. Morozov K. Watanabe T. Taniguchi L. A. Ponomarenko R. V. Gorbachev, A. K. Geim. Strong coulomb drag and broken symmetry in double-layer graphene. *Nat Phys*, page 1745, 2012. doi: 10.1038/nphys2441.
(Cited on page 77.)
- [99] K. S. Novoselov, D. Jiang, F. Schedin, T. J. Booth, V. V. Khotkevich, S. V. Morozov, and A. K. Geim. Two-dimensional atomic crystals. *Proceedings of the National Academy of Sciences of the United States of America*, 102:10451, 2005. doi: 10.1073/pnas.0502848102.
(Cited on page 78.)
- [100] M. I. Katsnelson. Coulomb drag in graphene single layers separated by a thin spacer. *Phys. Rev. B*, 84:041407, 2011. doi: 10.1103/PhysRevB.84.041407.
(Cited on pages 78 and 94.)
- [101] N. M. R. Peres, J. M. B. Lopes dos Santos, and A. H. Castro Neto. Coulomb drag and high-resistivity behavior in double-layer graphene. *EPL (Europhysics Letters)*, 95:18001, 2011. doi: 10.1209/0295-5075/95/18001.
(Cited on page 114.)
- [102] E. H. Hwang, Rajdeep Sensarma, and S. Das Sarma. Coulomb drag in monolayer and bilayer graphene. *Phys. Rev. B*, 84:245441, 2011. doi: 10.1103/PhysRevB.84.245441.
(Not cited.)
- [103] B. N. Narozhny, M. Titov, I. V. Gornyi, and P. M. Ostrovsky. Coulomb drag in graphene: Perturbation theory. *Phys. Rev. B*, 85:195421, 2012. doi: 10.1103/PhysRevB.85.195421.
(Cited on pages 78, 79, 88, 93, 94, 96, 103, 109, 110, and 114.)
- [104] M Carrega, T Tudorovskiy, A Principi, M I Katsnelson, and M Polini. Theory of coulomb drag for massless dirac fermions. *New Journal of Physics*, 14:063033, 2012. doi: 10.1088/1367-2630/14/6/063033.
(Cited on pages 78, 94, and 114.)
-

- [105] Jonathan Lux and Lars Fritz. Kinetic theory of coulomb drag in two monolayers of graphene: From the dirac point to the fermi liquid regime. *Phys. Rev. B*, 86:165446, 2012. doi: 10.1103/PhysRevB.86.165446.
(Cited on pages 81 and 89.)
- [106] K. Kechedzhi, O. Kashuba, and Vladimir I. Fal'ko. Quantum kinetic equation and universal conductance fluctuations in graphene. *Phys. Rev. B*, 77:193403, 2008. doi: 10.1103/PhysRevB.77.193403.
(Cited on page 81.)
- [107] R. V. Gorbachev, A. K. Geim, M. I. Katsnelson, K. S. Novoselov, T. Tudorovskiy, I. V. Grigorieva, A. H. MacDonald, S. V. Morozov, K. Watanabe, T. Taniguchi, and L. A. Ponomarenko. Strong coulomb drag and broken symmetry in double-layer graphene. *Nat Phys*, page 1745, 2012. doi: 10.1038/nphys2441.
(Cited on pages 95, 96, 109, 111, and 120.)
- [108] Seyoung Kim and Emanuel Tutuc. Strong coulomb drag and broken symmetry in double-layer graphene. *Solid States Communication*, 152:1283, 2012. doi: 10.1016/j.ssc.2012.04.032.
(Cited on pages 95, 96, 108, 109, and 120.)
- [109] Irene D'Amico and Giovanni Vignale. Theory of spin coulomb drag in spin-polarized transport. *Phys. Rev. B*, 62:4853–4857, 2000. doi: 10.1103/PhysRevB.62.4853.
(Cited on page 99.)
- [110] Karsten Flensberg, Thomas Stibius Jensen, and Niels Asger Mortensen. Diffusion equation and spin drag in spin-polarized transport. *Phys. Rev. B*, 64:245308, 2001. doi: 10.1103/PhysRevB.64.245308.
(Cited on page 99.)
- [111] M. Pustilnik, E. G. Mishchenko, and O. A. Starykh. Generation of spin current by coulomb drag. *Phys. Rev. Lett.*, 97:246803, 2006. doi: 10.1103/PhysRevLett.97.246803.
(Cited on page 99.)
- [112] Y. Adamov, I. V. Gornyi, and A. D. Mirlin. Interaction effects on magneto-oscillations in a two-dimensional electron gas. *Phys. Rev. B*, 73:045426, 2006. doi: 10.1103/PhysRevB.73.045426.
(Cited on page 99.)
- [113] Martin Christian Bønsager, Karsten Flensberg, Ben Yu-Kuang Hu, and Antti-Pekka Jauho. Frictional coulomb drag in strong magnetic fields. *Phys. Rev. B*, 56:10314–10325, 1997. doi: 10.1103/PhysRevB.56.10314.
(Cited on page 103.)
- [114] Martin Christian Bønsager, Karsten Flensberg, Ben Yu-Kuang Hu, and Antti-Pekka Jauho. Magneto-coulomb drag: Interplay of electron-electron interactions and landau quantization. *Phys. Rev. Lett.*, 77:1366–1369, 1996. doi: 10.1103/PhysRevLett.77.1366.
(Cited on page 103.)
- [115] Leonid A. Ponomarenko et al. Privat communications. 2012.
(Cited on pages 108, 109, and 120.)

-
- [116] B. N. Narozhny. Coulomb drag as a measure of trigonal warping in doped graphene. *Physical Review B (Condensed Matter and Materials Physics)*, 76:153409, 2007. doi: 10.1103/PhysRevB.76.153409.
(Cited on page 114.)
- [117] W. Tse, B. H. Yu-Kuang, and S. Das Sarma. Theory of coulomb drag in graphene. *Physical Review B (Condensed Matter and Materials Physics)*, 76:081401, 2007. doi: 10.1103/PhysRevB.76.081401.
(Cited on page 114.)
- [118] B. N. Narozhny, I. L. Aleiner, and Ady Stern. Mesoscopic fluctuations of the coulomb drag at $\nu = 1/2$. *Phys. Rev. Lett.*, 86:3610–3613, 2001. doi: 10.1103/PhysRevLett.86.3610.
(Cited on page 114.)
- [119] H.L. Stormer Y.-W. Tan, Y. Zhang and P. Kim. Temperature dependent electron transport in graphene. *Eur. Phys. J. Special Topics*, 148:15–18, 2007. doi: 10.1140/epjst/e2007-00221-9.
(Cited on page 115.)
- [120] P. M. Ostrovsky, I. V. Gornyi, and A. D. Mirlin. Conductivity of disordered graphene at half filling. *The European Physical Journal Special Topics*, 148:63–72, 2007. doi: 10.1140/epjst/e2007-00226-4.
(Cited on page 115.)
- [121] P. M. Ostrovsky, I. V. Gornyi, and A. D. Mirlin. Quantum criticality and minimal conductivity in graphene with long-range disorder. *Phys. Rev. Lett.*, 98:256801, 2007. doi: 10.1103/PhysRevLett.98.256801.
(Cited on page 115.)
- [122] J. C. W. Song and L. S. Levitov. Energy-driven drag at charge neutrality in graphene. 2012. doi: 10.1103/PhysRevLett.109.236602.
(Cited on pages 165, 167, and 168.)

